Nonlinear Dynamics of the Tippedisk:
a holistic analysis

Von der Fakultät Konstruktions-, Produktions- und Fahrzeugtechnik
der Universität Stuttgart zur Erlangung der Würde eines
Doktor-Ingenieurs (Dr.-Ing.) genehmigte Abhandlung

Vorgelegt von
Simon Sailer
aus Göppingen (D)

Hauptberichter:	Prof. Dr. ir. habil. Remco I. Leine
Mitberichter:	Ao.Univ.-Prof.i.R. Dipl.-Ing. Dr.techn. Alois Steindl

Tag der mündlichen Prüfung: 27.10.2023

Institut für Nichtlineare Mechanik
der Universität Stuttgart

2023

To Alfred

Preface

This Monograph is the outcome of my time at the Institute for Nonlinear Mechanics of the University of Stuttgart. I want to thank Prof. Dr. Remco I. Leine for his dedicated supervision. Not only do I appreciate our time-intensive discussions, but also the freedom I have been given to pursue my scientific passion.

I would like to thank Prof. Dr. Alois Steindl for reviewing my thesis, whose work inspired me to apply singular perturbation theory to vehicle dynamics.

Dr. Simon R. Eugster's enthusiasm and his role as a second source of my mechanical education are deeply appreciated and I am deeply grateful to him. Special thanks go to Jonas Harsch for his friendship and our academic excursions, which greatly enhanced the tedious process of writing my dissertation. Together we are driven by our shared passion and plans for the future. Moreover, I would like to extend my appreciation to all my colleagues at the INM. In particular, I would like to thank Matthias Hinze and Pascal Preiswerk for the numerous dialogues and joint side projects, as well as for reading a good part of the thesis. Furthermore, I am grateful to Fabia Bayer for her excellent proofreading. I thank her, Yassine Karoui, and Lisa Eberhardt for our pleasant trips to conferences. Thanks also go to my students, especially Tianxiang Dai, Markus Hahn, and Simon Schuck.

The deepest gratitude, however, is reserved for my family and my beloved Sina, whose love and unconditional support are the basis of my drive.

Stuttgart, July 2023 Simon Sailer

Contents

Abstract

This dissertation deals with the tippedisk which is a new mechanical-mathematical archetype for friction-induced instabilities and exhibits an energetically counterintuitive inversion phenomenon.

In a holistic analysis, the dynamics of the tippedisk is investigated numerically in the field of multibody simulation, theoretically in the field of nonlinear dynamics, and experimentally in the focus of applied physics. Based on different nonsmooth rigid body models with set-valued force laws, the main physical mechanisms inducing the inversion behavior are identified and the governing system equations are derived. Subsequent model reduction results in a reduced system in the form of an ordinary differential equation, which is suited to be studied in the context of nonlinear dynamics. Both the local stability behavior of the non-inverted and inverted stationary spinning motions as well as the global proof of an existing heteroclinic saddle connection allow the dynamic behavior of the tippedisk to be captured analytically. The particular structure of the mathematical model reveals a singularly perturbed dynamics that evolves on multiple time scales and is characterized by slow rolling and fast sliding motions of the tippedisk. Utilizing perturbation expansions and an analysis in dimensionless quantities, the qualitative dynamics is characterized by closed-form expressions, from which a global stability map is deduced. Based on this complete stability map, three different bifurcation scenarios are identified, which correspond to different geometric and inertia properties, defining three qualitatively different types of tippedisks.

Finally, the mathematical investigation is complemented by high-speed experiments on a real test specimen. Qualitative comparison of experimental measurements with simulations at different levels of abstraction completes the holistic approach to the dynamic analysis of the tippedisk.

Zusammenfassung

Diese Dissertation befasst sich mit der Stehaufscheibe (engl. Tippedisk), die einen neuen mechanisch-mathematischen Archetyp für reibungsinduzierte Instabilitäten bildet und ein energetisch nicht intuitives Inversionsphänomen aufweist.

In einer ganzheitlichen Analyse wird die Dynamik der Stehaufscheibe sowohl numerisch im Bereich der Mehrkörpersimulation als auch theoretisch im Gebiet der nichtlinearen Dynamik und experimentell im Fokus der angewandten Physik untersucht. Basierend auf verschiedenen nicht glatten Starrkörpermodellen mit mengenwertigen Reibgesetzen, werden die erforderlichen physikalischen Mechanismen identifiziert, die das Inversionsverhalten induzieren. Die anschließende Modellreduktion resultiert in einem reduzierten System, in Gestalt einer gewöhnlichen Differentialgleichung, das im Hinblick auf die nichtlineare Dynamik untersucht wird. Sowohl die lokalen Stabilitätseigenschaften der nicht-invertierten und invertierten Drehbewegungen als auch der globale Nachweis eines heteroklinen Orbits erlauben es, das dynamische Verhalten der Stehaufscheibe analytisch zu erfassen. Hierbei offenbart die Systemstruktur eine singuläre Dynamik auf mehreren Zeitskalen, die sich durch langsame Rollbewegungen und schnelles Gleiten auszeichnet. Mithilfe von Störungsansätzen und dimensionsloser Analyse wird die qualitative Dynamik in geschlossener Form charakterisiert, woraus sich eine globale Stabilitätskarte ableiten lässt. Anhand der ermittelten Stabilitätskarte lassen sich drei Bifurkationsszenarien erkennen, die wiederum drei qualitativ verschiedene Typen von Stehaufscheiben definieren.

Die mathematische Untersuchung wird abschließend durch exemplarische Experimente an einem realen Prüfkörper ergänzt. Ein qualitativer Vergleich von experimentellen Messungen mit Simulationen auf verschiedenen Abstraktionsleveln komplettiert die ganzheitliche Analyse der Stehaufscheibe.

CHAPTER 1

Introduction

This monograph presents a holistic analysis of the tippedisk, a novel mechanical-mathematical archetype for friction-induced instabilities that exhibits a counterintuitive inversion phenomenon. To analyze the qualitative behavior of this archetype, various mechanical models are derived based on first principles and set-valued force laws, whose complexity is subsequently reduced by model order reduction. Based on the reduced models, concepts and tools of nonlinear dynamics such as singular perturbation theory and the Melnikov function method are used and applied to unveil the fundamental dynamics of the tippedisk. The introduction of dimensionless quantities allows to characterize the global behavior by closed-form expressions and reveals a variety of qualitatively different dynamics, implying different physical types of tippedisks. The theoretical analysis is complemented by high-speed measurements of experiments with a real specimen to complete the holistic approach.

This introductory chapter motivates the study of nonlinear mechanical archetypes for friction-induced phenomena and serves as an outline of this monograph. In addition, the relevant literature and the aims and objectives of this thesis are discussed.

1.1 Motivation

The ultimate goal of the research field of nonlinear dynamics is to understand the qualitative behavior of real-world systems that evolve with time. In particular, applications in mechanical engineering or robotics and control with the objective to influence a system in a predefined way by developing new mechanisms, applying control strategies or finding optimal solutions are real-world technical problems. An alternative issue in engineering application is the characterization of safe operating conditions, such as the under- and oversteering behavior of automobiles [118], loss of stability during aircraft ground maneuvers [100], the instability of towed wheels, also known as wheel shimmy [92], or even the characterization of critical speeds at which resonances lead to catastrophic failure of structural integrity [121, 12]. Regardless of the technical challenges, such as adapting an existing system or characterizing its qualitative behavior, appropriate mathematical models that predict the physical behavior are needed to access the dynamics.

Most systems in modern engineering include mechanical components in combination with mechatronic and electrical elements, which can be well-modeled by applying classical mechanics and models based on first principles. The modeling on first principles in combination with a non-trivial technical complexity of the system naturally results in large state dimensions. For example, finite element modeling is a common modeling approach in industrial research, easily involving thousands of degrees of freedom. In addition, more complex systems such as ones with constraints, friction, or impacts, are described by differential algebraic equations, or nonsmooth dynamical systems. However, most state-of-the-art tools and concepts in nonlinear dynamics are primarily applicable to smooth ordinary differential equations (ODEs). Moreover, the application to systems exceeding few states becomes cumbersome, which makes a closed-form analysis hardly possible. Therefore, it is rather difficult to apply the full repertoire of methods provided by nonlinear dynamics to real-world applications. As a result, engineers are often left with the only option of numerical simulation, which provides a system solution for a given parameter setting and one specific initial condition without offering any qualitative insight into the dynamics.

From an academic point of view, one may argue that nonlinear dynamics, as a branch of applied mathematics, is universally applicable and is not limited to the qualitative study of real-world systems. Consequently, for simplicity, fundamental theorems and methods are tested on examples and benchmark systems that are mostly just abstract ordinary differential equations with hardly any visible relationship to real-world applications, such as the Mathieu equation [106], which is assumed to describe the capsizing of ships. By restricting the techniques of nonlinear analysis (e.g., local and global stability analysis [63], Harmonic Balance Method [120], Melnikov theory [80], ...) to either abstract ODEs or almost trivial systems (e.g., the pendulum [119], the Duffing system [56], or the van Pol oscillator [55]) the research field of nonlinear dynamics risks to miss its ultimate goal, which is to understand and predict real-world phenomena.

At the same time, attempts are made to apply the collection of methods from nonlinear dynamics to engineering applications. For this purpose, expert knowledge from the specific field is used to derive a high-dimensional model to which numerical methods from nonlinear dynamics are applied, while closed-form analysis is usually unattainable. Moreover, these large systems often show a plethora of different phenomena. A further system reduction using expert knowledge eventually leads to simplified models that are better suited for analysis, but may also have lost their physical interpretability and are therefore not comprehensible to other researchers attempting to develop new methods in the field of nonlinear dynamics.

This motivates the search for nontrivial, real-world problems that exhibit a particular nonlinear phenomenon and can be studied in a laboratory set-up. Moreover, the behavior of such systems should be well described by dynamics with small state dimensions, and preceding reduction steps should not lead to a loss of physical interpretation. Ideally, the system should be technically simple and optimally 'handheld', facilitating dissemination to make the nonlinear phenomenon accessible to a wider audience. The above characteristics are quite demanding, which is why these systems are not just 'scientific toys', but must be considered as 'mathematical archetype systems'.

At this point, various gyroscopic systems enter the scene, consisting of a single rigid body in contact with a frictional support. In virtue of their technical simplicity, naturally low state dimension, and intrinsically nonlinear physical behavior, they are perfect candidates for mathematical archetype systems. Since their nature lies in mechanics, these systems are referred to as 'mechanical-mathematical archetypes'. Rolling and sliding disks, as well as spinning tops are examples of such mechanical-mathematical archetype systems and provide a scientific playground for the study of theoretical mechanics and nonlinear dynamics.

1.2 Literature

This section gives an overview of relevant literature, ranging from the modeling of nonsmooth systems, the fundamentals of theoretical and applied nonlinear dynamics to already existing mechanical-mathematical archetype systems in frictional contact. Since there exists a tremendous number of papers and books on nonlinear dynamics and nonsmooth mechanics in general, this literature review is far from complete. However, the main relevant topics and methods which are required for modeling and analyzing the tippedisk are listed in summarized form.

Nonsmooth dynamics

The research field of nonsmooth dynamics is about modeling and analysis of nonsmooth dynamical systems, i.e., systems with non-differentiable or even discontinuous solutions. When the focus is on a mechanical system, as in this monograph, the research is more precisely referred to as nonsmooth mechanics, with foundations laid by MOREAU [85, 84] and JEAN [58].

In multibody dynamics the Lagrange formalism, developed by LAGRANGE [69], as well as the formalism of projected Newton–Euler equations, provide a variational approach to modern mechanics. The books of BREMER [24] and PFEIFFER and SCHINDLER [96] give a good overview of the Lagrange formalism. For an introduction to the projected Newton–Euler equations, the reader is referred to the works of WITTENBURG [132], PFEIFFER and SCHINDLER [96], and GLOCKER [44]. Both formalisms offer a structured way to derive the equations of motion in generalized coordinates, taking into account inertia and potential forces. Assuming the potential to be smooth and differentiable, as in the case of the gravity potential, the resulting equations of motion correspond to ordinary differential equations. However, using the concept of virtual work [44], additional forces like friction or normal contact forces can easily be embedded in this generalized framework.

Especially, friction has a long tradition, with fundamentals laid by AMONTONS and COULOMB, in the 17th and 18th centuries, respectively. According to the laws of AMONTONS, friction is proportional to the normal contact force and independent of the size of the contact area. Classical viscous friction, i.e., a friction force that smoothly depends on the relative sliding velocity of the contact point and is scaled by the normal contact force, satisfies AMONTONS laws and, when incorporated into the equations of motion, again results in an ordinary differential equation. Based on COULOMB'S observation, which states that dry sliding friction is independent of the velocity and constant in magnitude opposing sliding direction, dry Coulomb friction is obtained by assuming a force with constant magnitude whose direction changes as a function of sliding velocity, see the introduction of LEINE and NIJMEIJER [74]. Including Coulomb friction into the system equations yields a hybrid dynamics consisting of multiple systems of ordinary differential equations and a switching law that selects the active one. A similar hybrid structure is also found in switching systems with constraint activation, as in models for walking robots [39] when a contact closes or opens. Assuming Coulomb friction, solutions may end up in a sliding mode on the so-called switching manifold that characterizes pure rolling motions, i.e., motions with zero sliding velocity and thus motions for which the frictional force is not defined. Moreover, according to the switching nature, a local stability analysis of pure rolling motions is infeasible.

The framework of nonsmooth dynamics utilizes convex analysis, treated in the books of ROCKAFELLAR [103] and CLARK [30], to develop set-valued force and impact laws, as done by PFEIFFER and GLOCKER [95, 44]. Set-valued spatial Coulomb friction, discussed in the book of GLOCKER [44], is an essential friction law that is valid for both sliding and rolling motions. Assuming persistent contacts in combination with set-valued Coulomb friction yields a system of differential algebraic inclusions. Corresponding to the set-valued nature, the local stability of pure rolling motions is again infeasible. To incorporate tangential sliding and pivoting friction in a single set-valued force law, LEINE and GLOCKER [73] extended spatial set-valued Coulomb friction to the more generalized Coulomb–Contensou friction law. In persistent contact when the relative pivoting velocity is non-zero, the set-valued Coulomb–Contensou friction degenerates to a smooth friction law, allowing to perform a local stability analysis, cf. the linear stability analysis of the tippetop [73].

In the most general case, when dealing with unilateral contact and impacts, the equations of motion with corresponding set-valued friction and normal contact laws have to be complemented by impact equations with associated impact laws. The resulting dynamical systems have the form of measure differential equations, cf. the book of LEINE and VAN DE WOUW [75]. When dealing with nonsmooth dynamics, it is essential to also acknowledge the comprehensive contributions of ACARY and BROGLIATO [1, 26]. Their works encompass numerical implementation and offer a broad overview.

Fundamentals of nonlinear dynamics

Nonlinear dynamics is a research field in applied mathematics that emerged in the late 19th century with the aim of understanding the qualitative behavior of dynamical systems, i.e., systems whose states evolve with time. The dynamic behavior of these systems is determined by mathematical models, whereas their origin in mechanics, electronics, biology, etc. often plays only a minor role. The books authored by KHALIL [63] and STROGATZ [119] provide a good overview of the field. To characterize asymptotic dynamics, the stability behavior is of particular importance. The local behavior of a linear system is (in the hyperbolic case) characterized by the real part of the eigenvalues, cf. [76, 63]. Based on the works of ROUTH [104] and HURWITZ [57], the Routh–Hurwitz criterion was established which determines the location of the corresponding eigenvalues in the complex plane and thus the stability of the linear system.

For nonlinear systems, LYAPUNOV introduced a more general concept of stability to study asymptotic behavior in the neighborhood of equilibria [63, 64]. Based on the concept of Lyapunov stability, the research branch of bifurcation theory emerged, which studies system behavior in dependence of system parameters, see also the book of KUZNETSOV [68]. Exploiting the system structure allows to get deeper understanding by using tools from geometrical mathematics. For example, FENICHEL [35, 34] used geometric structure to study system behavior on invariant manifolds, which forms the foundations of singular perturbation theory. A more detailed introduction to singular perturbation theory can be found in the books of WIGGINS [130], VERHULST [125], and SHCHEPAKINA et al. [115].

Since the beginning of dynamics, scientists and researchers analyzed mechanical systems to study their qualitative behavior. As their system description originates from mechanical principles but tools and concepts from nonlinear dynamics are applied, this approach defines the research field of nonlinear mechanics.

In engineering applications such as vehicle dynamics, there are many example mechanical systems that exhibit nonlinear behavior. The hunting motion of railroad vehicles induces lateral vibrations if the traveling speed exceeds a certain value, see TRUE [123] and GARG [41]. For a planar two-wheeled vehicle, a slow-fast system behavior caused by stiff tire interactions can be observed, as shown by STEINDL et al. [118]. In summary, the nonlinear dynamics of mechanical systems strongly depends on the underlying modeling assumptions and requires a holistic approach.

Mechanical-mathematical archetypes

Already in the 18th and 19th centuries, EULER and POINSOT [97] analyzed the gyroscopic behavior of a single rigid body and presented description of its motion. For example, the intermediate axis theorem, also known as the tennis racket theorem [8] was predicted by Euler and Poinsot. In the 20th century, the cosmonaut V.A. Dzhanibekov observed a recurring flipping behavior of a wing nut in space, which is why the intermediate axis theorem is also known as the Dzhanibekov effect [122]. This particular gyroscopic behavior is also crucial during free flight in rockfall simulations, so numerical integration schemes must be able to capture this behavior, see LEINE et al. [72].

When a rigid body interacts with a frictional support, the interplay of gyroscopic and contact forces causes even richer dynamics. In this monograph, the focus is on the dynamic behavior of the tippedisk, which is essentially an unbalanced disk-like rigid object in frictional contact, forming a novel mechanical-mathematical archetype. Since there is already a lot of preliminary work on other rigid body systems in frictional contact, the most relevant mechanical-mathematical archetype systems are discussed below.

Spinning and rolling disks

The problem of a thin disk in contact with a flat support has a long history and dates back to the 19th century. Classical literature distinguishes between inherently different assumptions, i.e., the contact is assumed to be either infinitely smooth or rough. Accordingly, the system equations are obtained either by neglecting the frictional forces or by formulating nonholonomic constraints. CHAPLYGIN [28] showed the integrability of a homogeneous disk under pure rolling assumption. Independently of each other APPELL [7] and GALLOP [38] presented a solution to the problem. In the work of ROUTH [105], the local dynamical behavior of steady state motions was studied. About three decades ago, a complete stability analysis of rolling and sliding disks was presented by O'REILLY [91]. In addition, the presence of heteroclinic orbits was mentioned. For an infinitely thin disk under the assumption of pure rolling, BORISOV et al. [19] conducted a qualitative analysis and revealed the system to be Hamiltonian. In the works of BATISTA [9, 10], the system was extended to a disk with finite thickness. Considering an infinitely smooth or rough ground, the disk is either in the state of pure sliding or pure rolling. Therefore, the above mentioned works neglect dissipation, e.g., due to sliding friction or air resistance. Strictly speaking, this is not physically valid for a real specimen on a table.

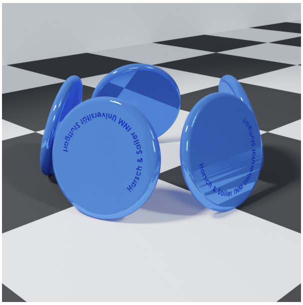

Figure 1.1: Circular rolling motion of a disk.

However, considering the dynamical behavior on different time scales enables one to focus on the most important physical effects and neglect the effect of, e.g., friction on short time scales. Even with minimal dissipation, a rolling disk will eventually reach equilibrium on a long time scale. Neglecting dissipation mechanisms such as air drag or sliding friction, the circular rolling motion shown in Figure 1.1 is a good description and motivates the analysis of stationary and dissipative free pure rolling motions, cf. [94]. Following OLSSON [89], the coin spinning on a table is described by neglecting friction forces as the lying down rate is small compared to the precession rate. The assumption of viscous friction at the contact point of a rolling disk allowed the study of the asymptotic dynamics, e.g., PRZYBYLSKA and RAUCH-WOJCIECHOWSKI [99] showed that the asymptotic solutions of straight-line rolling, vertical rotation and tumbling are characterized by the existence of first integrals.

The consideration of dissipation opens the door to a plethora of different phenomena and various mechanical-mathematical gyroscopic archetype systems, forming a scientific playground for research in theoretical mechanics.

Euler's disk

The Euler disk from Figure 1.2 is an archetype for finite-time singularities, describing the final stage of motion when a disk falls down and finally comes to an abrupt halt of the motion. According to dissipation, the energy decreases and the inclination approaches zero, while the rolling velocity of the contact point diverges to infinity. In particular, different dissipation mechanisms have been hypothesized in various works on the dynamics of Euler's disk.

In his pioneering article, MOFFATT [81] considered aerodynamic drag as main dissipation mechanism of Euler's disk. A generalized form of velocity-dependent friction was studied by MCDONALD and MCDONALD [79]. In KESSLER and O'REILLY [62], the effect of physical rolling, sliding and pivoting friction has been analyzed. However, the derived model shows an asymptotic energy decrease and therefore does not have a finite-time singularity. Applying set-valued friction laws from nonsmooth mechanics LE SAUX et al. [70] succeeded in obtaining a model that exhibits finite-time singularity. In addition, the energy decay was investigated in dependence on various friction laws. The experimental analysis of LEINE [71] questioned the drag of air as dominant dissipation mechanism and suggests the importance of contour friction. Following the Euler disk, in a recent study, BORISOV et al. [17] analyzed the retrograde motion of a rolling ring and concluded that, again, frictional effects outweigh aerodynamic drag.

Figure 1.2: Euler's disk, with finite-time singularity.

Rattleback

Figure 1.3 shows a half ellipsoid with inertia asymmetry in contact with a flat support, also called a rattleback. If this ratteback is spun in clockwise direction, the axis of rotation remains persistent. In contrast, if spun in counter-clockwise direction, an instability causes the the rattleback to reverse its axis of rotation.

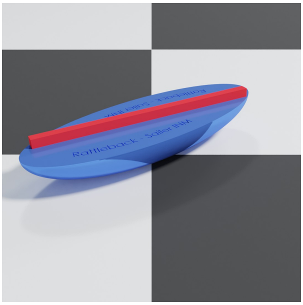

Figure 1.3: A rattleback whose inertia tensor implies stable clockwise rotation.

Therefore, the rattleback takes the role of a mechanical-mathematical archetype describing friction-induced spin reversal. In a first approach to analyze this phenomenon, WALKER [129] assumed dissipation free rolling of an ellipsoid and showed that stable motions only occur in one spin direction. However, MAGNUS [78] questioned the pure rolling condition and motivated a viscous friction law. A detailed theoretical and experimental investigation of the rattleback was performed by GARCIA and HUBBARD [40]. Later, BORISOV and MAMAEV [18] analyzed the dynamical behavior of the rattleback in pure rolling and numerically revealed the rich global dynamics, even containing strange attractors. Due to its interesting global behavior, the rattleback is still a topic of current research, e.g., GONCHENKO et al. [46] and RAUCH-WOJCIECHOWSKI and PRZYBYLSKA [102].

Tippetop and spinning axisymmetric bodies

The tippetop is another mechanical-mathematical archetype, showing a friction-induced inversion phenomenon of a mushroom shaped toy top, invented by the German nurse HELENE SPERL [117] in the late 19th century. In Figure 1.4, the inversion phenomenon of the tippetop is depicted. On the left side, the top rotates in a non-inverted spinning configuration. Since the non-inverted motion is unstable, the top starts to wobble (see center) until it reverses its orientation and reaches the inverted spinning configuration on the right side.

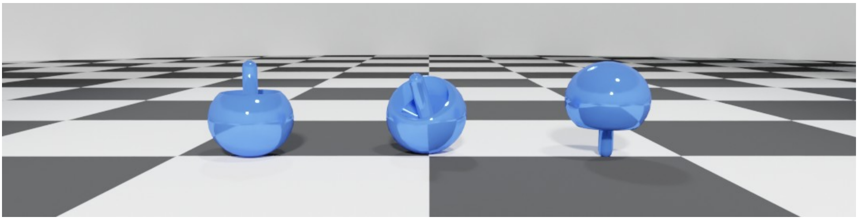

Figure 1.4: Inversion phenomenon of the tippetop.

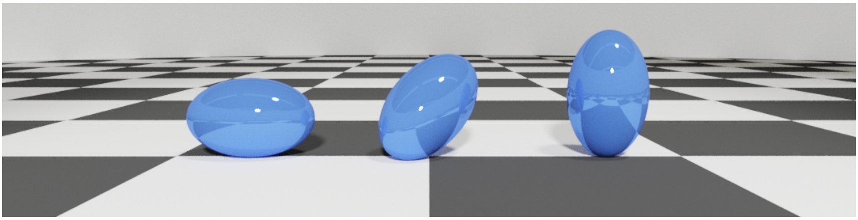

Figure 1.5: Rising phenomenon of an axisymmetric spinning body in form of a (prolate) spheroid.

With a rise of the center of gravity, it seems like gyroscopic and friction forces defy gravity. In the work of COHEN [31], it was shown that sliding friction in the contact point, i.e., a constant friction force acting in negative sliding direction, is suited to describe the inversion of the tippetop. Later, OR [90] assumed a viscous friction law and concluded that both sliding friction and viscous friction cause the inversion phenomenon, cf. the earlier work of O'BRIEN [88]. As a benchmark system for set-valued Coulomb–Contensou friction, LEINE [73] introduced a full model of the tippetop considering sliding and pivoting frictional forces. For a rotating state, Coulomb–Contensou friction degenerates to a smooth friction law and thus meets the necessary conditions for stable spinning motions of the tippetop outlined by MAGNUS [77]. The subsequent analysis of BOURABEE [20] evidenced a heteroclinic connection between non-inverted and inverted spinning. Moreover, it was shown that translational effects play a minor role and that the translational energy of the tippetop is negligible. By utilizing the findings of JELLET [59], RAUCH–WOJCIECHOWSKI [101] obtained the 'main equation for the tippetop', in form of a first-order time dependent ordinary differential equation.

Similar to the tippetop, spinning eggs also exhibit a rise of the center of gravity if spun on a flat support. The scientific toy 'PhiTOP'[1], is basically the symmetric equivalent to an egg, and has been studied extensively by the scientific research community. In Figure 1.5, the rising phenomenon of an axisymmetric spinning body in form of a prolate spheroid is depicted. Similar behavior can be observed for oblate spheroids. Unlike the tippetop, a spinning spheroid does not invert its orientation because non-inverted and inverted motions correspond to rotations about the same axes, and the non-raised and raised stationary motions of a spheroid indicate rotations about orthogonal axes. In the paper series [82, 83, 116, 22, 23]

---

[1] http://www.thephitop.com/

of MOFFATT, SHIMOMURA and BRANICKI, the dynamics of axisymmetric bodies spinning on flat support has been extensively studied. For axisymmetric bodies, MOFFATT [82] claimed that sliding friction must be present to observe a 'rise' phenomenon. In this preliminary work, it has been assumed that friction is weak and the spinning speed is large, which causes the Coriolis force to dominate, yielding a first-order ordinary differential equation governed by gyroscopic balancing. Moreover, by assuming weak friction the horizontal velocity components were taken to be zero. This is not accurate from a physical point of view. It is, nonetheless, a reasonable approximation. In the second paper, MOFFATT [83] applied 'dry' and viscous friction laws to the problem and studied the stability by a local analysis.[2] In addition, it was found that the normal force can decrease to zero, suggesting self-induced jumping, which was subsequently investigated by SHIMOMURA [116]. To close the paper series, BRANICKI [22, 23] extended the previous findings to general axisymmetric convex bodies. Even though the early research on these rising archetypes dates back to the mid-19th century [37, 21, 88], the topic is still of current scientific interest interest [32, 61, 16, 65].

The tippedisk and its variants

At this point, it is interesting to note that the phenomenon of inversion also occurs with unbalanced disk-like objects, shown in Figure 1.6. The first example can easily be made from a paperclip and corresponds to an unbalanced circularly shaped ring. In Figure 1.6(a), the ring-shaped paperclip is depicted in an almost inverted spinning configuration. The 'orbit spinning top' from Figure 1.6(b) is a commercial toy, consisting of a thin disk and an eccentrically attached sphere, and also shows the inversion phenomenon [47]. The only sources which mention or discuss the inversion phenomenon of asymmetric disks are non-academic and either from social media or from websites of producers of scientific toys. According to their technical simplicity and the fascinating counterintuitive behavior, these unbalanced disk-like bodies exhibit inversion phenomena and are used to enthuse people about physics, cf. UCKE [124]. The inversion behavior of an unbalanced disk attracted plenty of attention on social media [127, 128]. Although there is enormous fascination and enthusiasm for these types of systems, there is no rigorous scientific analysis and all existing explanations are based on intuitive considerations and pseudo-scientific statements such as 'the disk inverts because this is energetically beneficial' or the

---

[2] The terminology 'dry' friction in the context of nonsmooth mechanics suggests a friction law that describes both sliding and sticking in one set-valued force law. Here, however, 'dry friction' means a constant force acting in the counter-slip direction, with the magnitude of the scaled normal force.

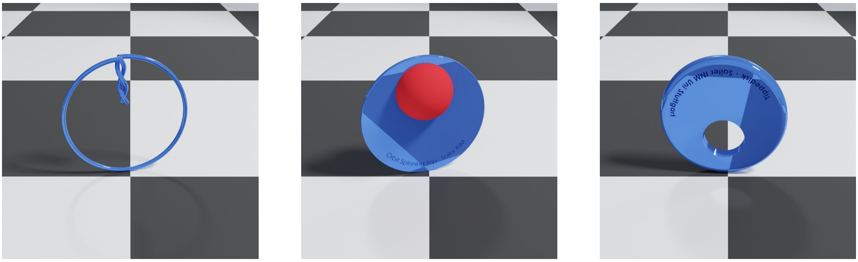

(a) Ring-shaped paperclip (b) Orbit Spinning Top (c) Tippedisk

Figure 1.6: Mechanical-mathematical archetype systems with disk-like shape that exhibit an inversion phenomenon when spun on a flat support. All three examples are depicted in an almost inverted spinning configuration.

inversion is explained by the ‘effect of the tippetop’, which is obviously neither a physical effect nor a principle. From a phenomenological point of view, the Dzhanibekov effect is also attributed for this behavior. However, this argumentation can be directly falsified by the fact that the inversion is a one-way process.

Unlike the tippetop, these spinning unbalanced disk-like bodies do not have any rotational symmetry in geometry or inertia, and are therefore inherently different. Consequently, the tippedisk as a novel mechanical-mathematical archetype was introduced by the author to study the dynamical behavior of spinning unbalanced disk-like bodies in frictional contact. A detailed list of the relevant publications on the tippedisk is given in Section 1.5. In Figure 1.6(c), the tippedisk is depicted in an inverted spinning configuration. By changing inertia and dimensional properties, the dynamics of the tippedisk contains both the dynamics of the unbalanced paperclip and the orbit spinning top. Thereby, the tippedisk to some extent closes the gap between the dynamics of spinning and rolling disks and the spinning of axisymmetric rigid bodies.

1.3 Objectives

The overall aim of this monograph is to introduce the tippedisk as a new mechanical-mathematical archetype for friction-induced instabilities and to present a holistic analysis of its dynamics, ranging from the fields of rigid body mechanics to nonlinear dynamics and experimental investigations.

To this aim, four main objectives are of particular importance and are defined below.

Objective 1. Introduction of the tippedisk as a novel mechanical-mathematical archetype and explanation of its inversion behavior from a phenomenological point of view to a wide audience.

Objective 2. Embedding of the tippedisk in the context of rigid body dynamics and nonsmooth mechanics:

> **Objective 2.1.** Derivation of full nonsmooth numerical simulation models based on first principles and state-of-the art contact mechanics to describe the inversion phenomenon from **Objective 1**.
>
> **Objective 2.2.** Comparison of different set-valued and smooth friction laws in order to identify the main relevant effects that cause inversion.
>
> **Objective 2.3.** Implementation of different model parametrizations in order to obtain a problem description in physical coordinates.

Objective 3. Perform an in-depth nonlinear dynamical analysis to characterize the qualitative system behavior of the tippedisk:

> **Objective 3.1.** Reduction and simplification of the system equations of the mechanical models resulting from **Objective 2**.
>
> **Objective 3.2.** Execution of an in-depth global analysis for the tippedisk introduced with respect to **Objective 1**.
>
> **Objective 3.3.** Identification of system parameter domains that characterize various bifurcation scenarios and thus different types of tippedisks.
>
> **Objective 3.4.** Description of the qualitative system behavior by closed-form expressions validated through application of numerical tools and methods.

Objective 4. Conduct an experimental investigation of a real specimen:

> **Objective 4.1.** Implementation of high-speed measurements using object tracking and camera fusion.
>
> **Objective 4.2.** Comparison of the experimental behavior of a real specimen with the qualitative findings of the nonlinear dynamics analysis from **Objective 3** and full model simulations as results from **Objective 2**.

1.4 Contributions

This monograph contributes to a variety of research fields ranging from engineering to applied mathematics, like the fields of rigid body and nonsmooth mechanics, nonlinear dynamics, and experimental physics, by presenting a holistic analysis of the novel mechanical-mathematical archetype, the tippedisk.

The above objectives are addressed in the contributions of the thesis.

Contribution 1. With respect to **Objective 1**, the first contribution of this thesis is the introduction of the tippedisk as a new mechanical-mathematical archetype, showing a counterintuitive inversion phenomenon. For a specific specimen, the dimension and inertia properties are discussed, stationary spinning solutions are introduced, and the inversion behavior is described using a stroboscopic sequence of a preliminary experiment.

The technical simplicity of the tippedisk allows to manufacture a palm-sized mechanical system that exhibits an interesting behavior because it is inherently nonlinear due to gyroscopic forces. Moreover, the real-world problem can easily be studied in a laboratory setup.

Contribution 2. As a contribution in the field of rigid body dynamics and to address **Objective 2.1**, various mechanical models of the tippedisk are derived based on first principles, using various set-valued and/or smooth friction laws considering different parametrizations. Based on full model simulations, the main underlying physical effects causing the inversion behavior are identified, see **Objective 2.2** and **Objective 2.3**.

The derived models are perfectly suited to test numerical integration schemes, as their nature is highly nonlinear, the contact can be either considered to be unilateral or persistent, and different friction laws can be applied.

Moreover, the Blender-based animation application developed by the author enables a qualitative comparison of real experiments with high-quality renderings of simulation results. In the scope of **Objective 1**, this also serves to present the inversion behavior of the disk in a visually appealing way to a non-scientific audience.

Contribution 3. Utilizing the findings of the investigations on the mechanical models, this thesis shows that the inversion phenomenon of the tippdisk can be described by an ordinary differential equation.

By providing a set of nonlinear system equations, the dynamics can be analyzed using concepts and methods from the field of nonlinear dynamics.

Contribution 4. To link the field of rigid body mechanics to the research branch of nonlinear dynamics and to answer **Objective 3.1**, this monograph performs a model order reduction based on physical principles and assumptions with the result of a low-dimensional nonlinear dynamical system that qualitatively describes the inversion phenomenon of the tippedisk.

Contribution 5. In addition, this thesis contributes to the field of nonlinear mechanics by revealing a singularly perturbed dynamical structure induced by specific friction laws of mechanical systems whose motions resemble pure rolling.

Vice versa, the slow-fast system behavior determined by singularly perturbed dynamics can be physically interpreted in the context of rigid body dynamics.

Contribution 6. A global bifurcation analysis for a specific specimen is performed with respect to **Objective 3.2**.

In detail, the specific contributions are:

> **Contribution 6.1** For the full mechanical and reduced tippedisk models, the local stability of stationary inverted and non-inverted spinning solutions is investigated, evidencing the existence of a Hopf bifurcation.
>
> **Contribution 6.2** To identify the type of Hopf bifurcation, a perturbation expansion of the harmonic balance method is applied, which provides a closed-form characterization.
>
> **Contribution 6.3** The singularly perturbed dynamical structure of the system equations is exploited to provide a conclusive stability analysis over time scales.
>
> The asymptotic dynamics on the slow manifold manifests as a regularly perturbed Hamiltonian system, allowing for the application of the Melnikov theory.
>
> **Contribution 6.4** The Melnikov function method is adapted and applied to the dynamics on the slow manifold, to obtain a necessary condition for the existence of a heteroclinic saddle connection. Utilizing perturbation expansions, various closed-form approximations of the involved integrals are presented, ultimately providing an approximation of the heteroclinic spinning velocity.

All of these **Contributions 6.1-6.4** are crucial to conduct the global analysis requested in **Objective 3.2**. The closed-form expressions derived by utilizing perturbation expansions are consistent with numerical validations, justifying the nonlinear analysis in terms of **Objective 3.4**.

Contribution 7. Based on the closed-form findings, a normalization is performed to identify dimensionless system parameters that characterize qualitatively different bifurcation scenarios and thus imply further variants of the tippedisk, as requested in **Objective 3.3**.

Again, the corresponding results are validated numerically to meet **Objective 3.4**.

In the framework of nonlinear dynamics, the reduced model of the tippedisk is perfectly suited to test novel tools and methods, e.g., to characterize stable/unstable heteroclinic connections, fold bifurcations, sub- or supercritical Hopf bifurcations and to analyze slow-fast system behavior.

Contribution 8. As a final contribution to the field of applied mechanics in context of **Objective 4.1** and **Objective 4.2**, this thesis compares results of high-speed measurements of an experiment on a real specimen with the findings of nonlinear analysis and the physics-based simulation models.

In addition, the self-developed high-speed setup and object tracking system enables the fusion of measurements from multiple cameras at different perspectives, resulting in accurate measurement and an uninterrupted time signal. Consequently, the implemented high-speed measurement setup and object tracking system set a standard for subsequent experimental investigations.

1.5 List of own publications

In this monograph, findings from previous publications are supplemented with new results to obtain a holistic and self-consistent analysis of the tippedisk.
The relevant publications of the author are:

- S. Sailer, S. R. Eugster, and R. I. Leine. The tippedisk: a tippetop without rotational symmetry. *Regul. Chaot. Dyn.*, 25(6):553–580, 2020
- S. Sailer, S. R. Eugster, and R. I. Leine. The tippedisk: A minimal model for friction-induced inversion. In *Proceedings of the ECCOMAS Thematic Conference on Multibody Dynamics, Budapest*, 2021
- S. Sailer and R. I. Leine. Model reduction of the tippedisk: a path to the full analysis. *Nonlinear Dyn*, 105(3):1955–1975, 2021
- S. Sailer and R. I. Leine. Singularly perturbed dynamics of the tippedisk. *Proc. R. Soc. A*, 477(2256), 2021
- S. Sailer and R. I. Leine. Why does the tippedisk invert? Theory and experiments. In *Proceedings of the ENOC 2020+2 Conference, Lyon*, 2022

- S. Sailer and R. I. Leine. Heteroclinic bifurcation analysis of the tippedisk through the use of Melnikov theory. *Proc. R. Soc. A*, 2023
- S. Sailer and R. Leine. A complete stability chart for the tippedisk. In *Proceedings of the NODYCON 2023 Conference, Rome*, 2023

1.6 Outline

The first introductory chapter motivates the research and embeds the monograph in the relevant literature. It also presents the objectives and contributions of this thesis.

Chapter 2 introduces, from a phenomenological perspective, the tippedisk as a new mechanical-mathematical archetype that exhibits a counterintuitive inversion phenomenon caused by frictional and gyroscopic effects. Moreover, Section 2.2 presents the dimension and inertia properties for a particular specimen, which is subsequently studied in the following of this monograph.

The main body of Chapter 3 has been published in [107] and is presented in a revised form. After a short general introduction into rigid body kinematics and kinetics in Sections 3.1-3.3, Section 3.4 introduces the kinematics of the tippedisk. In Section 3.5, several contact laws are discussed, distinguishing between normal and frictional forces. In particular, friction plays an important role in describing the inversion behavior of the tippedisk. Therefore, the set-valued Coulomb, Coulomb–Contensou, pivoting and contour friction laws are discussed, accompanied by the smooth regularized Coulomb friction law. In Section 3.6, a non-singular parametrization using unit quaternions is derived, which is complemented by a second parametrization in physical coordinates. The applied numerical integration concepts are presented in Section 3.7, followed by the simulation results in Section 3.8, which are subsequently discussed in Section 3.9.

Based on the physical rigid body models derived in Chapter 3, a reparametrization is performed in Chapter 4 and Lyapunov's indirect method is applied in Section 4.1 to analyze the local stability behavior. In Section 4.2, a qualitative model reduction is performed by numerically introducing physical constraints. The corresponding dynamical behavior is subsequently investigated by a linear stability analysis and the application of the harmonic balance method, validated by the implementation of a numerical shooting and continuation procedure, as discussed in Sections 4.3-4.5.

The body of Chapter 5 has been published in [113]. Section 5.1 and Section 5.2 introduce singular perturbation theory and the Melnikov function method. The two fundamental sections set notation for the subsequent application of the presented methodologies to the dynamics of the tippedisk, cf. Section 5.3. Section 5.4 presents the bifurcation diagram of the tippedisk, with properties from Table 2.1. The following Section 5.5 reveals a second physical tippedisk variant, motivating to study the global behavior in a dimensionless context.

The last theoretical Chapter 6 conducts a global analysis by normalizing system equations and conditions from the preceding investigations. The dimensionless analysis finally allows to identify three parameter groups, implying three different qualitative bifurcation diagrams, cf. Section 6.4.

Chapter 7 presents an experimental investigation of a real specimen, i.e., the tippedisk *V1* defined in Section 2. In Section 7.1, the experimental setup of the developed high-speed object-tracking system is described. The results of four experiments each, initially starting in inverted and non-inverted spinning configurations, are presented in Section 7.2. The experimental chapter closes with a comparison of two example experiments with their respective predictions from full and reduced model simulations, followed by a discussion, see Section 7.3 and Section 7.4.

Finally, Chapter 8 concludes the thesis by recapping the big picture of the holistic analysis, and summarizing the main contributions of this monograph. In addition, an outlook is given on further scientific issues arising from the results of this monograph, including possible applications of the proposed methodology.

Chapter 2

The tippedisk

The tippedisk is a mechanical-mathematical archetype for a peculiar friction-induced inversion phenomenon, first introduced to the academic research community and scientifically studied in [107].

2.1 The phenomenon of inversion

Essentially, the tippedisk is an eccentric disk whose center of gravity (COG) does not coincide with the geometric center G of the disk. One way to construct such a tippedisk is to take a homogeneous disk and remove mass at an arbitrary distance, e.g., by drilling a hole at an arbitrary point that does not coincide with the geometric center. If such a specimen is placed on a flat support, like a flat table, in the gravitational field, it is quite obvious that there are two equilibria where the gravitational force and the normal contact force balance each other. Namely, an equilibrium where the COG is below the geometric center G and one where the COG is vertically above G. From an energetic point of view, the equilibrium with the center of gravity below the geometric center has a lower potential energy than the second equilibrium with an elevated center of gravity. In analogy to the mathematical pendulum, it is natural to refer to the equilibrium with the lower potential as *non-inverted equilibrium*, while the configuration with the COG above is called *inverted equilibrium*.

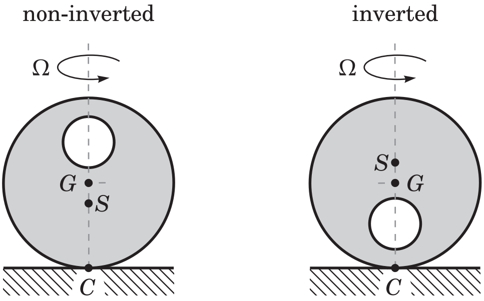

Figure 2.1: Stationary motions of the tippedisk. For *non-inverted* spinning, the center of gravity S is located below the geometric center G and the disk is spinning about the in-plane axis through S and G and the contact point C. The *inverted* motion is similar to non-inverted spinning, but with S located above G.

Neglecting the influence of pivoting friction, two qualitatively different stationary motions can be observed, corresponding to a spinning of the non-inverted and inverted equilibrium configuration about the vertical. Accordingly, these stationary spinning motions are called non-inverted and inverted spinning and are shown in Figure 2.1. If other dissipation mechanisms such as pivoting friction, which depends on the micro structure, or even air resistance are taken into account, the energy inevitably decreases. From this energetic point of view, one may naturally be tempted to assume that the non-inverted spinning of the disk is energetically somewhat more 'beneficial' than the spinning in the inverted configuration. However, the stroboscopic sequence of a laboratory experiment in Figure 2.2 shows the inversion of the disk obtained from high-speed recordings at 500 fps. If the non-inverted tippedisk is spun fast around an in-plane axis, the center of gravity rises until the disk ends in an inverted configuration, this somewhat contradicts the energetic intuition from above. As the disk transitions from a non-inverted state of spinning to an inverted one, accompanied by an increase of the potential energy this transient process is called the inversion phenomenon of the tippedisk. The experimental observations qualitatively indicate that for a fastly spinning tippedisk, non-inverted spinning is unstable, while inverted spinning appears to be attractive. Moreover, the non-inverted spinning solution corresponds to an isolated point in the region of attraction of the inverted spinning. In particular, stable inverted spinning attracts trajectories corresponding to a perturbed spinning in non-inverted configuration. In analogy to the well-known tippetop, which also shows an inversion phenomenon

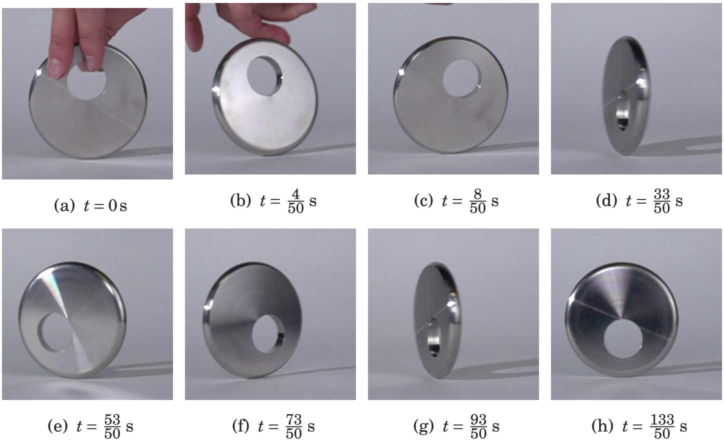
(a) $t = 0\,\mathrm{s}$ (b) $t = \frac{4}{50}\,\mathrm{s}$ (c) $t = \frac{8}{50}\,\mathrm{s}$ (d) $t = \frac{33}{50}\,\mathrm{s}$

(e) $t = \frac{53}{50}\,\mathrm{s}$ (f) $t = \frac{73}{50}\,\mathrm{s}$ (g) $t = \frac{93}{50}\,\mathrm{s}$ (h) $t = \frac{133}{50}\,\mathrm{s}$

Figure 2.2: Experiment: Stroboscopic sequence showing the inversion behavior of the tippedisk. The experiment is started in the non-inverted configuration.

when spun rapidly, the name *tippedisk* becomes clear.

Instead of arguing by potentially misleading intuition, the subsequent analysis of the dynamics of the tippedisk is based on rigorous modeling and system analysis in the context of nonlinear dynamics. In order not to overload the complexity of the equations by analyzing different parameter influences and identifying dimensionless quantities, a real specimen is first considered in the following analysis. Later, the results are used to define dimensionless quantities that allow to classify various qualitative bifurcation scenarios and thus different variants of tippedisks.

2.2 Dimension and inertia properties of a real specimen

Figure 2.3 shows the dimensions of a real specimen considered in the first part of this monograph. The main dimensions of the tippedisk are the radius r and the thickness h; the rounding of the edge is neglected. For a given body-fixed frame $B = (G, \boldsymbol{e}_x^B, \boldsymbol{e}_y^B, \boldsymbol{e}_z^B)$, see Figure 2.3, the considered specimen of the tippedisk has a hole of radius a, whose center lies in a point with distance b with respect to G along the negative $\boldsymbol{e}_x^B$-axis. The associated dimensions are listed in the upper

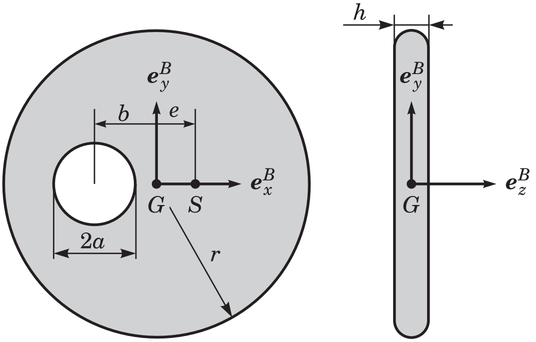

Figure 2.3: Dimensions of the tippedisk; the inertia tensor ${}_B\boldsymbol{\Theta}_G$ is given with respect to the depicted body-fixed B-frame.

part of Table 2.1. By considering a homogeneous disk with constant density ρ, the eccentricity

$$e = \frac{ba^2}{r^2 - a^2}$$

is obtained from the surface weighted distance and defines the center of gravity S, trough $\boldsymbol{r}_{GS} = e\boldsymbol{e}_x^B$. The inertia tensor of a solid disk with radius r, height h, and mass $m_r = \rho\pi r^2 h$ is given in the principal axis system, with respect to its geometric center, by

$${}_B\boldsymbol{\Theta}_{r,G} = \begin{bmatrix} \frac{1}{12} m_r(h^2 + 3r^2) & 0 & 0 \\ 0 & \frac{1}{12} m_r(h^2 + 3r^2) & 0 \\ 0 & 0 & \frac{6}{12} m_r r^2 \end{bmatrix}.$$

Introducing the negative mass $m_a = -\rho\pi a^2 h$ of the 'hole', the inertia tensor of removed mass with respect to the geometric center G of the solid disk is given by

$${}_B\boldsymbol{\Theta}_{a,G} = \begin{bmatrix} \frac{1}{12} m_a(h^2 + 3a^2) & 0 & 0 \\ 0 & \frac{1}{12} m_a(h^2 + 3a^2) + m_r b^2 & 0 \\ 0 & 0 & \frac{6}{12} m_a a^2 + m_a b^2 \end{bmatrix}.$$

Consequently, the inertia tensor of the tippedisk from Figure 2.3 results as the sum

$${}_B\boldsymbol{\Theta}_G = {}_B\boldsymbol{\Theta}_{r,G} + {}_B\boldsymbol{\Theta}_{a,G},$$

of single inertia contributions. For the following analysis, a stainless steel disk is considered, whose dimension and mass properties can be found in Table 2.1. In

Table 2.1: Dimension and inertia properties of the tippedisk

Property	Formula	Magnitude	Unit
Disk radius r	-	0.045	m
Hole radius a	-	0.015	m
Distance b	-	0.02	m
Disk height h	-	0.01	m
Eccentricity e	$\frac{ba^2}{r^2-a^2}$	$2.5\cdot 10^{-3}$	m
Density ρ	-	7700	kg/m^3
Mass m	$m_r + m_a = \rho\pi(r^2-a^2)h$	0.435	kg
${}_B\mathbf{\Theta}_G(1,1) = A$	$\frac{\rho\pi h}{12}\left(3r^4 + r^2h^2 - a^2h^2 - 3a^4\right)$	$0.249\cdot 10^{-3}$	kg m^2
${}_B\mathbf{\Theta}_G(2,2) = B$	$\frac{\rho\pi h}{12}\left(3r^4 + r^2h^2 - a^2h^2 - 3a^4 - 12a^2b^2\right)$	$0.227\cdot 10^{-3}$	kg m^2
${}_B\mathbf{\Theta}_G(3,3) = C$	$\frac{\rho\pi h}{12}\left(6r^4 - 6a^4 - 12a^2b^2\right)$	$0.468\cdot 10^{-3}$	kg m^2
${}_B\mathbf{\Theta}_S(2,2) = \bar{B}$	$B - me^2$	$0.224\cdot 10^{-3}$	kg m^2

addition, the auxiliary quantity $\bar{B} = B - me^2$ is listed, which corresponds to the second principal moment of inertia ${}_B\mathbf{\Theta}_S(2,2)$ with respect to the center of gravity S of the tippedisk with removed mass.

The qualitative analysis of the tippedisk ultimately leads to different bifurcation scenarios and thus different disk types, which are influenced by the physical parameters, i.e., the dimension and the mass properties. Although a qualitative analysis in dimensionless quantities is beneficial to identify the influence of the parameters, the starting point of the subsequent investigation is the modeling and simulation of the real specimen, with dimensions discussed and presented in this section. By doing so, the dynamics of the resulting mathematical model in dimensional quantities can be directly related to real physics, and thus to intuitive motions of the tippedisk, without being bothered with transformations between a dimensionless state-space and the physical behavior of the disk.

CHAPTER 3

Mechanical model of the tippedisk

The present chapter introduces the mechanical model of the tippedisk and is organized as follows.

In Section 3.1 and Section 3.2, the coordinate-free spatial kinematics and kinetics of a general rigid body are discussed, followed by explicit coordinate representations in Section 3.3. Based on the general rigid body dynamics, the kinematics of the tippedisk in contact with a flat support is introduced in Section 3.4. In Section 3.5, the utilized set-valued and smooth force laws are discussed. Section 3.6 provides two parametrizations of the mechanical rigid body model, each with its own advantages. Application of the numerical schemes from Section 3.7 various simulation results are presented in Section 3.8. Finally, the results are discussed in Section 3.9.

3.1 Rigid body kinematics

The configuration of a rigid body may be given by the position of an arbitrary body-fixed reference point P and the orientation of a body-fixed orthonormal B-frame, relative to a given non-moving inertial system $I = (O, \boldsymbol{e}_x^I, \boldsymbol{e}_y^I, \boldsymbol{e}_z^I)$. The two kinematic quantities, position vector $\boldsymbol{r}_{OP}$ and rotation tensor $\boldsymbol{R}$, fully embed the rigid body in the three-dimensional Euclidean space $\mathbb{E}^3$, see Figure 3.1. More precisely, the position $\boldsymbol{\xi} \in \mathbb{E}^3$ of any material particle can be addressed by a vector chain

$$\boldsymbol{\xi} = \boldsymbol{r}_{OP} + \boldsymbol{\rho},$$

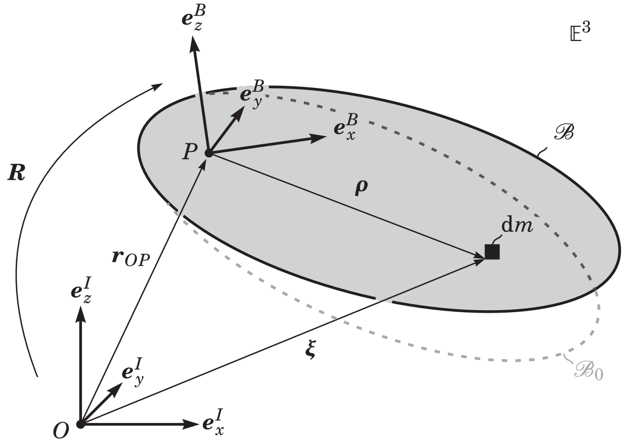

Figure 3.1: Kinematics of a rigid body.

with the reference vector $\boldsymbol{r}_{OP} \in \mathbb{E}^3$ and the relative particle vector $\boldsymbol{\rho} \in \mathscr{B}(\boldsymbol{R})$. The closed subset $\mathscr{B} \subset \mathbb{E}^3$ depends on the orientation of the body-fixed B-frame, as the rotation tensor $\boldsymbol{R} \in SO(3, \mathbb{E})$ rotates a reference configuration $\mathscr{B}_0$ onto the current configuration of the body $\mathscr{B}$. A detailed discussion about rotations, rotation tensors $\boldsymbol{R}$, and rotation matrices ${}_I\boldsymbol{R}$ can be found in Appendix A.

Multibody dynamics aims to characterize body configurations that evolve over time and are called motions of the system. Therefore, the position $\boldsymbol{\xi}(t)$ of each material particle can be considered as a function of time t. The corresponding particle velocity is given by the time derivative $\dot{\boldsymbol{\xi}}$, where the notation $\dot{\bullet} = \frac{\mathrm{d}}{\mathrm{d}t}\bullet$ is used. In the context of rigid body kinematics, the reference vector $\boldsymbol{r}_{OP}(t)$ and the rotation $\boldsymbol{R}(t)$, which define the configuration of a body, are also functions that depend on time t and therefore induce a velocity field

$$\dot{\boldsymbol{\xi}} = \dot{\boldsymbol{r}}_{OP} + \dot{\boldsymbol{\rho}} \tag{3.1}$$

on the rigid body. Introducing the linear and bijective mapping

$$\boldsymbol{j}: \quad \mathbb{E}^3 \to so(3, \mathbb{E}): \quad \boldsymbol{a} = a_i \boldsymbol{e}_i \mapsto \tilde{\boldsymbol{a}} = -\epsilon_{ijk} a_k \boldsymbol{e}_i \otimes \boldsymbol{e}_j, \tag{3.2}$$

between a vector $\boldsymbol{a} \in \mathbb{E}^3$ and an element $\tilde{\boldsymbol{a}}$ of the tangent space $so(3, \mathbb{E})$ at the point $\boldsymbol{R} \in SO(3, \mathbb{E})$, allows to introduce the angular velocity of the current configuration $\mathscr{B}$ as

$$\boldsymbol{\Omega} := \boldsymbol{j}^{-1}\left(\dot{\boldsymbol{R}}\boldsymbol{R}^{\mathrm{T}}\right), \tag{3.3}$$

an element of $\mathbb{E}^3$.

Since the relative particle vector $\boldsymbol{\rho}$ in the reference configuration $\mathscr{B}_0$ is constant, its absolute derivative is given by the vector product

$$\dot{\boldsymbol{\rho}} = \boldsymbol{\Omega} \times \boldsymbol{\rho}.$$

Introducing the absolute velocity $\boldsymbol{v}_P := \dot{\boldsymbol{r}}_{OP}$, of the reference point P, allows to rewrite Eq. (3.1) as

$$\dot{\boldsymbol{\xi}} = \boldsymbol{v}_P + \boldsymbol{\Omega} \times \boldsymbol{\rho}, \tag{3.4}$$

which is also known as the rigid body formula. The absolute particle acceleration

$$\ddot{\boldsymbol{\xi}} = \boldsymbol{a}_P + \boldsymbol{\Psi} \times \boldsymbol{\rho} + \boldsymbol{\Omega} \times \left(\boldsymbol{\Omega} \times \boldsymbol{\rho}\right) \tag{3.5}$$

is derived by differentiating the velocities $\boldsymbol{\Omega}$ and $\boldsymbol{v}_P$ with respect to time t, where $\boldsymbol{a}_P := \dot{\boldsymbol{v}}_P$ defines the linear acceleration and $\boldsymbol{\Psi} := \dot{\boldsymbol{\Omega}}$ denotes the angular acceleration of the body.

In general, the virtual displacement of a particle is defined as the variation

$$\delta\boldsymbol{\xi} := \left.\frac{\partial\hat{\boldsymbol{\xi}}}{\partial\varepsilon}\right|_{\varepsilon=\varepsilon_0} \delta\varepsilon,$$

where $\hat{\boldsymbol{\xi}}(t;\varepsilon)$ is introduced as a family of curves depending on the variation parameter ε, for which $\boldsymbol{\xi}(t) = \hat{\boldsymbol{\xi}}(t;\varepsilon_0)$ holds. However, for a rigid body, only admissible variations of particles that preserve the rigidity of the body are allowed. Therefore, families of reference positions $\hat{\boldsymbol{r}}_{OP}(t;\varepsilon)$ and rotation tensors $\hat{\boldsymbol{R}}(t;\varepsilon)$ are introduced, with the properties $\boldsymbol{r}_{OP}(t) = \hat{\boldsymbol{r}}_{OP}(t;\varepsilon_0)$ and $\boldsymbol{R}(t) = \hat{\boldsymbol{R}}(t;\varepsilon_0)$. The associated variations read as

$$\delta\boldsymbol{r}_P = \left.\frac{\partial\hat{\boldsymbol{r}}_{OP}}{\partial\varepsilon}\right|_{\varepsilon=\varepsilon_0} \delta\varepsilon \quad \text{and} \quad \delta\boldsymbol{R} = \left.\frac{\partial\hat{\boldsymbol{R}}}{\partial\varepsilon}\right|_{\varepsilon=\varepsilon_0} \delta\varepsilon,$$

in which the variation $\delta\boldsymbol{R}$ of the rotation tensor $\boldsymbol{R}$ is directly connected to the variation

$$\delta\boldsymbol{\varphi} = \boldsymbol{j}^{-1}\left(\delta\boldsymbol{R}\boldsymbol{R}^{\mathrm{T}}\right),$$

given the mapping $\boldsymbol{j}(\bullet)$ defined in Eq. (3.2). The angular variation $\delta\boldsymbol{\varphi}$ can be interpreted in axis-angle description as an infinitesimal rotation with angle $\phi = \|\delta\boldsymbol{\varphi}\|$ around the axis

$$\boldsymbol{ax} = \frac{\delta\boldsymbol{\varphi}}{\|\delta\boldsymbol{\varphi}\|}.$$

These variations of the reference vector $\delta\boldsymbol{r}_P$ and the orientation $\delta\boldsymbol{\varphi}$, induce the field

$$\delta\boldsymbol{\xi}_{\text{rig}} = \delta\boldsymbol{r}_P + \delta\boldsymbol{\varphi} \times \boldsymbol{\rho} \tag{3.6}$$

of virtual rigid body displacements. Comparison of the rigid body formula (3.4) with the variational field in Eq. (3.6), shows that velocities and variations of particles behave in a similar way, e.g., depend linearly on the derivatives of the reference position $\hat{\boldsymbol{r}}_{OP}$ and the orientation $\hat{\boldsymbol{R}}$.

In summary, the kinematics of a rigid body is given by three kinematic quantities, the body configuration

$$\boldsymbol{Q} = \left(\boldsymbol{r}_{OP}, \boldsymbol{R}\right) \in \mathbb{E}^3 \times SO(3,\mathbb{E}),$$

the body velocity

$$\boldsymbol{U} = \left(\boldsymbol{v}_P, \boldsymbol{\Omega}\right) \in \mathbb{E}^3 \times \mathbb{E}^3,$$

and the associated body variation

$$\delta\boldsymbol{S} = \left(\delta\boldsymbol{r}_P, \delta\boldsymbol{\varphi}\right) \in \mathbb{E}^3 \times \mathbb{E}^3,$$

defining the position $\boldsymbol{\xi} = \boldsymbol{\xi}(\boldsymbol{Q})$, the velocity $\dot{\boldsymbol{\xi}} = \dot{\boldsymbol{\xi}}(\boldsymbol{Q},\boldsymbol{U})$ and associated variation $\delta\boldsymbol{\xi}_{\mathrm{rig}} = \delta\boldsymbol{\xi}_{\mathrm{rig}}(\boldsymbol{Q},\delta\boldsymbol{S})$ of each material point. The corresponding particle acceleration $\ddot{\boldsymbol{\xi}} = \ddot{\boldsymbol{\xi}}(\boldsymbol{Q},\boldsymbol{U},\dot{\boldsymbol{U}})$ follows from Eq. (3.5).

The body state is introduced as the pair

$$\boldsymbol{X} := (\boldsymbol{Q}, \boldsymbol{U}) \in \mathbb{E}^3 \times SO(3,\mathbb{E}) \times \mathbb{E}^3 \times \mathbb{E}^3,$$

of the configuration $\boldsymbol{Q}$ and the velocity $\boldsymbol{U}$. It completely defines the current configuration and velocity field on a rigid body.

3.2 Rigid body kinetics

An elegant axiomatic access to classical mechanics is given by the variational approach, cf. [33].

The virtual work δW of a system $\mathscr{S}$ is defined as the linear functional

$$\delta W[\delta\boldsymbol{\xi}] := \int_{\mathscr{S}} \delta\boldsymbol{\xi} \cdot \left(\ddot{\boldsymbol{\xi}}\mathrm{d}m - \mathrm{d}\boldsymbol{F}\right),$$

where $\mathrm{d}m$ characterizes the mass density and $\mathrm{d}\boldsymbol{F}$ an arbitrary distribution of forces acting on the system $\mathscr{S}$. Each material point is addressed by its associated particle coordinate $\boldsymbol{\xi} \in \mathbb{E}^3$. To shorten notation, the argument of the expression $\delta W[\delta\boldsymbol{\xi}]$ is subsequently omitted, well knowing that the virtual work δW is a functional. Furthermore, to distinguish between internal and external actions, the total force

$\boldsymbol{F} = \int_{\mathscr{S}} \mathrm{d}\boldsymbol{F}$ is decomposed into internal forces $\boldsymbol{F}^{\mathrm{int}}$ and external forces $\boldsymbol{F}^{\mathrm{ext}}$. According to the variational law of interaction [33], the virtual work

$$\delta W^{\mathrm{int}} = \int_{\mathscr{S}} \delta\boldsymbol{\xi} \cdot \mathrm{d}\boldsymbol{F}^{\mathrm{int}} = \delta\boldsymbol{\xi} \cdot \boldsymbol{F}^{\mathrm{int}}$$

of internal forces $\boldsymbol{F}^{\mathrm{int}}$ vanishes when the system is subjected to virtual rigid body motions $\delta\boldsymbol{\xi}_{\mathrm{rig}}$, implying

$$\delta W = \int_{\mathscr{S}} \delta\boldsymbol{\xi}_{\mathrm{rig}} \cdot \left(\ddot{\boldsymbol{\xi}}\mathrm{d}m - \mathrm{d}\boldsymbol{F}^{\mathrm{ext}}\right).$$

Following the principle of virtual work, as a postulate, the system is in the state of dynamic equilibrium, if the virtual work vanishes for all variations $\delta\boldsymbol{\xi}$, especially for all rigid virtual displacements $\delta\boldsymbol{\xi}_{\mathrm{rig}}$.

Applying the variational law of interaction and the principle of virtual work to a single rigid body $\mathscr{B}$, yields the balance

$$\delta W^{\mathscr{B}} = \int_{\mathscr{B}} \delta\boldsymbol{\xi}_{\mathrm{rig}} \cdot \left(\ddot{\boldsymbol{\xi}}\mathrm{d}m - \mathrm{d}\boldsymbol{F}^{\mathrm{ext}}\right) = \delta W^{\mathrm{dyn}} + \delta W^{\mathrm{ext}} = 0 \quad \forall \delta\boldsymbol{\xi}_{\mathrm{rig}}$$

of virtual works, containing contributions from inertia and external forces:

$$\delta W^{\mathrm{dyn}} = \int_{\mathscr{B}} \delta\boldsymbol{\xi}_{\mathrm{rig}} \cdot \ddot{\boldsymbol{\xi}}\mathrm{d}m, \quad \text{and} \quad \delta W^{\mathrm{ext}} = -\int_{\mathscr{B}} \delta\boldsymbol{\xi}_{\mathrm{rig}} \cdot \mathrm{d}\boldsymbol{F}^{\mathrm{ext}}. \tag{3.7}$$

Together with the rigid virtual displacements from Eq. (3.6), the absolute particle acceleration in Eq. (3.5), the virtual work of inertia forces is given as

$$\delta W^{\mathrm{dyn}} = \int_{\mathscr{B}} (\delta\boldsymbol{r}_P + \delta\boldsymbol{\varphi} \times \boldsymbol{\rho}) \cdot \left(\dot{\boldsymbol{v}}_P + \dot{\boldsymbol{\Omega}} \times \boldsymbol{\rho} + \boldsymbol{\Omega} \times \left(\boldsymbol{\Omega} \times \boldsymbol{\rho}\right)\right) \mathrm{d}m. \tag{3.8}$$

Abusing notation in the sense of embedding tensor calculus in 'matrix' form, see Appendix A.6, and knowing that the variations $\delta\boldsymbol{r}_P$ and $\delta\boldsymbol{\varphi}$ are constant on the whole body $\mathscr{B}$, allows to rewrite the virtual work from Eq. (3.8) in a compact form

$$\delta W^{\mathrm{dyn}} = \begin{bmatrix} \delta\boldsymbol{r}_P \\ \delta\boldsymbol{\varphi} \end{bmatrix}^{\mathrm{T}} \cdot \int_{\mathscr{B}} \begin{bmatrix} \mathbb{1} & \tilde{\boldsymbol{\rho}}^{\mathrm{T}} \\ \tilde{\boldsymbol{\rho}} & \tilde{\boldsymbol{\rho}}\tilde{\boldsymbol{\rho}}^{\mathrm{T}} \end{bmatrix} \begin{bmatrix} \boldsymbol{v}_P \\ \boldsymbol{\Omega} \end{bmatrix}^{\bullet} - \begin{bmatrix} -\boldsymbol{\Omega} \times \left(\boldsymbol{\Omega} \times \boldsymbol{\rho}\right) \\ -\boldsymbol{\Omega} \times \left(\tilde{\boldsymbol{\rho}}\tilde{\boldsymbol{\rho}}^{\mathrm{T}}\boldsymbol{\Omega}\right) \end{bmatrix} \mathrm{d}m, \tag{3.9}$$

where the equality $\delta\boldsymbol{\varphi} \times \boldsymbol{\rho} = \delta\boldsymbol{\varphi}^{\mathrm{T}} \cdot \tilde{\boldsymbol{\rho}}$ and the Jacobi identity $\tilde{\boldsymbol{\rho}} \cdot \boldsymbol{\Omega} \times \left(\boldsymbol{\Omega} \times \boldsymbol{\rho}\right) = \boldsymbol{\Omega} \times \left(\tilde{\boldsymbol{\rho}}\tilde{\boldsymbol{\rho}}^{\mathrm{T}} \cdot \boldsymbol{\Omega}\right)$ are used.

Therein, three inertia integrals

$$m\mathbb{1} := \int_{\mathscr{B}} \mathbb{1}\mathrm{d}m, \quad m\tilde{\boldsymbol{r}}_{PS} := \int_{\mathscr{B}} \tilde{\boldsymbol{\rho}}\,\mathrm{d}m \quad \text{and} \quad \boldsymbol{\Theta}_P := \int_{\mathscr{B}} \tilde{\boldsymbol{\rho}}\tilde{\boldsymbol{\rho}}^{\mathrm{T}}\,\mathrm{d}m \tag{3.10}$$

are identified, defining the mass m, the relative vector $\boldsymbol{r}_{PS}$ of the center of gravity S, and the moment of inertia $\boldsymbol{\Theta}_P$ with respect to the chosen reference point P.

Substitution of the rigid virtual displacement (3.6) into the virtual work of external forces δW^{ext} from Eq. (3.7) yields the integral

$$\delta W^{\mathrm{ext}} = -\begin{bmatrix} \delta\boldsymbol{r}_P \\ \delta\boldsymbol{\varphi} \end{bmatrix}^{\mathrm{T}} \cdot \int_{\mathscr{B}} \begin{bmatrix} \mathrm{d}\boldsymbol{F}^{\mathrm{ext}} \\ \boldsymbol{\rho} \times \mathrm{d}\boldsymbol{F}^{\mathrm{ext}} \end{bmatrix},$$

where $\boldsymbol{\rho} \times \mathrm{d}\boldsymbol{F}^{\mathrm{ext}}$ measures the resulting torque $\mathrm{d}\boldsymbol{M}_P^{\mathrm{ext}}$ with respect to the reference point P. Since a rigid body $\mathscr{B}$ is blind to the individual force distribution and feels only the resulting force $\boldsymbol{F}^{\mathrm{ext}}$ and torque $\boldsymbol{M}_P^{\mathrm{ext}}$, the virtual work of the external forces simplifies to

$$\delta W^{\mathrm{ext}} = -\begin{bmatrix} \delta\boldsymbol{r}_P \\ \delta\boldsymbol{\varphi} \end{bmatrix}^{\mathrm{T}} \cdot \begin{bmatrix} \boldsymbol{F}^{\mathrm{ext}} \\ \boldsymbol{M}_P^{\mathrm{ext}} \end{bmatrix}. \tag{3.11}$$

In total, the virtual work of a single rigid body with the inertia quantities from Eq. (3.10), the virtual work of dynamic forces δW^{dyn} in Eq. (3.9), and the virtual work of external forces δW^{ext} from Eq. (3.11) is given as

$$\delta W^{\mathscr{B}} = \begin{bmatrix} \delta\boldsymbol{r}_P \\ \delta\boldsymbol{\varphi} \end{bmatrix}^{\mathrm{T}} \cdot \left(\begin{bmatrix} m\mathbb{1} & m\tilde{\boldsymbol{r}}_{PS}^{\mathrm{T}} \\ m\tilde{\boldsymbol{r}}_{PS} & \boldsymbol{\Theta}_P \end{bmatrix} \begin{bmatrix} \boldsymbol{v}_P \\ \boldsymbol{\Omega} \end{bmatrix}^{\bullet} - \begin{bmatrix} -m\boldsymbol{\Omega} \times (\boldsymbol{\Omega} \times \boldsymbol{r}_{PS}) \\ -\boldsymbol{\Omega} \times (\boldsymbol{\Theta}_P \boldsymbol{\Omega}) \end{bmatrix} \right) + \delta W^{\mathrm{ext}}. \tag{3.12}$$

This virtual work from Eq. (3.12) forms the basis for rigid body dynamics and is the most general coordinate-free description when the kinematics from Section 3.1 is assumed. In rigid multibody dynamics, it is convenient to calculate the total virtual work of the system by accumulation

$$\delta W^{\mathscr{S}} = \textstyle\sum_i \delta W^{\mathscr{B}_i}$$

of the individual virtual work contributions $\delta W^{\mathscr{B}_i}$ of all rigid bodies $\mathscr{B}_i$. The interaction between the bodies is accounted for by the virtual work contribution $\delta W^{\mathrm{ext}_i}$ of the individual bodies. Although the above virtual work $\delta W^{\mathscr{B}}$ is based on rigid body assumptions, structurally similar expressions of the virtual work can be found in finite element formulations of geometrically nonlinear structural elements, e.g., cosserat rod finite elements [51].

3.3 Coordinate representation

So far, the kinematics and kinetics of a rigid body have been introduced and discussed in a coordinate-free manner, i.e., by describing vectors and tensors in the three-dimensional Euclidean space $\mathbb{E}^3$. However, this representation is not suited for simulation or to analyze the dynamics with respect to system states, as the introduced configuration $\boldsymbol{Q}$, the body velocity $\boldsymbol{U}$ and the variations $\delta\boldsymbol{S}$ are couples of coordinate-free quantities, and thus abstract objects. Therefore, this section discusses the coordinate representation and transformation properties of vector and tensor objects.

For a given vector $\boldsymbol{c} \in \mathbb{E}^3$, the linear coordinate map

$$\begin{aligned} \mathscr{K}_A &: \mathbb{E}^3 \to \mathbb{R}^3 \\ \boldsymbol{c} &\mapsto {}_A\boldsymbol{c} = \left(\boldsymbol{c}\cdot\boldsymbol{e}_i^A\right) {}_A\boldsymbol{e}_i^A = \begin{bmatrix} \boldsymbol{c}\cdot\boldsymbol{e}_x^A \\ \boldsymbol{c}\cdot\boldsymbol{e}_y^A \\ \boldsymbol{c}\cdot\boldsymbol{e}_z^A \end{bmatrix} \end{aligned}$$

collects the components $c_i^A = \left(\boldsymbol{c}\cdot\boldsymbol{e}_i^A\right)$ in the tuple ${}_A\boldsymbol{c} \in \mathbb{R}^3$. As a tensor $\boldsymbol{T} = T_{ij}\,\boldsymbol{e}_i \otimes \boldsymbol{e}_j$ is spanned by the basis $\boldsymbol{e}_i \otimes \boldsymbol{e}_j$, the application of the coordinate map $\mathscr{K}_A$ to the tensor $\boldsymbol{T} = T_{ij}\,\boldsymbol{e}_i \otimes \boldsymbol{e}_j = T_{ij}^A\boldsymbol{e}_i^A \otimes \boldsymbol{e}_j^A$ yields the matrix

$${}_A\boldsymbol{T} = T_{ij}^A \mathscr{K}_A(\boldsymbol{e}_i)\mathscr{K}_A{}^{\mathrm{T}}(\boldsymbol{e}_j) = \begin{bmatrix} T_{11}^A & T_{12}^A & T_{13}^A \\ T_{21}^A & T_{22}^A & T_{23}^A \\ T_{31}^A & T_{32}^A & T_{33}^A \end{bmatrix} \in \mathbb{R}^{3\times3},$$

being the tensor representation with respect to the A-basis. Assuming a second basis B with the associated coordinate mapping $\mathscr{K}_B$, tuple and matrix representations of $\boldsymbol{c}$ and $\boldsymbol{T}$ are obtained as ${}_B\boldsymbol{c}$ and ${}_B\boldsymbol{T}$.

The relation between A- and B-representations is governed by the transformations

$${}_A\boldsymbol{c} = \boldsymbol{A}_{AB}\,{}_B\boldsymbol{c} \quad \text{and} \quad {}_A\boldsymbol{T} = \boldsymbol{A}_{AB}\,{}_B\boldsymbol{T}\boldsymbol{A}_{AB}^{\mathrm{T}},$$

where the coordinate transformation matrix $\boldsymbol{A}_{AB} = \left[\boldsymbol{e}_i^A \cdot \boldsymbol{e}_j^B\right] \in \mathbb{R}^{3\times3}$ is introduced. In Appendix A, it is shown that the transformation matrix $\boldsymbol{A}_{AB}$ is related to a associated rotation tensor $\boldsymbol{R}_{BA}$ by the relation $\boldsymbol{A}_{AB} = {}_A\boldsymbol{R}_{BA}$.

Similar to Eq. (3.3), the relative angular velocity $\boldsymbol{\omega}_{AB}$ of the B-frame with respect to the A-frame is given by

$$\boldsymbol{\omega}_{AB} := \boldsymbol{j}^{-1}\left(\dot{\boldsymbol{R}}_{BA}\boldsymbol{R}_{BA}^{\mathrm{T}}\right),$$

and may be expressed in the A-frame as

$${}_A\boldsymbol{\omega}_{AB} := \boldsymbol{j}_{\mathbb{R}}^{-1}\left(\dot{\boldsymbol{A}}_{AB}\boldsymbol{A}_{AB}^{\mathrm{T}}\right),$$

where the linear and bijective mapping

$$\boldsymbol{j}_{\mathbb{R}}: \quad \mathbb{R}^3 \to so(3,\mathbb{R}): \quad {}_A\boldsymbol{v} = \begin{bmatrix} v_1^A \\ v_2^A \\ v_3^A \end{bmatrix} \mapsto {}_A\tilde{\boldsymbol{c}} = \begin{bmatrix} 0 & -c_3^A & c_2^A \\ c_3^A & 0 & -c_1^A \\ -c_2^A & c_1^A & 0 \end{bmatrix}$$

is used, where ${}_A\tilde{\boldsymbol{c}}$ is a skew-symmetric matrix, being an element of the tangent space $so(3,\mathbb{R})$ at the point ${}_A\boldsymbol{R}_{BA}$ in the manifold $SO(3,\mathbb{R})$.

The time derivative of a vector, spanned by a moving A-basis, yields

$$\dot{\boldsymbol{c}} = \dot{c}_i^A \boldsymbol{e}_i^A + c_i^A \dot{\boldsymbol{e}}_i^A, \tag{3.13}$$

in which the derivative of the i-th basis vector $\boldsymbol{e}_i^A$, is given by

$$\dot{\boldsymbol{e}}_i^A = \boldsymbol{\omega}_{AI} \times \boldsymbol{e}_i^A. \tag{3.14}$$

Combining Eq. (3.13) and Eq. (3.14) yields the absolute derivative

$$\dot{\boldsymbol{c}} = \dot{c}_i^A \boldsymbol{e}_i^A + \boldsymbol{\omega}_{AI} \times c_i^A \boldsymbol{e}_i^A, \tag{3.15}$$

which may be transformed by $\mathscr{K}_A$ in A-coordinates as

$${}_A(\dot{\boldsymbol{c}}) = {}_A\dot{\boldsymbol{c}} + {}_A\boldsymbol{\omega}_{IA} \times {}_A\boldsymbol{c}, \tag{3.16}$$

also known as Euler's differentiation rule.

3.4 Kinematics of the tippedisk

The previous Section 3.1 describes the kinematics of a single rigid body, by characterizing a reference vector pointing from the origin to the chosen reference point, and by a relative orientation of a body-fixed B-frame with respect to an inertial I-frame. In the current section, this kinematic rigid body description is used to embed the tippedisk in the three-dimensional Euclidean space $\mathbb{E}^3$, which allows the introduction of different parametrizations in a natural way.

Configuration of the tippedisk

In Figure 3.2, the mechanical model of the tippedisk is displayed, depicting an infinitely thin disk with radius r and eccentricity e above a flat support. To obtain a mechanical model with a minimal number of degrees of freedom that describes the macroscopic dynamic effects and neglects local deformations at the contact point,

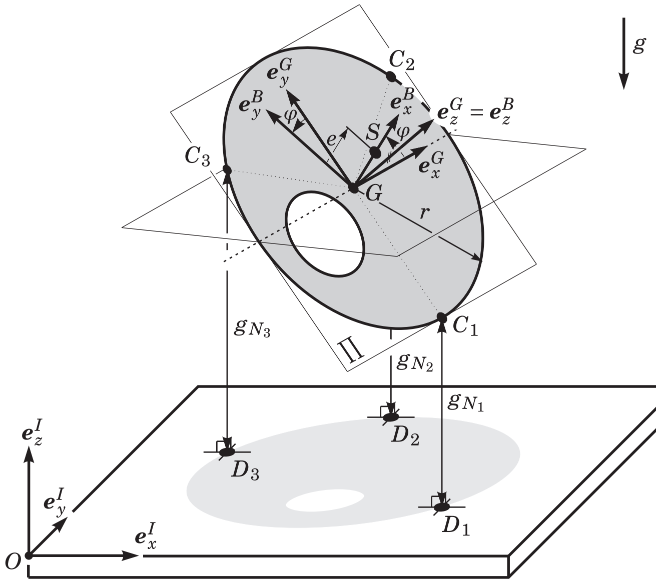

Figure 3.2: Mechanical model of the tippedisk in contact with a flat frictional support.

the disk and the flat support are assumed to be rigid. The assumption of zero thickness facilitates the contact kinematics, as the contact point lies on a circle around the geometric center and thus on a one-dimensional curve.

To describe the orientation of the tippedisk in the three-dimensional Euclidean space $\mathbb{E}^3$, an orthonormal inertial I-frame $I = (O, \boldsymbol{e}_x^I, \boldsymbol{e}_y^I, \boldsymbol{e}_z^I)$ is attached to the inertial origin O, with the unit vector $\boldsymbol{e}_z^I$ pointing vertically upward and orthogonal to the supporting hyperplane spanned by $\boldsymbol{e}_x^I$ and $\boldsymbol{e}_y^I$. Without loss of generality, assuming the support to be homogeneous and isotropic, the origin O can be chosen as an arbitrary point of the support. Due to isotropy, any unit vector of the hyperplane can be defined as the first basis vector $\boldsymbol{e}_x^I$, so that the right-handed frame is completed by the definition $\boldsymbol{e}_y^I := \boldsymbol{e}_z^I \times \boldsymbol{e}_x^I$. In addition, a right-handed body-fixed frame $B = (G, \boldsymbol{e}_x^B, \boldsymbol{e}_y^B, \boldsymbol{e}_z^B)$ is attached to the geometric center G of the disk, such that $\boldsymbol{e}_z^B$ is normal to the surface of the disk. Introducing the unit vector $\boldsymbol{e}_x^B$ as the normalized relative vector of

$$\boldsymbol{r}_{GS} = e\,\boldsymbol{e}_x^B \tag{3.17}$$

pointing from the geometric center G to the center of gravity S, and $\boldsymbol{e}_y^B := \boldsymbol{e}_z^B \times \boldsymbol{e}_x^B$, the body-fixed B-frame is uniquely defined. The relative orientation of the body-fixed frame with respect to the inertial I-frame is characterized by the rotation tensor $\boldsymbol{R} \in SO(3,\mathbb{E})$, induced by the relation $\boldsymbol{e}_i^B = \boldsymbol{R} \cdot \boldsymbol{e}_i^I$, for $i \in \{x, y, z\}$.

Definition of contact points

To describe the interaction between the disk and the support, the floating frame $G = (G, \boldsymbol{e}_x^G, \boldsymbol{e}_y^G, \boldsymbol{e}_z^G)$ is introduced, with $\boldsymbol{e}_z^G = \boldsymbol{e}_z^B$, which is attached to the geometric center G. For non-horizontal configurations of the disk, the cross product $\boldsymbol{e}_z^I \times \boldsymbol{e}_z^B$ is perpendicular to $\boldsymbol{e}_z^I$ and $\boldsymbol{e}_z^B$, implying the horizontally floating unit vector

$$\boldsymbol{e}_x^G := \frac{\boldsymbol{e}_z^I \times \boldsymbol{e}_z^B}{\|\boldsymbol{e}_z^I \times \boldsymbol{e}_z^B\|}. \tag{3.18}$$

Obviously, this definition is only valid for non-horizontal orientations, i.e., $\boldsymbol{e}_z^I \times \boldsymbol{e}_z^B \neq 0$. If the disk enters a horizontal configuration, the floating vector $\boldsymbol{e}_x^G$ can be chosen arbitrarily, as long $\boldsymbol{e}_x^G \cdot \boldsymbol{e}_z^G = 0$ and $\boldsymbol{e}_z^G = \boldsymbol{e}_z^B$ hold. For the numerical implementation, the continuity condition $\boldsymbol{e}_x^G(t_i) = \boldsymbol{e}_x^G(t_{i-1})$ is assumed, if the disk passes a horizontal configuration, i.e., the G-frame from the previous step is used, cf. [70]. Assuming that the third and first basis vectors $\boldsymbol{e}_z^B$ and $\boldsymbol{e}_x^G$ are given, the two vectors can be completed by introducing the second basis vector

$$\boldsymbol{e}_y^G := \boldsymbol{e}_z^B \times \boldsymbol{e}_x^G, \tag{3.19}$$

yielding the right-handed orthonormal G-frame.

With $\boldsymbol{e}_y^G$ from Eq. (3.19) the projection $\boldsymbol{e}_z^I \cdot \boldsymbol{e}_y^G$ results in the triple product

$$\boldsymbol{e}_z^I \cdot \boldsymbol{e}_y^G = \boldsymbol{e}_x^G \cdot \left[\boldsymbol{e}_z^I \times \boldsymbol{e}_z^B\right],$$

where the circular shifting property has been applied. Subsequent substitution of $\boldsymbol{e}_x^G$ from Eq. (3.18) reveals that for non-horizontal configurations the inner product

$$\boldsymbol{e}_z^I \cdot \boldsymbol{e}_y^G = \frac{\boldsymbol{e}_z^I \times \boldsymbol{e}_z^B}{\|\boldsymbol{e}_z^I \times \boldsymbol{e}_z^B\|} \cdot \left[\boldsymbol{e}_z^I \times \boldsymbol{e}_z^B\right]$$

is greater than zero. As a consequence, the relative vector from the geometric center G to the contact point C_1 with minimal height is given as

$$\boldsymbol{r}_{GC_1} = -r\,\boldsymbol{e}_y^G. \tag{3.20}$$

In general, the rotation tensor

$$\boldsymbol{R}_z^G(\vartheta) := \mathbb{1} + \sin\vartheta\, \boldsymbol{j}(\boldsymbol{e}_z^G) + (1-\cos\vartheta)\boldsymbol{j}^2(\boldsymbol{e}_z^G),$$

in the axis angle description, characterizes rotations around the unit vector $\boldsymbol{e}_z^G$ with corresponding angle ϑ. Thus, two additional contact points C_2 and C_3 can be constructed (cf. LE SAUX et al. [70]) by rotating the relative vector $\boldsymbol{r}_{GC_1}$ with angle $\vartheta_{2,3} = \pm\frac{2\pi}{3}$ around the axis $\boldsymbol{e}_z^G$, resulting in the rotated vectors

$$\boldsymbol{r}_{GC_2} = \boldsymbol{R}_z^G(\vartheta_2)\boldsymbol{r}_{GC_1} \quad \text{and} \quad \boldsymbol{r}_{GC_3} = \boldsymbol{R}_z^G(\vartheta_3)\boldsymbol{r}_{GC_1}, \tag{3.21}$$

with associated rotations

$$\boldsymbol{R}_z^{G_z}(\vartheta_2) := -\frac{1}{2}\left(\mathbb{1} - \sqrt{3}\,\boldsymbol{j}(\boldsymbol{e}_z^G)\right) \quad \text{and} \quad \boldsymbol{R}_z^{G_z}(\vartheta_3) := -\frac{1}{2}\left(\mathbb{1} + \sqrt{3}\,\boldsymbol{j}(\boldsymbol{e}_z^G)\right). \tag{3.22}$$

In accordance with [70], the Eqs. (3.21) and (3.22) allow, for any given vector $\boldsymbol{r}_{GC_1}$, to introduce the relative contact vectors

$$\boldsymbol{r}_{GC_2} = -\frac{1}{2}\boldsymbol{r}_{GC_1} + \frac{\sqrt{3}}{2}\left(\boldsymbol{e}_z^G \times \boldsymbol{r}_{GC_1}\right) \quad \text{and} \quad \boldsymbol{r}_{GC_3} = -\frac{1}{2}\boldsymbol{r}_{GC_1} - \frac{\sqrt{3}}{2}\left(\boldsymbol{e}_z^G \times \boldsymbol{r}_{GC_1}\right), \tag{3.23}$$

yielding three angle-equidistant contact points C_1, C_2 and C_3, see Figure 3.3. The corresponding gap distance g_k between each contact point C_k and the corresponding point D_k on the flat support is equal to the projection of $\boldsymbol{r}_{OC_k}$ onto the $\boldsymbol{e}_z^I$-axis.

Assuming the given reference vector $\boldsymbol{r}_{OG}$, the gap functions g_{N_k} are defined with Eq. (3.20) and Eq. (3.23) and yield the projections

$$g_{N_k} = \boldsymbol{r}_{OC_k} \cdot \boldsymbol{e}_z^I = \left(\boldsymbol{r}_{OG} + \boldsymbol{r}_{GC_k}\right) \cdot \boldsymbol{e}_z^I, \quad k = 1,2,3.$$

In general, the configuration $\boldsymbol{Q}$ of the tippedisk is fully defined by choosing an arbitrary reference point P with the associated position vector $\boldsymbol{r}_{OP} \in \mathbb{E}^3$ and introducing the body-fixed B-frame whose orientation is given by the rotation tensor $\boldsymbol{R} \in SO(3,\mathbb{E})$. Since the introduced B-frame is uniquely aligned with respect to the disk, the orientation given by the rotation tensor $\boldsymbol{R} \in SO(3,\mathbb{E})$ is also unique. In contrast, the choice of an appropriate reference point P is not unique. For the tippedisk, three characteristic points are of special importance. In particular, the geometric center G of the disk, the center of gravity S and the contact point C_1 are characteristic points that may be chosen as reference points.

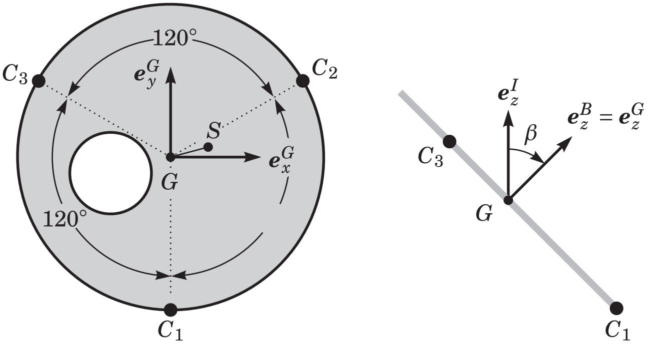

(a) view in $-\boldsymbol{e}_z^G$-direction (b) view in $+\boldsymbol{e}_x^G$-direction

Figure 3.3: Definition of the contact points C_k with $k = 1,2,3$. The angle β measures the inclination of the disk.

Physical coordinates

To interpret the orientation in physical coordinates, three angles α, β and γ are defined without any dependence on a chosen parametrization. Therefore, these angles have a physical meaning and must be constructed by projections of given configurations $\boldsymbol{Q}$. Here, the *spinning angle*

$$\alpha := \operatorname{arctan2}\left(\boldsymbol{e}_x^G \cdot \boldsymbol{e}_y^I, \boldsymbol{e}_x^G \cdot \boldsymbol{e}_x^I\right) \in [-\pi, +\pi),$$

the *inclination angle*

$$\beta := \arccos\left(\boldsymbol{e}_z^I \cdot \boldsymbol{e}_z^G\right) \in [0, +\pi],$$

and the *rolling angle*

$$\gamma := \operatorname{arctan2}\left(\boldsymbol{e}_x^B \cdot \boldsymbol{e}_y^G, \boldsymbol{e}_x^B \cdot \boldsymbol{e}_x^G\right) \in [-\pi, +\pi),$$

are introduced, characterizing relative orientations of specific coordinate frames. Due to trigonometric ambiguity, these definitions are not unique, since they map to compact intervals. However, by taking periodicity properties into account, the discontinuous signals (i.e., $\alpha(t), \beta(t), \gamma(t)$) can be unwrapped into continuous ones.

In Figure 3.4, the physical angles α, β and γ are depicted for three particular configurations of the tippedisk.

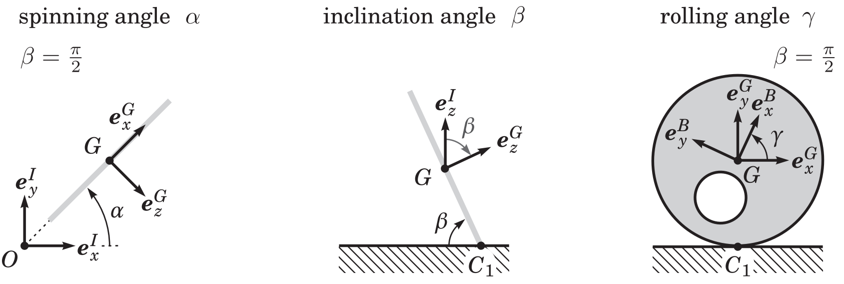

(a) view in $-e_z^I$-direction (b) view in $+e_x^G$-direction (c) view in $-e_z^G$-direction

Figure 3.4: Physical angles of the tippedisk. In Figure 3.4(a) and Figure 3.4(c), the disk is assumed to be vertically inclined, i.e., $\beta = \frac{\pi}{2}$, for a clearer illustration.

Velocities

So far, the static configuration $\boldsymbol{Q}$ of the tippedisk has been discussed, defining the current position and orientation. To describe the motion of the tippedisk, velocities and accelerations must be introduced as time derivatives of the configuration, which determine the dynamic behavior over time t.

The body velocity $\boldsymbol{U}$ of the tippedisk, i.e., the angular velocity $\boldsymbol{\Omega}$ and an absolute velocity $\boldsymbol{v}_P$ of the reference point P, is related to the configuration $\boldsymbol{Q}$ by the kinematic equation

$$\left.\begin{aligned} \boldsymbol{v}_P &= \dot{\boldsymbol{r}}_{OP} \\ \boldsymbol{\Omega} &= \boldsymbol{j}^{-1}\left(\boldsymbol{R}^{\mathrm{T}}\dot{\boldsymbol{R}}\right) \end{aligned}\right\} \quad \Leftrightarrow \quad \boldsymbol{U} = \boldsymbol{F}^{-1}(\boldsymbol{Q})\dot{\boldsymbol{Q}}. \tag{3.24}$$

From Eq. (3.24) the inverse mapping

$$\left.\begin{aligned} \dot{\boldsymbol{r}}_{OP} &= \boldsymbol{v}_P \\ \dot{\boldsymbol{R}} &= \boldsymbol{R}\boldsymbol{j}(\boldsymbol{\Omega}) \end{aligned}\right\} \quad \Leftrightarrow \quad \dot{\boldsymbol{Q}} = \boldsymbol{F}(\boldsymbol{Q})\boldsymbol{U},$$

can be constructed, which characterizes the derivative $\dot{\boldsymbol{Q}}$ of the configuration as a function of the configuration $\boldsymbol{Q}$ and the body velocity $\boldsymbol{U}$. According to the rigid body formula from Eq. (3.1), the absolute velocity of the contact point C_k is given by

$$\boldsymbol{v}_{C_k} = \boldsymbol{v}_P + \boldsymbol{\Omega} \times \boldsymbol{r}_{PC_k}, \quad k = 1,2,3, \tag{3.25}$$

which reveals the absolute velocity $\boldsymbol{v}_{C_k}(\boldsymbol{Q},\boldsymbol{U})$ is a function that depends on the configuration and is linear in the body velocity.

Projection of the absolute velocity $\boldsymbol{v}_{C_k}$, of the contact point C_k, onto the orthonormal I-frame yields the normal relative contact velocity

$$\gamma_{N_k} := \boldsymbol{v}_{C_k} \cdot \boldsymbol{e}_z^I \tag{3.26}$$

and the two-dimensional tangential relative contact velocity as the 2-tuple

$$\boldsymbol{\gamma}_{T_k} := \begin{bmatrix} \gamma_{Tx_k} \\ \gamma_{Ty_k} \end{bmatrix} = \begin{bmatrix} \boldsymbol{v}_{C_k} \cdot \boldsymbol{e}_x^I \\ \boldsymbol{v}_{C_k} \cdot \boldsymbol{e}_y^I \end{bmatrix}, \tag{3.27}$$

where γ_{Tx_k} and γ_{Ty_k} are the relative sliding velocities in $\boldsymbol{e}_x^I$- and $\boldsymbol{e}_y^I$-direction, respectively. Furthermore, the pivoting velocity

$$\gamma_{\tau_k} := \varepsilon_k \, \omega_{IB} \tag{3.28}$$

is introduced as the relative spinning speed $\omega_{IB} := \boldsymbol{\Omega} \cdot \boldsymbol{e}_z^I$ scaled with a constant contact radius $\varepsilon_k > 0$. Herein, the contact radius ε_k corresponds to the radius of the contact area between disk an support, which is assumed to be circular but idealized to be a point, see [73] for further details.

Above, the floating G-frame is introduced, which is constructed from the inertial I-frame and the body-fixed B-frame. As the I-frame is assumed to be motionless, the angular velocity $\boldsymbol{\Omega}$ induces also the angular velocity $\boldsymbol{\omega}$ of the floating G-frame. With these two angular velocities, the relative velocity of the moving contact point C_k, with respect to the associated body-fixed material point which momentarily agrees with it, holds as

$$\gamma_{R_k} := \big((\boldsymbol{\omega} - \boldsymbol{\Omega}) \times \boldsymbol{r}_{PC_k}\big) \cdot \boldsymbol{e}_x^G = -r\dot{\varphi}. \tag{3.29}$$

Here, the relative rolling velocity γ_{R_k} is a measure of how fast the contact point wanders on the one-dimensional outer ring of the disk.

3.5 Contact laws

The contact laws of the contact forces at the contact points C_k will be described within the framework of nonsmooth dynamics [85, 73, 71]. Frictional contacts have a set-valued nature and can conveniently be expressed using normal cone inclusions.

To write force laws as normal cone inclusions, the definition of normal cone

$$\mathcal{N}_{\mathscr{C}}(\boldsymbol{x}) := \left\{ \boldsymbol{y} \in \mathbb{R}^n \,\middle|\, \boldsymbol{y}^{\mathrm{T}}(\boldsymbol{x}^* - \boldsymbol{x}) \leq 0, \quad \boldsymbol{x} \in \mathscr{C}, \forall \boldsymbol{x}^* \in \mathscr{C} \right\}$$

to a closed convex non-empty set $\mathscr{C} \subset \mathbb{R}^n$ at point $\boldsymbol{x}$ is used [103]. For $\boldsymbol{x} \notin \mathscr{C}$ the normal cone is empty, i.e., $\mathcal{N}_{\mathscr{C}}(\boldsymbol{x}) = \emptyset$.

Normal contact laws

To prevent the disk from penetrating the support, a unilateral constraint in normal direction is assumed. Therefore, Signorini's law

$$0 \leq g_{N_k} \perp \lambda_{N_k} \geq 0 \tag{3.30}$$

is used as the contact law in normal direction, which determines the normal force λ_{N_k} at the contact point.

Utilizing Moreau's viability lemma [85], Proposition 2.4, Signorini's normal contact law on position level from Eq. (3.30), can equivalently be formulated on velocity level as

$$g_{N_k} = 0: \quad 0 \leq \gamma_{N_k} \perp \lambda_{N_k} \geq 0,$$

whenever γ_{N_k} is continuous.

Following [85, 45, 74], the generalized Newton's impact law yields the normal cone inclusion

$$\xi_{N_k} \in \mathcal{N}_{\mathbb{R}_0^-}(-\Lambda_{N_k}) \quad \text{with} \quad \xi_{N_k} = \gamma_{N_k}^+ + e_{N_k}\gamma_{N_k}^-.$$

Herein, the parameter e_{N_k} indicates the restitution coefficient, the kinematic quantities $\gamma_{N_k}^+$ and $\gamma_{N_k}^-$ are post- and preimpact velocities, and Λ_{N_k} denotes the corresponding impulsive force in normal direction [45].

Frictional contact laws

Classical spatial Coulomb friction is described by the set-valued force law

$$\boldsymbol{\gamma}_{T_k} \in \mathcal{N}_{C_{T_k}}(-\boldsymbol{\lambda}_{T_k}), \tag{3.31}$$

where C_{T_k} is a closed convex set denoting the negative force reservoir. For isotropic friction the negative force reservoir C_{T_k} is equal to a disk with radius $\mu\lambda_{N_k}$, where μ is identified as friction coefficient, i.e., $C_{T_k} = \{-\boldsymbol{\lambda}_{T_k} \in \mathbb{R}^2 \,|\, \|\boldsymbol{\lambda}_{T_k}\| \leq \mu\lambda_{N_k}\}$. In [73], it was shown that the coupling between sliding friction and pivoting friction is essential for the inversion of the tippetop. The Coulomb–Contensou friction model from [73] expresses the coupling between the tangential friction forces $\boldsymbol{\lambda}_T$ and the pivoting torque λ_τ, both of which depend on the tangential sliding velocity $\boldsymbol{\gamma}_{T_k}$ and the scaled angular spinning speed γ_{τ_k}. Together with the triples

$$\boldsymbol{\gamma}_{F_k} = \begin{bmatrix} \boldsymbol{\gamma}_{T_k} \\ \gamma_{\tau_k} \end{bmatrix} \quad \text{and} \quad \boldsymbol{\lambda}_{F_k} = \begin{bmatrix} \boldsymbol{\lambda}_{T_k} \\ \lambda_{\tau_k} \end{bmatrix},$$

the Coulomb–Contensou friction law yields the normal cone inclusion

$$\boldsymbol{\gamma}_{F_k} \in \mathcal{N}_{B_{F_k}}(-\boldsymbol{\lambda}_{F_k}). \tag{3.32}$$

For a parabolic pressure distribution at the contact area with radius ε_k (see [73]), the friction ball $B_{F_k}(\lambda_N)$ can be expressed with the auxiliary quantities

$$\bar{\xi} = \frac{\|\boldsymbol{\lambda}_{T_k}\|}{\mu\lambda_N} \quad \text{and} \quad \bar{\eta} = \frac{\lambda_{\tau_k}}{\mu\lambda_N}$$

and

$$\xi^* = \frac{9}{32}\pi \quad \text{and} \quad \eta^* = \frac{9}{128}\pi$$

as

$$B_{F_k} := \begin{cases} \left\{\boldsymbol{\lambda}_{F_k} \,\middle|\, \frac{9}{64}\left(\frac{\bar{\eta}}{\eta^*}\right)^2 + \frac{9}{8}\left(\frac{\bar{\xi}}{\xi^*}\right)^2 - \frac{243}{1024}\left(\frac{\bar{\xi}}{\xi^*}\right)^4 + O\left(\left(\frac{\bar{\xi}}{\xi^*}\right)^6\right) \leq 1\right\}, & \bar{\xi} \leq \xi^* \\ \left\{\boldsymbol{\lambda}_{F_k} \,\middle|\, \bar{\xi}^2 + 5\bar{\eta}^2 - \frac{75}{7}\bar{\eta}^4 + O(\bar{\eta}^6) \leq 1\right\}, & \bar{\xi} > \xi^*. \end{cases}$$

To describe impacts, we restrict us to the classical spatial Coulomb friction impact law

$$\boldsymbol{\xi}_{T_k} \in \mathcal{N}_{C_{T_k}}\left(-\Lambda_{T_k}\right) \quad \text{with} \quad \boldsymbol{\xi}_{T_k} = \boldsymbol{\gamma}_{T_k}^+ + e_{T_k}\boldsymbol{\gamma}_{T_k}^-,$$

with negative force reservoir C_{T_k}, cf. [45] .

The Coulomb–Contensou friction law incorporates the coupling between sliding and pivoting friction and describes the Contensou effect [73]. For vanishing pivoting speed one retrieves the set-valued Coulomb friction law for sliding, whereas it is strongly regularized for large values of γ_τ. For a fast spinning disk, i.e., $|\gamma_\tau| \gg \|\boldsymbol{\gamma}_T\|$, Coulomb–Contensou yields a smooth tangential friction law, motivating the introduction of the regularized Coulomb friction law

$$\boldsymbol{\lambda}_{T_k} = -\mu\lambda_{N_k}\frac{\boldsymbol{\gamma}_{T_k}}{\|\boldsymbol{\gamma}_{T_k}\| + \varepsilon}, \tag{3.33}$$

with friction parameter μ and smoothing coefficient ε.

As isolated force law for pivoting friction, dry pivoting friction

$$\gamma_{\tau_k} \in \mathcal{N}_{C_{\tau_k}}(-\lambda_{\tau_k})$$

is assumed, with the corresponding negative force reservoir $C_{\tau_k} := \{x \in \mathbb{R} \,|\, |x| \leq \mu_\tau\, \lambda_{N_k}\}$. Equivalently, dry contour friction

$$\gamma_{R_k} \in \mathcal{N}_{C_{R_k}}(-\lambda_{R_k})$$

is introduced to describe the resistance against rolling, where C_{R_k} corresponds to the negative force reservoir $C_{R_k} := \{x \in \mathbb{R} \,|\, |x| \leq \mu_R\, \lambda_{N_k}\}$, cf. [70].

3.6 Parametrization

For finite dimensional mechanical systems, the task of a parametrization is to fully define the configuration and the velocity field of the mechanical system, using generalized coordinates $\boldsymbol{q} \in \mathbb{R}^n$ and generalized velocities $\boldsymbol{u} \in \mathbb{R}^\nu$. For rigid body systems, it is common to take, for each rigid body, one point as reference and to describe the orientation of any rigid body by a representative rotation matrix, i.e., the position vector $\boldsymbol{r}_{OP} \in \mathbb{E}^3$ of the reference point P together with a parametrized rotation tensor $\boldsymbol{R}(\boldsymbol{p}) \in SO(3,\mathbb{E})$, depending on rotation parameters $\boldsymbol{p}$, defines the current configuration of each rigid body.

Introducing the velocity $\boldsymbol{v}_P \in \mathbb{E}^3$ of the reference point P and the angular velocity $\boldsymbol{\Omega} \in \mathbb{E}^3$, the body-velocity field is fully defined. This way of parametrization is not the most general, but it is the most common for a rigid body and allows to directly obtain the system equations in the well-known form

$$\begin{aligned} \dot{\boldsymbol{q}} &= \boldsymbol{F}(\boldsymbol{q})\boldsymbol{u} + \boldsymbol{\chi}(\boldsymbol{q},t) \\ \boldsymbol{M}(\boldsymbol{q},t)\,\dot{\boldsymbol{u}} &= \boldsymbol{h}(\boldsymbol{q},\boldsymbol{u},t) + \boldsymbol{f}(\boldsymbol{q},\boldsymbol{u},t). \end{aligned} \tag{3.34}$$

The first line of Eq. (3.34) is the kinematic equation, which relates the time derivatives of coordinates $\boldsymbol{q}$ to the generalized velocity $\boldsymbol{u}$. The second equation identifies as the equation of motion describing the kinetics and contains the mass matrix $\boldsymbol{M}(\boldsymbol{q},t)$, the vector of gyroscopic forces $\boldsymbol{h}(\boldsymbol{q},\boldsymbol{u},t)$, and additional external forces $\boldsymbol{f}(\boldsymbol{q},\boldsymbol{u},t)$, e.g., damping or friction forces.

Since several parametrizations will be introduced in this monograph, all of which have their own advantages and allow for different physical interpretations, a general parametrization will be performed here as an example to shorten the subsequent chapters. A single rigid body may be parametrized in the above described manner, by defining the position vector $\boldsymbol{r}_{OP}$ of the reference point P as tuples

$${}_A\boldsymbol{r}_{OP} := \begin{bmatrix} x \\ y \\ z \end{bmatrix} \in \mathbb{R}^3, \tag{3.35}$$

expressed with respect to an A-frame, and by introducing the rotation matrix ${}_I\boldsymbol{R}(\boldsymbol{p})$ as element of $SO(3,\mathbb{R})$, defining the orientation of the body-fixed B-frame relative to the inertial I-frame. In mechanics it is common to describe the reference point in Cartesian coordinates. Alternatively, cylindrical, spherical or other curved coordinates can be chosen to describe a reference point of a mechanical system [27]. The choice of the representing coordinates is far from trivial and depends strongly on the respective application and the subsequent analysis. In a first step, the rotation matrix is assumed to be parametrized by nine matrix components

$$\boldsymbol{p} := \begin{bmatrix} R_{11} & R_{12} & \dots & R_{33} \end{bmatrix} \in \mathbb{R}^9,$$

yielding the rotation matrix

$$_I\boldsymbol{R}(\boldsymbol{p}) := \begin{bmatrix} R_{11} & R_{12} & R_{13} \\ R_{21} & R_{22} & R_{23} \\ R_{31} & R_{32} & R_{33} \end{bmatrix} \in \mathbb{R}^{3\times 3}. \tag{3.36}$$

Together with the parametrizations from Eq. (3.35) and Eq. (3.36), the configuration of the body is fully defined by the chosen coordinates

$$\boldsymbol{q} := \begin{bmatrix} _A\boldsymbol{r}_{OP}, & \boldsymbol{p} \end{bmatrix} = \begin{bmatrix} x & y & z & R_{11} & R_{12} & \dots & R_{33} \end{bmatrix} \in \mathbb{R}^{12}.$$

To parametrize the velocity and variation fields, the minimal velocities

$$\boldsymbol{u} = \begin{bmatrix} _A\boldsymbol{v}_P, & _B\boldsymbol{\Omega} \end{bmatrix} \in \mathbb{R}^6,$$

and the corresponding variations

$$\delta\boldsymbol{s} = \begin{bmatrix} _A\delta\boldsymbol{r}_P, & _B\delta\boldsymbol{\varphi} \end{bmatrix} \in \mathbb{R}^6$$

are chosen. Here, the angular velocity $_B\boldsymbol{\Omega} = [\omega_x, \omega_y, \omega_z] \in \mathbb{R}^3$ and the associated anguar variation $_B\delta\boldsymbol{\varphi} = [\delta\varphi_x, \delta\varphi_y, \delta\varphi_z] \in \mathbb{R}^3$ are expressed in the body-fixed B-frame, which are connected to the derivatives of the parameters $\boldsymbol{p}$ by

$$_B\boldsymbol{\Omega} = \boldsymbol{A}_{IB}^{\mathrm{T}} \boldsymbol{j}_{\mathbb{R}}^{-1} \left[\left(\frac{\partial _I\boldsymbol{R}(\boldsymbol{p})}{\partial \boldsymbol{p}} \dot{\boldsymbol{p}} \right) {_I\boldsymbol{R}(\boldsymbol{p})}^{\mathrm{T}} \right] \tag{3.37}$$

and

$$_B\delta\boldsymbol{\varphi} = \boldsymbol{A}_{IB}^{\mathrm{T}} \boldsymbol{j}_{\mathbb{R}}^{-1} \left[\left(\frac{\partial _I\boldsymbol{R}(\boldsymbol{p})}{\partial \boldsymbol{p}} \delta\boldsymbol{p} \right) {_I\boldsymbol{R}(\boldsymbol{p})}^{\mathrm{T}} \right],$$

respectively. According to Eq. (3.16) the velocity $_A\boldsymbol{v}_P$ yields

$$_A\boldsymbol{v}_P = {_A\dot{\boldsymbol{r}}_{OP}} + {_A\boldsymbol{\omega}_{IA}} \times {_A\boldsymbol{r}_{OP}}. \tag{3.38}$$

From Eq. (3.37) and Eq. (3.38), the kinematic equation $\dot{\boldsymbol{q}} = \boldsymbol{F}(\boldsymbol{q})\boldsymbol{u} + \boldsymbol{\chi}(\boldsymbol{q}, t)$ is identified. Again, using Eq. (3.16) the linear acceleration $_A\boldsymbol{a}_P$ and the angular acceleration $_B\boldsymbol{\Psi}$ are given in coordinates by

$$_A\boldsymbol{a}_P = {_A\dot{\boldsymbol{v}}_P} + {_A\boldsymbol{\omega}_{IA}} \times {_A\boldsymbol{v}_P}, \tag{3.39}$$

and

$$ {}_B\boldsymbol{\Psi} = {}_B\dot{\boldsymbol{\Omega}}, \tag{3.40} $$

where the identity ${}_B\boldsymbol{\omega}_{IB} \times {}_B\boldsymbol{\Omega} = {}_B\boldsymbol{\Omega} \times {}_B\boldsymbol{\Omega} = 0$ has been used. Combination of Eq. (3.39) and Eq. (3.40) yields the expression

$$ \begin{bmatrix} {}_A\boldsymbol{a}_P \\ {}_B\boldsymbol{\Psi} \end{bmatrix} = \begin{bmatrix} {}_A\boldsymbol{v}_P \\ {}_B\boldsymbol{\Omega} \end{bmatrix}^{\bullet} + \begin{bmatrix} {}_A\boldsymbol{\omega}_{IA} \times {}_A\boldsymbol{v}_P \\ 0 \end{bmatrix} = \dot{\boldsymbol{u}} + \boldsymbol{b}(\boldsymbol{q},\boldsymbol{u}). \tag{3.41} $$

In Equation (3.12) the virtual work of a rigid body is introduced, which can be expressed with respect to the chosen minimal velocity $\boldsymbol{u}$ and the corresponding variation $\delta\boldsymbol{s}$ as

$$ \begin{aligned} \delta W^{\mathscr{B}} = \begin{bmatrix} {}_A\delta\boldsymbol{r}_P \\ {}_B\delta\boldsymbol{\varphi} \end{bmatrix}^{\mathrm{T}} \Bigg(& \begin{bmatrix} m\mathbf{1} & m\boldsymbol{A}_{AB}\,{}_B\tilde{\boldsymbol{r}}_{PS}^{\mathrm{T}} \\ m\,{}_B\tilde{\boldsymbol{r}}_{PS}\boldsymbol{A}_{AB}^{\mathrm{T}} & {}_B\boldsymbol{\Theta}_P \end{bmatrix} \begin{bmatrix} {}_A\boldsymbol{a}_P \\ {}_B\boldsymbol{\Psi} \end{bmatrix} \\ & - \begin{bmatrix} -m\boldsymbol{A}_{AB}\,{}_B\boldsymbol{\Omega} \times \left({}_B\boldsymbol{\Omega} \times {}_B\boldsymbol{r}_{PS}\right) \\ -{}_B\boldsymbol{\Omega} \times \left({}_B\boldsymbol{\Theta}_P\,{}_B\boldsymbol{\Omega}\right) \end{bmatrix} \Bigg) + \delta W^{\mathrm{ext}}. \end{aligned} \tag{3.42} $$

Inserting the accelerations from Eq. (3.41) and identifying the variations $\delta\boldsymbol{s}$ finally yields the virtual work

$$ \begin{aligned} \delta W^{\mathscr{B}} = \delta\boldsymbol{s}^{\mathrm{T}} \Bigg(& \begin{bmatrix} m\mathbf{1} & m\boldsymbol{A}_{AB}\,{}_B\tilde{\boldsymbol{r}}_{PS}^{\mathrm{T}} \\ m\,{}_B\tilde{\boldsymbol{r}}_{PS}\boldsymbol{A}_{AB}^{\mathrm{T}} & {}_B\boldsymbol{\Theta}_P \end{bmatrix} \dot{\boldsymbol{u}} \\ & - \begin{bmatrix} -m\,{}_A\boldsymbol{\omega}_{IA} \times {}_A\boldsymbol{v}_P - m\boldsymbol{A}_{AB}\,{}_B\boldsymbol{\Omega} \times \left({}_B\boldsymbol{\Omega} \times {}_B\boldsymbol{r}_{PS}\right) \\ -m\,{}_B\tilde{\boldsymbol{r}}_{PS}\boldsymbol{A}_{AB}^{\mathrm{T}}({}_A\boldsymbol{\omega}_{IA} \times {}_A\boldsymbol{v}_P) - {}_B\boldsymbol{\Omega} \times \left({}_B\boldsymbol{\Theta}_P\,{}_B\boldsymbol{\Omega}\right) \end{bmatrix} \Bigg) + \delta W^{\mathrm{ext}}, \end{aligned} \tag{3.43} $$

with respect to the minimal velocities $\boldsymbol{u}$. Identifying the mass matrix

$$ \boldsymbol{M}(\boldsymbol{q},t) = \begin{bmatrix} m\mathbf{1} & m\boldsymbol{A}_{AB}\,{}_B\tilde{\boldsymbol{r}}_{PS}^{\mathrm{T}} \\ m\,{}_B\tilde{\boldsymbol{r}}_{PS}\boldsymbol{A}_{AB}^{\mathrm{T}} & {}_B\boldsymbol{\Theta}_P \end{bmatrix} \tag{3.44} $$

and the vector of gyroscopic terms

$$ \boldsymbol{h}(\boldsymbol{q},\boldsymbol{u},t) = \begin{bmatrix} -m\,{}_A\boldsymbol{\omega}_{IA} \times {}_A\boldsymbol{v}_P - m\boldsymbol{A}_{AB}\,{}_B\boldsymbol{\Omega} \times \left({}_B\boldsymbol{\Omega} \times {}_B\boldsymbol{r}_{PS}\right) \\ -m\,{}_B\tilde{\boldsymbol{r}}_{PS}\boldsymbol{A}_{AB}^{\mathrm{T}}({}_A\boldsymbol{\omega}_{IA} \times {}_A\boldsymbol{v}_P) - {}_B\boldsymbol{\Omega} \times \left({}_B\boldsymbol{\Theta}_P\,{}_B\boldsymbol{\Omega}\right) \end{bmatrix} \tag{3.45} $$

reveals the compact expression

$$ \delta W = \delta\boldsymbol{s}^{\mathrm{T}}\big(\boldsymbol{M}(\boldsymbol{q},t)\dot{\boldsymbol{u}} - \boldsymbol{h}(\boldsymbol{q},\boldsymbol{u},t)\big) + \delta W^{\mathrm{ext}} \tag{3.46} $$

of the virtual work from Eq. (3.43). Therein, the virtual work of external forces δW^{ext} in generalized velocities $\boldsymbol{u}$ reads as

$$ \delta W^{\mathrm{ext}} = -\delta\boldsymbol{s}^{\mathrm{T}}\boldsymbol{f}(\boldsymbol{q},\boldsymbol{u},t), $$

where the corresponding generalized force $\boldsymbol{f}(\boldsymbol{q},\boldsymbol{u},t) = \boldsymbol{f}_g(\boldsymbol{q},t) + \sum_k \boldsymbol{f}_{\gamma_k}(\boldsymbol{q},\boldsymbol{u},t)$ contains all external forces acting on the rigid body. In particular, the generalized gravitational force is given by

$$\boldsymbol{f}_g(\boldsymbol{q},t) = {}_I\boldsymbol{J}_S{}^{\mathrm{T}}\,{}_I\boldsymbol{F}_g,$$

with Jacobian

$${}_I\boldsymbol{J}_S = \frac{\partial_I \boldsymbol{v}_S}{\partial \boldsymbol{u}}$$

and gravitational force ${}_I\boldsymbol{F}_g = [0, 0, -mg]^{\mathrm{T}}$.

Contact forces, i.e., normal and frictional forces, are characterized by a relative velocity γ_k and corresponding force (or moment) λ_k, which is projected onto the velocity coordinates by the generalized force direction

$$\boldsymbol{w}_{\gamma_k}^{\mathrm{T}} = \frac{\partial \gamma_k}{\partial \boldsymbol{u}},$$

resulting in the associated generalized force contributions

$$\boldsymbol{f}_{\gamma_k}(\boldsymbol{q},\boldsymbol{u},t) = \boldsymbol{w}_{\gamma_k}\,\lambda_k.$$

Following the principle of virtual work, which states that the virtual work (3.46) must vanish for all virtual displacements $\delta\boldsymbol{s}$ at each instant of time t, the equations of motion are given by

$$\boldsymbol{M}(\boldsymbol{q},t)\,\dot{\boldsymbol{u}} = \boldsymbol{h}(\boldsymbol{q},\boldsymbol{u},t) + \boldsymbol{f}(\boldsymbol{q},\boldsymbol{u},t). \tag{3.47}$$

The kinematic relationships from Eq. (3.37) and Eq. (3.38) yield the kinematic equation

$$\dot{\boldsymbol{q}} = \boldsymbol{F}(\boldsymbol{q})\boldsymbol{u} + \boldsymbol{\chi}(\boldsymbol{q},t) \tag{3.48}$$

where $\boldsymbol{F}(\boldsymbol{q}) \in \mathbb{R}^{12\times 6}$ and $\boldsymbol{\chi}(\boldsymbol{q},t) \in \mathbb{R}^{12}$ are not given here in full detail. Herein, $\boldsymbol{q}$ has to satisfy the six orthogonality conditions ${}_I\boldsymbol{R}^{\mathrm{T}}{}_I\boldsymbol{R} = \mathbf{1}$, which implies that $\boldsymbol{F}(\boldsymbol{q})$ is such that the velocity constraint $\frac{\mathrm{d}}{\mathrm{d}t}\left({}_I\boldsymbol{R}^{\mathrm{T}}{}_I\boldsymbol{R}\right) = 0$ is fulfilled. With Equation (3.47) and Eq. (3.48), the system

$$\begin{aligned} \dot{\boldsymbol{q}} &= \boldsymbol{F}(\boldsymbol{q})\boldsymbol{u} + \boldsymbol{\chi}(\boldsymbol{q},t) \\ \boldsymbol{M}(\boldsymbol{q},t)\,\dot{\boldsymbol{u}} &= \boldsymbol{h}(\boldsymbol{q},\boldsymbol{u},t) + \boldsymbol{f}(\boldsymbol{q},\boldsymbol{u},t) \end{aligned} \tag{3.49}$$

in first-order form is obtained, governing the non-impulsive motion of the body $\mathscr{B}$.

In the following sections, various mechanical models of the tippedisk in different parametrizations are presented, each of which has its own advantages.

Geometric center G described in the inertial frame

Choosing the geometric center G as reference point of the tippedisk leads to simplified generalized force directions, with the disadvantage of more cumbersome gyroscopic terms and coupling between the translational and rotational motion in the mass matrix. It is a choice to parametrize the position of the reference point G in inertial I-coordinates, i.e.,

$$ {}_I\boldsymbol{r}_{OG} = \begin{bmatrix} x & y & z \end{bmatrix}^{\mathrm{T}} \in \mathbb{R}^3, \tag{3.50}$$

with associated velocity

$$ {}_I\boldsymbol{v}_G = \begin{bmatrix} \dot{x} & \dot{y} & \dot{z} \end{bmatrix}^{\mathrm{T}} \in \mathbb{R}^3. \tag{3.51}$$

At this point the question arises: how to parametrize the orientation and angular velocity of the body?

In the following, a parametrization in quaternions and one in Euler angles are presented. The quaternion based model has the advantage of singular free description and provides a symmetric structure that allows more efficient numerical integration. The parametrization in Euler angles leads to a singular description and an asymmetric system structure with numerical drawbacks, but corresponds to a minimal formulation that allows for a direct physical interpretation. Therefore, the model in Euler angles is more suitable for the nonlinear analysis. Since the dynamics of the tippedisk contains different time scales and is highly nonlinear, the convergence of the numerical integration is far from trivial. Therefore, the redundant parametrization allows to demonstrate the convergence of the numerical solutions.

Quaternion based Model

One way to parametrize the rotation matrix ${}_I\boldsymbol{R}$ is by using a unit quaternion $\boldsymbol{p} = [p_0, p_1, p_2, p_3]^{\mathrm{T}} \in \mathbb{R}^4$, with $\|\boldsymbol{p}\|_4 = 1$, where $\|.\|_4$ denotes the Euclidean norm in $\mathbb{R}^4$. By splitting the quaternion $\boldsymbol{p}$ into its scalar real part p_0 and the three-dimensional complex part $\boldsymbol{p}_c = [p_1, p_2, p_3]^{\mathrm{T}} \in \mathbb{R}^3$, the rotation matrix ${}_I\boldsymbol{R}$ is parametrized by

$$ {}_I\boldsymbol{R}(\boldsymbol{p}) = \boldsymbol{1} + 2\left(p_0\tilde{\boldsymbol{p}}_c + \tilde{\boldsymbol{p}}_c^2\right) = \boldsymbol{A}_{IB}, \tag{3.52}$$

and fulfills the orthogonality condition ${}_I\boldsymbol{R}_I^{\mathrm{T}}\boldsymbol{R} = \boldsymbol{1}$, if the quaternion $\boldsymbol{p}$ satisfies the constraint $\|\boldsymbol{p}\|_4 = 1$. Evaluation of the parametrization from Eq. (3.52) yields the nine components of the rotation matrix

$$ {}_I\boldsymbol{R}(\boldsymbol{p}) = \begin{bmatrix} 2(p_0^2+p_1^2)-1 & 2(p_1p_2-p_0p_3) & 2(p_1p_3+p_0p_2) \\ 2(p_1p_2+p_0p_3) & 2(p_0^2+p_2^2)-1 & 2(p_2p_3-p_0p_1) \\ 2(p_1p_3-p_0p_2) & 2(p_2p_3+p_0p_1) & 2(p_0^2+p_3^2)-1 \end{bmatrix}. \tag{3.53}$$

Together with the position ${}_I\boldsymbol{r}_{OG}$ and velocity ${}_I\boldsymbol{v}_G$ of the reference point G, from Eq. (3.50) and Eq. (3.51), the parametrization is fully defined by choosing the generalized coordinates

$$\boldsymbol{q} := \begin{bmatrix}{}_I\boldsymbol{r}_{OG}^{\mathrm{T}} & \boldsymbol{p}^{\mathrm{T}}\end{bmatrix}^{\mathrm{T}} = \begin{bmatrix}x & y & z & p_0 & p_1 & p_2 & p_3\end{bmatrix}^{\mathrm{T}} \in \mathbb{R}^7 \tag{3.54}$$

and the minimal velocities

$$\boldsymbol{u} := \begin{bmatrix}\dot{x} & \dot{y} & \dot{z} & \omega_x & \omega_y & \omega_z\end{bmatrix}^{\mathrm{T}} \in \mathbb{R}^6, \tag{3.55}$$

where the angular velocity $\boldsymbol{\Omega}$ of the tippedisk expressed in the body-fixed B-frame is given as

$${}_B\boldsymbol{\Omega} =: \begin{bmatrix}\omega_x & \omega_y & \omega_z\end{bmatrix}^{\mathrm{T}} = {}_B\boldsymbol{J}_R\,\boldsymbol{u}, \tag{3.56}$$

with associated Jacobian

$${}_B\boldsymbol{J}_R = \begin{bmatrix}0 & 0 & 0 & 1 & 0 & 0\\ 0 & 0 & 0 & 0 & 1 & 0\\ 0 & 0 & 0 & 0 & 0 & 1\end{bmatrix}. \tag{3.57}$$

The linear kinematic equation $\dot{\boldsymbol{q}} = \boldsymbol{F}(\boldsymbol{q})\boldsymbol{u}$ is obtained using the time derivative of $\|\boldsymbol{p}\|_4^2 = \boldsymbol{p}^{\mathrm{T}}\boldsymbol{p} = 1$ and yields

$$\dot{\boldsymbol{q}} = \boldsymbol{F}(\boldsymbol{q})\boldsymbol{u} = \begin{bmatrix}\boldsymbol{1} & \boldsymbol{0}\\ \boldsymbol{0} & \frac{1}{2}\bar{\boldsymbol{H}}^{\mathrm{T}}\end{bmatrix}\boldsymbol{u}, \tag{3.58}$$

with

$$\bar{\boldsymbol{H}}^{\mathrm{T}} = \begin{bmatrix}-p_1 & -p_2 & -p_3\\ p_0 & -p_3 & p_2\\ p_3 & p_0 & -p_1\\ -p_2 & p_1 & p_0\end{bmatrix} = \begin{bmatrix}-\boldsymbol{p}_c^{\mathrm{T}}\\ p_0\boldsymbol{1} + \tilde{\boldsymbol{p}}_c\end{bmatrix},$$

cf. [87]. Following the general parametrization from above, with the geometric center as reference point $P = G$, the relative vector ${}_B\boldsymbol{r}_{GS} = [e, 0, 0]^{\mathrm{T}}$ (cf. Eq. (3.17)), the parametrization of ${}_I\boldsymbol{R}(\boldsymbol{p})$ from Eq. (3.53), and the angular velocity ${}_B\boldsymbol{\Omega}$ from Eq. (3.56), yields the equation of motion

$$\boldsymbol{M}(\boldsymbol{q})\dot{\boldsymbol{u}} = \boldsymbol{h}(\boldsymbol{q},\boldsymbol{u}) + \boldsymbol{f}(\boldsymbol{q},\boldsymbol{u})$$

parametrized in generalized coordinates $\boldsymbol{q}$ given in Eq. (3.54) and the minimal velocities $\boldsymbol{u}$ defined in Eq. (3.55), with the corresponding mass matrix

$$\boldsymbol{M}(\boldsymbol{q}) = \begin{bmatrix}m\boldsymbol{1} & m_I\boldsymbol{R}(\boldsymbol{p})_B\tilde{\boldsymbol{r}}_{GS}^{\mathrm{T}}\\ m_B\tilde{\boldsymbol{r}}_{GSI}\boldsymbol{R}(\boldsymbol{p})^{\mathrm{T}} & {}_B\boldsymbol{\Theta}_G\end{bmatrix}, \tag{3.59}$$

and the associated vector of gyroscopic forces

$$\boldsymbol{h}(\boldsymbol{q},\boldsymbol{u}) = \begin{bmatrix} -m\,{}_I\boldsymbol{\Omega}\times\left({}_I\boldsymbol{\Omega}\times{}_I\boldsymbol{r}_{GS}\right) \\ -{}_B\boldsymbol{\Omega}\times\left({}_B\boldsymbol{\Theta}_P\,{}_B\boldsymbol{\Omega}\right) \end{bmatrix}. \tag{3.60}$$

The angular velocity $\boldsymbol{\Omega}$ and the relative position vector $\boldsymbol{r}_{GS}$ are given with respect to the I-frame by the transformations ${}_I\boldsymbol{\Omega} = {}_I\boldsymbol{R}(\boldsymbol{p})_B\boldsymbol{\Omega}$ and ${}_I\boldsymbol{r}_{GS} = {}_I\boldsymbol{R}(\boldsymbol{p})_B\boldsymbol{r}_{GS}$. Note that for the chosen coordinates $\boldsymbol{q}$ from Eq. (3.54) and the generalized velocities $\boldsymbol{u}$ from Eq. (3.55), the equations of motion do not depend explicitly on time t, which would be the case, for example, if the body reference point P is parametrized with respect to a moving basis.

To determine the external, generalized forces $\boldsymbol{f}(\boldsymbol{q},\boldsymbol{u})$, gravitational and contact forces must be taken into account. The gravitational force ${}_I\boldsymbol{F}_g = [0,0,-mg]^{\mathrm{T}}$ is applied at the center of gravity S. The velocity of S is determined by using the rigid body formula (3.4) yielding

$${}_I\boldsymbol{v}_S = {}_I\boldsymbol{v}_G - {}_I\tilde{\boldsymbol{r}}_{GS}\,{}_I\boldsymbol{R}(\boldsymbol{p})_B\boldsymbol{\Omega} = \begin{bmatrix}\mathbf{1} & {}_I\boldsymbol{r}_{GS}^{\mathrm{T}}\,{}_I\boldsymbol{R}(\boldsymbol{p})\end{bmatrix}\boldsymbol{u},$$

from which the Jacobian

$${}_I\boldsymbol{J}_S = \begin{bmatrix}\mathbf{1} & {}_I\boldsymbol{r}_{GS}^{\mathrm{T}}\,{}_I\boldsymbol{R}(\boldsymbol{p})\end{bmatrix}$$

with respect to the chosen minimal velocities $\boldsymbol{u}$ is extracted. The generalized gravitational force then gives

$$\boldsymbol{f}_g = {}_I\boldsymbol{J}_S^{\mathrm{T}}\,{}_I\boldsymbol{F}_g. \tag{3.61}$$

Similarly, the relative velocity ${}_I\boldsymbol{\gamma}_k = [\boldsymbol{\gamma}_{T_k}^{\mathrm{T}}, \gamma_{N_k}]^{\mathrm{T}}$ of all contact points, is obtained by using again the rigid body formula

$${}_I\boldsymbol{\gamma}_k = {}_I\boldsymbol{v}_{C_k} = {}_I\boldsymbol{v}_G - {}_I\boldsymbol{r}_{GC_k}\times{}_I\boldsymbol{\Omega} = \begin{bmatrix}\mathbf{1} & {}_I\tilde{\boldsymbol{r}}_{GC_k}^{\mathrm{T}}\,{}_I\boldsymbol{R}(\boldsymbol{p})\end{bmatrix}\boldsymbol{u}.$$

The generalized force directions of the normal and tangential contact forces are then given as the components in $\boldsymbol{e}_x^I$-, $\boldsymbol{e}_y^I$- and $\boldsymbol{e}_z^I$-direction. For a single contact point C_k, the generalized normal force direction is obtained as

$$\boldsymbol{w}_{N_k} = \begin{bmatrix}({}_I\boldsymbol{e}_z^I)^{\mathrm{T}} & -({}_I\boldsymbol{e}_z^I)^{\mathrm{T}}\,{}_I\tilde{\boldsymbol{r}}_{GC_k}\,{}_I\boldsymbol{R}(\boldsymbol{p})\end{bmatrix}^{\mathrm{T}} \in \mathbb{R}^{6\times 1}$$

and the generalized tangential force direction as

$$\boldsymbol{W}_{T_k} = \begin{bmatrix}({}_I\boldsymbol{e}_x^I)^{\mathrm{T}} & -({}_I\boldsymbol{e}_x^I)^{\mathrm{T}}\,{}_I\tilde{\boldsymbol{r}}_{GC_k}\,{}_I\boldsymbol{R}(\boldsymbol{p}) \\ ({}_I\boldsymbol{e}_y^I)^{\mathrm{T}} & -({}_I\boldsymbol{e}_y^I)^{\mathrm{T}}\,{}_I\tilde{\boldsymbol{r}}_{GC_k}\,{}_I\boldsymbol{R}(\boldsymbol{p})\end{bmatrix}^{\mathrm{T}} \in \mathbb{R}^{6\times 2}.$$

Gathering of these force directions allows to introduce the matrix representations

$$\boldsymbol{W}_N = \begin{bmatrix}\boldsymbol{w}_{N_1} & \boldsymbol{w}_{N_2} & \boldsymbol{w}_{N_3}\end{bmatrix} \in \mathbb{R}^{6\times 3}$$

and

$$\boldsymbol{W}_T = \begin{bmatrix} \boldsymbol{W}_{T_1} & \boldsymbol{W}_{T_2} & \boldsymbol{W}_{T_3} \end{bmatrix} \in \mathbb{R}^{6\times 6},$$

which leads to compact expressions. To obtain the generalized force directions of pivoting and contour frictional forces, the relative spin velocity

$$\omega_{IB} := ({}_I\boldsymbol{e}_z^I)^{\mathrm{T}}\, {}_I\boldsymbol{\Omega} = ({}_I\boldsymbol{e}_z^I)^{\mathrm{T}}\, {}_I\boldsymbol{R}(\boldsymbol{p})\, {}_B\boldsymbol{\Omega},$$

is defined, from which the relative pivoting velocity

$$\gamma_{\tau_k} := \varepsilon_k\, \omega_{IB}$$

is deduced for each contact point C_k. Together with the rotational Jacobian ${}_B\boldsymbol{J}_R$ from Eq. (3.57), the generalized force direction

$$\boldsymbol{w}_{\tau_k} = \varepsilon_k \begin{bmatrix} 0 & 0 & 0 & ({}_I\boldsymbol{e}_z^I)^{\mathrm{T}}\, {}_I\boldsymbol{R}(\boldsymbol{p}) \end{bmatrix}^{\mathrm{T}} \in \mathbb{R}^{6\times 1}$$

is identified. The generalized force directions for pivoting friction of all contact points are collected in the matrix

$$\boldsymbol{W}_\tau = \begin{bmatrix} \boldsymbol{w}_{\tau_1} & \boldsymbol{w}_{\tau_2} & \boldsymbol{w}_{\tau_3} \end{bmatrix} \in \mathbb{R}^{6\times 3}.$$

To consider contour friction, the relative velocity

$$\gamma_{R_k} = -r\dot{\varphi} \tag{3.62}$$

is introduced. Differentiating the horizontality condition $\boldsymbol{e}_x^G \cdot \boldsymbol{e}_z^I \equiv 0$ allows to deduce the velocity

$$\dot{\varphi} = \begin{bmatrix} \frac{R_{31}R_{33}}{R_{31}^2+R_{32}^2} & \frac{R_{32}R_{33}}{R_{31}^2+R_{32}^2} & 1 \end{bmatrix} {}_B\boldsymbol{J}_R\, \boldsymbol{u}$$

of the grinding angle φ, from which the corresponding generalized force direction

$$\boldsymbol{w}_{R_1} = -r \begin{bmatrix} \frac{R_{31}R_{33}}{R_{31}^2+R_{32}^2} & \frac{R_{32}R_{33}}{R_{31}^2+R_{32}^2} & 1 \end{bmatrix} {}_B\boldsymbol{J}_R \in \mathbb{R}^{6\times 1}$$

is extracted. The definition of the contact point C_1 is valid only for non-horizontal configurations, i.e., configurations with only one contact point, therefore the generalized force direction for contour friction is given as

$$\boldsymbol{W}_R = -r \begin{bmatrix} 0 & 0 & 0 & \frac{R_{31}R_{33}}{R_{31}^2+R_{32}^2} & \frac{R_{32}R_{33}}{R_{31}^2+R_{32}^2} & 1 \\ 0 & 0 & 0 & 0 & 0 & 0 \\ 0 & 0 & 0 & 0 & 0 & 0 \end{bmatrix}^{\mathrm{T}} \in \mathbb{R}^{6\times 3}.$$

For a horizontally orientated disk, the contact points C_k are not properly defined [70], resulting in the trivial generalized force direction $\boldsymbol{W}_R = \boldsymbol{0} \in \mathbb{R}^{6\times 3}$.

As the quaternion based model is already written in first-order form, the generalized force directions $\boldsymbol{W} = \left[\boldsymbol{W}_N, \boldsymbol{W}_T, \boldsymbol{W}_\tau, \boldsymbol{W}_R\right]$ and corresponding contact forces $\boldsymbol{\lambda} = \left[\boldsymbol{\lambda}_N^{\mathrm{T}}, \boldsymbol{\lambda}_T^{\mathrm{T}}, \boldsymbol{\lambda}_\tau^{\mathrm{T}}, \boldsymbol{\lambda}_R^{\mathrm{T}}\right]^{\mathrm{T}}$ are collected in matrices, allowing the system equations to be compactly written as

$$\begin{aligned} \dot{\boldsymbol{q}} &= \boldsymbol{F}(\boldsymbol{q})\boldsymbol{u} \\ \boldsymbol{M}(\boldsymbol{q})\dot{\boldsymbol{u}} &= \boldsymbol{h}(\boldsymbol{q},\boldsymbol{u}) + \boldsymbol{f}_g + \boldsymbol{W}\boldsymbol{\lambda}, \end{aligned} \tag{3.63}$$

with the mass matrix $\boldsymbol{M}(\boldsymbol{q})$ from Eq. (3.59), the vector of gyroscopic forces $\boldsymbol{h}(\boldsymbol{q},\boldsymbol{u})$ from Eq. (3.60), the generalized gravitational force $\boldsymbol{f}_g$ from Eq. (3.61) and the kinematic equation from Eq. (3.58).

For a quaternion based model, the orthogonality condition ${}_I\boldsymbol{R}(\boldsymbol{p})^{\mathrm{T}}{}_I\boldsymbol{R}(\boldsymbol{p}) = \boldsymbol{1}$ is fulfilled through the constraint on the norm $\|\boldsymbol{p}\|_4 = 1$ of the quaternion. The latter, however, is by Eq. (3.58) only kept on velocity level. This implies that the quaternion needs to be properly initialized such that ${}_I\boldsymbol{R}(\boldsymbol{p}(t_0))^{\mathrm{T}}{}_I\boldsymbol{R}(\boldsymbol{p}(t_0)) = \boldsymbol{1}$ holds. In addition, note that Eq. (3.63) does not contain an associated Lagrange multiplier, which may prevent the constraint from drifting. Therefore, in a numerical scheme, drift correction may be required, when Eq. (3.63) is integrated numerically. To prevent this condition from drifting, the quaternion is normalized after each time step.

Euler angles

Alternatively, the rotation matrix can be described by the three Euler angles $\boldsymbol{\varphi} = [\alpha, \beta, \gamma]^{\mathrm{T}}$ in an intrinsic z-x-z-convention. This specific choice of Euler angles enables a straightforward physical interpretation, since each Euler angle corresponds to a physical angle, cf. Figure 3.4. Therefore, the R-frame with $\boldsymbol{e}_z^R = \boldsymbol{e}_z^I$, $\boldsymbol{e}_x^R = \cos\alpha\, \boldsymbol{e}_x^I + \sin\alpha\, \boldsymbol{e}_y^I$ and $\boldsymbol{e}_y^R = \boldsymbol{e}_z^R \times \boldsymbol{e}_x^R$ is introduced, by rotating the inertial I-frame around $\boldsymbol{e}_z^R$. The sequence of rotation is then given as the first rotation with angle α around the $\boldsymbol{e}_z^I$-axis, the second rotation with angle β around the $\boldsymbol{e}_x^R$-axis and the third rotation with angle γ around the $\boldsymbol{e}_z^G$-axis. The corresponding elemental transformations are

$$\boldsymbol{A}_{IR} = \begin{bmatrix} \mathrm{c}\alpha & -\mathrm{s}\alpha & 0 \\ \mathrm{s}\alpha & \mathrm{c}\alpha & 0 \\ 0 & 0 & 1 \end{bmatrix}, \boldsymbol{A}_{RG} = \begin{bmatrix} 1 & 0 & 0 \\ 0 & \mathrm{c}\beta & -\mathrm{s}\beta \\ 0 & \mathrm{s}\beta & \mathrm{c}\beta \end{bmatrix}, \boldsymbol{A}_{GB} = \begin{bmatrix} \mathrm{c}\gamma & -\mathrm{s}\gamma & 0 \\ \mathrm{s}\gamma & \mathrm{c}\gamma & 0 \\ 0 & 0 & 1 \end{bmatrix}, \tag{3.64}$$

where the abbreviations $\mathrm{s}\alpha = \sin(\alpha)$, $\mathrm{c}\alpha = \cos(\alpha)$ etc. have been used to shorten notation. The rotation matrix

$$ {}_I\boldsymbol{R}(\boldsymbol{\varphi}) = \begin{bmatrix} \mathrm{c}\alpha\mathrm{c}\gamma - \mathrm{s}\alpha\mathrm{c}\beta\mathrm{s}\gamma & -\mathrm{c}\alpha\mathrm{s}\gamma - \mathrm{s}\alpha\mathrm{c}\beta\mathrm{c}\gamma & \mathrm{s}\alpha\mathrm{s}\beta \\ \mathrm{s}\alpha\mathrm{c}\gamma + \mathrm{c}\alpha\mathrm{c}\beta\mathrm{s}\gamma & -\mathrm{s}\alpha\mathrm{s}\gamma + \mathrm{c}\alpha\mathrm{c}\beta\mathrm{c}\gamma & -\mathrm{c}\alpha\mathrm{s}\beta \\ \mathrm{s}\beta\mathrm{s}\gamma & \mathrm{s}\beta\mathrm{c}\gamma & \mathrm{c}\beta \end{bmatrix} = \boldsymbol{A}_{IB}, \tag{3.65} $$

is obtained by the series multiplication $\boldsymbol{A}_{IB} = \boldsymbol{A}_{IR}\boldsymbol{A}_{RG}\boldsymbol{A}_{GB}$ of transformation matrices and subsequent identification of ${}_I\boldsymbol{R}(\boldsymbol{\varphi}) = \boldsymbol{A}_{IB}$. According to the group properties of $SO(3,\mathbb{R})$ the constructed rotation matrix per se fulfills the orthogonality condition ${}_I\boldsymbol{R}^{\mathrm{T}}\,{}_I\boldsymbol{R} = \boldsymbol{1}$. The corresponding angular velocity $\boldsymbol{\Omega}$ expressed in the body-fixed B-frame results from the sum

$$ {}_B\boldsymbol{\Omega} = \dot{\alpha}\boldsymbol{A}_{RB}^{\mathrm{T}}\,{}_R\boldsymbol{e}_z^R + \dot{\beta}\boldsymbol{A}_{GB}^{\mathrm{T}}\,{}_G\boldsymbol{e}_x^G + \dot{\gamma}\,{}_B\boldsymbol{e}_z^B = \begin{bmatrix} \dot{\alpha}\mathrm{s}\beta\mathrm{s}\gamma + \dot{\beta}\mathrm{c}\gamma \\ \dot{\alpha}\mathrm{s}\beta\mathrm{c}\gamma - \dot{\beta}\mathrm{s}\gamma \\ \dot{\alpha}\mathrm{c}\beta + \dot{\gamma} \end{bmatrix} =: \begin{bmatrix} \omega_x \\ \omega_y \\ \omega_z \end{bmatrix}, \tag{3.66} $$

with the transformation matrix $\boldsymbol{A}_{RB} = \boldsymbol{A}_{RG}\boldsymbol{A}_{GB}$. Making use of the transformation $\boldsymbol{A}_{IB} = {}_I\boldsymbol{R}(\boldsymbol{\varphi})$, the angular velocity expressed with respect to the I-frame yields the tuple

$$ {}_I\boldsymbol{\Omega} = \boldsymbol{A}_{IB}\,{}_B\boldsymbol{\Omega} = \begin{bmatrix} \dot{\beta}\mathrm{c}\alpha + \dot{\gamma}\mathrm{s}\alpha\mathrm{s}\beta \\ \dot{\beta}\mathrm{s}\alpha - \dot{\gamma}\mathrm{c}\alpha\mathrm{s}\beta \\ \dot{\alpha} + \dot{\gamma}\mathrm{c}\beta \end{bmatrix}. $$

If in addition the geometric center G is chosen as reference point with position vector ${}_I\boldsymbol{r}_{OG}$ from Eq. (3.50) given in the inertial I-frame, the configuration of the tippedisk is fully defined. This kinematic description implicates the generalized coordinates

$$ \boldsymbol{q} := \begin{bmatrix} x & y & z & \alpha & \beta & \gamma \end{bmatrix}^{\mathrm{T}} \in \mathbb{R}^6. \tag{3.67} $$

Since these generalized coordinates $\boldsymbol{q}$ allow to characterize the configuration of the tippedisk, without additional dependencies, they are called minimal coordinates of the free tippedisk.

Equivalent to the quaternion based model, the translational velocity ${}_I\boldsymbol{v}_G$ of the geometric center G given in Eq. (3.51) and the angular velocity from Eq. (3.66) are a valid choice

$$ \boldsymbol{u} := \begin{bmatrix} \dot{x} & \dot{y} & \dot{z} & \omega_x & \omega_y & \omega_z \end{bmatrix}^{\mathrm{T}} \in \mathbb{R}^6 \tag{3.68} $$

of minimal velocities. With $\boldsymbol{q}$ and $\boldsymbol{u}$ the configuration and the body velocity of the tippedisk is fully defined.

From Eq. (3.51) and Eq. (3.66) the Jacobian matrix of translation

$$ {}_I\boldsymbol{J}_G = \frac{\partial {}_I\boldsymbol{v}_G}{\partial \dot{\boldsymbol{q}}} = \begin{bmatrix} 1 & 0 & 0 & 0 & 0 & 0 \\ 0 & 1 & 0 & 0 & 0 & 0 \\ 0 & 0 & 1 & 0 & 0 & 0 \end{bmatrix}, $$

and the Jacobian matrix of rotation

$$ {}_B\boldsymbol{J}_R = \frac{\partial {}_B\boldsymbol{\Omega}}{\partial \dot{\boldsymbol{q}}} = \begin{bmatrix} 0 & 0 & 0 & \mathrm{s}\beta\mathrm{s}\gamma & \mathrm{c}\gamma & 0 \\ 0 & 0 & 0 & \mathrm{s}\beta\mathrm{c}\gamma & -\mathrm{s}\gamma & 0 \\ 0 & 0 & 0 & \mathrm{c}\beta & 0 & 1 \end{bmatrix} \tag{3.69} $$

are deduced, implying the kinematic relation

$$ \boldsymbol{u} = \begin{bmatrix} {}_I\boldsymbol{v}_G \\ {}_B\boldsymbol{\Omega} \end{bmatrix} = \boldsymbol{A}(\boldsymbol{q})\,\dot{\boldsymbol{q}} = \begin{bmatrix} {}_I\boldsymbol{J}_G \\ {}_B\boldsymbol{J}_R \end{bmatrix} \dot{\boldsymbol{q}} \tag{3.70} $$

between the generalized velocities $\boldsymbol{u}$ from Eq. (3.68) and the time derivatives $\dot{\boldsymbol{q}}$ of the generalized position coordinates $\boldsymbol{q}$ from Eq. (3.67). For non-singular configurations the linear function ${}_B\boldsymbol{\Omega} = {}_B\boldsymbol{\Omega}(\dot{\boldsymbol{\varphi}})$ is invertible, allowing to define for these configurations the kinematic equation

$$ \dot{\boldsymbol{q}} = \boldsymbol{B}(\boldsymbol{q})\boldsymbol{u}, \quad \text{with} \quad \boldsymbol{B}(\boldsymbol{q}) = \boldsymbol{A}(\boldsymbol{q})^{-1}. \tag{3.71} $$

Evaluation of the system equation (3.49) in coordinates $\boldsymbol{q}$ and velocities $\boldsymbol{u}$ gives with the kinematic equation from Eq. (3.71) the mechanical system

$$ \begin{aligned} \dot{\boldsymbol{q}} &= \boldsymbol{B}(\boldsymbol{q})\boldsymbol{u} \\ \boldsymbol{M}(\boldsymbol{q})\dot{\boldsymbol{u}} &= \boldsymbol{h}(\boldsymbol{q},\boldsymbol{u}) + \boldsymbol{f}(\boldsymbol{q},\boldsymbol{u}), \end{aligned} \tag{3.72} $$

in first-order form with the associated mass matrix

$$ \boldsymbol{M}(\boldsymbol{q}) = \begin{bmatrix} m\boldsymbol{1} & m\,{}_I\boldsymbol{R}(\boldsymbol{\varphi})\,{}_B\tilde{\boldsymbol{r}}_{GS}^{\mathrm{T}} \\ m\,{}_B\tilde{\boldsymbol{r}}_{GS}\,{}_I\boldsymbol{R}(\boldsymbol{\varphi})^{\mathrm{T}} & {}_B\boldsymbol{\Theta}_G \end{bmatrix}, \tag{3.73} $$

and the vector of gyroscopic forces

$$ \boldsymbol{h}(\boldsymbol{q},\boldsymbol{u}) = \begin{bmatrix} -m\,{}_I\boldsymbol{\Omega} \times \left({}_I\boldsymbol{\Omega} \times {}_I\boldsymbol{r}_{GS}\right) \\ -{}_B\boldsymbol{\Omega} \times \left({}_B\boldsymbol{\Theta}_P\,{}_B\boldsymbol{\Omega}\right) \end{bmatrix}, \tag{3.74} $$

cf. Eq. (3.44) and Eq. (3.45). Structurally, the mass matrix and the vector of gyroscopic forces from Eq. (3.73) and Eq. (3.74) are equal to the mass matrix and the vector of gyroscopic forces from Eq. (3.59) and Eq. (3.60). This structural equality comes from the fact, that both models are derived with respect to the same minimal velocities $\boldsymbol{u}$. However, the evaluated identities are different, as the rotation matrix ${}_I\boldsymbol{R}(\boldsymbol{\varphi})$ is parametrized differently.

Substitution of Eq. (3.70) into the dynamics from Eq. (3.72), renders the kinematic equation trivial. Moreover, by pre-multiplying the equation of motion with the matrix $\boldsymbol{A}(\boldsymbol{q})^{\mathrm{T}}$, a step which may be motivated through the virtual work, the Lagrangian system

$$\bar{\boldsymbol{M}}(\boldsymbol{q})\,\ddot{\boldsymbol{q}} = \bar{\boldsymbol{h}}(\boldsymbol{q},\dot{\boldsymbol{q}}) + \bar{\boldsymbol{f}}(\boldsymbol{q},\dot{\boldsymbol{q}},t) \tag{3.75}$$

is obtained. Equation (3.75) defines the equations of motion for generalized coordinates $\boldsymbol{q}$, where $\bar{\boldsymbol{M}}(\boldsymbol{q})$ describes the mass matrix and $\bar{\boldsymbol{h}}(\boldsymbol{q},\dot{\boldsymbol{q}})$ a vector containing all inertia forces which are not linear in the generalized accelerations $\ddot{\boldsymbol{q}}$, i.e., gyroscopic forces. In detail, the mass matrix and the vector of gyroscopic forces are given as:

$$\bar{\boldsymbol{M}} := \boldsymbol{A}(\boldsymbol{q})^{\mathrm{T}}\,\boldsymbol{M}(\boldsymbol{q})\,\boldsymbol{A}(\boldsymbol{q}) = \begin{bmatrix} \bar{\boldsymbol{M}}_{11} & \bar{\boldsymbol{M}}_{12} \\ \bar{\boldsymbol{M}}_{21} & \bar{\boldsymbol{M}}_{22} \end{bmatrix} \tag{3.76}$$

with submatrices

$$\begin{aligned}
\bar{\boldsymbol{M}}_{11} &= \begin{bmatrix} m & 0 & 0 \\ 0 & m & 0 \\ 0 & 0 & m \end{bmatrix}, \quad \bar{\boldsymbol{M}}_{21} = \bar{\boldsymbol{M}}_{12}^{\mathrm{T}} \\
\bar{\boldsymbol{M}}_{12} &= me \begin{bmatrix} -\mathrm{c}\alpha\mathrm{c}\beta\mathrm{s}\gamma - \mathrm{s}\alpha\mathrm{c}\gamma & \mathrm{s}\alpha\mathrm{s}\beta\mathrm{s}\gamma & -\mathrm{c}\alpha\mathrm{s}\gamma - \mathrm{s}\alpha\mathrm{c}\beta\mathrm{c}\gamma \\ -\mathrm{s}\alpha\mathrm{c}\beta\mathrm{s}\gamma + \mathrm{c}\alpha\mathrm{c}\gamma & -\mathrm{c}\alpha\mathrm{s}\beta\mathrm{s}\gamma & -\mathrm{s}\alpha\mathrm{s}\gamma + \mathrm{c}\alpha\mathrm{c}\beta\mathrm{c}\gamma \\ 0 & \mathrm{c}\beta\mathrm{s}\gamma & \mathrm{s}\beta\mathrm{c}\gamma \end{bmatrix} \\
\bar{\boldsymbol{M}}_{22} &= \begin{bmatrix} (A\mathrm{s}^2\gamma + B\mathrm{c}^2\gamma)\mathrm{s}^2\beta + Cc^2\beta & (A-B)\mathrm{s}\beta\mathrm{s}\gamma\mathrm{c}\gamma & C\mathrm{c}\beta \\ (A-B)\mathrm{s}\beta\mathrm{s}\gamma\mathrm{c}\gamma & A\mathrm{c}^2\gamma + B\mathrm{s}^2\gamma & 0 \\ C\mathrm{c}\beta & 0 & C \end{bmatrix}
\end{aligned}$$

and

$$\begin{aligned}
\bar{\boldsymbol{h}}(\boldsymbol{q},\dot{\boldsymbol{q}}) &:= \boldsymbol{A}(\boldsymbol{q})^{\mathrm{T}}\big(\boldsymbol{h}(\boldsymbol{q},\boldsymbol{A}(\boldsymbol{q})\dot{\boldsymbol{q}}) - \boldsymbol{M}(\boldsymbol{q},t)\dot{\boldsymbol{A}}(\boldsymbol{q})\dot{\boldsymbol{q}}\big) \\
&= \begin{bmatrix} \bar{h}_1 & \bar{h}_2 & \bar{h}_3 & \bar{h}_4 & \bar{h}_5 & \bar{h}_6 \end{bmatrix}^{\mathrm{T}}
\end{aligned} \tag{3.77}$$

with

$$\begin{aligned}
\bar{h}_1 &= me\left[\dot{\alpha}^2(\mathrm{c}\alpha\mathrm{c}\gamma-\mathrm{s}\alpha\mathrm{c}\beta\mathrm{s}\gamma)-\dot{\beta}^2\mathrm{s}\alpha\mathrm{c}\beta\mathrm{s}\gamma+\dot{\gamma}^2(\mathrm{c}\alpha\mathrm{c}\gamma-\mathrm{s}\alpha\mathrm{c}\beta\mathrm{s}\gamma)\right.\\
&\qquad\left.-2\dot{\alpha}\dot{\beta}\mathrm{c}\alpha\mathrm{s}\beta\mathrm{s}\gamma-2\dot{\alpha}\dot{\gamma}(\mathrm{s}\alpha\mathrm{s}\gamma-\mathrm{c}\alpha\mathrm{c}\beta\mathrm{c}\gamma)-2\dot{\beta}\dot{\gamma}\mathrm{s}\alpha\mathrm{s}\beta\mathrm{c}\gamma\right],\\
\bar{h}_2 &= me\left[\dot{\alpha}^2(\mathrm{s}\alpha\mathrm{c}\gamma+\mathrm{c}\alpha\mathrm{c}\beta\mathrm{s}\gamma)+\dot{\beta}^2\mathrm{c}\alpha\mathrm{c}\beta\mathrm{s}\gamma+\dot{\gamma}^2(\mathrm{s}\alpha\mathrm{c}\gamma+\mathrm{c}\alpha\mathrm{c}\beta\mathrm{s}\gamma)\right.\\
&\qquad\left.-2\dot{\alpha}\dot{\beta}\mathrm{s}\alpha\mathrm{s}\beta\mathrm{s}\gamma+2\dot{\alpha}\dot{\gamma}(\mathrm{c}\alpha\mathrm{s}\gamma+\mathrm{s}\alpha\mathrm{c}\beta\mathrm{c}\gamma)+2\dot{\beta}\dot{\gamma}\mathrm{c}\alpha\mathrm{s}\beta\mathrm{c}\gamma\right],\\
\bar{h}_3 &= me\left[\dot{\beta}^2\mathrm{s}\beta\mathrm{s}\gamma+\dot{\gamma}^2\mathrm{s}\beta\mathrm{s}\gamma-2\dot{\beta}\dot{\gamma}\mathrm{c}\beta\mathrm{c}\gamma\right],\\
\bar{h}_4 &= -\dot{\beta}^2(A-B)\mathrm{c}\beta\mathrm{s}\gamma\mathrm{c}\gamma-2\dot{\alpha}\dot{\beta}(A\mathrm{s}^2\gamma+B\mathrm{c}^2\gamma-C)\mathrm{s}\beta\mathrm{c}\beta\\
&\qquad-2\dot{\alpha}\dot{\gamma}(A-B)\mathrm{s}^2\beta\mathrm{s}\gamma\mathrm{c}\gamma-\dot{\beta}\dot{\gamma}\mathrm{s}\beta\left[(A-B)(\mathrm{c}^2\gamma-\mathrm{s}^2\gamma)-C\right],\\
\bar{h}_5 &= \dot{\alpha}^2\mathrm{s}\beta\mathrm{c}\beta(A\mathrm{s}^2\gamma+B\mathrm{c}^2\gamma-C)-\dot{\alpha}\dot{\gamma}\mathrm{s}\beta\left[(A-B)(\mathrm{c}^2\gamma-\mathrm{s}^2\gamma)+C\right]\\
&\qquad+2\dot{\beta}\dot{\gamma}(A-B)\mathrm{s}\gamma\mathrm{c}\gamma,\\
\bar{h}_6 &= \dot{\alpha}^2(A-B)\mathrm{s}^2\beta\mathrm{s}\gamma\mathrm{c}\gamma-\dot{\beta}^2\mathrm{s}\gamma\mathrm{c}\gamma(A-B)+\dot{\alpha}\dot{\beta}\mathrm{s}\beta\left[(A-B)(\mathrm{c}^2\gamma-\mathrm{s}^2\gamma)+C\right].
\end{aligned}\tag{3.78}$$

With Eqs. (3.76)-(3.78) all inertia forces are determined. The generalized vector $\bar{\boldsymbol{f}}$ of external forces contains gravitational, normal contact and friction forces. Instead of a transformation, the generalized force directions of external forces $\boldsymbol{F}^{\mathrm{ext}}$ are directly extracted from the corresponding Jacobians.

To take gravitational forces into account, we express the position of the center of gravity S as

$$_I\boldsymbol{r}_{OS} = {_I\boldsymbol{r}_{OG}} + e\,{_I\boldsymbol{e}_x^B} = \begin{bmatrix} x+e(\mathrm{c}\alpha\mathrm{c}\gamma-\mathrm{s}\alpha\mathrm{c}\beta\mathrm{s}\gamma)\\ y+e(\mathrm{s}\alpha\mathrm{c}\gamma+\mathrm{c}\alpha\mathrm{c}\beta\mathrm{s}\gamma)\\ z+e\mathrm{s}\beta\mathrm{s}\gamma\end{bmatrix}.$$

The time derivative leads to the velocity

$$_I\boldsymbol{v}_S = \begin{bmatrix} \dot{x}-e\left[\dot{\alpha}(\mathrm{s}\alpha\mathrm{c}\gamma+\mathrm{c}\alpha\mathrm{c}\beta\mathrm{s}\gamma)-\dot{\beta}\mathrm{s}\alpha\mathrm{s}\beta\mathrm{s}\gamma+\dot{\gamma}(\mathrm{c}\alpha\mathrm{s}\gamma+\mathrm{s}\alpha\mathrm{c}\beta\mathrm{c}\gamma)\right]\\ \dot{y}+e\left[\dot{\alpha}(\mathrm{c}\alpha\mathrm{c}\gamma-\mathrm{s}\alpha\mathrm{c}\beta\mathrm{s}\gamma)-\dot{\beta}\mathrm{c}\alpha\mathrm{s}\beta\mathrm{s}\gamma-\dot{\gamma}(\mathrm{s}\alpha\mathrm{s}\gamma-\mathrm{c}\alpha\mathrm{c}\beta\mathrm{c}\gamma)\right]\\ \dot{z}+e(\dot{\beta}\mathrm{c}\beta\mathrm{s}\gamma+\dot{\gamma}\mathrm{s}\beta\mathrm{c}\gamma)\end{bmatrix},$$

from which the translational Jacobian matrix

$$_I\boldsymbol{J}_S = \left[\begin{array}{c|ccc} & -e(\mathrm{s}\alpha\mathrm{c}\gamma+\mathrm{c}\alpha\mathrm{c}\beta\mathrm{s}\gamma) & e\mathrm{s}\alpha\mathrm{s}\beta\mathrm{s}\gamma & -e(\mathrm{c}\alpha\mathrm{s}\gamma+\mathrm{s}\alpha\mathrm{c}\beta\mathrm{c}\gamma)\\ \boldsymbol{1} & e(\mathrm{c}\alpha\mathrm{c}\gamma-\mathrm{s}\alpha\mathrm{c}\beta\mathrm{s}\gamma) & -e\mathrm{c}\alpha\mathrm{s}\beta\mathrm{s}\gamma & -e(\mathrm{s}\alpha\mathrm{s}\gamma-\mathrm{c}\alpha\mathrm{c}\beta\mathrm{c}\gamma)\\ & 0 & e\mathrm{c}\beta\mathrm{s}\gamma & e\mathrm{s}\beta\mathrm{c}\gamma \end{array}\right]$$

of the center of gravity is extracted. Using this Jacobian, the gravitational force $_I\boldsymbol{F}_g = [0,0,-mg]^{\mathrm{T}}$ is projected onto the generalized velocity space, and yields the generalized force

$$\bar{\boldsymbol{f}}_g(\boldsymbol{q}) = {_I\boldsymbol{J}_S^{\mathrm{T}}}\,{_I\boldsymbol{F}_g} = -mg\begin{bmatrix}0 & 0 & 1 & 0 & e\mathrm{c}\beta\mathrm{s}\gamma & e\mathrm{s}\beta\mathrm{c}\gamma\end{bmatrix}^{\mathrm{T}}. \tag{3.79}$$

Following the rigid body formula (3.25), the velocity of the contact point C_1 follows as

$$ {}_I\boldsymbol{v}_{C_1} = {}_I\boldsymbol{v}_G + {}_I\boldsymbol{\Omega} \times {}_I\boldsymbol{r}_{GC_1} = \begin{bmatrix} \dot{x} + r(\dot{\alpha}\mathrm{c}\alpha\mathrm{c}\beta - \dot{\beta}\mathrm{s}\alpha\mathrm{s}\beta + \dot{\gamma}\mathrm{c}\alpha) \\ \dot{y} + r(\dot{\alpha}\mathrm{s}\alpha\mathrm{c}\beta + \dot{\beta}\mathrm{c}\alpha\mathrm{s}\beta + \dot{\gamma}\mathrm{s}\alpha) \\ \dot{z} - r\dot{\beta}\mathrm{c}\beta \end{bmatrix}. $$

Since the support is not moving, the velocity ${}_I\boldsymbol{v}_{C_1}$ is equivalent to the relative contact velocity of the contact point C_1. The components of ${}_I\boldsymbol{v}_{C_1}$ can be split according to Eq. (3.26) and Eq. (3.27) into the normal relative velocity

$$ \gamma_{N_1} = \dot{z} - r\dot{\beta}\mathrm{c}\beta \tag{3.80} $$

and into the tangential sliding velocity

$$ \boldsymbol{\gamma}_{T_1} = \begin{bmatrix} \dot{x} + r(\dot{\alpha}\mathrm{c}\alpha\mathrm{c}\beta - \dot{\beta}\mathrm{s}\alpha\mathrm{s}\beta + \dot{\gamma}\mathrm{c}\alpha) \\ \dot{y} + r(\dot{\alpha}\mathrm{s}\alpha\mathrm{c}\beta + \dot{\beta}\mathrm{c}\alpha\mathrm{s}\beta + \dot{\gamma}\mathrm{s}\alpha) \end{bmatrix}. \tag{3.81} $$

The corresponding generalized normal force direction $\boldsymbol{w}_{N_1}$ is obtained from Eq. (3.80) as

$$ \bar{\boldsymbol{w}}_{N_1} = \left(\frac{\partial \gamma_{N_1}}{\partial \dot{\boldsymbol{q}}}\right)^{\mathrm{T}} = \begin{bmatrix} 0 & 0 & 1 & 0 & -r\mathrm{c}\beta & 0 \end{bmatrix}^{\mathrm{T}} \in \mathbb{R}^{6\times 1}, $$

whereas Eq. (3.81) provides the generalized force directions

$$ \bar{\boldsymbol{W}}_{T_1} = \left(\frac{\partial \boldsymbol{\gamma}_{T_1}}{\partial \dot{\boldsymbol{q}}}\right)^{\mathrm{T}} = \begin{bmatrix} 1 & 0 & 0 & r\mathrm{c}\alpha\mathrm{c}\beta & -r\mathrm{s}\alpha\mathrm{s}\beta & r\mathrm{c}\alpha \\ 0 & 1 & 0 & r\mathrm{s}\alpha\mathrm{c}\beta & r\mathrm{c}\alpha\mathrm{s}\beta & r\mathrm{s}\alpha \end{bmatrix}^{\mathrm{T}} \in \mathbb{R}^{6\times 2}, $$

for the tangential friction forces. The generalized normal and tangential force directions for the contact points C_2 and C_3 are calculated analogously using Eqs. (3.25) and (3.23). Finally, the contact force directions are collected in a matrix of generalized normal force directions

$$ \bar{\boldsymbol{W}}_N = \begin{bmatrix} \bar{\boldsymbol{w}}_{N_1} & \bar{\boldsymbol{w}}_{N_2} & \bar{\boldsymbol{w}}_{N_3} \end{bmatrix} \in \mathbb{R}^{6\times 3} \tag{3.82} $$

and a matrix containing generalized tangential force directions

$$ \bar{\boldsymbol{W}}_T = \begin{bmatrix} \bar{\boldsymbol{W}}_{T_1} & \bar{\boldsymbol{W}}_{T_2} & \bar{\boldsymbol{W}}_{T_3} \end{bmatrix} \in \mathbb{R}^{6\times 6}. $$

The relative pivoting velocity is given as

$$ \gamma_{\tau_k} := \varepsilon_k\, \omega_{IB}, $$

with corresponding generalized pivoting friction force direction

$$ \bar{\boldsymbol{w}}_{\tau_k} = \left(\frac{\partial \gamma_{\tau_k}}{\partial \dot{\boldsymbol{q}}}\right)^{\mathrm{T}} = \varepsilon_k \begin{bmatrix} 0 & 0 & 0 & 1 & 0 & \cos(\beta) \end{bmatrix}^{\mathrm{T}} \in \mathbb{R}^{6\times 1}, $$

for a single contact point C_k, which can be gathered in the matrix of force directions

$$\bar{\boldsymbol{W}}_\tau = \begin{bmatrix} \bar{\boldsymbol{w}}_{\tau_1} & \bar{\boldsymbol{w}}_{\tau_2} & \bar{\boldsymbol{w}}_{\tau_3} \end{bmatrix} \in \mathbb{R}^{6\times 3}.$$

The relative contour velocity γ_R of the contact point C_k with respect to its body-fixed point is defined in Eq. (3.62). Since the angular velocity $\dot{\varphi}$ equals the derivative $\dot{\gamma}$ of the third Euler angle, the contour friction velocity directly yields

$$\gamma_{R_k} = -r\dot{\varphi} = -r\dot{\gamma}.$$

With generalized velocities $\dot{\boldsymbol{q}}$, the generalized force direction follows as

$$\bar{\boldsymbol{w}}_{R_k} = r\begin{bmatrix} 0 & 0 & 0 & 0 & 0 & -1 \end{bmatrix}^{\mathrm{T}} \in \mathbb{R}^{6\times 1}.$$

For an inclined disk, i.e., there exists a unique contact point with minimal height, the generalized force direction for contour friction is given as

$$\bar{\boldsymbol{W}}_R = r\begin{bmatrix} 0 & 0 & 0 & 0 & 0 & -1 \\ 0 & 0 & 0 & 0 & 0 & 0 \\ 0 & 0 & 0 & 0 & 0 & 0 \end{bmatrix}^{\mathrm{T}} \in \mathbb{R}^{6\times 3}. \tag{3.83}$$

Note that the generalized force direction $\bar{\boldsymbol{W}}_R$ should be adapted for a horizontally oriented disk. As this horizontal configuration is intrinsically equal to the singularity of the Euler angles and leads to a singular mass matrix [52], it is sufficient to consider $\bar{\boldsymbol{W}}_R$ for the inclined tippedisk. As it will show up, this singularity does not play a role during the inversion phenomenon.

Together with the kinetic quantities, i.e., mass matrix $\bar{\boldsymbol{M}}(\boldsymbol{q})$ from Eq. (3.76), the vector of gyroscopic forces $\bar{\boldsymbol{h}}(\boldsymbol{q},\dot{\boldsymbol{q}})$ from Eq. (3.77), the gravitational force $\bar{\boldsymbol{f}}_g(\boldsymbol{q})$ from Eq. (3.79), and the generalized force directions from Eqs. (3.82)-(3.83) the equations of motion yield

$$\bar{\boldsymbol{M}}(\boldsymbol{q})\ddot{\boldsymbol{q}} = \bar{\boldsymbol{h}}(\boldsymbol{q},\dot{\boldsymbol{q}}) + \bar{\boldsymbol{f}}_g(\boldsymbol{q}) + \bar{\boldsymbol{W}}_N\boldsymbol{\lambda}_N + \bar{\boldsymbol{W}}_T\boldsymbol{\lambda}_T + \bar{\boldsymbol{W}}_\tau\boldsymbol{\lambda}_\tau + \bar{\boldsymbol{W}}_R\boldsymbol{\lambda}_R,$$

and give in compact form

$$\bar{\boldsymbol{M}}(\boldsymbol{q})\ddot{\boldsymbol{q}} = \bar{\boldsymbol{h}}(\boldsymbol{q},\dot{\boldsymbol{q}}) + \bar{\boldsymbol{f}}_g + \bar{\boldsymbol{W}}\boldsymbol{\lambda} \tag{3.84}$$

with $\bar{\boldsymbol{W}} = [\bar{\boldsymbol{W}}_N, \bar{\boldsymbol{W}}_T, \bar{\boldsymbol{W}}_\tau, \bar{\boldsymbol{W}}_R]$ and $\boldsymbol{\lambda} = \begin{bmatrix}\boldsymbol{\lambda}_N^{\mathrm{T}}, \boldsymbol{\lambda}_T^{\mathrm{T}}, \boldsymbol{\lambda}_\tau^{\mathrm{T}}, \boldsymbol{\lambda}_R^{\mathrm{T}}\end{bmatrix}^{\mathrm{T}}$. Introducing the trivial kinematic relationship $\boldsymbol{v} = \dot{\boldsymbol{q}}$, or more formal $\dot{\boldsymbol{q}} = \bar{\boldsymbol{B}}\boldsymbol{v}$ with $\bar{\boldsymbol{B}}(\boldsymbol{q}) = \boldsymbol{1}$ (for a unified numerical treatment), the second-order differential equation from Eq. (3.84) reformulated in first-order form gives

$$\begin{aligned} \dot{\boldsymbol{q}} &= \bar{\boldsymbol{B}}(\boldsymbol{q})\boldsymbol{v} \\ \bar{\boldsymbol{M}}(\boldsymbol{q})\dot{\boldsymbol{v}} &= \bar{\boldsymbol{h}}(\boldsymbol{q},\boldsymbol{v}) + \bar{\boldsymbol{f}}_g + \bar{\boldsymbol{W}}\boldsymbol{\lambda}, \end{aligned} \tag{3.85}$$

which is structurally similar to Eq. (3.72), and parametrized with respect to the same minimal coordinates $\boldsymbol{q}$ but with different minimal velocities $\boldsymbol{u} \neq \boldsymbol{v}$. To distinguish between the two first-order forms from Eq. (3.72) and Eq. (3.85), the notation using bars has been introduced.

In the case of Euler angles the orthogonality condition ${}_I\boldsymbol{R}^{\mathrm{T}}{}_I\boldsymbol{R} = \mathbf{1}$ is always satisfied on position level, such that any initialization is admissible and constraint violation is not possible. Therefore, no additional projection is needed for drift compensation.

3.7 Numerical integration

In the previous section, different parametrizations of the tippedisk have been introduced and discussed. These parametrizations are complemented by constitutive laws that determine the normal and tangential contact forces and possibly additional dissipation mechanisms, resulting in complete mechanical models that describe the physics of the tippedisk. Based on the applied force laws, the resulting systems are described by differential algebraic inclusions (DAIs) or differential algebraic equations (DAEs).

In this section two integration schemes are presented. In particular, Moreau's time-stepping scheme is utilized to solve DAIs, i.e., models in which set-valued force laws are applied. In addition, a second scheme is presented that uses mechanical structure to reformulate a index three DAE as an ODE, which allows to use any standard integrator for ODEs.

Nonsmooth time-stepping scheme

Moreau's time-stepping scheme [85] is a numerical simulation method for multibody systems with frictional unilateral constraints which falls under the class of velocity-impulse based integration methods. The scheme may be derived from a direct discretization of an equality of measures, incorporating the equation of motion and the impact equation, together with a discrete approximation of the combined contact and impact laws. Here, only the final stepping scheme is presented, taking care to explain how the sophisticated contact laws are treated, and refer the reader to [85, 45, 1, 74] for a detailed discussion of the integration scheme.

An equidistant grid $t_0 < t_1 < \ldots < t_i < t_{i+1} < \ldots < t_{\mathrm{final}}$ with $t_{i+1} - t_i = \Delta t$ is used, with approximated coordinates $\boldsymbol{q}_i \approx \boldsymbol{q}(t_i)$ and velocities $\boldsymbol{u}_i \approx \boldsymbol{u}(t_i)$. Moreau's time-stepping scheme is a one step scheme that calculates from known positions $\boldsymbol{q}_A := \boldsymbol{q}_i$

and velocities $\boldsymbol{u}_A := \boldsymbol{u}_i$ at the beginning A of the timestep the unknown quantities $\boldsymbol{q}_E := \boldsymbol{q}_{i+1}$ and $\boldsymbol{u}_E := \boldsymbol{u}_{i+1}$ at the end E.

Moreau's time-stepping scheme:

1. Calculate the midpoint $t_M = t_A + \frac{1}{2}\left(t_E - t_A\right) = t_A + \frac{1}{2}\Delta t$
2. Approximate the midpoint position at time t_M using a forward Euler step: $\boldsymbol{q}_M = \boldsymbol{q}_A + \frac{1}{2}\boldsymbol{F}(\boldsymbol{q}_A)\boldsymbol{u}_A\,\Delta t$
3. Evaluate the mass matrix $\boldsymbol{M}_M := \boldsymbol{M}(\boldsymbol{q}_M)$, generalized force directions $\boldsymbol{W}_{*M} := \boldsymbol{W}_*(\boldsymbol{q}_M)$, the vector of gyroscopic forces $\boldsymbol{h}_M := \boldsymbol{h}(\boldsymbol{q}_M, \boldsymbol{u}_A)$ and $\boldsymbol{f}_{g,M} := \boldsymbol{f}_g(\boldsymbol{q}_M)$ at the midpoint and identify the set $\mathscr{I} = \{i \,|\, g_{Ni}(\boldsymbol{q}_M) \le 0\}$ of active contacts. Calculate the contact velocities $\gamma_{A*_i} = \boldsymbol{w}_{*M_i}^{\mathrm{T}}\boldsymbol{u}_A$ for all active contact, i.e., $i \in \mathscr{I}$, at the beginning of the timestep, where $*$ has been used generically for N, T, τ and R.
4. Solve contact problem using the fixed-point iteration scheme:

$$\boldsymbol{u}_E^k = \boldsymbol{u}_A + \boldsymbol{M}_M^{-1}\Big(\boldsymbol{h}_M\Delta t + \sum_{i\in\mathscr{I}}\Big(\boldsymbol{w}_{NM_i}P_{Ni}^k + \boldsymbol{W}_{TM_i}\boldsymbol{P}_{Ti}^k + \boldsymbol{w}_{\tau M_i}P_{\tau i}^k + \boldsymbol{w}_{RM_i}P_{Ri}^k\Big)\Big)$$

$$\begin{aligned} \gamma_{E*_i} &= \boldsymbol{w}_{*M_i}^{\mathrm{T}}\boldsymbol{u}_E^k && \forall i \in \mathscr{I} \\ \xi_{*_i} &= \gamma_{E*_i} + e_i\gamma_{A*_i} && \forall i \in \mathscr{I} \end{aligned}$$

$$\begin{aligned} P_{Ni}^{k+1} &= -\mathrm{prox}_{C_{N_i}}\left(-P_{Ni}^k + r_N\,\xi_{N_i}^k\right) && \forall i \in \mathscr{I} \\ \boldsymbol{P}_{Ti}^{k+1} &= -\mathrm{prox}_{C_{T_i}(C_{N_i})}\left(-\boldsymbol{P}_{Ti}^k + r_T\,\boldsymbol{\xi}_{T_i}^k\right) && \forall i \in \mathscr{I} \\ P_{\tau i}^{k+1} &= -\mathrm{prox}_{C_{\tau_i}(C_{N_i})}\left(-P_{\tau i}^k + r_\tau\,\xi_{\tau_i}^k\right) && \forall i \in \mathscr{I} \\ P_{Ri}^{k+1} &= -\mathrm{prox}_{C_{R_i}(C_{N_i})}\left(-P_{Ri}^k + r_R\,\xi_{R_i}^k\right) && \forall i \in \mathscr{I} \end{aligned}$$

   As stopping criterion, the accumulated force difference

$$\text{error} = \sum_{i\in\mathscr{I}}\left(|P_{Ni}^{k+1} - P_{Ni}^k| + \|\boldsymbol{P}_{Ti}^k - \boldsymbol{P}_{Ti}^k\|_2 + |P_{\tau i}^{k+1} - P_{\tau i}^k| + |P_{Ri}^{k+1} - P_{Ri}^k|\right) < \text{tol}$$

   is utilized.
5. Upon convergence of the iteration in 4) giving $\boldsymbol{u}_E$, the position $\boldsymbol{q}_E$ at t_E is updated as $\boldsymbol{q}_E = \boldsymbol{q}_M + \frac{1}{2}\boldsymbol{F}(\boldsymbol{q}_M)\boldsymbol{u}_E\,\Delta t$.
6. Projection step $\boldsymbol{p}_E^\star = \frac{\boldsymbol{p}_E(\boldsymbol{q}_E)}{\|\boldsymbol{p}_E(\boldsymbol{q}_E)\|}$ to normalize quaternions, i.e., $\|\boldsymbol{p}_E^\star\| = 1$.

In the above scheme various contact force laws have been taken into account. At this point it is important to note that the scheme above applies only to models with separated Coulomb and pivoting friction. For other friction models, like Coulomb–Contensou friction or smoothed Coulomb friction, this scheme has to be modified by replacing the corresponding contact laws.

Simulation of the model with bilateral constraint

For a spinning disk in persistent contact with the support one may formulate the dynamics as an ODE and solve it with standard methods for ordinary differential equations. Under the hypothesis, that the contact point C_1 does not detach during the inversion, the bilateral constraint $g_{N1}(\boldsymbol{q}) = 0$ is applied, forcing the contact point C_1 to the ground. If this constraint is initially satisfied on position level $g_{N1}(\boldsymbol{q}_0) = 0$, the constraint equation on velocity level yields

$$\gamma_{N1}(\boldsymbol{q},\boldsymbol{u}) = \boldsymbol{w}_{N1}^{\mathrm{T}}\,\boldsymbol{u} = 0. \tag{3.86}$$

Similarly, if the constraints on position and velocity level

$$g_{N1}(\boldsymbol{q}_0) = \gamma_{N1}(\boldsymbol{q}_0,\boldsymbol{u}_0) = 0$$

initially hold, the constraint on velocity level from Eq. (3.86) can be derived to obtain an equivalent bilateral constraint

$$\begin{aligned}\dot{\gamma}_{N1}(\boldsymbol{q},\boldsymbol{u},\dot{\boldsymbol{u}}) &= \frac{\partial \gamma_{N1}(\boldsymbol{q},\boldsymbol{u})}{\partial \boldsymbol{u}}\,\dot{\boldsymbol{u}} + \dot{\boldsymbol{w}}_{N1}^{\mathrm{T}}\boldsymbol{u} \\ &= \boldsymbol{w}_{N1}^{\mathrm{T}}\,\dot{\boldsymbol{u}} + \dot{\boldsymbol{w}}_{N1}^{\mathrm{T}}\boldsymbol{u} = 0,\end{aligned} \tag{3.87}$$

on acceleration level. Under the assumption of only regularized Coulomb friction given in Eq. (3.33) (i.e., no additional friction forces like contour or pivoting friction), Eq. (3.87) together with the system equations from Eq. (3.63) or Eq. (3.85) form a linear system of the form

$$\underbrace{\begin{bmatrix} \boldsymbol{I} & \boldsymbol{0} & \boldsymbol{0} \\ \boldsymbol{0} & \boldsymbol{M} & -\boldsymbol{W}_{NT} \\ \boldsymbol{0} & \boldsymbol{w}_{N1}^{\mathrm{T}} & \boldsymbol{0} \end{bmatrix}}_{\boldsymbol{A}} \begin{bmatrix} \dot{\boldsymbol{q}} \\ \dot{\boldsymbol{u}} \\ \lambda_N \end{bmatrix} = \begin{bmatrix} \boldsymbol{F}(\boldsymbol{q})\boldsymbol{u} \\ \boldsymbol{h} + \boldsymbol{f}_g \\ -\dot{\boldsymbol{w}}_{N1}^{\mathrm{T}}\boldsymbol{u} \end{bmatrix}. \tag{3.88}$$

Since the tangential force is linear in the Lagrange multiplier λ_N, the matrix

$$\boldsymbol{W}_{NT} := \boldsymbol{w}_{N1} - \mu \boldsymbol{W}_{T1} \frac{\boldsymbol{\gamma}_{T1}}{\|\boldsymbol{\gamma}_{T1}\| + \varepsilon}$$

is introduced as a generalized force direction, containing both normal and tangential forces. For sufficiently small μ, the matrix $\boldsymbol{A}$ is of full rank, such that the system from Eq. (3.88) can be integrated with every standard integrator for ordinary differential equations, e.g., the stiff integrator $ode15s$ from MATLAB.

3.8 Simulation results

In this section, the simulation results for different models are presented and discussed. In order to keep the result interpretable and to ensure the comparability of the models, the initial conditions as well as the simulation results are expressed in physical coordinates and their corresponding derivatives, cf. Section 3.4. In Section 3.6, Euler angles in z-x-z-convention are introduced in conformity with the physical angles α, β and γ, making a postprocessing of the orientation obsolete for the corresponding models.

As shown in Figure 3.5, the tippedisk is *non-inverted*, if $\beta = \frac{\pi}{2}$ and $\gamma = -\frac{\pi}{2}$ holds, which indicates that the center of gravity S is below the geometric center G. Vice versa, the disk is *inverted* if $\beta = \frac{\pi}{2}$ and $\gamma = \frac{\pi}{2}$ holds, i.e., the COG is located above the geometric center. Due to trigonometric ambiguities this definition is not unique, as $\beta = -\frac{\pi}{2}$ and $\gamma = \frac{\pi}{2}$ describes also an inverted orientation of the tippedisk. Since the inclination angle is restricted to $\beta \in [0, \pi)$, this ambiguity is not present. However, as the rolling angle γ is not restricted to an interval, $\beta = \frac{\pi}{2}$ and e.g. $\gamma = 3\frac{\pi}{2}$ also describe non-inverted configurations of the disk. In addition, a *perturbed non-inverted* configuration is shown in Figure 3.5 on the right-hand side.

In Table 3.1, the initial conditions, at time $t_0 = 0\,\mathrm{s}$, are given for the following simulations. The simulation end time is set to $t_1 = 5\,\mathrm{s}$, with equidistant time step $\Delta t = 1\mathrm{e}^{-5}\,\mathrm{s}$. The initial conditions were chosen such that the disk spins in a perturbed non-inverted orientation ($\Delta\gamma = 0.1\,\mathrm{rad}$), without slip and in persistent contact with the support, see Figure 3.5. This particular initial condition is suitable for full model simulation with unilateral contact and impacts, as well as a valid initial condition for models that assume bilateral contact, which plays an important role in the following analysis.

For the quaternion based models, the corresponding coordinates are deduced from the equivalence of the rotation matrix ${}_I\boldsymbol{R} = {}_I\boldsymbol{R}(\boldsymbol{p}) = {}_I\boldsymbol{R}(\boldsymbol{\varphi})$ introduced in Eq. (3.53) and Eq. (3.65). For non-horizontal configurations, i.e., when the rotation matrix parametrized with Euler angles is non-singular, such as the configuration

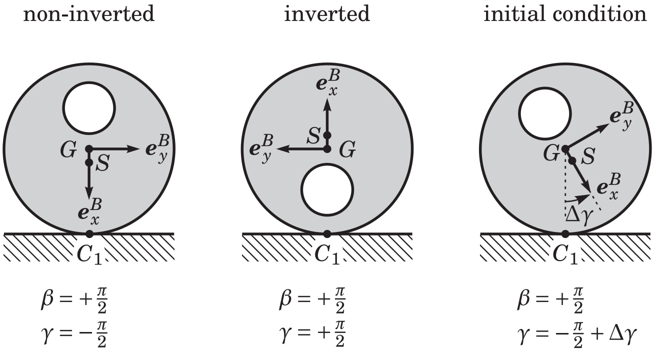

Figure 3.5: Configuration of the tippedisk: The left image shows a non-inverted tippedisk, while the middle image corresponds to an inverted disk. In the right image, the tippedisk is in a perturbed non-inverted spinning configuration.

Table 3.1: Initial conditions

Coordinate	Magnitude	Unit	Velocity	Magnitude	Unit
x_0	0	m	$\dot{x}_0$	0	m/s
y_0	0	m	$\dot{y}_0$	0	m/s
z_0	0.045	m	$\dot{z}_0$	0	m/s
α_0	0	rad	$\dot{\alpha}_0$	40	rad/s
β_0	0.5π	rad	$\dot{\beta}_0$	0	rad/s
γ_0	$-0.5\pi + 0.1$	rad	$\dot{\gamma}_0$	$-\dot{\alpha}_0 \cos(\beta_0) = 0$	rad/s

defined in Table 3.1, a mapping $\boldsymbol{p} = \boldsymbol{p}(\boldsymbol{\varphi})$ can be deduced.[1] The associated minimal velocities are induced by the kinematic coupling

$$\begin{bmatrix} \dot{x}_0 \\ \dot{y}_0 \\ \dot{z}_0 \\ \omega_{x0} \\ \omega_{y0} \\ \omega_{z0} \end{bmatrix} = \begin{bmatrix} \mathbf{1} & \mathbf{0} \\ \mathbf{0} & {}_B\boldsymbol{J}_R \end{bmatrix} \begin{bmatrix} \dot{x}_0 \\ \dot{y}_0 \\ \dot{z}_0 \\ \dot{\alpha}_0 \\ \dot{\beta}_0 \\ \dot{\gamma}_0 \end{bmatrix},$$

---

[1] According to the two-to-one bijection ${}_I\boldsymbol{R}(\boldsymbol{p}) = {}_I\boldsymbol{R}(-\boldsymbol{p})$, two different maps $\boldsymbol{p}(\boldsymbol{\varphi})$ could be obtained. However, since the simulation results are interpreted and compared in physical coordinates without closer inspection of the specific quaternion, this can be neglected.

with Jacobian ${}_B\boldsymbol{J}_R$ from Eq. (3.69). Using these relations, the initial condition for the quaternion based models can be computed directly from Table 3.1, making explicit specification unnecessary. In the evaluation of results, the two-to-one bijection of unit quaternions and rotation matrices does not matter, since the results in physical coordinates are equal.

For the following numerical simulations, the usual values for the contact parameters, the friction, restitution, and smoothing coefficients μ, e, and ε, from Table 3.2 are assumed. In addition, the integration parameters are given by

time-stepping tolerance: $tol = 10^{-8}$

proximal point scaling: $r_N = r_T = r_\tau = 0.1$ and $r_R = 10^{-4}$

With the dimension and mass properties from Table 2.1, the contact properties from Table 3.2 and the above integration parameters, all parameters are given to obtain the following simulation results.

Table 3.2: Contact parameters containing friction, smoothing and restitution coefficients.

Property	value	Property	value
μ_T	3×10^{-1}	e_T	0
μ_τ	3×10^{-3}	e_τ	0
μ_R	3×10^{-3}	e_R	0
ε	0.1 m/s	e_N	0

In Table 3.3, models with different parametrizations and modeling levels are listed. Here, all models assume that the geometric center G is parametrized with respect to the inertial I-frame, cf. Eq. (3.50) and Eq. (3.51). The orientation is parameterized either in quaternions or in Euler angles, with the corresponding system equations from Eq. (3.63) and Eq. (3.85), respectively. The abbreviation ‘E’ denotes a model with Euler angles, ‘Q’ implies a quaternion based one. Any combination of the friction laws from Section 3.5 can be chosen as dissipation mechanism. In the following, the different simulation results are identified by the model name to indicate which dissipation mechanisms and parametrization were used.

Time-stepping with set-valued Coulomb friction

Figure 3.6 shows the simulation results of the models (Model 1 and Model 2) where spatial Coulomb friction is incorporated by a set-valued friction law. The upper

Table 3.3: Various models with different parametrizations and friction laws.

Model name	-	Integrator	Dissipation Mechanisms (friction)
ODE Model 1	E	$ode15s$	smooth Coulomb
ODE Model 2	Q	$ode15s$	smooth Coulomb
Model 1	E	Moreau	set-valued Coulomb
Model 2	Q	Moreau	set-valued Coulomb
Model 3	E	Moreau	Coulomb–Contensou
Model 4	Q	Moreau	Coulomb–Contensou
Model 5	E	Moreau	smooth Coulomb
Model 6	Q	Moreau	smooth Coulomb
Model 7	E	Moreau	set-valued Coulomb, pivoting, contour
Model 8	Q	Moreau	set-valued Coulomb, pivoting, contour
Model 9	E	Moreau	smooth Coulomb, pivoting, contour
Model 10	Q	Moreau	smooth Coulomb, pivoting, contour

left graph shows the time evolution of the inclination angle β (blue, dotted) and the rolling angle γ (red, dashed). For $t = 0\,\mathrm{s}$, the configuration of the tippedisk is near to the non-inverted spinning solution, cf. the initial condition in Figure 3.5. After short time, the rolling angle γ increases and a periodic oscillation around the inverted configuration occurs. During this process, the angle β does only change slightly, whereas the angle γ is oscillating with a large amplitude. The height z_S of the center of gravity S in the upper right plot increases initially, but instead of reaching the fully inverted height $r + e$, it oscillates aperiodically around $0.044\,\mathrm{m}$ (arithmetic mean of z_S for $t \in [1\,\mathrm{s}, 5\,\mathrm{s}]$, for the model in Euler angles). The graphs from Figure 3.6(c) and 3.6(d) depict the potential energy E_{pot} (red, dashed), the kinetic energy E_{kin} (blue, dotted) and total energy E_{tot} (green, dash-dotted) of the tippedisk. During the transient phase $t \in [0\,\mathrm{s}, 0.5\,\mathrm{s}]$, the potential energy increases while the kinetic energy decreases. The total energy E_{tot}, reveals energy dissipation during $t \in [0\,\mathrm{s}, 0.5\,\mathrm{s}]$ and remains almost constant for $t \in [0.5\,\mathrm{s}, 5\,\mathrm{s})$, accompanied by a dynamic exchange of kinetic and potential energy. The lower graphs, Figure 3.6(e) and Figure 3.6(f), show that the contact distance g_{N1} of the contact point C_1 is non-positive but nearly zero, indicating that the contact point C_1 does not detach. For the Model 1 in Euler angles, the contact distance g_{N1} changes with high frequency between zero and $-2 \cdot 10^{-9}\,\mathrm{m}$. Using the quaternion based Model 2, the height of the contact point C_1 decreases monotonically, i.e., the simulation suffers from constraint drift in the normal contact, as no penetration correction was applied at the end of each time-step.

Time-stepping with Coulomb–Contensou friction

Figure 3.7 shows the simulation results for Model 3 with a description in Euler angles and the quaternion based Model 4 under consideration of the Coulomb–Contensou friction from Eq. (3.32), i.e., a single friction law that couples pivoting and tangential friction. Contour friction is neglected. According to Figure 3.7(a) the the tippedisk inverts its orientation. For $t \in [0\,\mathrm{s}, 0.5\,\mathrm{s}]$, the rolling angle γ (red, dashed) initially increases, which is followed by a damped oscillation that appears to converge asymptotically to $\gamma = \frac{\pi}{2}$. The inclination angle β (blue, dotted) performs a damped oscillation around $\beta = \frac{\pi}{2}$. In both graphs γ and β start to oscillate with high frequency at $t \approx 2\,\mathrm{s}$. In the upper right graph, Figure 3.7(b), the height of the center of gravity drops slightly before converging to the inverted height $r + e$. The energy graphs from Figure 3.7(c) and Figure 3.7(d), show that the potential energy E_{pot} (red, dashed) increases, whereas the kinetic energy E_{kin} (blue, dotted) decreases during the inversion. The total energy E_{tot} (green, dash-dotted) decreases fastly during the transient inversion process. After the disk reaches an almost inverted spinning motion, the rate of dissipation drops, but remains non-zero due to the pivoting friction. The contact distance g_{N1} of the contact point C_1 behaves similar to the results based on set-valued Coulomb friction. Like for Model 2, the Model 4 suffers from constraint penetration, which saturates at $-1.36 \cdot 10^{-5}\,\mathrm{m}$.

Time-stepping with smooth Coulomb friction

Figure 3.8 shows simulation results for Model 5 parametrized in Euler angles and the quaternion based Model 6 under consideration of smooth Coulomb friction. Additional dissipation mechanisms, such as contour or pivoting friction, are neglected. In the interval $t \in [0\,\mathrm{s}, 0.5\,\mathrm{s}]$, the rolling angle γ (red, dashed) increases. After this transient dynamics, a damped oscillation around $\gamma = \frac{\pi}{2}$ occurs. During the entire motion, the inclination angle β (blue, dashed) oscillates with decreasing amplitude around $\beta = \frac{\pi}{2}$. In both angles γ and β small oscillations with high frequency start to occur at $t \approx 1\,\mathrm{s}$. In the upper right graph, Figure 3.8(b), the height z_s of the center of gravity S drops slightly and then grows asymptotically to the inverted height $r + e$. The energy plots from Figure 3.8(c) and Figure 3.8(d) reveal that the kinetic energy E_{kin} (blue, dotted) decreases during the inversion process, whereas the potential energy E_{pot} (red, dashed) increases, which is directly related to the height of the COG. The total energy E_{tot} (green, dash-dotted) drops during the initial inversion phase.

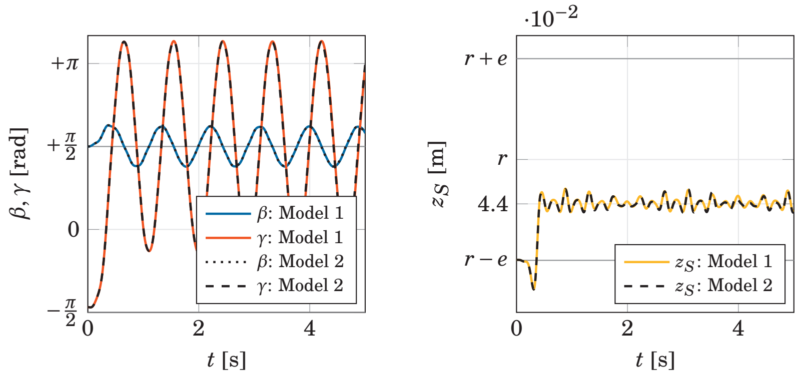

(a) inclination and rolling angles

(b) height of COG

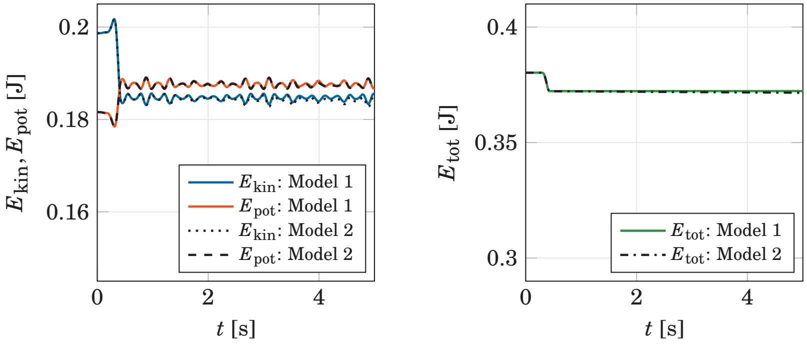

(c) kinetic and potential energy

(d) total energy

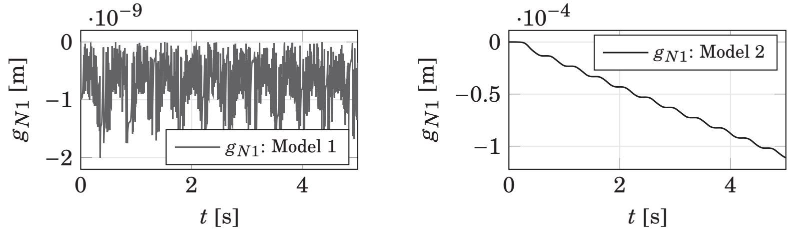

(e) gap distance g_{N1}: Model 1

(f) gap distance g_{N1}: Model 2

Figure 3.6: Simulation results for set-valued Coulomb friction from Eq. (3.31).

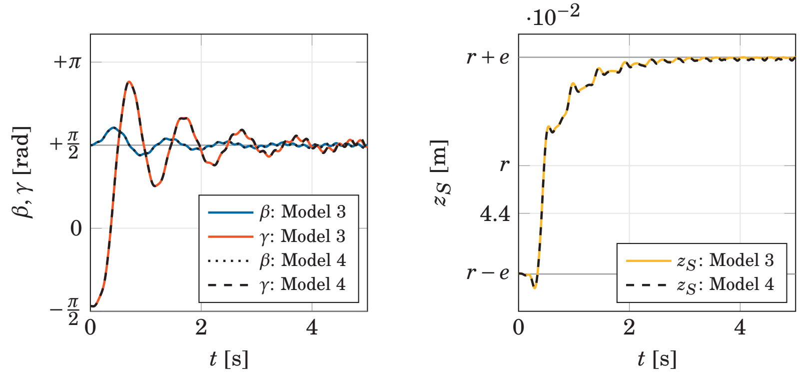

(a) inclination and rolling angles (b) height of COG

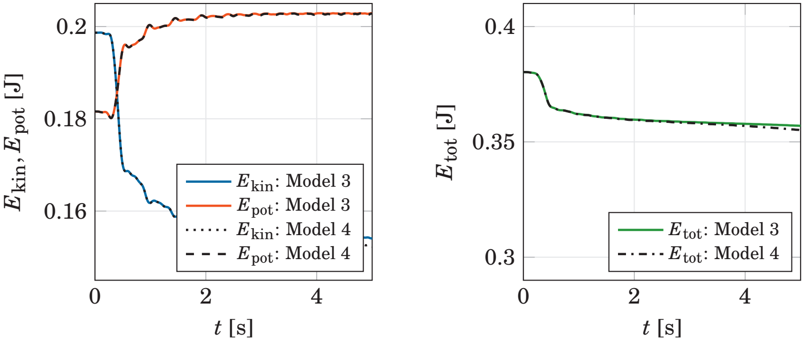

(c) kinetic and potential energy (d) total energy

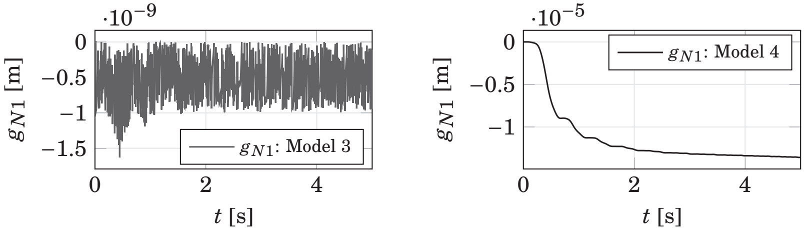

(e) gap distance g_{N1}: Model 3 (f) gap distance g_{N1}: Model 4

Figure 3.7: Simulation results for Coulomb–Contensou friction from Eq. (3.32).

In the inverted configuration, the total energy tends to decrease slowly. As in the case of set-valued Coulomb friction, the contact distance g_{N1} is never greater than zero for the case of smooth Coulomb friction, see Figure 3.8(e) and Figure 3.8(f). A closer look at the left g_{N1} graph shows that Model 5, parametrized in Euler angles, yields an aperiodic oscillation of the contact distance g_{N1} in a band with a width of $10^{-9}\,\mathrm{m}$. In contrast, for the quaternion based Model 6 the height of the contact point C_1 decreases from $0\,\mathrm{m}$ and saturates at $-7.5\cdot 10^{-6}\,\mathrm{m}$.

Ordinary differential equation with smooth Coulomb friction

Both models ODE Model 1 and ODE Model 2 assume a bilateral constrained contact point C_1 and assume smooth Coulomb friction. Additional dissipation mechanism are neglected. Figure 3.9 presents the results of the corresponding simulations. In contrast to the previous models with unilateral contact, both ODE models assume a priori a persistent normal contact. The height of the contact point C_1 and the corresponding gap distance g_{N1} are numerically forced and therefore irrelevant and are not shown for this reason. In the upper left graph, Figure 3.9(a), the rolling angle γ rises quickly from $-\frac{\pi}{2}$ and ends in an asymptotic oscillation around $+\frac{\pi}{2}$. The inclination angle β does only change slightly for $t \in [0\,\mathrm{s}, 0.5\,\mathrm{s}]$. Similar to the previous models, both the inclination angle β and the rolling angle γ are increasingly superimposed by small oscillations with higher frequency. The height of the center of gravity S is shown in the upper right Figure 3.9(b) and grows from $r-e$ to $r+e$, i.e., the disk starts in a non-inverted configuration and ends in a configuration close to inverted spinning. Consequently, the potential energy E_{pot} (red, dashed) increases during inversion, whereas the kinetic energy E_{kin} (blue, dotted) decreases. During inversion the total energy dissipates from $0.38\,\mathrm{J}$ to $0.36\,\mathrm{J}$. After this fast decay $t < 0.5\,\mathrm{s}$ the system slowly dissipates energy.

Comparison of models

Figure 3.10 provides a comparison of the dynamic behavior exhibited by various rigid body mechanical models incorporating different dissipation mechanisms. According to Figures 3.6-3.9, quaternion and Euler angle based models yield the same results. To keep the plot in Figure 3.10 clearer, only the simulation results of the quaternion based models are shown. The inversion motion is mainly characterized by the rolling angle γ, shown in the left graph, Figure 3.10(a). The COG height z_S is depicted in the right diagram, Figure 3.10(b). For set-valued Coulomb friction, Model 2 (black), the solution settles on a periodic oscillation around $\gamma = \frac{\pi}{2}$ with slightly increasing amplitude. Since the height z_S does not reach the inverted

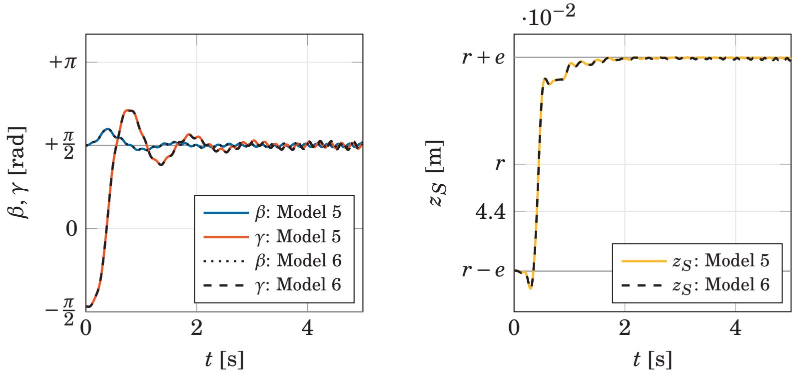

(a) inclination and rolling angles (b) height of COG

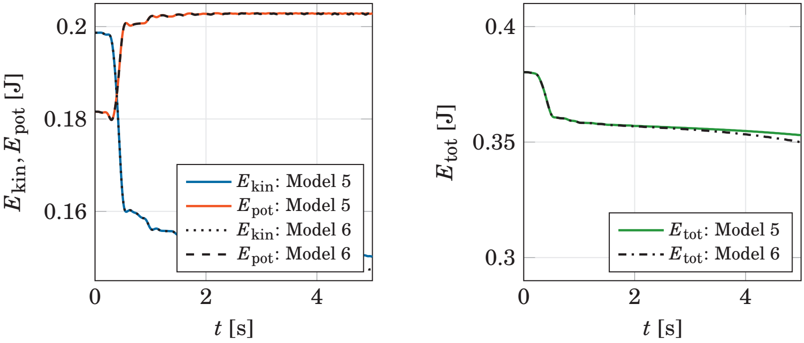

(c) kinetic and potential energy (d) total energy

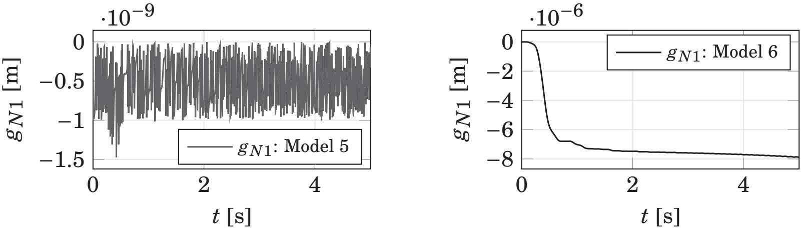

(e) gap distance g_{N1}: Model 5 (f) gap distance g_{N1}: Model 6

Figure 3.8: Simulation results for smooth Coulomb friction from Eq. (3.33).

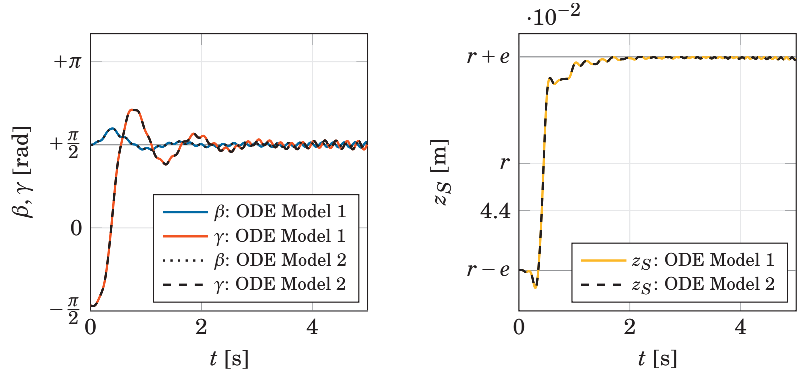

(a) inclination and rolling angles (b) height of COG

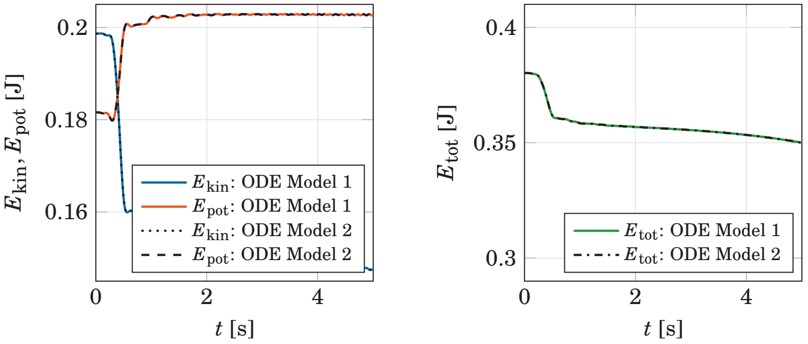

(c) kinetic and potential energy (d) total energy

Figure 3.9: Simulation results of models with a bilaterally constrained contact point C_1 and the application of smooth Coulomb friction from Eq. (3.33).

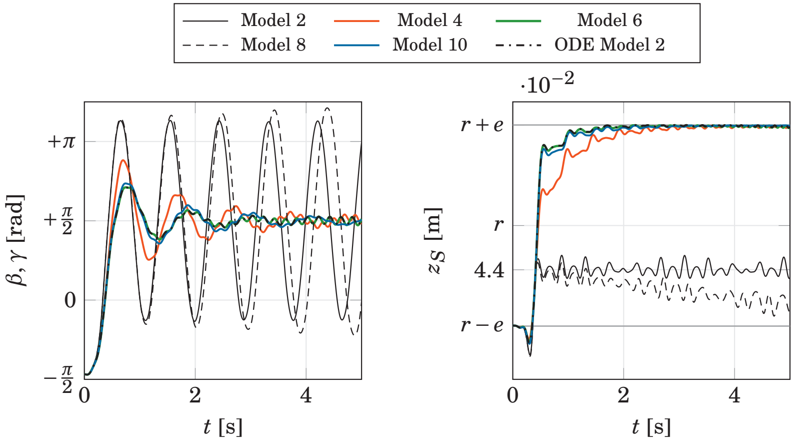

(a) inclination and rolling angles

(b) height of COG

Figure 3.10: Comparison of the introduced models from Table 3.3 on a relatively short time scale, i.e., during the initial phase of motion.

height $r+e$, the simulation under assumption of set-valued Coulomb friction does not describe the inversion phenomenon of the tippedisk. If contour and pivoting friction are added, see Model 8 (black, dashed), the behavior during the transient process is similar to that of purely set-valued Coulomb friction. After the COG height saturates at $z_S = 0.044\,\mathrm{m}$, the height and thus the potential energy of the disk decreases, i.e., more energy is dissipated during the periodic oscillation. As a consequence the amplitude of the rolling angle γ increases significantly. Assumption of set-valued Coulomb–Contensou friction, Model 4 (red), shows that to rolling angle γ increases, and after the transient interval $t \in [0, 0.3\,\mathrm{s}]$, a decaying oscillation occurs, such that the disk ends in an almost inverted spinning configuration. For this friction law, the COG height increases until is saturates at $z_S = r+e$, implying a complete inversion of the disk. Smooth Coulomb friction, Model 6 (green), leads to qualitatively similar behavior as the Coulomb–Contensou friction model. Adding contour and pivoting friction, as considered in Model 10 (blue), affects the inversion motion slightly, but the qualitative behavior remains the same. Finally, the simulation results for the ODE model 2 (black, dash-dotted), which considers smooth Coulomb friction and a persistent contact, are identical to the solution of Model 6.

The right Figure 3.8(b) reveals that models with smooth tangential friction behavior are suited to describe the inversion phenomenon. Consideration of additional dissipation mechanisms, e.g., pivoting and contour friction, has a quantitative effect on inversion motion. However, these additional dissipation mechanisms do not significantly affect qualitative behavior. On the one hand, it is striking that solutions of models with additional dissipation mechanisms do not differ qualitatively from the model with only smooth Coulomb friction on a small time scale, cf. Model 6 and Model 10. On the other hand, adding more dissipation by accounting for additional frictional forces has a major impact on the long-term behavior. Since Model 2 and Model 8, which assume set-valued Coulomb friction, are not suitable for describing the phenomenon of inversion, neither model will be considered in the following.

The long-term behavior of the tippedisk is shown in Figure 3.11 for the time interval $t \in [0, 25\,\mathrm{s}]$. Here, the left graph, Figure 3.11(a), depicts the rolling angle γ, whereas the right graph shows the total energy E_{tot} of the mechanical rigid body system. The red graph describes the solution using the quaternion based Model 4 with Coulomb–Contensou friction, neglecting additional frictional effects. After the inversion, an increasing vibration around $+\frac{\pi}{2}$ occurs, until the tippedisk falls down at $t \approx 17\,\mathrm{s}$. Both models Model 6 (green) and ODE Model 2 (black, dash-dotted) with pure and smooth Coulomb friction, are showing similar behavior. After γ converges to $+\frac{\pi}{2}$, energy is being dissipated, meaning that the disk falls down and comes to rest. This decay depends strongly on the chosen friction parameters. Simulation results of Model 10 considering smooth Coulomb, contour and pivoting friction are shown in blue. At an initial stage of the motion, the rolling angle γ increases and after a short time oscillates asymptotically to $\gamma = \pi/2$. After $t \approx 5\,\mathrm{s}$ this asymptotic decay seems to end in a periodic oscillation with constant amplitude. According to the pivoting friction mechanism, this oscillation cannot be a limit set for this system, because the rotating disk dissipates energy. As a result, the tippedisk will fall down and end up in a horizontal configuration. The differences in the long-term behavior depend on the applied dissipation mechanisms and cannot be attributed to numerical convergence. To show this, the solutions of the models based on quaternions were compared with the models parametrized in Euler angles. In the right-hand plot, Figure 3.11(b), the total energy E_{tot} is depicted for the long-term simulations. It is counterintuitive that Model 10 stays in the inverted configuration longer even though more dissipation mechanisms were considered, i.e., contour friction may act as a stabilizing effect of the inverted spinning solution. In summary, additional dissipation mechanisms, like contour or pivoting friction, hardly play a role during the inversion process. However, the long-term behavior of the tippedisk is strongly influenced by dissipation, and air friction may also play a role.

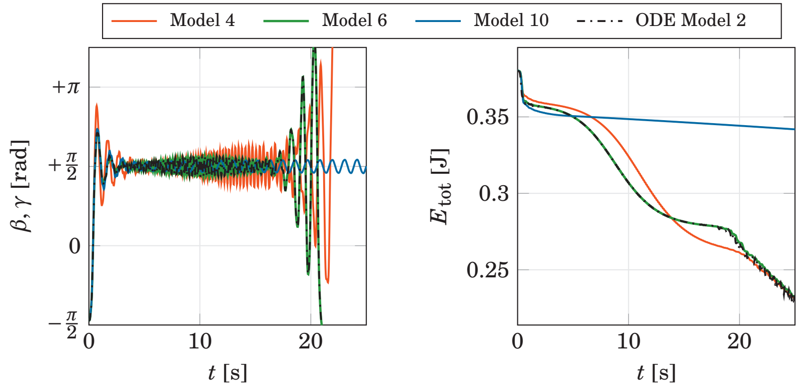

(a) inclination and rolling angles

(b) total Energy

Figure 3.11: Long-term simulations comparing the effect of additional dissipation mechanisms, e.g., contour and pivoting friction. The colors of the displayed solutions match the colors from Figure 3.10.

The stroboscopic sequence in Figure 3.12, shows a preliminary experiment that comes from recordings with a high-speed camera at 500 fps. Here the video of the inversion process is discretized into eight time instants. The initial angular velocity, in the non-inverted configuration, is identified to be $\dot{\alpha} \approx -50\,\text{rad/s}$. For comparison, Figure 3.13 depicts renderings of the numerical experiment using Euler angles and smooth Coulomb friction, more specifically the ODE Model 1. The initial angular spinning velocity $\dot{\alpha} = -50\,\text{rad/s}$ is chosen in agreement with the experiment. A visual comparison between both stroboscopic image sequences, shows that the presented model is able to describe the real system qualitatively, during the process of inversion. It is essential to note here that the parameters of the numerical model have not been fitted to the experiment and are listed in Tables 2.1 and 3.2. The corresponding integration parameters are chosen in Section 3.8. Nevertheless, the quantitative agreement between the numerical and the laboratory experiment is striking.

3.9 Discussion of the full model simulations

The previous section has shown that the application of set-valued Coulomb friction is not sufficient to describe the inversion phenomenon of the tippedisk. For

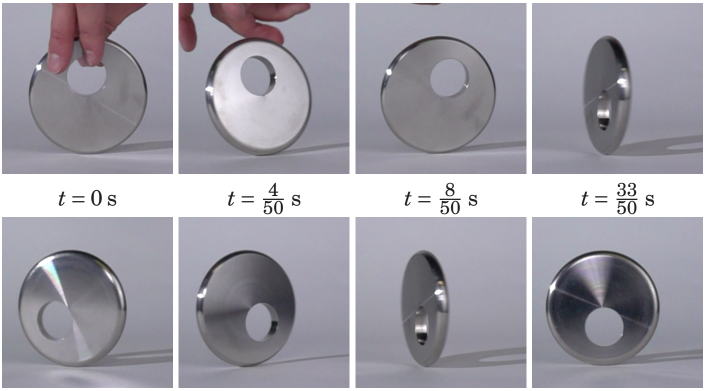

$t = 0\,\mathrm{s}$ $t = \frac{4}{50}\,\mathrm{s}$ $t = \frac{8}{50}\,\mathrm{s}$ $t = \frac{33}{50}\,\mathrm{s}$

$t = \frac{53}{50}\,\mathrm{s}$ $t = \frac{73}{50}\,\mathrm{s}$ $t = \frac{93}{50}\,\mathrm{s}$ $t = \frac{133}{50}\,\mathrm{s}$

Figure 3.12: Stroboscopic image sequence showing the inversion of the tippedisk during a real experiment.

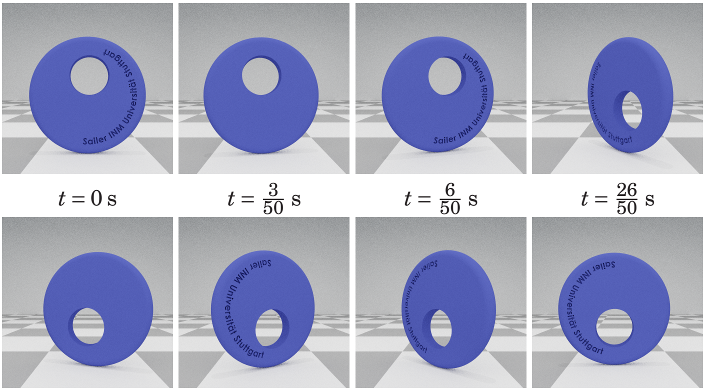

$t = 0\,\mathrm{s}$ $t = \frac{3}{50}\,\mathrm{s}$ $t = \frac{6}{50}\,\mathrm{s}$ $t = \frac{26}{50}\,\mathrm{s}$

$t = \frac{43}{50}\,\mathrm{s}$ $t = \frac{60}{50}\,\mathrm{s}$ $t = \frac{83}{50}\,\mathrm{s}$ $t = \frac{111}{50}\,\mathrm{s}$

Figure 3.13: Stroboscopic image sequence of the tippedisk inversion phenomenon obtained by numerical simulation.

this friction law, the rolling angle γ keeps on oscillating periodically, whereas the COG height z_S oscillates about a constant value, cf. Figure 3.10. In particular, in case of set-valued Coulomb friction, the tippedisk is captured by a pure rolling motion where the center of gravity S is not above the geometric center G of the disk. Adding pivoting and contour friction also does not result in inversion behavior. The application of Coulomb–Contensou friction, developed in [73], leads to a mechanical model that exhibits a full inversion of the tippedisk. During the inversion the disk is always in spinning state. Therefore, Coulomb–Contensou friction motivates the application of a smooth Coulomb friction law, which leads to numerical results consistent with experiments, see Figure 3.12 and Figure 3.13. Moreover, the time-stepping simulations show that the contact point C_1 does not detach from the flat support during the inversion process. This observation supports the assumption that the unilateral constraint between disk and support may be replaced for the considered motion by a bilateral constraint, introduced in Eq. (3.86). In Figure 3.10, the evolution of the angle γ is depicted in the left graph for the most relevant models. Comparing the angle γ of the time-stepping model with smooth Coulomb friction with the smooth ODE-models, both solutions are similar with respect to numerical error. In the case of smooth Coulomb friction in combination with pivoting and contour friction, the qualitative behavior remains similar to the case of (only) smooth Coulomb friction. At short time scales, the models with additional dissipation mechanisms do not differ from the models that consider only smooth Coulomb friction. However, in the long-term simulations, additional dissipation mechanisms strongly influence the asymptotic dynamics. For $\varepsilon \downarrow 0$, the solutions under smooth Coulomb friction converge to the solutions under set-valued Coulomb friction resulting in pure rolling motions, i.e., $\boldsymbol{\gamma}_T = 0$. The convergence of all numerical results is checked by comparing the models based on quaternions and the models in Euler angles. Numerical experiments of quaternion based models converge faster for decreasing time steps. In contrast, the models in Euler angles do not suffer from constraint drift as much as the quaternion based models. For both models, penetration of the contact point in the time-stepping solutions is a consequence from the application of Signorini's law on velocity level, which is used to formulate a single set-valued contact law that combines Signorini's normal law and Newton's impact law. To prevent these inadmissible penetrations, a correction step could have been added at the end of each time step, see [70]. For the inversion phenomenon, however, these penetrations are negligible.

In this chapter, mechanical models of the tippedisk with different modeling assumptions and various parametrizations have been presented. In particular, the orientation of the disk is parametrized with respect to unit quaternions and Euler angles in z-x-z-convention. Each parametrization has its own advantages. The quaternion based models with minimal velocities from Eq. (3.55) converge faster, but lead to more pronounced inadmissible penetration of the contact point if no constraint correction is applied. In contrast, the convergence of models in Euler angles with trivial kinematic equation is slower. However, these models lead to less penetration of the contact point and allow the system states to be interpreted as physical coordinates. According to the presented comparison of various models with different dissipation mechanisms, it is shown that regularized smooth Coulomb friction is sufficient to describe the inversion phenomenon of the tippedisk on a relatively fast time scale. The long-term behavior of the disk is strongly influenced by the application of additional friction laws that act on the contour Eq. (3.29) or pivoting velocity Eq. (3.28), e.g., friction laws such as Coulomb–Contensou, pivoting and contour friction. Hence, the solution from inverted spinning to a static horizontal configuration depends strongly on these additional friction effects.

In order to understand the short-time inversion behavior of the tippedisk, the minimal model with Euler angles and smooth Coulomb friction will be the basis for the subsequent qualitative dynamic analysis.

Chapter 4

Stability analysis and model reduction

As discussed in Section 2, there are two steady state solutions for the tippedisk when the dissipation caused by pivoting friction is neglected, i.e., non-inverted stationary spinning if the center of gravity S is below the geometric center G, and inverted stationary spinning with S above G.

In the previous chapter, various full mechanical models of the tippedisk have been derived that are suited to describe the inversion phenomenon. The terminology *full* indicates that the rigid body system is modeled with respect to first principles and thus describes real physics without simplification or reduction of the model order. For the following analysis, the most minimal model (ODE Model 1) is considered, which is parametrized in Euler angles and assumes smooth Coulomb friction without accounting for additional dissipation mechanisms. Therefore, the mechanical model neglects pivoting torques, such that inverted and non-inverted spinning correspond to stationary motions characterized by a constant spinning speed. A good starting point to analyze the dynamic behavior is to study the local stability properties of these two spinning solutions. The corresponding orientations are shown in the left an middle drawings in Figure 3.5. Utilizing the generalized coordinates $\boldsymbol{q}$ introduced in Eq. (3.67) and the associated trivial velocities $\boldsymbol{v} = \dot{\boldsymbol{q}}$, the two stationary spinning solutions in a non-inverted and inverted configuration may be described by coordinates

$$\boldsymbol{q}^{-}(t) = \begin{bmatrix} 0 \\ 0 \\ r \\ -\Omega t \\ +\frac{\pi}{2} \\ -\frac{\pi}{2} \end{bmatrix}; \qquad \boldsymbol{q}^{+}(t) = \begin{bmatrix} 0 \\ 0 \\ r \\ \Omega t \\ +\frac{\pi}{2} \\ +\frac{\pi}{2} \end{bmatrix}$$

and the constant velocities $\boldsymbol{v}^{-} = -\boldsymbol{v}^{+} = \begin{bmatrix} 0 & 0 & 0 & -\Omega & 0 & 0 \end{bmatrix}^{\mathrm{T}}$. Both stationary spinning solutions are characterized by a vertical inclination angle $\beta = \frac{\pi}{2}$. For $\gamma = -\frac{\pi}{2}$, the COG is below the geometric center G, indicating a non-inverted configuration. Inverted spinning is indicated by $\gamma = +\frac{\pi}{2}$, where S is above G.

4.1 Linear stability analysis - 6 DOF

As a first step in the analysis of the dynamic behavior of the tippedisk, the local stability properties of inverted and non-inverted spinning solutions are analyzed using Lyapunov's indirect method. Since the tippedisk inverts its orientation when spun fast enough, the inverted spinning solution seems attractive, while the non-inverted spinning must be repulsive. Instead of linearizing the system equations around both non-inverted and inverted spinning, symmetry is used to avoid repeated calculations. More precisely, the system equations are linearized around the inverted configuration given by $\boldsymbol{q}^{+}$. Local behavior of non-inverted spinning is then obtained by overloading e with $-e$ and considering a π-shift of the rolling angle.

Stationary spinning is characterized by a constant rotational velocity $\dot{\alpha} = \Omega$, resulting in a linear time dependence $\alpha(t) = \Omega t + \alpha_0$ of the spinning angle. Linearizing the equations of motion from Eq. (3.75) around any stationary spinning solution with generalized coordinates $\boldsymbol{q}^{*} \in \{\boldsymbol{q}^{-}, \boldsymbol{q}^{+}\}$ and associated minimal velocities $\boldsymbol{v}^{*} \in \{\boldsymbol{v}^{-}, \boldsymbol{v}^{+}\}$, results in a linear system of the form

$$\boldsymbol{M}(t)\ddot{\boldsymbol{y}} + \boldsymbol{B}(t)\dot{\boldsymbol{y}} + \boldsymbol{C}(t)\boldsymbol{y} = 0,$$

with $\boldsymbol{y}(t) = \boldsymbol{q}(t) - \boldsymbol{q}^{*}(t)$ and $\boldsymbol{M}(t) = \bar{\boldsymbol{M}}(\boldsymbol{q}^{*}(t))$. The time dependent matrices $\boldsymbol{B}(t)$ and $\boldsymbol{C}(t)$ are extracted from the gyroscopic force vector $\bar{\boldsymbol{h}}\left(\boldsymbol{q}^{*}(t), \boldsymbol{v}^{*}\right)$, and the generalized force $\bar{\boldsymbol{f}}\left(\boldsymbol{q}^{*}(t), \boldsymbol{v}^{*}\right)$ which contains the gravitational and the contact forces. Since the mass matrix $\bar{\boldsymbol{M}}(\boldsymbol{q})$ from Eq. (3.76) depends on the spinning angle $\alpha(t)$ and thus linearly on time, the linear system is non-autonomous. As a consequence, Lyapunov's indirect method is not applicable in the current parametrization and one would need to resort to Floquet theory, which usually cannot be performed in closed-form [36]. In contrast, physical intuition suggests that the absolute value of the spinning angle does not influence the qualitative behavior. The question therefore arises whether the time dependence of the spinning angle is omitted or decoupled when the system is parametrized in other, more appropriate coordinates.

Reparametrization

In the previous chapter, different models have been introduced, which parametrize the geometric center with respect to the inertial I-frame, cf. Eq. (3.50). This description of the reference point G with a rotation matrix parametrized in Euler angles leads to a time dependent mass matrix $\bar{\boldsymbol{M}}$ and therefore to a non-autonomous system in coordinates

$$\boldsymbol{q} = \begin{bmatrix} x & y & z & \alpha & \beta & \gamma \end{bmatrix}^{\mathrm{T}} \in \mathbb{R}^6,$$

cf. Eq. (3.84) and recall that additional dissipation mechanisms are neglected. Introducing new minimal coordinates

$$\boldsymbol{z} = \begin{bmatrix} \bar{x} & \bar{y} & z & \alpha & \beta & \gamma \end{bmatrix}^{\mathrm{T}} \in \mathbb{R}^6, \tag{4.1}$$

where the position of the geometric center G

$${}_R\boldsymbol{r}_{OG} = \begin{bmatrix} \bar{x} \\ \bar{y} \\ z \end{bmatrix}$$

is expressed with respect to the co-rotating R-frame, which results from rotation of the I-frame with the angle α around the $\boldsymbol{e}_z^I$-vector, the kinematic relation

$$\boldsymbol{q} = \begin{bmatrix} \boldsymbol{A}_{IR} & 0 \\ 0 & \boldsymbol{1} \end{bmatrix} \boldsymbol{z} = \boldsymbol{H}(\boldsymbol{z})\boldsymbol{z} = \boldsymbol{q}(\boldsymbol{z}) \tag{4.2}$$

between coordinates $\boldsymbol{q}$ and $\boldsymbol{z}$ is given with the transformation matrix $\boldsymbol{A}_{IR}$ from Eq. (3.64). The relationship between $\dot{\boldsymbol{q}}$ and $\dot{\boldsymbol{z}}$ is deduced by differentiating Eq. (4.2) with respect to time and gives

$$\dot{\boldsymbol{q}} = \boldsymbol{H}(\boldsymbol{z})\dot{\boldsymbol{z}} + \dot{\boldsymbol{H}}(\boldsymbol{z})\boldsymbol{z} = \boldsymbol{B}(\boldsymbol{z})\dot{\boldsymbol{z}}, \tag{4.3}$$

where the kinematic matrix

$$\boldsymbol{B}(\boldsymbol{z}) = \left[\begin{array}{cccccc} \mathrm{c}\alpha & -\mathrm{s}\alpha & 0 & -\mathrm{s}\alpha\bar{x} - \mathrm{c}\alpha\bar{y} & 0 & 0 \\ \mathrm{s}\alpha & \mathrm{c}\alpha & 0 & \mathrm{c}\alpha\bar{x} - \mathrm{s}\alpha\bar{y} & 0 & 0 \\ 0 & 0 & 1 & 0 & 0 & 0 \\ & \boldsymbol{0} & & & \boldsymbol{1} & \end{array}\right]$$

is identified. Together with Eq. (4.2) and Eq. (4.3), the equations of motion

$$\bar{\boldsymbol{M}}(\boldsymbol{q})\ddot{\boldsymbol{q}} = \bar{\boldsymbol{h}}(\boldsymbol{q},\dot{\boldsymbol{q}}) + \bar{\boldsymbol{f}}_g + \bar{\boldsymbol{W}}\boldsymbol{\lambda}$$

from Eq. (3.84) transform to

$$\boldsymbol{B}^{\mathrm{T}}\bar{\boldsymbol{M}}(\boldsymbol{q}(\boldsymbol{z}))\boldsymbol{B}\ddot{\boldsymbol{z}} = \boldsymbol{B}^{\mathrm{T}}\left[\bar{\boldsymbol{h}}(\boldsymbol{q}(\boldsymbol{z}),\boldsymbol{B}\dot{\boldsymbol{z}}) - \bar{\boldsymbol{M}}(\boldsymbol{q}(\boldsymbol{z}))\dot{\boldsymbol{B}}\dot{\boldsymbol{z}}\right] + \boldsymbol{B}^{\mathrm{T}}\bar{\boldsymbol{f}}_g + \boldsymbol{B}^{\mathrm{T}}\bar{\boldsymbol{W}}\boldsymbol{\lambda},$$

which can be written in short form as

$$\boldsymbol{M}(\boldsymbol{z})\ddot{\boldsymbol{z}} = \boldsymbol{h}(\boldsymbol{z},\dot{\boldsymbol{z}}) + \boldsymbol{f}_g + \boldsymbol{W}\boldsymbol{\lambda}, \tag{4.4}$$

where the letters without a dash indicate transformed quantities. Equation (4.4) corresponds to equations of motion in the new minimal coordinates $\boldsymbol{z}$ and is identified as a second-order ordinary differential equation. Here it is assumed that the generalized contact force $\boldsymbol{\lambda} = \left[\lambda_N, \boldsymbol{\lambda}_T^{\mathrm{T}}\right]^{\mathrm{T}}$ only contains a scalar normal and a two-dimensional tangential friction force. This assumption is valid if only smooth Coulomb friction is considered and additional friction forces are neglected, cf. the assumptions of ODE Model 1. The symmetric mass matrix $\boldsymbol{M}$ and the vector of gyroscopic forces $\boldsymbol{h}$ are given as

$$\begin{aligned}\boldsymbol{M}(\boldsymbol{z}) &:= \boldsymbol{B}^{\mathrm{T}}\bar{\boldsymbol{M}}(\boldsymbol{q}(\boldsymbol{z}))\boldsymbol{B}\\ &:= \begin{bmatrix}\boldsymbol{M}_{11} & \boldsymbol{M}_{12}\\ \boldsymbol{M}_{21} & \boldsymbol{M}_{22}\end{bmatrix},\end{aligned} \tag{4.5}$$

with

$$\boldsymbol{M}_{11} = \begin{bmatrix} m & 0 & 0\\ 0 & m & 0\\ 0 & 0 & m\end{bmatrix}, \quad \boldsymbol{M}_{21} = \boldsymbol{M}_{12}^{\mathrm{T}},$$

$$\boldsymbol{M}_{12} = \begin{bmatrix} -m\bar{y} - me\mathrm{c}\beta\mathrm{s}\gamma & 0 & -me\mathrm{s}\gamma\\ m\bar{x} + me\mathrm{c}\gamma & -me\mathrm{s}\beta\mathrm{s}\gamma & me\mathrm{c}\beta\mathrm{c}\gamma\\ 0 & me\mathrm{c}\beta\mathrm{s}\gamma & me\mathrm{s}\beta\mathrm{c}\gamma\end{bmatrix},$$

$$\boldsymbol{M}_{22} = \begin{bmatrix} M_{22,11} & \cdot & \mathrm{sym.}\\ M_{22,12} & A\mathrm{c}^2\gamma + B\mathrm{s}^2\gamma & \cdot\\ M_{22,13} & 0 & C\end{bmatrix},$$

$$\begin{aligned}M_{22,11} &= m(\bar{x}^2 + \bar{y}^2) + 2me(\bar{x}\mathrm{c}\gamma + \bar{y}\mathrm{c}\beta\mathrm{s}\gamma)\\ &\quad + (A\mathrm{s}^2\gamma + B\mathrm{c}^2\gamma)\mathrm{s}^2\beta + C\mathrm{c}^2\beta,\\ M_{22,12} &= (A - B)\mathrm{s}\beta\mathrm{s}\gamma\mathrm{c}\gamma - me\bar{x}\mathrm{s}\beta\mathrm{s}\gamma,\\ M_{22,13} &= me\bar{x}\mathrm{c}\beta\mathrm{c}\gamma + me\bar{y}\mathrm{s}\gamma + C\mathrm{c}\beta,\end{aligned}$$

and

$$\begin{aligned}\boldsymbol{h}(\boldsymbol{z},\dot{\boldsymbol{z}}) &:= \boldsymbol{B}^{\mathrm{T}}\left[\bar{\boldsymbol{h}}(\boldsymbol{q}(\boldsymbol{z}),\boldsymbol{B}\dot{\boldsymbol{z}}) - \bar{\boldsymbol{M}}(\boldsymbol{q}(\boldsymbol{z}))\dot{\boldsymbol{B}}\dot{\boldsymbol{z}}\right] \\ &:= \begin{bmatrix} h_1 & h_2 & h_3 & h_4 & h_5 & h_6 \end{bmatrix}^{\mathrm{T}}\end{aligned}$$

with

$$\begin{aligned}
h_1 =& m\left[\bar{x}\dot{\alpha}^2 + 2\dot{\bar{y}}\dot{\alpha}\right] + me\left[(\dot{\alpha}^2+\dot{\gamma}^2)\mathrm{c}\gamma - 2\dot{\alpha}\dot{\beta}\mathrm{s}\beta\mathrm{s}\gamma + 2\dot{\alpha}\dot{\gamma}\mathrm{c}\beta\mathrm{c}\gamma\right],\\
h_2 =& m\left[\bar{y}\dot{\alpha}^2 - 2\dot{\bar{x}}\dot{\alpha}\right] + me\left[(\dot{\alpha}^2+\dot{\beta}^2+\dot{\gamma}^2)\mathrm{c}\beta\mathrm{s}\gamma + 2\dot{\alpha}\dot{\gamma}\mathrm{s}\gamma + 2\dot{\beta}\dot{\gamma}\mathrm{s}\beta\mathrm{c}\gamma\right],\\
h_3 =& me\left[\dot{\beta}^2\mathrm{s}\beta\mathrm{s}\gamma + \dot{\gamma}^2\mathrm{s}\beta\mathrm{s}\gamma - 2\dot{\beta}\dot{\gamma}\mathrm{c}\beta\mathrm{c}\gamma\right],\\
h_4 =& -2m\left[\bar{x}\dot{\bar{x}}\dot{\alpha} + \bar{y}\dot{\bar{y}}\dot{\alpha}\right]\\
& - me\left[2\dot{\bar{x}}\dot{\alpha}\mathrm{c}\gamma + (2\dot{\bar{y}}\dot{\alpha} - \bar{x}\dot{\beta}^2 - \bar{x}\dot{\gamma}^2)\mathrm{c}\beta\mathrm{s}\gamma\right.\\
& \left. - 2\bar{x}\dot{\alpha}\dot{\gamma}\mathrm{s}\gamma - 2\bar{x}\dot{\beta}\dot{\gamma}\mathrm{s}\beta\mathrm{c}\gamma + \bar{y}\dot{\gamma}^2\mathrm{c}\gamma - 2\bar{y}\dot{\alpha}\dot{\beta}\mathrm{s}\beta\mathrm{s}\gamma + 2\bar{y}\dot{\alpha}\dot{\gamma}\mathrm{c}\beta\mathrm{c}\gamma\right]\\
& - (A-B)\left[\dot{\beta}^2\mathrm{c}\beta\mathrm{s}\gamma\mathrm{c}\gamma + 2\dot{\alpha}\dot{\gamma}\mathrm{s}^2\beta\mathrm{s}\gamma\mathrm{c}\gamma + \dot{\beta}\dot{\gamma}\mathrm{s}\beta(\mathrm{c}^2\gamma - \mathrm{s}^2\gamma)\right]\\
& - 2(A\mathrm{s}^2\gamma + B\mathrm{c}^2\gamma - C)\dot{\alpha}\dot{\beta}\mathrm{s}\beta\mathrm{c}\beta + C\dot{\beta}\dot{\gamma}\mathrm{s}\beta,\\
h_5 =& me\left[2\dot{\bar{x}}\dot{\alpha} - \bar{y}\dot{\alpha}^2\right]\mathrm{s}\beta\mathrm{s}\gamma + (A-B)\left[2\dot{\beta}\dot{\gamma}\mathrm{s}\gamma\mathrm{c}\gamma - \dot{\alpha}\dot{\gamma}\mathrm{s}\beta(\mathrm{c}^2\gamma - \mathrm{s}^2\gamma)\right]\\
& + (A\mathrm{s}^2\gamma + B\mathrm{c}^2\gamma)\dot{\alpha}^2\mathrm{s}\beta\mathrm{c}\beta - C\left[\dot{\alpha}^2\mathrm{s}\beta\mathrm{c}\beta + \dot{\alpha}\dot{\gamma}\mathrm{s}\beta\right],\\
h_6 =& -me\left[2\dot{\bar{y}}\dot{\alpha} + \bar{x}\dot{\alpha}^2\right]\mathrm{s}\gamma - me\left[2\dot{\bar{x}}\dot{\alpha} - \bar{y}\dot{\alpha}^2\right]\mathrm{c}\beta\mathrm{c}\gamma\\
& + (A-B)\left[(\dot{\alpha}^2\mathrm{s}^2\beta - \dot{\beta}^2)\mathrm{s}\gamma\mathrm{c}\gamma + \dot{\alpha}\dot{\beta}(\mathrm{c}^2\gamma - \mathrm{s}^2\gamma)\mathrm{s}\beta\right] + C\dot{\alpha}\dot{\beta}\mathrm{s}\beta.
\end{aligned} \tag{4.6}$$

Equations (4.5)-(4.6) determine the inertia forces. The generalized gravitational force yields

$$\begin{aligned}\boldsymbol{f}_g(\boldsymbol{z}) &:= \boldsymbol{B}^{\mathrm{T}}\bar{\boldsymbol{f}}(\boldsymbol{q}(\boldsymbol{z}))\\ &:= -mg\begin{bmatrix} 0 & 0 & 1 & 0 & e\mathrm{c}\beta\mathrm{s}\gamma & e\mathrm{s}\beta\mathrm{c}\gamma \end{bmatrix}^{\mathrm{T}}.\end{aligned}$$

From the transformed matrix of generalized force directions $\boldsymbol{W} := \boldsymbol{B}^{\mathrm{T}}\bar{\boldsymbol{W}}$ the generalized normal force direction with respect to the coordinates $\boldsymbol{z}$ is identified as the first column

$$\boldsymbol{w}_N = \begin{bmatrix} 0 & 0 & 1 & 0 & -r\mathrm{c}\beta & 0 \end{bmatrix}^{\mathrm{T}} \tag{4.7}$$

of the matrix $\boldsymbol{W}$. The matrix

$$\begin{aligned}\boldsymbol{W}_T &:= \boldsymbol{B}^{\mathrm{T}}\bar{\boldsymbol{W}}_T\begin{bmatrix} \mathrm{c}\alpha & -\mathrm{s}\alpha \\ \mathrm{s}\alpha & \mathrm{c}\alpha \end{bmatrix}\\ &:= \begin{bmatrix} 1 & 0 & 0 & r\mathrm{c}\beta - \bar{y} & 0 & r \\ 0 & 1 & 0 & \bar{x} & r\mathrm{s}\beta & 0 \end{bmatrix}^{\mathrm{T}},\end{aligned} \tag{4.8}$$

of tangential force directions collects the α-transformed second and third columns of $\boldsymbol{W}$. The linear α-transformation allows to identify the generalized tangential force directions with physical sliding directions of the tippedisk, i.e., sliding in longitudinal rolling direction $\boldsymbol{e}_x^R$ and the lateral sliding direction $\boldsymbol{e}_y^R$. With the transformed relative sliding velocity

$$\boldsymbol{\gamma}_T = \boldsymbol{W}_T^{\mathrm{T}} \dot{\boldsymbol{z}} = \begin{bmatrix} \boldsymbol{v}_{C_1} \cdot \boldsymbol{e}_x^R \\ \boldsymbol{v}_{C_1} \cdot \boldsymbol{e}_y^R \end{bmatrix}, \tag{4.9}$$

the isotropic smooth Coulomb friction law from Eq. (3.33) yields the same qualitative behavior, as in the case of the tangential relative velocity from Eq. (3.27). Note, however, that the transformed system equations do not depend on the spinning angle α explicitly, allowing to proceed with Lyapunov's indirect method.

Linear stability analysis of the full system

To study the local dynamics of inverted and non-inverted spinning, the resulting equations of motion given in Eq. (4.4) are partially linearized in the inclination angle β and the rolling angle γ, as well as in the co-rotating small horizontal deviations $\bar{x}$ and $\bar{y}$.

Using symmetry, the linearized equations for non-inverted spinning motions are similar to the linearized equations of motion for inverted spinning and differ only in the sign of the eccentricity e. Therefore, the linearization of the reparametrized system Eq. (4.4) is performed here only for the inverted tippedisk. The non-inverted dynamics can be easily derived by considering symmetry. This motivates the introduction of the shifted angles $\bar{\beta} = \beta - \pi/2 \ll 1$ and $\bar{\gamma} = \gamma - \pi/2 \ll 1$, which initially implies an inverted configuration of the disk. Since the height $z = r$ is constant and the spinning angle α increases with time, the generalized coordinates of the small quantities are introduced as

$$\hat{\boldsymbol{z}} := \begin{bmatrix} \bar{x} & \bar{y} & \bar{\beta} & \bar{\gamma} \end{bmatrix}^{\mathrm{T}}$$

to quantify the deviation from a stationary inverted spinning solution. Consequently, nearly inverted spinning is characterized by $\mathcal{O}(\|\hat{\boldsymbol{z}}\|) \ll 1$. Assuming the orders

$$\mathcal{O}(\bar{x}) = \mathcal{O}(\bar{y}) = \mathcal{O}(\bar{\beta}) = \mathcal{O}(\bar{\gamma}) \ll 1$$

yields the following approximations

$$\begin{aligned}
\sin\beta &= \cos\bar{\beta} = 1 + \mathcal{O}(\bar{\beta}^2), \\
\cos\beta &= -\sin\bar{\beta} = -\bar{\beta} + \mathcal{O}(\bar{\beta}^3), \\
\sin\gamma &= \cos\bar{\gamma} = 1 + \mathcal{O}(\bar{\gamma}^2), \\
\cos\gamma &= -\sin\bar{\gamma} = -\bar{\gamma} + \mathcal{O}(\bar{\gamma}^3).
\end{aligned}$$

of trigonometric expressions. Inspection of the third z-component of the system reveals that

$$m\ddot{z} = -mg + \lambda_N + \mathscr{O}(\|\hat{\boldsymbol{z}}\|^2). \tag{4.10}$$

As shown by the simulation results presented in the Section 3.8, the contact remains persistent, i.e., the contact distance $g_{N1} = z - r\sin\beta = z - r\cos\bar{\beta}$ between the contact point C_1 on the rim of the disk and the support is zero. Assuming persistent contact yields for slightly perturbed inverted motions that the second time derivative

$$\ddot{z} = -r(\ddot{\bar{\beta}}\sin\bar{\beta} - \dot{\bar{\beta}}^2\cos\bar{\beta}) = 0 + \mathscr{O}(\|\hat{\boldsymbol{z}}\|^2) \tag{4.11}$$

of z vanishes in the linear analysis. Substituting Eq. (4.11) into Eq. (4.10) results in

$$\mathscr{O}(\|\hat{\boldsymbol{z}}\|^2) = -mg + \lambda_N \Rightarrow \lambda_N = mg + \mathscr{O}(\|\hat{\boldsymbol{z}}\|^2). \tag{4.12}$$

For motions in the vicinity of stationary spinning in place, the normal contact force is equal to the weight of the disk. Moreover, for stationary spinning, the relative tangential velocity $\boldsymbol{\gamma}_T$ defined in Eq. (4.9) vanishes, which motivates the linearization

$$\boldsymbol{\lambda}_T = -\frac{\mu\lambda_N}{\varepsilon}\boldsymbol{\gamma}_T = -d\boldsymbol{\gamma}_T, \tag{4.13}$$

of smooth Coulomb friction Eq. (3.33). According to Eq. (4.12), the normal contact force λ_N is equal to the weight of the disk, resulting in the dissipation constant $d = \frac{\mu mg}{\varepsilon}$ introduced in Eq. (4.13). Substitution of the relative contact velocity from Eq. (4.9) into the linearized Coulomb friction law yields the generalized friction force

$$\begin{aligned}
\boldsymbol{W}_T\boldsymbol{\lambda}_T &= -d\,\boldsymbol{W}_T\boldsymbol{W}_T^{\mathrm{T}}\dot{\boldsymbol{z}} + \mathscr{O}(\|\boldsymbol{\gamma}_T\|^3)\\
&= -d\begin{bmatrix} 1 & 0 & 0 & -r\bar{\beta} - \bar{y} & 0 & r\\ 0 & 1 & 0 & \bar{x} & r & 0\\ 0 & 0 & 0 & 0 & 0 & 0\\ 0 & 0 & 0 & 0 & 0 & 0\\ 0 & r & 0 & \bar{x}r & r^2 & 0\\ r & 0 & 0 & -r^2\bar{\beta} - r\bar{y} & 0 & r^2 \end{bmatrix}\dot{\boldsymbol{z}} + \mathscr{O}(\|\hat{\boldsymbol{z}}\|^2).
\end{aligned} \tag{4.14}$$

With the generalized tangential force direction from Eq. (4.8), the matrix product $\boldsymbol{W}_T\boldsymbol{W}_T^{\mathrm{T}}$ yields a symmetric matrix. However, in Eq. (4.14), all higher-order terms of $\boldsymbol{W}_T\boldsymbol{W}_T^{\mathrm{T}}\dot{\boldsymbol{z}}$ must be consistently shifted into big $\mathscr{O}(\|\hat{\boldsymbol{z}}\|^2)$ resulting in a matrix tuple expression with non-symmetric matrix. According to Eq. (4.14), tangential friction does not affect the third and forth generalized coordinates α and z. Neglecting higher-order terms in the fourth generalized coordinate, results in a vanishing angular spinning acceleration $\ddot{\alpha} = 0$. As a consequence, the angular velocity $\dot{\alpha} \approx \Omega$ is about constant, which implies the linear time dependence $\alpha(t)=\alpha_0+\Omega t$ of the spinning angle. The corresponding inverted stationary spinning solution is described in transformed $\boldsymbol{z}$-coordinates by

$$\begin{aligned}\boldsymbol{z}_0 &= \begin{bmatrix}0 & 0 & r & \alpha_0+\Omega t & 0 & 0\end{bmatrix}^{\mathrm{T}}\\ \dot{\boldsymbol{z}}_0 &= \begin{bmatrix}0 & 0 & 0 & \Omega & 0 & 0\end{bmatrix}^{\mathrm{T}},\end{aligned} \tag{4.15}$$

which can equivalently be expressed in $\boldsymbol{q}$-coordinates by

$$\begin{aligned}\boldsymbol{q}_0 &= \begin{bmatrix}0 & 0 & r & \alpha_0+\Omega t & \pi/2 & \pi/2\end{bmatrix}^{\mathrm{T}}\\ \dot{\boldsymbol{q}}_0 &= \begin{bmatrix}0 & 0 & 0 & \Omega & 0 & 0\end{bmatrix}^{\mathrm{T}}.\end{aligned}$$

Without loss of generality, the initial angle α_0 is set to zero since the friction law is assumed to be isotropic. Neglecting the higher-order terms $\mathcal{O}(\|\hat{\boldsymbol{z}}\|^2)$ reveals a splitting of linearized systems equations, i.e., the linearized dynamics of third and forth row is decoupled. Consequently, the normal contact force λ_N used in the tangential Coulomb friction law and the rotational velocity $\dot{\alpha}=\Omega$ in the linearization are no longer degrees of freedom but become parameters of the reduced linear system. Any stationary spinning solution is identified by the specific height $z=r$ of the geometric center G and a constant angular velocity $\Omega\in\mathbb{R}$. Since for each $\Omega\in\mathbb{R}$, there exists a stationary spinning solution, the parameter Ω yields a foliation of the state-space.

Introducing the linear relations $\hat{\boldsymbol{z}}=\boldsymbol{C}\boldsymbol{z}$ and $\dot{\hat{\boldsymbol{z}}}=\boldsymbol{C}\dot{\boldsymbol{z}}$ with associated selection matrix

$$\boldsymbol{C}=\begin{bmatrix}1&0&0&0&0&0\\0&1&0&0&0&0\\0&0&0&0&1&0\\0&0&0&0&0&1\end{bmatrix},$$

any stationary spinning solution from Eq. (4.15) is characterized by the trivial equilibrium $\hat{\boldsymbol{z}}_0=\dot{\hat{\boldsymbol{z}}}_0=\boldsymbol{0}$. This projections allows to study the linear stability on one leaf of the foliated state-space. Pre-multiplication of the equations of motion from Eq. (4.4) with the selection matrix $\boldsymbol{C}$ leads to a deletion of the third and fourth line. Linearization around zero using the constant spinning speed $\dot{\alpha}=\Omega$ gives the four-dimensional linear system

$$\boldsymbol{M}^{4\times4}\ddot{\hat{\boldsymbol{z}}}+\boldsymbol{G}_{\boldsymbol{h}}^{4\times4}\dot{\hat{\boldsymbol{z}}}+\boldsymbol{K}_{\boldsymbol{h}}^{4\times4}\hat{\boldsymbol{z}}=-\boldsymbol{K}_{\boldsymbol{f}}^{4\times4}\hat{\boldsymbol{z}}-\boldsymbol{D}_{C}^{4\times4}\dot{\hat{\boldsymbol{z}}}-\boldsymbol{B}_{C}^{4\times4}\hat{\boldsymbol{z}} \tag{4.16}$$

of second-order with constant system matrices

$$\boldsymbol{M}^{4\times4} = \begin{bmatrix} m & 0 & 0 & -me \\ 0 & m & -me & 0 \\ 0 & -me & B & 0 \\ -me & 0 & 0 & C \end{bmatrix},$$

$$\boldsymbol{G}_{\boldsymbol{h}}^{4\times4} = \begin{bmatrix} 0 & -2m\Omega & +2me\Omega & 0 \\ +2m\Omega & 0 & 0 & -2me\Omega \\ -2me\Omega & 0 & 0 & -D\Omega \\ 0 & +2me\Omega & +D\Omega & 0 \end{bmatrix},$$

$$\boldsymbol{K}_{\boldsymbol{h}}^{4\times4} = \begin{bmatrix} -m\Omega^2 & 0 & 0 & +me\Omega^2 \\ 0 & -m\Omega^2 & +me\Omega^2 & 0 \\ 0 & +me\Omega^2 & (A-C)\Omega^2 & 0 \\ +me\Omega^2 & 0 & 0 & (A-B)\Omega^2 \end{bmatrix}, \tag{4.17}$$

$$\boldsymbol{K}_{\boldsymbol{f}}^{4\times4} = -\begin{bmatrix} 0 & 0 & 0 & 0 \\ 0 & 0 & 0 & 0 \\ 0 & 0 & mg(e+r) & 0 \\ 0 & 0 & 0 & mge \end{bmatrix},$$

$$\boldsymbol{D}_C^{4\times4} = -\begin{bmatrix} d & 0 & 0 & dr \\ 0 & d & dr & 0 \\ 0 & dr & dr^2 & 0 \\ dr & 0 & 0 & dr^2 \end{bmatrix}$$

and

$$\boldsymbol{B}_C^{4\times4} = -\begin{bmatrix} 0 & -d\Omega & -dr\Omega & 0 \\ d\Omega & 0 & 0 & 0 \\ dr\Omega & 0 & 0 & 0 \\ 0 & -dr\Omega & -dr^2\Omega & 0 \end{bmatrix} = \boldsymbol{B}_{\text{sym}}^{4\times4} + \boldsymbol{B}_{\text{skew}}^{4\times4}.$$

To shorten notation the abbreviation $D = (A - B - C)$ is used in Eq. (4.17). Since the spinning speed $\dot{\alpha}$ is constant in the reduced system from Eq. (4.16), it describes motions of the tippedisk in permanent rotation, cf. [13, 66]. The linearization of the vector $\boldsymbol{h}$ of gyroscopic forces yields a skew-symmetric gyro matrix $\boldsymbol{G}_{\boldsymbol{h}}^{4\times4}$ and a symmetric stiffness matrix $\boldsymbol{K}_{\boldsymbol{h}}^{4\times4}$. Gravitation and normal contact induce a symmetric matrix $\boldsymbol{K}_{\boldsymbol{f}}^{4\times4}$. Linearized Coulomb friction includes linear terms in $\dot{\boldsymbol{z}}$, which induce the symmetric matrix $\boldsymbol{D}_C^{4\times4}$. Moreover, Coulomb friction leads to linear terms in

$\hat{\boldsymbol{z}}$, which occur symmetrically with $\boldsymbol{B}^{4\times4}_{\text{sym}}$ and skew symmetric with $\boldsymbol{B}^{4\times4}_{\text{skew}}$. Defining the matrices $\boldsymbol{D}^{4\times4} := \boldsymbol{D}^{4\times4}_{C}$, $\boldsymbol{G}^{4\times4} := \boldsymbol{G}^{4\times4}_{\boldsymbol{h}}$, $\boldsymbol{K}^{4\times4} := \boldsymbol{K}^{4\times4}_{\boldsymbol{h}} + \boldsymbol{K}^{4\times4}_{\boldsymbol{f}} + \boldsymbol{B}^{4\times4}_{\text{sym}}$ and $\boldsymbol{N}^{4\times4} := \boldsymbol{B}^{4\times4}_{\text{skew}}$, the linearized equations of motion become

$$\boldsymbol{M}^{4\times4}\ddot{\hat{\boldsymbol{z}}} + \left(\boldsymbol{D}^{4\times4} + \boldsymbol{G}^{4\times4}\right)\dot{\hat{\boldsymbol{z}}} + \left(\boldsymbol{K}^{4\times4} + \boldsymbol{N}^{4\times4}\right)\hat{\boldsymbol{z}} = 0,$$

forming a system of linear ordinary differential equations with constant coefficients suitable for eigenvalue analysis. The matrices $\boldsymbol{M}^{4\times4}$, $\boldsymbol{D}^{4\times4}$ and $\boldsymbol{K}^{4\times4}$ have a symmetric structure. The matrices $\boldsymbol{G}^{4\times4}$ and $\boldsymbol{N}^{4\times4}$ are skew symmetric. To study the local stability of permanent rotations spinning around the vertical axis, the constant spinning velocity Ω takes the role of a bifurcation parameter. In the associated state-space with natural choice of states $\hat{\boldsymbol{z}}$ and $\dot{\hat{\boldsymbol{z}}}$, the corresponding eight eigenvalues are computed numerically.

Figure 4.1 shows the evolution of the eight eigenvalues $\lambda_1 - \lambda_8$ of the stationary inverted spinning solution for $\Omega \in [0, 50\,\text{rad/s}]$. Here, the complex conjugate pairs of eigenvalues are sorted in the order of their imaginary part, followed by the two real eigenvalues. The real parts of $\lambda_1 - \lambda_6$ are depicted in Figure 4.1(a), while their imaginary parts are shown in Figure 4.1(b). Comparison of the real and imaginary parts shows that the eigenvalues λ_1 (red) and λ_2 (red, dashed) cross the imaginary axis as complex conjugated pair at the critical spinning velocity $\Omega_{\text{c}_2} \approx 30.2\,\text{rad/s}$, indicating a Hopf bifurcation. For small spinning speeds $\Omega < \Omega_{\text{c}_2}$, the red eigenvalues have a pronounced positive real part, so the inverted orientation of the disk is unstable. For supercritical spinning velocities $\Omega > \Omega_{\text{c}_2}$, their real part is negative, corresponding to a stable two-dimensional subspace. As the rotational speed increases, the real part of the eigenvalues λ_1 and λ_2 decreases further.

The green pair of conjugated eigenvalues λ_3 and λ_4 are purely imaginary and their magnitude is directly proportional to the spinning velocity Ω. These eigenvalues are connected to rigid body motions as the horizontal position of the disk is irrelevant.

For small spinning speeds, the eigenvalues λ_5 (blue) and λ_6 (blue, dashed) have negative real parts. With increasing rotational speed they become complex conjugate, and the resulting complex conjugate pair of blue eigenvalues crosses the imaginary axis at $\Omega_{\text{c}_1} \approx 27.1\,\text{rad/s}$. The bifurcation at Ω_{c_1} is therefore identified as a Hopf bifurcation, implying an unstable subspace for supercritical spinning velocities $\Omega > \Omega_{\text{c}_1}$.

In the lower right graph of Figure 4.1(d) both critical velocities Ω_{c_1} and Ω_{c_2} are depicted in a magnified plot, which where determined numerically. So within this eight-dimensional state-space, the inverted spinning motion $\hat{\boldsymbol{z}}_0 = \dot{\hat{\boldsymbol{z}}}_0 = \boldsymbol{0}$ is strictly

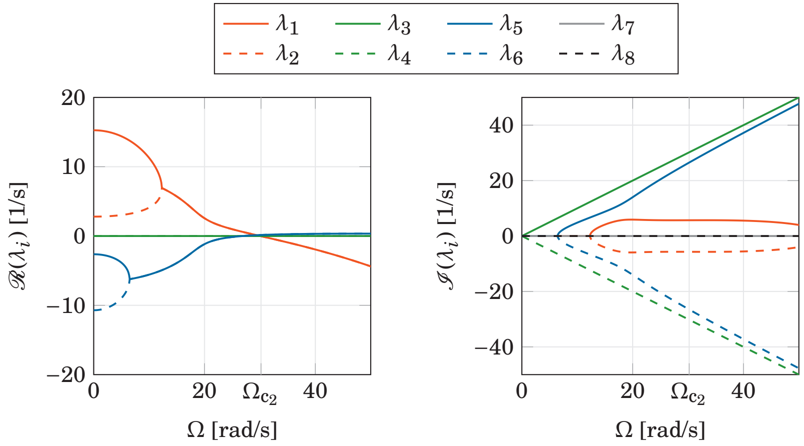

(a) real part $\mathscr{R}(\lambda_i)$ for $i = 1,\dots,6$

(b) imaginary part $\mathscr{I}(\lambda_i)$ for $i = 1,\dots,8$

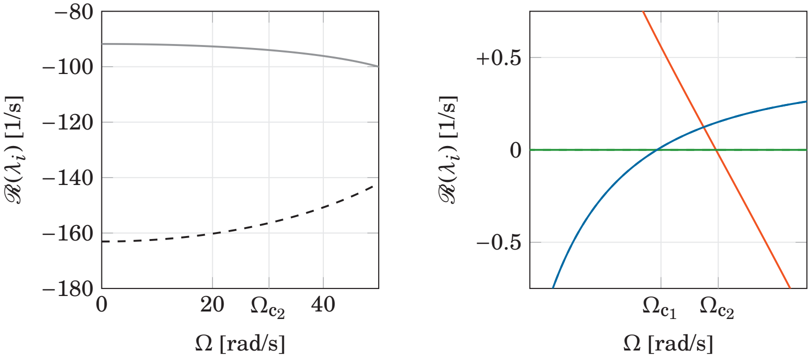

(c) real part $\mathscr{R}(\lambda_{7,8})$

(d) zoomed real part $\mathscr{R}(\lambda_i)$ for $i = 1,\dots,6$

Figure 4.1: Eigenvalues for the inverted tippedisk.

speaking never stable, since there exists for each Ω a pair of eigenvalues with positive real part.

In addition, there are two real eigenvalues λ_7 and λ_8, which are related to very fast sliding of the disk. Since their real parts are strongly negative, they are shown separately in Figure 4.1(c). The corresponding subspaces remain stable and do not change their qualitative stability behavior for $\Omega \leq 50\,\mathrm{rad/s}$.

For supercritical spinning speeds $\Omega > \Omega_{c_1}$, the eigenvalue pairs differ significantly in magnitude and each pair describes a motion on a distinct time scale. The eigenvalues λ_7 and λ_8 are related to very fast dynamics. The eigenvalues λ_1 and λ_2 characterize an intermediate time scale, whereas the blue eigenvalues λ_5 and λ_6 are connected to motions on a slow time scale. Moreover, the blue eigenvalues seem to behave almost like rigid body motions at large spin velocities, with an almost negligible real part.

In summary, the local stability analysis does not reflect the physical observation of an inverted spinning motion which, loosely speaking, seems to attract almost all trajectories. Apparently, it is not fruitful to analyze the asymptotic dynamical behavior applying Lyapunov's indirect method to the six-dimensional system from Eq. (4.4). Just because of the vanishing real parts of λ_3 and λ_4, a stability statement about the nonlinear system by neglecting higher-order terms is not possible.

The eight eigenvalues shown in Figure 4.2, characterize the local stability of permanent rotations in non-inverted configuration. Two eigenvalues λ_1 and λ_2 shown in red are real with pronounced positive and negative real part. The complex conjugate eigenvalues λ_3 and λ_4 with zero real part in green refer to rigid body motions, while the complex conjugate blue eigenvalues λ_5 and λ_6 have a negative real part for slow rotational velocity, which becomes positive when Ω is increased. The eigenvalues λ_7 and λ_8 are again related to fast motions whose real parts are strongly negative, cf. Figure 4.2(c). In conclusion, the non-inverted stationary solution is always unstable due to λ_1. This stability behavior is consistent with experimental observations, since it is not possible to rotate the disk so that it remains in a non-inverted configuration. It either falls over or ends in a permanent rotation with inverted orientation.

In summary, the linear stability analysis contradicts the physical observation for inverted spinning solutions. The reason for this contradiction could be the restrictive assumption of small $|\bar{x}| \ll 1$ and $|\bar{y}| \ll 1$. This hypothesis is supported by the fact that in the real experiment slight horizontal movements of the tippedisk are present during the inversion phenomenon. Although the linear analysis cannot properly describe the qualitative dynamics, it provides important results. On the one hand, inverted spinning of the disk is basically a permanent rotation, which

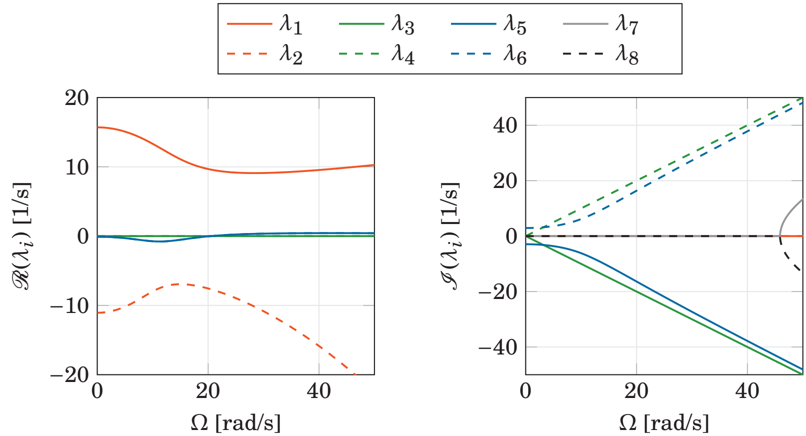

(a) real part $\mathscr{R}(\lambda_i)$ for $i = 1,\ldots,6$

(b) imaginary part $\mathscr{I}(\lambda_i)$ for $i = 1,\ldots,8$

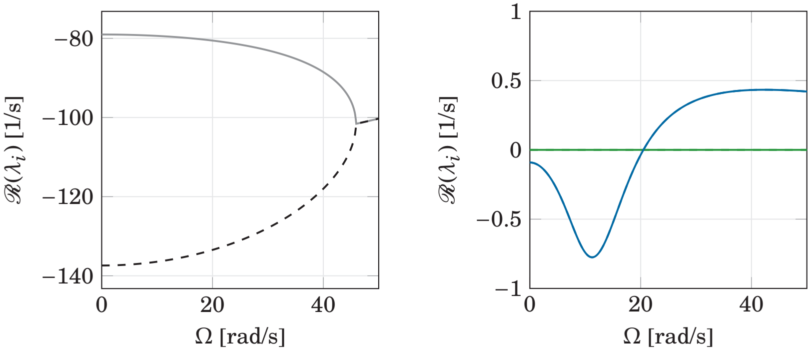

(c) real part $\mathscr{R}(\lambda_{7,8})$

(d) zoomed real part $\mathscr{R}(\lambda_i)$ for $i = 3,\ldots,6$

Figure 4.2: Eigenvalues for the non-inverted tippedisk.

manifests as an equilibrium in generalized coordinates $\hat{\boldsymbol{z}} \in \mathbb{R}^4$. On the other hand, the linearization of the 6 DOF system motivates a constant spinning velocity $\dot{\alpha} \approx \Omega$ and a constant normal contact force $\lambda_N \approx mg$. Furthermore, the large difference in the eigenvalues implies that the qualitative behavior can be decomposed into slow and fast dynamics, suggesting the application of singular perturbation theory and thus the theory of slow-fast systems.

4.2 Model reduction

In Chapter 3, a detailed mechanical model of the tippedisk is derived, which is able to capture the inversion phenomenon. Assuming regularized Coulomb friction, local stability of inverted and non-inverted spinning solutions is studied in Section 4.1. There, the full dynamics with six generalized coordinates introduced in Eq. (4.1) is linearized, giving a total dimension of twelve states. With the ultimate goal to understand the qualitative behavior, the full model is not suited. Therefore, this section focuses on the model reduction, aiming to obtain a simplified model with reduced states, which preserves the qualitative stability. In the following, several constraints are imposed to reduce the state dimension while preserving the qualitative behavior of the tippedisk near vertical rotations.

As the disk remains almost vertical during inversion ($\beta \approx \frac{\pi}{2}$), the additional contact points C_2 and C_3 have no particular meaning, while the contact in point C_1 is persistent. For the considered motion, the contact point C_1 can therefore be assumed to be bilaterally constrained.

This constraint is naturally satisfied for the full mechanical system during the inversion, cf. the numerical simulation results from Section 3.8. Accompanied by the assumption of a smooth friction law, the resulting dynamics is given by a system of differential algebraic equations.

After this first reduction step, new physically motivated constraints are introduced and validated numerically using simulations with fixed initial conditions. For the sake of clarity, Table 4.1 introduces model names for the reduced models with the assumptions made. As several constraints will be introduced in this section, the reduction procedure is explained once in a general way. The starting point of any reduction step is an *unconstrained* mechanical system of the form

$$\begin{aligned} \dot{\boldsymbol{q}} &= \boldsymbol{u} \\ \boldsymbol{M}(\boldsymbol{q})\dot{\boldsymbol{u}} &= \boldsymbol{h}(\boldsymbol{q},\boldsymbol{u}) + \boldsymbol{f}(\boldsymbol{q},\boldsymbol{u}) \end{aligned}$$

with generalized coordinates $\boldsymbol{q} \in \mathbb{R}^n$ and velocities $\boldsymbol{u} \in \mathbb{R}^n$. Adding a generic mechanical constraint equation $\boldsymbol{c}(\boldsymbol{q},\boldsymbol{u},\boldsymbol{\lambda}_c) = 0 \in \mathbb{R}^m$ yields an additional constraint force

Table 4.1: Assumptions on constraints of various models introduced in this monograph. The meaning of the constraints will be explained in following sections.

Constraints		Model 1.1	Model 1.2	Model 1.3	Model 1.4
Bilateral constraint	$g_N = 0$	✓	✓	✓	✓
Hor. fixed COG	$\boldsymbol{g}_S = 0$		✓	✓	✓
No tangential slip	$\gamma_x = 0$			✓	✓
Permanent rotation	$\gamma_\alpha = 0$				✓

$\boldsymbol{\lambda}_c \in \mathbb{R}^m$, i.e., a Lagrange multiplier, which is accounted for on the right-hand side of the equation of motion by $\boldsymbol{f}_c = \boldsymbol{W}_c \boldsymbol{\lambda}_c$. The matrix $\boldsymbol{W}_c \in \mathbb{R}^{n\times m}$ corresponds to the matrix of generalized force directions. In total, this yields the constrained system

$$\begin{aligned} \dot{\boldsymbol{q}} &= \boldsymbol{u} \\ \boldsymbol{M}(\boldsymbol{q})\dot{\boldsymbol{u}} &= \boldsymbol{h}(\boldsymbol{q},\boldsymbol{u}) + \boldsymbol{f}(\boldsymbol{q},\boldsymbol{u}) + \boldsymbol{W}_c\boldsymbol{\lambda}_c \\ \boldsymbol{c}(\boldsymbol{q},\boldsymbol{u},\boldsymbol{\lambda}_c) &= 0, \end{aligned} \tag{4.18}$$

which forms a differential algebraic equation (DAE), cf. [49]. In theory of DAEs it is possible to obtain the underlying ordinary differential equation (ODE) by successive differentiation of the constraint equation $\boldsymbol{c}(\boldsymbol{q},\boldsymbol{u},\boldsymbol{\lambda}_c) = 0$. The (differentiation) *index* of a DAE counts the differentiations needed to obtain an ODE for all states and Lagrange multipliers [49, 43]. Mechanical systems are restricted to constraints on position, velocity or acceleration level. Constraints on position level $\boldsymbol{g}_c(\boldsymbol{q}) = 0$, which depend only on the coordinates $\boldsymbol{q}$, can be differentiated once to obtain the corresponding constraint on velocity level

$$\boldsymbol{\gamma}_c(\boldsymbol{q},\boldsymbol{u}) = \frac{\partial \boldsymbol{g}_c(\boldsymbol{q})}{\partial \boldsymbol{q}}\dot{\boldsymbol{q}} = \frac{\partial \boldsymbol{g}_c(\boldsymbol{q})}{\partial \boldsymbol{q}}\boldsymbol{u} = 0.$$

Consequently, the differentiation of a constraint on velocity level yields the constraint on acceleration level

$$\begin{aligned} \dot{\boldsymbol{\gamma}}_c(\boldsymbol{q},\boldsymbol{u},\dot{\boldsymbol{u}}) &= \frac{\partial \boldsymbol{\gamma}_c(\boldsymbol{q},\boldsymbol{u})}{\partial \boldsymbol{u}}\dot{\boldsymbol{u}} + \frac{\partial \boldsymbol{\gamma}_c(\boldsymbol{q},\boldsymbol{u})}{\partial \boldsymbol{q}}\boldsymbol{u} \\ &= \frac{\partial \boldsymbol{\gamma}_c(\boldsymbol{q},\boldsymbol{u})}{\partial \boldsymbol{u}}\dot{\boldsymbol{u}} + \boldsymbol{\chi}_c(\boldsymbol{q},\boldsymbol{u}) = 0. \end{aligned} \tag{4.19}$$

Since the mass matrix $\boldsymbol{M}$ is symmetric, positive definite and thus invertible, the generalized acceleration yields

$$\dot{\boldsymbol{u}} = \boldsymbol{M}^{-1}(\boldsymbol{h} + \boldsymbol{f} + \boldsymbol{W}_c\boldsymbol{\lambda}_c). \tag{4.20}$$

For ideal constraints in the sense of d'Alembert, the matrix $\boldsymbol{W}_c$ of generalized force directions is deduced as

$$\boldsymbol{W}_c = \left(\frac{\partial \boldsymbol{g}_c}{\partial \boldsymbol{q}}\right)^{\mathrm{T}} = \left(\frac{\partial \boldsymbol{\gamma}_c}{\partial \boldsymbol{u}}\right)^{\mathrm{T}}$$

from the kinematic constraint. Substitution of Eq. (4.20) into Eq. (4.19) reveals the constraint on acceleration level

$$\begin{aligned}\dot{\boldsymbol{\gamma}}_c(\boldsymbol{q},\boldsymbol{u},\dot{\boldsymbol{u}}) &= \frac{\partial \boldsymbol{\gamma}_c(\boldsymbol{q},\boldsymbol{u})}{\partial \boldsymbol{u}} \boldsymbol{M}^{-1}(\boldsymbol{h}+\boldsymbol{f}+\boldsymbol{W}_c\boldsymbol{\lambda}_c)+\boldsymbol{\chi}_c \\ &= \underbrace{\boldsymbol{W}_c^{\mathrm{T}}\boldsymbol{M}^{-1}\boldsymbol{W}_c}_{=:\boldsymbol{D}_c}\boldsymbol{\lambda}_c + \boldsymbol{W}_c^{\mathrm{T}}\boldsymbol{M}^{-1}(\boldsymbol{h}+\boldsymbol{f})+\boldsymbol{\chi}_c \\ &= \boldsymbol{c}(\boldsymbol{q},\boldsymbol{u},\boldsymbol{\lambda}_c)\end{aligned} \tag{4.21}$$

as a function of $\boldsymbol{q}$, $\boldsymbol{u}$, and $\boldsymbol{\lambda}_c$. The square matrix $\boldsymbol{D}_c = \boldsymbol{W}_c^{\mathrm{T}}\boldsymbol{M}^{-1}\boldsymbol{W}_c$, defined in Eq. (4.21), is called the Delassus matrix [25]. It is symmetric, positive definite, and thus invertible if the matrix $\boldsymbol{W}_c$ of generalized force directions is of full column rank, i.e., if the kinematic constraints $\dot{\boldsymbol{\gamma}}_c$ are linearly independent. If the Delassus matrix $\boldsymbol{D}_c$ is invertible, the Lagrange multipliers $\boldsymbol{\lambda}_c$ can be explicitly calculated from Eq. (4.21). The underlying ODE is obtained by substituting the Lagrange multiplier in explicit form into the equation of motion. In general, constraints on acceleration level imply index 1 DAEs while constraints on velocity or position level yield index 2 and index 3 DAEs, respectively. The exploitation of the mechanical structure allows a numerical scheme that directly solves the index 1 DAE. Adding the constraint on acceleration level Eq. (4.21) to system (4.18) reveals the DAE of index 1

$$\begin{aligned}&\dot{\boldsymbol{q}} = \boldsymbol{u} \\ &\boldsymbol{M}(\boldsymbol{q})\dot{\boldsymbol{u}} = \boldsymbol{h}(\boldsymbol{q},\boldsymbol{u})+\boldsymbol{f}(\boldsymbol{q},\boldsymbol{u})+\boldsymbol{W}_c\boldsymbol{\lambda}_c \\ &\boldsymbol{c}(\boldsymbol{q},\boldsymbol{u},\boldsymbol{\lambda}_c) = \dot{\boldsymbol{\gamma}}_c(\boldsymbol{q},\boldsymbol{u},\dot{\boldsymbol{u}}) = \boldsymbol{W}_c^{\mathrm{T}}\dot{\boldsymbol{u}}+\boldsymbol{\chi}_c = 0;\end{aligned}$$

which is cast in linear matrix form as

$$\underbrace{\begin{bmatrix}\boldsymbol{I} & \boldsymbol{0} & \boldsymbol{0} \\ \boldsymbol{0} & \boldsymbol{M} & -\boldsymbol{W}_c \\ \boldsymbol{0} & \boldsymbol{W}_c^{\mathrm{T}} & \boldsymbol{0}\end{bmatrix}}_{\boldsymbol{A}}\begin{bmatrix}\dot{\boldsymbol{q}} \\ \dot{\boldsymbol{u}} \\ \boldsymbol{\lambda}_c\end{bmatrix} = \begin{bmatrix}\boldsymbol{u} \\ \boldsymbol{h}+\boldsymbol{f} \\ -\boldsymbol{\chi}_c\end{bmatrix}. \tag{4.22}$$

The square matrix $\boldsymbol{A}$ is of full rank as it can be transformed into the upper triangular matrix

$$\boldsymbol{A}^* = \begin{bmatrix}\boldsymbol{I} & \boldsymbol{0} & \boldsymbol{0} \\ \boldsymbol{0} & \boldsymbol{I} & -\boldsymbol{M}^{-1}\boldsymbol{W}_c \\ \boldsymbol{0} & \boldsymbol{0} & \boldsymbol{W}_c^{\mathrm{T}}\boldsymbol{M}^{-1}\boldsymbol{W}_c\end{bmatrix},$$

with a submatrix $\boldsymbol{A}_{33}^{*} = \boldsymbol{W}_c^{\mathrm{T}} \boldsymbol{M}^{-1} \boldsymbol{W}_c$, which is equal to the Delassus matrix $\boldsymbol{D}_c$ and thus of full rank if the constraints are linear independent. By solving Eq. (4.22) for each time step, any standard integrator for ordinary differential equations (e.g. the stiff integrator *ode15s* from MATLAB) can be utilized to obtain the solution of the constrained system. As the constraint is only forced to be fulfilled on acceleration level, the initial conditions must be admissible, i.e., they must be compatible with the associated constraints on position and velocity level. For the following simulations, the initial conditions from Table 3.1 are used, describing the perturbed spinning of the tippedisk in non-inverted configuration. This initial condition does not violate any of the following constraints.

Bilateral constraint

According to full model simulations from Chapter 3, the unilateral constraint expressing the impenetrability of the contact $g_N \geq 0$ remains persistent. It can therefore be replaced by a bilateral one

$$g_N(\boldsymbol{z}) = z - r\sin\beta = 0, \tag{4.23}$$

with the associated constraint force λ_N that prevent penetration of the contact point C.[1] Of course, this bilateral restriction does not apply to general motion of the tippedisk, but it is indeed fulfilled during the inversion process and is therefore not an approximation that contradicts physics. The equations of motion from Eq. (4.4) in reformulated coordinates $\boldsymbol{z}$ together with the bilateral constraint from Eq. (4.23) form a differential algebraic system

$$\begin{aligned} &\boldsymbol{M}(\boldsymbol{z})\ddot{\boldsymbol{z}} = \boldsymbol{h}(\boldsymbol{z},\dot{\boldsymbol{z}}) + \boldsymbol{f}_g + \boldsymbol{w}_N\lambda_N + \boldsymbol{W}_T\boldsymbol{\lambda}_T(\lambda_N,\boldsymbol{\gamma}_T), \\ &g_N(\boldsymbol{z}) = 0 \end{aligned}$$

with the generalized force directions $\boldsymbol{w}_N$ and $\boldsymbol{W}_T$ from Eq. (4.7) and Eq. (4.8), respectively. Since the bilateral constraint from Eq. (4.23) is formulated on position level, the DAE is of index 3. The generalized force direction in Eq. (4.7) equals the constraint Jacobian

$$\boldsymbol{w}_N = \left(\frac{\partial g_N(\boldsymbol{z})}{\partial \boldsymbol{z}}\right)^{\mathrm{T}},$$

which indicates that the associated Lagrange multiplier of the bilateral constraint is equal to the normal contact force λ_N. The tangential friction force

$$\boldsymbol{\lambda}_T(\lambda_N,\boldsymbol{\gamma}_T) = -\mu\lambda_N\frac{\boldsymbol{\gamma}_T}{\|\boldsymbol{\gamma}_T\| + \varepsilon}$$

---

[1] For better readability, the subscript notation is simplified to $C = C_1$ and $g_N(\boldsymbol{z}) := g_{N_1}(\boldsymbol{z})$.

from Eq. (3.33) depends linearly on the normal contact force λ_N. Differentiating the constraint Eq. (4.23), the velocity constraint

$$\gamma_N(\boldsymbol{z},\dot{\boldsymbol{z}}) = \frac{\partial g_N(\boldsymbol{z})}{\partial \boldsymbol{z}}\dot{\boldsymbol{z}} = \boldsymbol{w}_N^{\mathrm{T}}\dot{\boldsymbol{z}} = \dot{z} - r\dot{\beta}\cos\beta = 0 \tag{4.24}$$

is obtained. By replacing the constraint on position level with the constraint on velocity level, index reduction results in the DAE of index 2

$$\begin{aligned} \boldsymbol{M}(\boldsymbol{z})\ddot{\boldsymbol{z}} &= \boldsymbol{h}(\boldsymbol{z},\dot{\boldsymbol{z}}) + \boldsymbol{f}_g + \boldsymbol{w}_N\lambda_N + \boldsymbol{W}_T\boldsymbol{\lambda}_T(\lambda_N,\boldsymbol{\gamma}_T), \\ \gamma_N(\boldsymbol{q},\dot{\boldsymbol{z}}) &= \boldsymbol{w}_N^{\mathrm{T}}\dot{\boldsymbol{z}} = 0. \end{aligned} \tag{4.25}$$

Further time derivation of the constraint equation yields

$$\dot{\gamma}_N(\boldsymbol{z},\dot{\boldsymbol{z}},\ddot{\boldsymbol{z}}) = \boldsymbol{w}_N^{\mathrm{T}}\ddot{\boldsymbol{z}} + \dot{\boldsymbol{w}}_N^{\mathrm{T}}\dot{\boldsymbol{z}} = \ddot{z} - r\ddot{\beta}\cos\beta + r\dot{\beta}^2\sin\beta = 0,$$

making the DAE (4.25) an index 1 DAE

$$\begin{aligned} \boldsymbol{M}(\boldsymbol{z})\ddot{\boldsymbol{z}} &= \boldsymbol{h}(\boldsymbol{z},\dot{\boldsymbol{z}}) + \boldsymbol{f}_g + \boldsymbol{w}_N\lambda_N + \boldsymbol{W}_T\boldsymbol{\lambda}_T(\lambda_N,\boldsymbol{\gamma}_T), \\ \dot{\gamma}_N(\boldsymbol{z},\dot{\boldsymbol{z}},\ddot{\boldsymbol{z}}) &= \boldsymbol{w}_N^{\mathrm{T}}\ddot{\boldsymbol{z}} + \dot{\boldsymbol{w}}_N^{\mathrm{T}}\dot{\boldsymbol{z}} = 0. \end{aligned}$$

The introduction of the trivial velocity

$$\boldsymbol{u} := \dot{\boldsymbol{z}},$$

allows to reformulate the second-order differential equation to first-order form

$$\begin{aligned} \dot{\boldsymbol{z}} &= \boldsymbol{u} \\ \boldsymbol{M}(\boldsymbol{z})\dot{\boldsymbol{u}} &= \boldsymbol{h}(\boldsymbol{z},\boldsymbol{u}) + \boldsymbol{f}_g + \boldsymbol{w}_N\lambda_N + \boldsymbol{W}_T\boldsymbol{\lambda}_T(\lambda_N,\boldsymbol{\gamma}_T), \\ \dot{\gamma}_N(\boldsymbol{q},\boldsymbol{u},\dot{\boldsymbol{u}}) &= \boldsymbol{w}_N^{\mathrm{T}}\dot{\boldsymbol{u}} + \dot{\boldsymbol{w}}_N^{\mathrm{T}}\boldsymbol{u} = 0. \end{aligned}$$

Replacing the tangential contact force $\boldsymbol{\lambda}_T(\lambda_N,\boldsymbol{\gamma}_T)$ by the corresponding smooth Coulomb friction law yields the reformulated equation of motion

$$\boldsymbol{M}(\boldsymbol{z})\dot{\boldsymbol{u}} = \boldsymbol{h}(\boldsymbol{z},\boldsymbol{u}) + \boldsymbol{f}_g + \underbrace{\left(\boldsymbol{w}_N - \mu\boldsymbol{W}_T\frac{\boldsymbol{\gamma}_T}{\|\boldsymbol{\gamma}_T\| + \varepsilon}\right)}_{=:\boldsymbol{W}_{NT}}\lambda_N,$$

allowing to deduce the index 1 DAE in linear matrix form

$$\underbrace{\begin{bmatrix} \boldsymbol{I} & \boldsymbol{0} & \boldsymbol{0} \\ \boldsymbol{0} & \boldsymbol{M}(\boldsymbol{z}) & -\boldsymbol{W}_{NT} \\ \boldsymbol{0} & \boldsymbol{w}_N^{\mathrm{T}} & \boldsymbol{0} \end{bmatrix}}_{\boldsymbol{A}_0} \begin{bmatrix} \dot{\boldsymbol{z}} \\ \dot{\boldsymbol{u}} \\ \lambda_N \end{bmatrix} = \begin{bmatrix} \boldsymbol{u} \\ \boldsymbol{h}(\boldsymbol{z},\boldsymbol{u}) + \boldsymbol{f}_g \\ -\dot{\boldsymbol{w}}_N^{\mathrm{T}}\boldsymbol{u} \end{bmatrix} \tag{4.26}$$

depending on the coordinates $\boldsymbol{z}$, the velocities $\dot{\boldsymbol{z}}$, the accelerations $\dot{\boldsymbol{u}}$ as well as the normal force λ_N. The DAE given in Eq. (4.26) has the same structure as Eq. (3.88) with the same modeling assumptions, but different system coordinates, which is due to reparametrization in Section 4.1.

In general, the regularized Coulomb friction depends linearly on the normal contact force λ_N, rendering the matrix $\boldsymbol{A}_0$ asymmetric. Therefore, in principle, $\boldsymbol{A}_0$ is not guaranteed to be invertible. For nearly inverted and non-inverted spinning motions, the normal contact force is about equal to the weight of the disk, which motivates the approximation of a constant normal force $\lambda_N \approx mg$, motivating to simplify Eq. (4.26) to

$$\underbrace{\begin{bmatrix} \boldsymbol{I} & \boldsymbol{0} & \boldsymbol{0} \\ \boldsymbol{0} & \boldsymbol{M}(\boldsymbol{z}) & -\boldsymbol{w}_N \\ \boldsymbol{0} & \boldsymbol{w}_N^{\mathrm{T}} & 0 \end{bmatrix}}_{\boldsymbol{A}_1} \begin{bmatrix} \dot{\boldsymbol{z}} \\ \dot{\boldsymbol{u}} \\ \lambda_N \end{bmatrix} = \begin{bmatrix} \boldsymbol{u} \\ \boldsymbol{h}(\boldsymbol{z},\boldsymbol{u}) + \boldsymbol{f}_g + \boldsymbol{W}_T \boldsymbol{\lambda}_T \\ -\dot{\boldsymbol{w}}_N^{\mathrm{T}} \boldsymbol{u} \end{bmatrix} \tag{4.27}$$

with the adapted friction law

$$\boldsymbol{\lambda}_T = \begin{bmatrix} \lambda_{Tx} \\ \lambda_{Ty} \end{bmatrix} = -\mu m g \frac{\boldsymbol{\gamma}_T}{\|\boldsymbol{\gamma}_T\| + \varepsilon}. \tag{4.28}$$

Assuming that the normal force is constant in the friction law, the tangential friction force is independent of the constraint force λ_N, i.e., $\boldsymbol{\lambda}_T = \boldsymbol{\lambda}_T(\boldsymbol{z},\boldsymbol{u})$ holds. The resulting symmetric matrix $\boldsymbol{A}_1$ is structurally similar to the matrix $\boldsymbol{A}$ in Eq. (4.22), guaranteeing the solvability of Eq. (4.27).

Figure 4.3 shows the evolution of the angles β and γ during the inversion of the tippedisk starting from a perturbed non-inverted spinning solution, given in Table 3.1. The rolling angle γ (solid red and black dashed), starts from $\gamma_0 = -\pi/2 + 0.1\,\mathrm{rad}$ and increases in the interval $t \in [0\,\mathrm{s}, 0.5\,\mathrm{s}]$ until it converges at $\gamma = \pi/2$. During this first transient phase, the inclination angle β (blue, dotted) only changes slightly. Similar to previous results from Section 3.8, both inclination and rolling angles are superimposed with small oscillations occurring from $t \approx 0.5\,\mathrm{s}$. The solutions shown in color are obtained by solving the DAE of index 1 from Eq. (4.26), representing Model 1.1. These results are identical with respect to numerical errors to the simulation results of the ODE Model 2, presented in Figure 3.10. The solutions shown in black are obtained by assuming a constant normal force $\lambda_N \approx mg$, i.e., by combining Eq. (4.27) and the simplified friction law Eq. (4.28).

Comparison of the graphs in Figure 4.3 indicates that in the tangential friction law, the normal contact force λ_N can be assumed to be constant during inversion without significant impact on the qualitative and quantitative behavior. To be more

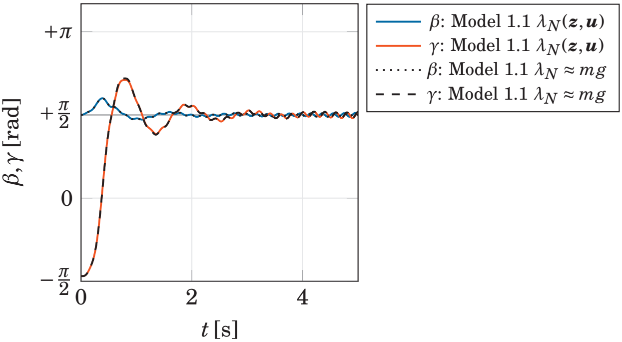

Figure 4.3: Simulation results for Model 1 with bilateral constrained contact point.

specific, the absolute differences $|\Delta\beta|$ and $|\Delta\gamma|$ are in the range of 10^{-2} rad. Neglecting the λ_N-dependence in the friction law allows to reduce the complexity of the system, by neglecting additional terms. For the sake of simplicity, the simplified friction law from Eq. (4.28) is used in the following.

COG constraint

A close look at the original system equations from Section 3.6 reveals that the dynamics (w.r.t the inertial I-frame) is not affected by the horizontal position of the disk. Moreover, only tangential friction forces act in horizontal direction, which depend on the relative sliding velocity at the contact point. Here, the relative sliding velocity can be decomposed into a part caused by horizontal translation and a part induced by angular velocities. Numerical simulations show that gyroscopic effects dominate the relative sliding velocity, therefore horizontal motion is negligible. This motivates the assumption of a horizontally fixed center of gravity, which is often used in the analysis of fast rotating rigid body systems in contact with a flat support [29, 66]. Experiments support this hypothesis as the disk drifts only slowly in the horizontal plane. On position level, the constraint that restricts horizontal motion of the COG

$$\boldsymbol{g}_S(\boldsymbol{z}) = \begin{bmatrix} \boldsymbol{e}_x^R \cdot \boldsymbol{r}_{OS} \\ \boldsymbol{e}_y^R \cdot \boldsymbol{r}_{OS} \end{bmatrix} = \begin{bmatrix} \bar{x} + e\cos\gamma \\ \bar{y} + e\cos\beta\sin\gamma \end{bmatrix} = 0$$

in terms of the transformed coordinates $\boldsymbol{z}$ from Eq. (4.1). This constraint equation implies the matrix

$$\boldsymbol{W}_S = \left(\frac{\partial \boldsymbol{g}_S(\boldsymbol{z})}{\partial \boldsymbol{z}}\right)^{\mathrm{T}} = \begin{bmatrix} 1 & 0 & 0 & 0 & 0 & -e\sin\gamma \\ 0 & 1 & 0 & 0 & -e\sin\beta\sin\gamma & +e\cos\beta\cos\gamma \end{bmatrix}^{\mathrm{T}}$$

of generalized force directions, which is used to reformulate the constraint on velocity level

$$\boldsymbol{\gamma}_S(\boldsymbol{z},\boldsymbol{u}) = \boldsymbol{W}_S^{\mathrm{T}}\boldsymbol{u} = 0. \tag{4.29}$$

Figure 4.4 shows the simulation results for the inversion process of Model 1.2, which assumes a bilaterally constrained contact point C, constant normal force scaling in the friction law, and a horizontally immobile center of gravity S. Qualitatively and quantitatively, the simulation results of Model 1.2 are very similar to the results of Model 1.1. However, the superimposed high-frequency oscillations present in Model 1.1 disappear in Model 1.2. The long-term behavior is strongly characterized by the dissipation and thus by the superimposed oscillations, cf. Figure 3.11. Nevertheless, on the short time scale, i.e., during the inversion of the tippedisk, these superimposed oscillations do not have any significant effects.

No tangential slip

The analysis in the following Chapter 5 reveals the singularly perturbed structure of the dynamical system. According to the slow-fast behavior the relative sliding velocity drops quickly to a small value, indicating slow motions that are close to pure rolling, characterized by a manifold of zero relative sliding velocity.

With the co-rotating R-frame introduced in Section 3.6, the projected relative velocity components $\gamma_x := \boldsymbol{e}_x^R \cdot \boldsymbol{v}_C$ and $\gamma_y := \boldsymbol{e}_y^R \cdot \boldsymbol{v}_C$ are defined as tangential and lateral sliding velocity, respectively. In order to graphically embed the the system dynamics in a three-dimensional state-space, the relative sliding velocity in tangential rolling direction, i.e., $\boldsymbol{e}_x^R$-direction, is assumed to vanish, implying the velocity constraint

$$\gamma_x(\boldsymbol{z},\boldsymbol{u}) = \boldsymbol{w}_x^{\mathrm{T}}\boldsymbol{u} = \boldsymbol{e}_x^R \cdot \boldsymbol{v}_C = 0, \tag{4.30}$$

where the force direction $\boldsymbol{w}_x$ corresponds to the first row of $\boldsymbol{W}_T$ from Eq. (4.8).

It is important to note that a model that assumes zero relative sliding velocity ($\boldsymbol{v}_C = 0$) in both the tangential and lateral directions does not describe the inversion phenomenon, since the disk is forced in a state of pure rolling motions. Similar behavior is observed in Figure 3.10 for Model 2, which assumes pure Coulomb friction. For the phenomenon of inversion, a slight sliding motion in at least one direction is essential.

Figure 4.4 shows the simulation results of Model 1.3 in blue assuming a bilateral constraint, a horizontally fixed center of gravity and zero relative velocity in rolling direction, cf. Table 4.1. Qualitatively, the simulation results of Model 1.3 are similar to Model 1.2.

Constant spinning velocity

For motion in the vicinity of stationary spinning solutions, the linearization of the system from Eq. (4.4) implies the constant spinning velocity $\dot{\alpha} = \Omega$. So assuming a permanent rotation with $\dot{\alpha} = \Omega$ is valid in the neighborhood of stationary spinning motions. Moreover, the simulation results of Model 1.1 show that the spinning velocity $\dot{\alpha}$ decreases by about 10%, indicating a nearly linear time evolution of the spinning angle α during the inversion process.

Constant spinning corresponds to the constraint on velocity level

$$\gamma_\alpha(\boldsymbol{z}, \boldsymbol{u}) = \boldsymbol{w}_\alpha^{\mathrm{T}} \boldsymbol{u} - \chi_\alpha = \dot{\alpha} - \Omega = 0, \tag{4.31}$$

with the associated generalized force direction

$$\boldsymbol{w}_\alpha = \begin{bmatrix} 0 & 0 & 0 & 1 & 0 & 0 \end{bmatrix}^{\mathrm{T}},$$

and the affine part $\chi_\alpha = \Omega = \text{const}$. Equation (4.31) corresponds to a holonomic constraint that yields in integrated form the associated rheonomic constraint equation

$$g_\alpha(\boldsymbol{z}, t) = \alpha(t) - \Omega t - \alpha_0 = 0$$

on position level, cf. [24]. The equations of motion (4.4) in reformulated coordinates $\boldsymbol{z}$ from Eq. (4.1) do not depend on the spinning angle α explicitly. For this reason, the initial spinning angle α_0 is set to zero without loss of generality.

From a physical point of view, the assumption of a constant spinning velocity $\dot{\alpha} = \Omega$ leads to energetic inconsistencies since a constant spinning speed implies a higher total energy level for the inverted spinning configuration than for non-inverted spinning at the same spinning speed. Form the perspective of dynamics, this assumption foliates the state-space with respect to one coordinate $\dot{\alpha}$, allowing to study a lower-dimensional subspace. Instead of assuming the spinning speed to be constant, the total energy could also be fixed. This would have resulted in a foliation of the state-space with more physical meaning since the total energy does not increase during the inversion. Nevertheless, the dissipation during inversion would be neglected. Since foliation in terms of total energy implies additional non-linear terms that complicate the analysis and do not really improve the energetic consistency, the spinning rate is assumed to be constant in the following. Moreover, this allows to treat the rotational velocity $\dot{\alpha} = \Omega$ as a bifurcation parameter of the system in accordance with the local stability analysis.

From an intuitive perspective, the spinning velocity is naturally assumed to be the bifurcation parameter, since the disk reverses its orientation if it is 'spun fast enough'.

Reduced system

Combining the bilateral constraint of the contact point (4.24), the assumption of a horizontal fixed center of gravity (4.29), zero tangential slip (4.30), and a constant spinning velocity (4.31) yields the constrained system

$$\begin{aligned}
&\dot{\boldsymbol{z}} = \boldsymbol{u} \\
&\boldsymbol{M}(\boldsymbol{z})\dot{\boldsymbol{u}} = \boldsymbol{h}(\boldsymbol{z},\boldsymbol{u}) + \boldsymbol{f}_g + \boldsymbol{w}_N\lambda_N + \boldsymbol{w}_y\lambda_{Ty} + \boldsymbol{W}_S\boldsymbol{\lambda}_S + \boldsymbol{w}_x\lambda_{Tx} + \boldsymbol{w}_\alpha\lambda_\alpha \\
&\dot{\gamma}_N(\boldsymbol{z},\boldsymbol{u},\dot{\boldsymbol{u}}) = 0 \\
&\dot{\boldsymbol{\gamma}}_S(\boldsymbol{z},\boldsymbol{u},\dot{\boldsymbol{u}}) = \boldsymbol{0} \\
&\dot{\gamma}_x(\boldsymbol{z},\boldsymbol{u},\dot{\boldsymbol{u}}) = 0 \\
&\dot{\gamma}_\alpha(\boldsymbol{z},\boldsymbol{u},\dot{\boldsymbol{u}}) = 0.
\end{aligned} \tag{4.32}$$

If all constraints are applied on acceleration level, the resulting DAE is of index 1 and can be written in linear matrix form

$$\underbrace{\begin{bmatrix} \boldsymbol{I} & \boldsymbol{0} & \boldsymbol{0} & \boldsymbol{0} & \boldsymbol{0} & \boldsymbol{0} \\ \boldsymbol{0} & \boldsymbol{M} & -\boldsymbol{w}_N & -\boldsymbol{W}_S & -\boldsymbol{w}_x & -\boldsymbol{w}_\alpha \\ \boldsymbol{0} & \boldsymbol{w}_N^{\mathrm{T}} & 0 & \boldsymbol{0} & 0 & 0 \\ \boldsymbol{0} & \boldsymbol{W}_S^{\mathrm{T}} & \boldsymbol{0} & \boldsymbol{0} & \boldsymbol{0} & \boldsymbol{0} \\ \boldsymbol{0} & \boldsymbol{w}_x^{\mathrm{T}} & 0 & \boldsymbol{0} & 0 & 0 \\ \boldsymbol{0} & \boldsymbol{w}_\alpha^{\mathrm{T}} & 0 & \boldsymbol{0} & 0 & 0 \end{bmatrix}}_{\boldsymbol{A}_{\mathrm{red}}} \begin{bmatrix} \dot{\boldsymbol{z}} \\ \dot{\boldsymbol{u}} \\ \lambda_N \\ \boldsymbol{\lambda}_S \\ \lambda_{Tx} \\ \lambda_\alpha \end{bmatrix} = \begin{bmatrix} \boldsymbol{u} \\ \boldsymbol{h} + \boldsymbol{f}_g + \boldsymbol{w}_y\lambda_{Ty} \\ -\dot{\boldsymbol{w}}_N^{\mathrm{T}}\boldsymbol{u} \\ -\dot{\boldsymbol{W}}_S^{\mathrm{T}}\boldsymbol{u} \\ -\dot{\boldsymbol{w}}_x^{\mathrm{T}}\boldsymbol{u} \\ -\dot{\boldsymbol{w}}_\alpha^{\mathrm{T}}\boldsymbol{u} \end{bmatrix}. \tag{4.33}$$

Since the applied constraints are linearly independent, the matrix $\boldsymbol{A}_{\mathrm{red}}$ is invertible, so the DAE from Eq. (4.33) can be solved numerically by explicit integration methods. However, this formulation on acceleration level can lead to drift problems and therefore to excessive constraint violation, e.g., penetration of the contact point. Furthermore, for a nonlinear analysis, an ordinary differential equation is advantageous.

In order to prevent constraint violation and to obtain an ODE description, a set of new minimal coordinates

$$\boldsymbol{x} = \begin{bmatrix} \beta \\ \gamma \end{bmatrix} \in \mathbb{R}^2 \tag{4.34}$$

is introduced such that $\boldsymbol{z} = \boldsymbol{z}(\boldsymbol{x})$ fulfills all constraints on position level

$$\begin{aligned} g_N(\boldsymbol{z}(\boldsymbol{x})) &\equiv 0 \ \forall \boldsymbol{x} \\ \boldsymbol{g}_S(\boldsymbol{z}(\boldsymbol{x})) &\equiv \boldsymbol{0} \ \forall \boldsymbol{x} \\ g_\alpha(\boldsymbol{z}(\boldsymbol{x})) &\equiv 0 \ \forall \boldsymbol{x} \end{aligned}$$

a priori. In addition, the new minimal velocity

$$y := \dot{\beta} \in \mathbb{R} \tag{4.35}$$

with associated kinematic equation

$$\boldsymbol{u} = \bar{\boldsymbol{B}}(\boldsymbol{x})y + \bar{\boldsymbol{\beta}}(\boldsymbol{x}, t),$$

is defined, where

$$\bar{\boldsymbol{B}}(\boldsymbol{z}) = \begin{bmatrix} 0 \\ e \sin\beta \sin\gamma \\ +r\cos\beta \\ 0 \\ 1 \\ 0 \end{bmatrix} \quad ; \quad \bar{\boldsymbol{\beta}}(\boldsymbol{x}, t) = \begin{bmatrix} -e\Omega\cos\beta\sin\gamma \\ +e\Omega\cos^2\beta\sin\gamma \\ 0 \\ \Omega \\ 0 \\ -\Omega\cos\beta \end{bmatrix}, \tag{4.36}$$

such that the velocity constraint

$$\gamma_x(\boldsymbol{z}(\boldsymbol{x}), \boldsymbol{u}(\boldsymbol{x}, y)) \equiv 0 \tag{4.37}$$

is intrinsically fulfilled for all $\boldsymbol{x}$ and for all y. The velocity constraint from Eq. (4.37) is non-integrable and therefore identified as a nonholonomic constraint [14, 15]. All constraints from (4.32) are said to be perfect in the sense of d'Alembert, as

$$\begin{aligned} \bar{\boldsymbol{B}}^{\mathrm{T}}\boldsymbol{w}_N &= 0 \\ \bar{\boldsymbol{B}}^{\mathrm{T}}\boldsymbol{W}_S &= \boldsymbol{0} \\ \bar{\boldsymbol{B}}^{\mathrm{T}}\boldsymbol{w}_x &= 0 \\ \bar{\boldsymbol{B}}^{\mathrm{T}}\boldsymbol{w}_\alpha &= 0 \end{aligned} \tag{4.38}$$

holds [93, 24]. With Equation (4.36), Eq. (4.38), Eq. (4.32) and the selection matrix

$$\boldsymbol{C} = \begin{bmatrix} 0 & 0 & 0 & 0 & 1 & 0 \\ 0 & 0 & 0 & 0 & 0 & 1 \end{bmatrix},$$

the reduced system

$$\begin{aligned} \dot{\boldsymbol{x}} &= \boldsymbol{C}\left(\bar{\boldsymbol{B}}(\boldsymbol{x})y + \bar{\boldsymbol{\beta}}(\boldsymbol{x},t)\right) \\ \bar{\boldsymbol{B}}^{\mathrm{T}}\boldsymbol{M}\bar{\boldsymbol{B}}\dot{y} &= \bar{\boldsymbol{B}}^{\mathrm{T}}\left(\boldsymbol{h}\left(\boldsymbol{z}(\boldsymbol{x}),\bar{\boldsymbol{B}}(\boldsymbol{x})y + \bar{\boldsymbol{\beta}}(\boldsymbol{x},t)\right) - \boldsymbol{M}(\dot{\bar{\boldsymbol{B}}}y + \dot{\bar{\boldsymbol{\beta}}})\right) + \bar{\boldsymbol{B}}^{\mathrm{T}}\boldsymbol{f}_g + \bar{\boldsymbol{B}}^{\mathrm{T}}\boldsymbol{w}_y\lambda_{Ty} \end{aligned}$$

is derived. This reduced system in minimal coordinates $\boldsymbol{x}$ and minimal velocities y forms a first-order ordinary differential equation of the form

$$\begin{aligned} \dot{\boldsymbol{x}} &= \boldsymbol{B}(\boldsymbol{x})y + \boldsymbol{\beta}(\boldsymbol{x},t) \\ M(\boldsymbol{x})\dot{y} &= h(\boldsymbol{x},y) + f_g(\boldsymbol{x}) + w_y(\boldsymbol{x})\lambda_{Ty}(\boldsymbol{x},y), \end{aligned} \tag{4.39}$$

with scalar mass matrix

$$M(\boldsymbol{x}) = A\cos^2\gamma + \bar{B}\sin^2\gamma + m(r + e\sin\gamma)^2\cos^2\beta, \tag{4.40}$$

scalar gyroscopic force term

$$\begin{aligned} h(\boldsymbol{x},y) = &+(A\cos^2\gamma + \bar{B}\sin^2\gamma)\Omega^2\sin\beta\cos\beta \\ &-2(A-\bar{B})\Omega\dot{\beta}\cos\beta\sin\gamma\cos\gamma \\ &+m(r+e\sin\gamma)^2\dot{\beta}^2\sin\beta\cos\beta \\ &+me(r+e\sin\gamma)\Omega^2\sin\beta\cos^3\beta\sin\gamma \\ &-me(r+e\sin\gamma)(3\sin^2\beta-2)\Omega\dot{\beta}\cos\beta\cos\gamma, \end{aligned} \tag{4.41}$$

generalized gravitational force

$$f_g(\boldsymbol{x}) = -mg(r + e\sin\gamma)\cos\beta \tag{4.42}$$

and generalized friction force $w_y\lambda_{Ty}$ with corresponding force direction

$$w_y(\boldsymbol{x}) = (r + e\sin\gamma)\sin\beta, \tag{4.43}$$

lateral sliding velocity

$$\gamma_y(\boldsymbol{x},y) = (r + e\sin\gamma)\sin\beta\dot{\beta} - e\Omega\sin^2\beta\cos\gamma \tag{4.44}$$

and constant scaled smooth Coulomb friction force

$$\lambda_{Ty}(\boldsymbol{x},y) = -\mu mg\frac{\gamma_y}{|\gamma_y| + \varepsilon}.$$

In Eqs. (4.40) and (4.41), the abbreviation $\bar{B} := B - me^2$ is introduced to shorten notation. Here, $\bar{B}$ corresponds to the second principal moment of inertia ${}_B\boldsymbol{\Theta}_S(2,2)$ with respect to the COG S. The kinematic part of (4.39) yields

$$\dot{\boldsymbol{x}} = \boldsymbol{B}(\boldsymbol{x})y + \boldsymbol{\beta}(\boldsymbol{x}, t) \tag{4.45}$$

with

$$\boldsymbol{B}(\boldsymbol{x}) = \begin{bmatrix} 1 \\ 0 \end{bmatrix} \quad \text{and} \quad \boldsymbol{\beta}(\boldsymbol{x}, t) = \begin{bmatrix} 0 \\ -\Omega \cos \beta \end{bmatrix}.$$

Both Eq. (4.33) and Eq. (4.39) describe the bilaterally constrained tippedisk with horizontally fixed center of gravity, zero slip condition in $\boldsymbol{e}_x^R$-direction and a constant spinning velocity, i.e., Model 1.4. Equation (4.33) constitutes a DAE of index 1, which can be solved numerically since all constraints are formulated on acceleration level. In contrast, Eq. (4.39) forms a first-order ordinary differential equation in minimal coordinates $\boldsymbol{x}$ and minimal velocities y satisfying the introduced constraints. Neglecting numerical drift, both approaches yield the same simulation results, which are shown in Figure 4.4 in yellow and black dashed, respectively.

Comparison

In the previous sections, several models on different modeling levels are derived by the application of additional constraints. These constraints are used to reduce the number of degrees of freedom, step by step, and to finally obtain a minimal model which qualitatively describes the inversion behavior of the tippedisk. In this section, the numerical solutions of all reduction stages are compared, starting from the initial conditions given in Table 3.1. The evolution of the rolling angle γ, the inclination angle β, and the spinning speed $\dot{\alpha}$ are shown in Figure 4.4 for Model 1.1-1.4.

The red graphs describe solutions of Model 1.1 under the assumption of a bilaterally constrained contact point. The green solutions correspond to Model 1.2 with the assumption of a bilateral constraint and a horizontally fixed center of gravity. The blue graph is obtained from the Model 1.3 simulations with an additional constraint on the tangential sliding velocity. Model 1.4 additionally assumes a constant spinning velocity and therefore directly implies a linear time dependency of the spinning angle α. The corresponding solutions are shown in yellow and dashed black and are obtained by the DAE description from Eq. (4.33) and the reduced ODE formulation from Eq. (4.39), respectively.

For all models, the rolling angle γ starts at $\gamma_0 = -\pi/2 + 0.1$ rad and quickly settles in a damped oscillation around $\gamma = \pi/2$. The inclination angle β remains close to $\pi/2$.

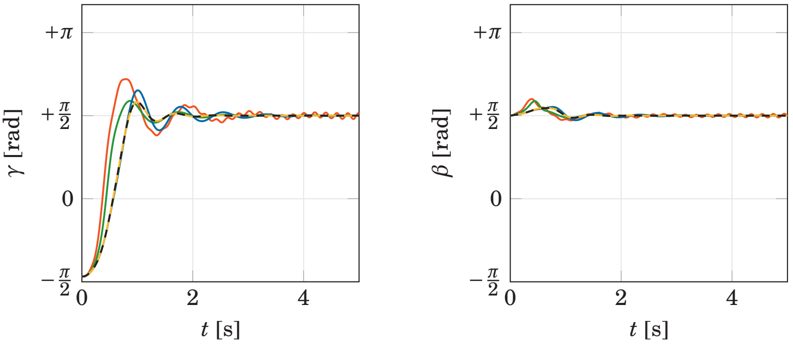

(a) Evolution of the rolling angle γ

(b) Evolution of the inclination angle β

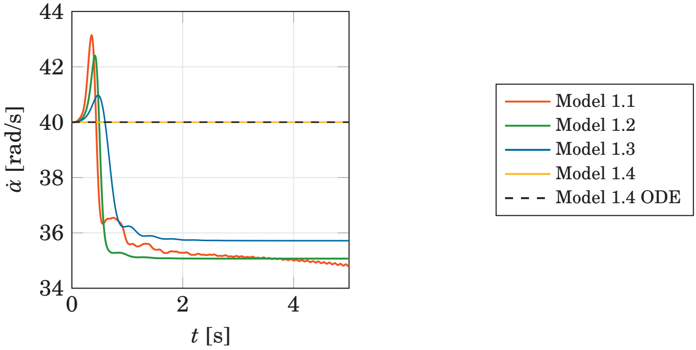

(c) Evolution of the spinning speed $\dot{\alpha}$

Figure 4.4: Comparison of different reduced order models listed in Table 4.1: The red graphs describe solutions of Model 1.1 under the assumption of a bilaterally constrained contact point. The green solutions correspond to Model 1.2 with the assumption of a bilateral constraint and a horizontally fixed center of gravity. The blue graph is obtained from the Model 1.3 with an additional constraint on the tangential sliding velocity. The yellow solutions correspond to results of Model 1.4 from Eq. (4.33), which assumes a constant spinning velocity $\dot{\alpha}$ and therefore implies directly a linear time dependency of α. In addition, the black dashed solutions follow from the reduced description of Model 1.4, cf. Eq. (4.39).

The qualitative behavior of all models is similar but differs slightly quantitatively. With increasing time, only Model 1.1 in red shows superimposed high-frequency oscillations of the inclination angle β and rolling angle γ, which are not present in the other models. It is also noted that the models with additional constraints overshoot less and converge faster to the inverted spinning solution. During the inversion, the corresponding spinning speed $\dot{\alpha}$ is depicted in Figure 4.2. For Models 1.1-1.3, the spinning velocity $\dot{\alpha}(t)$ drops slightly during the inversion from $\dot{\alpha}_0 = 40\,\mathrm{rad/s}$ to $\dot{\alpha} \approx 35\,\mathrm{rad/s}$. This drop in $\dot{\alpha}$ stems from the fact that the kinetic energy has to decrease when the potential energy rises during the inversion process. The exact decrease here depends on the respective model, but is in a similar order of magnitude. After the disk inverts its orientation, the rotational velocity $\dot{\alpha}$ remains nearly constant. In Model 1.4, the rotational velocity $\dot{\alpha}_0 = 40\,\mathrm{rad}$ is kept constant throughout the motion phase according to the constraint.

4.3 Linear stability analysis - 3 states

The reduced order model of the previous section given in Eq. (4.39) qualitatively describes the inversion behavior of the tippedisk. Similar to Section 4.1, a local stability analysis is performed first.

To study the behavior in the neighborhood of inverted spinning, the shifted angles $\bar{\beta}$ and $\bar{\gamma}$ are gathered in coordinates

$$\bar{\boldsymbol{x}} := \begin{bmatrix} \bar{\beta} \\ \bar{\gamma} \end{bmatrix} = \begin{bmatrix} \beta - \frac{\pi}{2} \\ \gamma - \frac{\pi}{2} \end{bmatrix}, \tag{4.46}$$

where the trivial equilibrium characterizes an inverted spinning motion. With $\bar{\beta} = \beta - \frac{\pi}{2}$, the shifted velocity $\bar{y} = \dot{\bar{\beta}} = \dot{\beta} = y$ follows by differentiation.

Linearizing Eq. (4.39) with respect to the shifted coordinates $\bar{\boldsymbol{x}}$ around the trivial equilibrium 'inverted spinning' gives the linear homogeneous system

$$\begin{bmatrix} \dot{\bar{\boldsymbol{x}}} \\ \dot{\bar{y}} \end{bmatrix} = \begin{bmatrix} \dot{\bar{\beta}} \\ \dot{\bar{\gamma}} \\ \ddot{\bar{\beta}} \end{bmatrix} = \begin{bmatrix} 0 & 0 & 1 \\ \Omega & 0 & 0 \\ A_{31} & A_{32} & A_{33} \end{bmatrix} \begin{bmatrix} \bar{\beta} \\ \bar{\gamma} \\ \dot{\bar{\beta}} \end{bmatrix} = \boldsymbol{A} \begin{bmatrix} \bar{\boldsymbol{x}} \\ \bar{y} \end{bmatrix} \tag{4.47}$$

with matrix coefficients

$$\begin{aligned} A_{31} &= \frac{mg}{\bar{B}}(r+e) - \Omega^2 = \mathcal{O}(1) \\ A_{32} &= -\frac{\mu m g}{\varepsilon \bar{B}} e (r+e)\Omega = \mathcal{O}\left(\tfrac{1}{\varepsilon}\right) \\ A_{33} &= -\frac{\mu m g}{\varepsilon \bar{B}} (r+e)^2 = \mathcal{O}\left(\tfrac{1}{\varepsilon}\right). \end{aligned} \tag{4.48}$$

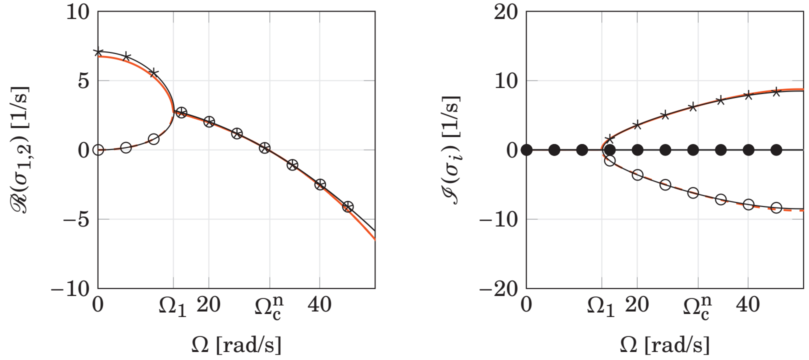

(a) real part $\mathscr{R}(\sigma_{1,2})$ (b) imaginary part $\mathscr{I}(\sigma_i)$

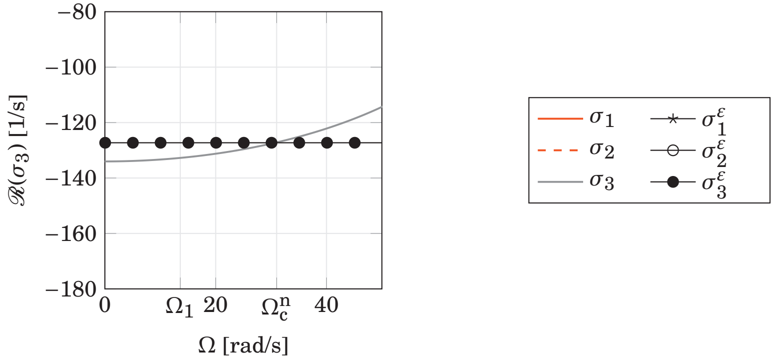

(c) real part $\mathscr{R}(\sigma_3)$

Figure 4.5: Eigenvalues for the inverted tippedisk for varying spinning velocity Ω.

Since the linear system (4.47) depends on the spinning speed and is autonomous, the corresponding eigenvalues directly characterize the stability of the inverted spinning depending on the bifurcation parameter Ω.

In Figure 4.5, the numerically calculated eigenvalues $\sigma_i \in \operatorname{eig}(\boldsymbol{A})$ of Eq. (4.47) are shown in color for $\Omega \in [0, 50\,\text{rad/s}]$. The upper left graph 4.5(a) shows the real parts $\mathscr{R}(\sigma_i)$ of the eigenvalues σ_1 and σ_2 in red while the lower left graph 4.5(c) contains the real part of the third eigenvalue σ_3 in gray. The upper right graph 4.5(b) displays the corresponding imaginary parts $\mathscr{I}(\sigma_i)$ of the eigenvalues $\sigma_{1,2,3}$. The third eigenvalue σ_3 is purely real and has a pronounced negative magnitude $\mathscr{R}(\sigma_3) < -100\,1/\mathrm{s}\ \forall\,\Omega \in [0, 50\,\mathrm{rad/s}]$. For $\Omega = 0$, the eigenvalues σ_1 and σ_2 are purely real and $\mathscr{R}(\sigma_1) > 0$, $\mathscr{R}(\sigma_2) = 0$ holds. As the spinning speed Ω increases, the eigenvalues σ_1 and σ_2 with positive real parts converge until they meet and form a complex conjugate pair at $\Omega_1 \approx 13.61\,\mathrm{rad/s}$. Increasing the spinning speed even further causes the red pair of complex conjugate eigenvalues $\sigma_{1,2}$ to enter the left half of the complex plane at the critical spinning velocity $\Omega_\mathrm{c}^\mathrm{n} \approx 31\,\mathrm{rad/s}$, which is determined numerically. For supercritical spinning speeds $\Omega > \Omega_\mathrm{c}^\mathrm{n}$ all eigenvalues have negative real part, so the inverted spinning equilibrium is locally asymptotically stable. For subcritical spinning speeds the equilibrium is unstable as σ_1 and σ_2 have a positive real part. With a pair of complex conjugate eigenvalues changing the sign of their real part at Ω_c, the stability boundary is characterized by a Hopf bifurcation. Due to the complexity of the system from Eq. (4.47), determining the eigenvalues $\sigma_{1,2,3}$ in closed-form is hardly feasible. However, the smoothing parameter $\varepsilon \ll 1$ is small, which motivates an asymptotic expansion to approximate the eigenvalues. Using the Laplace expansion, the characteristic polynomial $p(\sigma)$ yields

$$\begin{aligned} p(\sigma) &= \det(\boldsymbol{A} - \sigma \boldsymbol{I}) \\ &= (-\sigma)(-\sigma(A_{33} - \sigma)) + (+1)(A_{32}\Omega + A_{31}\sigma) \\ &= -\sigma^3 + A_{33}\sigma^2 + A_{31}\sigma + A_{32}\Omega \overset{!}{=} 0. \end{aligned} \tag{4.49}$$

Since the linear first-order system from Eq. (4.47) is three-dimensional, there is at least one purely real eigenvalue (here σ_3), so the characteristic polynomial takes the most general form

$$\begin{aligned} p(\sigma) &= (a - \sigma)(\sigma^2 + b\sigma + c) \\ &= -\sigma^3 + (a - b)\sigma^2 + (ab - c)\sigma + ac \overset{!}{=} 0. \end{aligned} \tag{4.50}$$

The comparison of coefficients from Eqs. (4.49) and (4.50) yields with Eq. (4.48) the constants

$$\begin{aligned} A_{31} &= ab - c \\ A_{32} &= \frac{ac}{\Omega} \\ A_{33} &= a - b. \end{aligned} \tag{4.51}$$

Combining Eq. (4.48) and (4.51) gives the orders of magnitude

$$a = \mathscr{O}\left(\frac{1}{\varepsilon}\right), \quad c = \mathscr{O}(1), \quad b = \mathscr{O}(\varepsilon),$$

implying for $\varepsilon \ll 1$ the polynomial coefficients

$$\begin{aligned}
a &\rightarrow A_{33} = -\frac{\mu m g}{\varepsilon \bar{B}}(r+e)^2 \\
c &\rightarrow \frac{A_{32}}{A_{33}}\Omega = \frac{e}{r+e}\Omega^2 \\
b &\rightarrow \frac{1}{a}(A_{31}+c) = -\frac{\varepsilon}{\mu}\left(\frac{1}{(r+e)} - \frac{r\bar{B}}{mg(r+e)^3}\Omega^2\right).
\end{aligned}$$

According to the polynomial decomposition from Eq. (4.50), the purely real eigenvalue is approximated by

$$\sigma_3^\varepsilon = a = A_{33} + \mathcal{O}(\varepsilon) = -\frac{\mu m g}{\varepsilon \bar{B}}(r+e)^2 + \mathcal{O}(\varepsilon) \approx -129.04\,\tfrac{1}{\mathrm{s}}. \tag{4.52}$$

Solving the quadratic polynomial factor $\sigma^2 + b\sigma + c = 0$ results in the approximation

$$\sigma_{1,2}^\varepsilon = \frac{-b \pm \sqrt{b^2 - 4c}}{2} \tag{4.53}$$

of $\sigma_{1,2}$. Equations (4.52) and (4.53) approximate the eigenvalues $\sigma_{1,2,3}$ of the linear system (4.47) in closed-form assuming a small smoothing parameter ε. In Figure 4.5, the approximated eigenvalues $\sigma_{1,2,3}^\varepsilon$ are depicted in black. The asymptotic expansion yields a good approximation of $\sigma_{1,2}$. The real eigenvalue σ_3 is approximately constant with average magnitude of $\sigma_3^\varepsilon \approx -129.04\,\tfrac{1}{\mathrm{s}}$.

In order to obtain a closed-form expression of the critical spinning speed Ω_c, the approximation Eq. (4.53) is used together with the condition

$$\mathcal{R}(\sigma_{1,2}(\Omega_\mathrm{c})) = 0$$

of vanishing real parts at the Hopf bifurcation point. For $\varepsilon \ll 1$, the argument $b^2 - 4c$ of the root in Eq. (4.53) is negative, implying a nontrivial imaginary part. Therefore, the real part of $\sigma_{1,2}$ is zero if the coefficient b vanishes, i.e., if

$$b \approx -\frac{\varepsilon}{\mu}\left(\frac{1}{(r+e)} - \frac{r\bar{B}}{mg(r+e)^3}\Omega^2\right) = 0 \tag{4.54}$$

holds. From Eq. (4.54) the approximation of the critical spinning speed

$$\Omega_\mathrm{c} = \sqrt{\frac{(r+e)^2}{r}\frac{mg}{\bar{B}}} = 30.92\,\frac{\mathrm{rad}}{\mathrm{s}} \tag{4.55}$$

is deduced[2]. The numerically determined critical spinning velocity $\Omega_\mathrm{c}^\mathrm{n} \approx 31\,\frac{\mathrm{rad}}{\mathrm{s}}$ is close to the spinning velocity from Eq. (4.55), validating the approximation. The associated purely complex eigenvalues are given as

$$\sigma_{1,2} = \pm\mathrm{i}\sqrt{c} = \pm 6.9\mathrm{i}\,\frac{1}{\mathrm{s}},$$

matching the numerical result, cf. Figure 4.5(b).

At a Hopf bifurcation it is a priori known that a pair $\sigma_{1,2} = \pm i\omega$ of purely complex eigenvalues crosses the imaginary axis, yielding with the polynomial from Eq. (4.50) the characteristic equation

$$\mathrm{i}\omega^3 - A_{33}\omega^2 + \mathrm{i}A_{31}\omega + A_{32}\Omega = 0.$$

Setting both the real and imaginary parts to zero yields two decouples expressions

$$\mathscr{R}: \quad -A_{33}\omega^2 + A_{32}\Omega = \frac{\mu m g}{\varepsilon \bar{B}}\left((r+e)^2\omega^2 - e(r+e)\Omega^2\right) = 0 \tag{4.56}$$

$$\mathscr{I}: \quad \left(\omega^2 + A_{31}\right)\omega = \left(\omega^2 + \frac{mg}{\bar{B}}(r+e) - \Omega^2\right)\omega = 0. \tag{4.57}$$

The first expression (4.56) gives the natural frequency

$$\omega^2 = \frac{e}{r+e}\Omega^2, \tag{4.58}$$

which is inserted into the second expression (4.57) and subsequently solved for $\Omega = \Omega_\mathrm{c}$, yielding

$$\Omega_\mathrm{c}^2 = \frac{(r+e)^2}{r}\frac{mg}{\bar{B}}.$$

Therefore, the critical spinning speed Ω_c from Eq. (4.55) is exact and not only an approximation for small values of the smoothing parameter ε. Moreover, the critical spinning velocity does not depend on the friction coefficient μ or the smoothing parameter ε, i.e., the friction parameters do not affect the location of the Hopf bifurcation. Similarly, the necessary stability condition of the tippetop presented in [77] does not depend on the friction coefficient, see [73].

Comparison of local stability properties

In Section 4.1, a linear stability analysis is performed. Here the local stability properties of inverted and non-inverted spinning are studied. The associated eigenvalues are depicted in Figure 4.1 and Figure 4.2. Non-inverted spinning is unstable

---

[2] Alternatively, the condition $c = -A_{31}$ yields the same critical spinning speed, indicating the correct estimation of the orders $\mathcal{O}$ of the coefficients a, b and c, cf. [110].

because one eigenvalue has a distinct positive real part. For inverted spinning the eigenvalue analysis it is not so straightforward to draw conclusions. Although a pair of complex conjugate eigenvalues λ_1 and λ_2 enters the left half of the complex plane at Ω_{c_2}, there is a second pair of complex conjugate eigenvalues λ_5 and λ_6 that has a slightly positive real part. Strictly speaking, therefore, inverted spinning is also unstable. However, the eigenvalues have very different magnitudes of their real part. Motions on a fast time scale, e.g., the inversion of the tippedisk, are strongly characterized by eigenvalues with a large magnitude of their real part, i.e., eigenvalues $\lambda_{1,2}$ and $\lambda_{7,8}$. In the long-time behavior, the two eigenvalues $\lambda_{5,6}$ with slightly positive real part cause an instability of the inverted spinning solution. By introducing several reduction steps in Section 4.2, the dimension of the state-space is reduced without changing the qualitative system behavior.

Originally, the state-space of the full system given in Eq. (4.4) has dimension 12. Since the α- and z-dynamics decouple in the linearization, eight eigenvalues $\lambda_{1,\ldots,8}$ are left. By constraining the contact point and assuming a permanent rotation with $\dot{\alpha} = \Omega$, the decoupled dynamics in α and z vanishes. In the analysis of Section 4.1, the two pairs of complex-conjugate eigenvalues in green $\lambda_{3,4}$ and blue $\lambda_{5,6}$ appear to characterize rigid body motions related to the horizontal drift behavior of the tippedisk. By neglecting the horizontal motions of the COG, these pairs of eigenvalues are suppressed. The real eigenvalues $\lambda_{7,8}$ are associated with fast sliding motions of the disk and have a strongly negative real part. The assumption of zero slip in rolling direction renders the eigenvalue λ_7 obsolete. This reduction step is not fully motivated here, but is applied to obtain a three-dimensional system that can be depicted graphically. However, the perturbation analysis in Section 5.3 will show that the disk is attracted to a state of almost pure rolling motions during the inversion, justifying the rolling constraint as a valid approximation.

As a result of the reduction procedure, the linearization from Eq. (4.47) around the inverted spinning equilibrium of the reduced system (4.39) has a total of three eigenvalues σ_i. The comparison of Figure 4.1 and Figure 4.5 reveals the relations $\lambda_{1,2} \sim \sigma_{1,2}$ and $\lambda_8 \sim \sigma_3$ between the eigenvalues of the full and reduced systems, linearized around inverted spinning solutions. In summary, the reduced system focuses on the dynamics on a relatively short time scale and is thus suitable to study the inversion phenomenon.

4.4 Harmonic balance approximation

According to the local stability analysis of the previous Section 4.3, the stability of inverted spinning on the short time scale is strongly determined by a Hopf bifurcation. Since the Hopf bifurcation cannot be fully characterized by a linear eigenvalue analysis, a harmonic balance analysis is performed in this section to obtain closed-form expressions for the periodic solution and thus identify the nature of the Hopf bifurcation as sub- or supercritical.

In order to approximate the periodic solution in the neighborhood of inverted spinning, the shifted coordinates $\bar{\boldsymbol{x}}$ introduced in Eq. (4.46) are used to approximate the system equations. To classify the nature of the Hopf bifurcation, the system equations from Eq. (4.39) must be expanded at least up to cubic orders.

Using the trigonometric relations

$$\begin{aligned}
\sin\beta &= \cos\bar{\beta} = 1-\tfrac{1}{2}\bar{\beta}^2+\mathcal{O}(\bar{\beta}^4),\\
\cos\beta &= -\sin\bar{\beta} = -\bar{\beta}+\tfrac{1}{6}\bar{\beta}^3+\mathcal{O}(\bar{\beta}^5),\\
\sin\gamma &= \cos\bar{\gamma} = 1-\tfrac{1}{2}\bar{\gamma}^2+\mathcal{O}(\bar{\gamma}^4),\\
\cos\gamma &= -\sin\bar{\gamma} = -\bar{\gamma}+\tfrac{1}{6}\bar{\gamma}^3+\mathcal{O}(\bar{\gamma}^5),
\end{aligned}$$

and isolating quartic orders $\mathcal{O}(\|\bar{\boldsymbol{x}}\|^4)$ in the dynamics of Model 1.4, given in Eq. (4.39), yields the local approximation

$$\dot{\bar{\gamma}} = +\Omega\bar{\beta}+\mathcal{O}(|\bar{\beta}|^3), \tag{4.59}$$

of the second kinematic equation and the expansion of the equation of motion

$$\tilde{M}(\bar{\boldsymbol{x}})\,\ddot{\bar{\beta}} = \tilde{h}(\bar{\boldsymbol{x}},\dot{\bar{\boldsymbol{x}}})+\tilde{f}(\bar{\boldsymbol{x}},\dot{\bar{\boldsymbol{x}}})+\mathcal{O}(\|\bar{\boldsymbol{x}}\|^4), \tag{4.60}$$

which corresponds to a scalar second-order differential equation for the shifted inclination angle $\bar{\beta}$. The approximations of the mass matrix $\tilde{M}(\bar{\boldsymbol{x}})$ and vector of gyroscopic forces $\tilde{h}(\bar{\boldsymbol{x}},y)$ are derived as

$$\tilde{M}(\bar{\boldsymbol{x}}) = (A-\bar{B})\bar{\gamma}^2+\bar{B}+m(r+e)^2\bar{\beta}^2+\mathcal{O}(\|\bar{\boldsymbol{x}}\|^4)$$

and

$$\begin{aligned}
\tilde{h}(\bar{\boldsymbol{x}},\dot{\bar{\boldsymbol{x}}}) = {}&-\bar{B}\Omega^2\bar{\beta}+(\bar{B}-A)\Omega^2\bar{\beta}\bar{\gamma}^2+\left[\frac{2}{3}\bar{B}-me(r+e)\right]\Omega^2\bar{\beta}^3\\
&-2\left[A-\bar{B}+me(r+e)\right]\Omega\dot{\bar{\beta}}\bar{\beta}\bar{\gamma}-m(r+e)^2\dot{\bar{\beta}}^2\bar{\beta}+\mathcal{O}(\|\bar{\boldsymbol{x}}\|^4).
\end{aligned}$$

The external generalized force $\tilde{f} := \tilde{f}_g+\tilde{w}_y\lambda_{Ty}$ contains both the gravitational force

$$\tilde{f}_g = +mg(r+e)\bar{\beta}-\frac{1}{2}mge\bar{\beta}\bar{\gamma}^3-\frac{1}{6}mg(r+e)\bar{\beta}^3+\mathcal{O}(\|\bar{\boldsymbol{x}}\|^4)$$

and the frictional force

$$\begin{aligned}
\tilde{w}_y\lambda_{Ty} = -\frac{\mu mg}{\varepsilon}\Bigg[&-\Omega e\frac{4e+r}{6}\bar{\gamma}^3+(r+e)^2\dot{\bar{\beta}}-\frac{3}{2}\Omega e(r+e)\bar{\beta}^2\bar{\gamma}\\
&-(r+e)^2\dot{\bar{\beta}}\bar{\beta}^2+e(r+e)\Omega\bar{\gamma}-e(r+e)\dot{\bar{\beta}}\bar{\gamma}^2\Bigg]+\mathcal{O}(\|\bar{\boldsymbol{x}}\|^4),
\end{aligned}$$

where the smooth Coulomb friction is approximated by the linearized friction law

$$\lambda_{Ty} = -\frac{\mu m g}{\varepsilon}\gamma_y. \tag{4.61}$$

To facilitate the qualitative analysis and to obtain more compact expressions, the linearized Coulomb friction law from Eq. (4.61) is assumed below. This assumption does not affect the qualitative dynamical behaviour. Assuming a linear friction law may seem artificial at this point, but its validity will be shown in Section 5.3.

Inserting the harmonic ansatz

$$\begin{aligned}\bar{\beta} &= C\sin(\omega t) \\ \bar{\gamma} &= D\sin(\omega t + \varphi),\end{aligned} \tag{4.62}$$

with amplitudes C, D, angular frequency ω and phase φ into the kinematic relation Eq. (4.59) reveals after comparison of the coefficients

$$\varphi = \frac{\pi}{2} \quad \text{and} \quad D = -C\frac{\Omega}{\omega}. \tag{4.63}$$

With Equation (4.63) the harmonic ansatz from Eq. (4.62) is written in vectorial form

$$\hat{\boldsymbol{x}} = \begin{bmatrix} C\sin(\omega t) \\ -C\frac{\Omega}{\omega}\cos(\omega t)\end{bmatrix}.$$

Substituting this harmonic ansatz in the cubic approximated system (4.60) yields the balance

$$-\hat{M}(C,\omega)C\omega^2\sin(\omega t) = \hat{h}(C,\omega) + \hat{f}(C,\omega) + \mathcal{O}(C^4), \tag{4.64}$$

with mass matrix $\hat{M}(C,\omega) := \tilde{M}(\hat{\boldsymbol{x}})$, vector of gyroscopic forces $\hat{h}(C,\omega) := \tilde{h}(\hat{\boldsymbol{x}},\dot{\hat{\boldsymbol{x}}})$ and external forces $\hat{f}(C,\omega) := \tilde{f}(\hat{\boldsymbol{x}},\dot{\hat{\boldsymbol{x}}})$. Equation (4.64) contains higher orders of trigonometric expressions ($\cos^2(\omega t)$, $\sin^2(\omega t)$, ...). By applying trigonometric addition theorems

$$\begin{aligned}\sin(\omega t)\cos^2(\omega t) &= \frac{1}{4}\sin\omega t + \frac{1}{4}\sin 3\omega t \\ \sin^2(\omega t)\cos(\omega t) &= \frac{1}{4}\cos\omega t - \frac{1}{4}\cos 3\omega t \\ \sin^3(\omega t) &= \frac{3}{4}\sin\omega t - \frac{1}{4}\sin 3\omega t \\ \cos^3(\omega t) &= \frac{3}{4}\cos\omega t + \frac{1}{4}\cos 3\omega t,\end{aligned}$$

the exponents are shifted into the arguments, resulting in terms containing 3rd-order harmonics. Neglecting higher harmonics in Eq. (4.64), the balance of the first harmonics sin(ωt) and cos(ωt) yields

$$\sin(\omega t): \qquad C^2\kappa_1 + \left[\bar{B}\left(\Omega^2-\omega^2\right) - mg(r+e)\right] = 0, \tag{4.65}$$

$$\cos(\omega t): \qquad \frac{1}{4}C^2\frac{\kappa_2}{\omega} + (r+e)\left[e\frac{\Omega^2}{\omega} - (r+e)\omega\right] = 0 \tag{4.66}$$

with the parameters

$$\begin{aligned}\kappa_1 =& \frac{1}{4}\left[\bar{B} - 3A - 2me(r+e)\right]\Omega^2 - \frac{1}{2}m(r+e)^2\omega^2 \\ &+ \frac{1}{8}mge\frac{\Omega^2}{\omega^2} - \frac{1}{4}(\bar{B}-A)\frac{\Omega^4}{\omega^2} + \frac{1}{8}mg(r+e)\end{aligned}$$

and

$$\kappa_2 = -e\frac{r+4e}{2}\frac{\Omega^4}{\omega^2} + \frac{3}{2}e(r+e)\Omega^2 + (r+e)^2\omega^2. \tag{4.67}$$

Neglecting quadratic orders $\mathcal{O}(C^2)$ in Eq. (4.66) results in

$$\omega^2 = \frac{e}{r+e}\Omega^2 + \mathcal{O}(C^2),$$

where ω is equal to the natural frequency already found in Eq. (4.58) and thus the imaginary part of the critical eigenvalues $\sigma_{1,2} = \pm i\omega$. To classify the Hopf bifurcation, quadratic terms have to be considered, i.e., the above approximation is too restrictive. However, to approximate the solution up to higher-order terms, the correction term $\delta = \delta(C,\omega)$ is added to obtain the ansatz

$$\omega^2 = \frac{e}{r+e}\Omega^2 + \delta C^2 + \mathcal{O}(C^4). \tag{4.68}$$

Multiplying Eq. (4.70) with the factor 4ω and inserting Eq. (4.67) yields

$$C^2\left[-e\frac{r+4e}{2(r+e)}\frac{\Omega^4}{\omega^2} + \frac{3}{2}e\Omega^2 + (r+e)\omega^2\right] + 4\left[e\Omega^2 - (r+e)\omega^2\right] = 0,$$

into which the adapted ansatz (4.68) is substituted to obtain

$$C^2\left[-\frac{r+4e}{2}\Omega^2 + \frac{5}{2}e\Omega^2\right] - 4(r+e)\delta C^2 = \mathcal{O}(C^4). \tag{4.69}$$

From Eq. (4.69) the correction term δ is given by

$$\delta = -\frac{1}{8}\frac{r-e}{r+e}\Omega^2 + \mathcal{O}(C^2).$$

Together with Eq. (4.68), the natural frequency reads as

$$\omega^2 = \left(\frac{e}{r+e} - \frac{1}{8}\frac{r-e}{r+e}C^2\right)\Omega^2 + \mathcal{O}(C^4), \tag{4.70}$$

which solves Eq. (4.66) up to quartic orders $\mathcal{O}(C^4)$. Substitution of ω^2 into the balance of $\sin(\omega t)$ from Eq. (4.65) results in a quadratic function

$$C^2\kappa_1 + \left[\bar{B}\left(1 - \left(\frac{e}{r+e} - \frac{1}{8}\frac{r-e}{r+e}C^2\right)\right)\Omega^2 - mg(r+e)\right] = \mathcal{O}(C^4),$$

of the amplitude C, which is simplified to

$$C^2\left(\kappa_1(r+e) + \frac{1}{8}\bar{B}(r-e)\Omega^2\right) + \left[\bar{B}r\Omega^2 - mg(r+e)^2\right] = \mathcal{O}(C^4). \tag{4.71}$$

Solving Eq. (4.71) for the amplitude C in closed-form gives

$$C = 2\sqrt{\frac{e}{r+e}}\sqrt{-\frac{\bar{B}r\Omega^2 - mg(r+e)^2}{\chi\Omega^2 + mge(r+e)}} + \mathcal{O}(C^4), \tag{4.72}$$

where the constant

$$\chi := A(r-2e) - \bar{B}\frac{2r^2 + e(r+e)}{2(r+e)} = 1.31 \cdot 10^{-7}\,\mathrm{kgm}^3 \tag{4.73}$$

has been used to shorten the expression and is calculated taking into account the parameters of Table 2.1.

The solution given in Eq. (4.72) is real if the argument under the square root is greater than zero, implying the existence of a periodic solution with amplitude C. As $\chi > 0$ with the parameters of Table 2.1, the denominator $\chi\Omega^2 + mge(r+e)$ is positive for all spinning velocities Ω, such that a real-valued amplitude C exists if

$$\Omega \leq \sqrt{\frac{mg}{\bar{B}}\frac{(r+e)^2}{r}} = \Omega_{\mathrm{c}}. \tag{4.74}$$

This condition is consistent with the critical spinning speed derived in Eq. (4.55), since a periodic solution vanishes at the bifurcation point, i.e., when the spinning speed Ω is equal to the critical spinning velocity Ω_{c}. According to the eigenvalue analysis from Section 4.3, the inverted spinning equilibrium is unstable for sub-critical spinning speeds $\Omega < \Omega_{\mathrm{c}}$. Near the Hopf bifurcation, the above amplitude

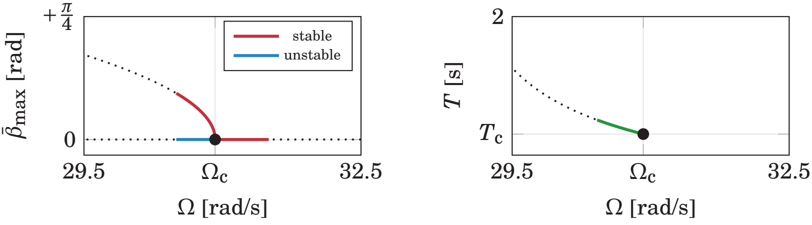

(a) Bifurcation diagram in $\bar{\beta}_{\max}$ (b) Period time T

Figure 4.6: Harmonic balance method (HBM) results obtained by local approximations around the Hopf bifurcation at Ω_c. The left bifurcation diagram shows the closed-form approximation of the supercritical Hopf bifurcation. The right plot depicts the period time T in dependency on the spinning speed Ω. For both plots, the extrapolations of the closed-form approximations are shown as a black dotted line.

condition (4.74) states the existence of a periodic solution for subcritical spinning speeds. The combination of both statements identifies the Hopf bifurcation at Ω_c as a supercritical[3] one. The angular frequency ω of the periodic solution is approximately given by

$$\omega = \Omega\sqrt{\frac{e}{r+e}\left(1+\frac{1}{2}\frac{(r-e)}{(r+e)}\frac{\bar{B}r\Omega^2 - mg(r+e)^2}{\chi\Omega^2 + mge(r+e)}\right)}, \tag{4.75}$$

which is obtained by substituting the amplitude from Eq. (4.72) into Eq. (4.70). The associated period time is given by $T = \frac{2\pi}{\omega}$. In particular, the period time $T_c = 0.886\,\mathrm{s}$ at the bifurcation point $\Omega = \Omega_c$ is deduced from Eq. (4.75) by inserting the critical spinning velocity given in Eq. (4.55). In Figure 4.6, the closed-form results of the harmonic balance method (HBM) are depicted. The left bifurcation diagram in Figure 4.6(a) depicts the $\bar{\beta}$-amplitude $\bar{\beta}_{\max}$ in dependency of the angular velocity Ω. In addition, the equilibrium associated with inverted spinning is represented by a horizontal line $\bar{\beta}_{\max} = 0$. For subcritical spinning speeds $\Omega \leq \Omega_c$, a stable periodic limit cycle (red) surrounds an unstable equilibrium (blue). The limit cycle vanishes at the bifurcation point Ω_c, which is characterized by a supercritical Hopf bifurcation. The right Figure 4.6(b) shows the associated period time T of the periodic limit

---

[3] The name *supercritical Hopf* is somewhat misleading, since the branch of stable periodic solutions exists for ‘subcritical’ spinning velocities $\Omega \leq \Omega_c$. Nevertheless, this terminology is common in the classic literature [68, 86] and characterizes a Hopf bifurcation for which a stable periodic solution exists around an unstable equilibrium.

cycle. The HBM approximation is truncated and is only valid for small values of C, i.e., in the neighborhood of the Hopf bifurcation. Therefore, the results in Figure 4.6 for larger amplitudes C are depicted by black dotted lines.

4.5 Continuation of periodic solutions

In the previous Section 4.3 and Section 4.4, the local behavior of inverted spinning was studied by a linearization and the harmonic balance method.

Approximations were made to obtain results in closed-form. In particular, near the Hopf bifurcation, the amplitude C is small, so that higher-order terms in the amplitude are neglected. Since the focus is on the first harmonic frequency, the higher harmonic oscillations can be neglected. According to these approximations, the presented results of the single harmonic balance approach have validity near the Hopf bifurcation when the amplitude C small, i.e., in the neighborhood $\Omega \approx \Omega_\mathrm{c}$. More accurate and global results could have been obtained with a multi-harmonic balance approach with local approximations of higher-order. However, this would not have been feasible in closed-form. To study the global dynamics, the periodic limit cycle is traced in dependency of the spinning speed Ω numerically.

The shooting method [86, 114] combined with a continuation method [3] is a popular approach to construct a numerical bifurcation diagram. For the tippedisk, a direct application of these classical numerical methods is not feasible because the singularly perturbed structure of the system (cf. Section 5.3) leads to an extremely stiff set of ordinary differential equations with multiple time scales. In particular, more elaborate variants such as the multiple shooting method and arclength continuation with variable step size are prone to convergence problems. To guarantee a robust continuation, single shooting in combination with sequential continuation is applied.

The aim of the classical shooting method is to find periodic solutions in dependency of a bifurcation parameter Ω. Using the periodicity condition, a two-point boundary value problem is formulated in terms of a zero-finding problem that can be solved by Newton-like methods. Sequentially changing the bifurcation parameter allows to track the periodic solution along the desired parameter range.

For a three-dimensional autonomous nonlinear system of the form

$$\dot{\boldsymbol{X}} = \boldsymbol{F}(\boldsymbol{X};\Omega) \in \mathbb{R}^3$$

depending on the bifurcation parameter Ω, each point $\boldsymbol{X}_0$ of a periodic limit cycle satisfies the periodicity condition with the three-dimensional residual

$$\boldsymbol{r}_{\mathrm{p}}(\boldsymbol{X}_0, T; \Omega) = \boldsymbol{\varphi}(\boldsymbol{X}_0, t_0 + T) - \boldsymbol{X}_0 = \int_{t_0}^{t_0+T} \boldsymbol{F}(\boldsymbol{X}(\tau); \Omega) \mathrm{d}\tau \in \mathbb{R}^3, \tag{4.76}$$

and the a priori unknown period time T. A periodic solution is thus characterized by an arbitrary point $\boldsymbol{X}_0 \in \mathbb{R}^3$ on the limit cycle and the associated period time $T \in \mathbb{R}$, i.e., in total by four unknown quantities. However, the periodicity condition from Eq. (4.76), which is a three-dimensional residual $\boldsymbol{r}_{\mathrm{p}}(\boldsymbol{X}_0, T; \Omega)$, yields only three integral equations. By introducing an additional equation in the form of a scalar anchor equation

$$0 = r_{\mathrm{a}}(\boldsymbol{X}_0, T; \Omega) \in \mathbb{R},$$

the two-point boundary value problem is complemented, which is formulated in terms of a zero-finding problem of the four-dimensional residual

$$\mathbf{0} \overset{!}{=} \boldsymbol{r}(\boldsymbol{X}_0, T; \Omega) := \begin{bmatrix} \boldsymbol{r}_{\mathrm{p}}(\boldsymbol{X}_0, T; \Omega) \\ r_{\mathrm{a}}(\boldsymbol{X}_0, T; \Omega) \end{bmatrix} \in \mathbb{R}^4. \tag{4.77}$$

A periodic limit cycle corresponds to a solution of the zero-finding problem with residual $\boldsymbol{r}(\boldsymbol{X}_0, T; \Omega) = \mathbf{0}$, which specifies a state $\boldsymbol{X}_0$ on the T-periodic solution. Any standard Newton-type algorithm can be used to solve the zero-finding problem of Eq. (4.77), starting with an initial guess $\left(\boldsymbol{X}_0^{(0)}, T_0^{(0)}\right)$ and, resulting in the converged solution $\left(\boldsymbol{X}_0^{(*)}, T_0^{(*)}\right)$. Since the residual $\boldsymbol{r}(\boldsymbol{X}_0, T; \Omega)$ implicitly depends on the bifurcation parameter Ω, the periodic limit cycle changes accordingly. The dependence on the bifurcation parameter can be studied by a sequential continuation procedure, where Ω_i is an element of the set $\mathscr{A} = \{\Omega_0, \Omega_1, ..., \Omega_n\}$ and the index $i \in \mathbb{N}$ is incremented step wise. Sequential continuation combines a predictor step, where the initial estimate $\left(\boldsymbol{X}_0^{(0),i}, T_0^{(0),i}\right)$ for a given Ω_i comes from the solution $\left(\boldsymbol{X}_0^{(*),i-1}, T_0^{(*),i-1}\right)$ of the shooting step at Ω_{i-1} with a subsequent corrector step, viz. the shooting procedure. This decoupling of predictor and following corrector step allows for a robust shooting continuation procedure.

By introducing the state vector

$$\boldsymbol{X} = \begin{bmatrix} \boldsymbol{x} \\ y \end{bmatrix} = \begin{bmatrix} \beta \\ \gamma \\ \dot{\beta} \end{bmatrix} \in \mathbb{R}^3 \tag{4.78}$$

the reduced dynamics of the tippedisk from Eq. (4.39) is rewritten into a three-dimensional autonomous nonlinear system

$$\dot{\boldsymbol{X}} = \boldsymbol{F}(\boldsymbol{X}; \Omega) \in \mathbb{R}^3, \tag{4.79}$$

Table 4.2: Initial guess for sequential continuation

Estimated quantity	Magnitude	Unit
$\bar{\beta}_0$	0	rad
$\bar{\gamma}_0$	1.69	rad
$\dot{\bar{\beta}}_0$	−1.72	rad/s
T_0	1.10	s

depending on the spinning speed Ω. Choosing the explicit anchor equation

$$r_a(\boldsymbol{X}_0, T; \Omega) = \beta_0 - \frac{\pi}{2} \in \mathbb{R},$$

which characterizes a vertically inclined disk, the periodicity condition of Eq. (4.76) is complemented to a four-dimensional residual of the form Eq. (4.77). The initial starting point of the shooting procedure is given for $\Omega_0 = \Omega_\mathrm{c} - 0.5\,\mathrm{rad/s}$ in Table 4.2. In a first sequential continuation step, the spinning speed Ω is increased step wise, according to the set

$$\mathscr{A}^\mathrm{in} = \left\{\Omega_{i+1} \in \mathbb{R} \middle| \Omega_{i+1} = \Omega_i + \left(\Omega_\mathrm{c} - \Omega_i\right)/100,\ i \in \mathscr{I}\right\},$$

with respect to the index set $\mathscr{I} = \{1, 2, \ldots, 400\}$. In a second step, the evolution of the periodic limit cycle for decreasing Ω is analyzed by defining the decreasing Ω-set

$$\mathscr{A}^\mathrm{de} = \left\{\Omega_{i+1} \in \mathbb{R} \middle| \Omega_{i+1} = \Omega_i + \left(\Omega_\mathrm{h} - \Omega_i\right)/100,\ i \in \mathscr{I}\right\}.$$

The spinning speed $\Omega_\mathrm{h} = 30.07\,\frac{\mathrm{rad}}{\mathrm{s}}$ corresponds to a heteroclinic spinning velocity found in a previous application of numerical shooting.

Both sets $\mathscr{A}^\mathrm{in}$ and $\mathscr{A}^\mathrm{de}$ are generated by convergent sequences, resulting in a fine resolution around the Hopf bifurcation Ω_c and a heteroclinic bifurcation Ω_h. Figure 4.7 shows the results of the considered shooting procedure. The diagram in Figure 4.7(a) depicts the bifurcation diagram with respect to the β-amplitude $\bar{\beta}_\mathrm{max}$. The right Figure 4.7(b) shows the corresponding period time T. For comparison, the closed-form solutions obtained by the harmonic balance approach from Figure 4.6 are depicted in black. Near the Hopf bifurcation, the results of the sequential shooting method are in accordance with the HBM approximations since a stable periodic solution exists for subcritical spinning velocities $\Omega < \Omega_\mathrm{c}$. However, as the distance to the Hopf bifurcation increases, the results diverge as the HBM approximation loses its validity. For decreasing spinning velocities, the periodic solution vanishes at $\Omega_\mathrm{h} = 30.07\,\frac{\mathrm{rad}}{\mathrm{s}}$ with corresponding period time $T_\mathrm{h} \to \infty$, which is later identified as a heteroclinic bifurcation in Section 5.3.

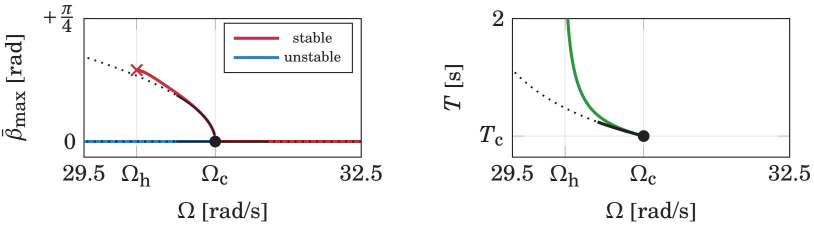

(a) Bifurcation diagram in $\bar{\beta}_{\mathrm{max}}$

(b) Period time T

Figure 4.7: Numerical results from the shooting continuation procedure. The left bifurcation diagram shows a heteroclinic bifurcation at Ω_{h}, where a stable periodic solution arises. This limit cycle collapses into the trivial equilibrium at the supercritical Hopf bifurcation at Ω_{c}. The right diagram shows the period time T of the associated limit cycle in dependency on the spinning speed Ω. For $\Omega \downarrow \Omega_{\mathrm{h}}$, the period time T diverges to infinity. The closed-form HBM approximation is shown in black for comparison.

In summary, the qualitative dynamics of the tippedisk from Section 2 is characterized by a heteroclinic bifurcation at Ω_{h}, at which a stable periodic limit cycle emerges that shrinks until it degenerates in a supercritical Hopf bifurcation at Ω_{c}.

CHAPTER 5

Slow-fast dynamics of the tippedisk

The eigenvalue analysis in Chapter 4 has shown that the dynamics of the tippedisk is governed by different time scales, which motivates to analyze the system behavior in the framework of slow-fast dynamics.

5.1 Basics of singular perturbation theory

Singular perturbation theory is a mathematical concept for studying problems involving multiple time scales. In a variety of physical and engineering applications, singularly perturbed system equations are induced by a small system parameter, causing slow-fast behavior. Singular perturbation theory provides a powerful set of tools to reduce and approximate the dynamic behavior. More detailed introductions can be found in [115, 131, 54, 48].

Basics of singular perturbation theory

In the context of dynamics, singular perturbation theory deals with systems of the form

$$\begin{aligned}\dot{\boldsymbol{x}} &= \boldsymbol{f}(t,\boldsymbol{x},\boldsymbol{y};\varepsilon)\\ \varepsilon\dot{\boldsymbol{y}} &= \boldsymbol{g}(t,\boldsymbol{x},\boldsymbol{y};\varepsilon),\end{aligned}$$

where $0 < \varepsilon \ll 1$ is a small and fixed perturbation parameter representing the ratio of time scales. It is assumed that both functions $\boldsymbol{f}$ and $\boldsymbol{g}$ are sufficiently smooth, which is a common assumption, cf. [67]. For the following application, this general framework is too broad as the reduced dynamics of the tippedisk is time autonomous [126]. To focus on the principal concepts in dense form, it suffices to consider autonomous singularly perturbed dynamics of the form

$$\begin{aligned} \dot{\boldsymbol{x}} &= \boldsymbol{f}(\boldsymbol{x},\boldsymbol{y};\varepsilon) \\ \varepsilon\dot{\boldsymbol{y}} &= \boldsymbol{g}(\boldsymbol{x},\boldsymbol{y};\varepsilon), \end{aligned} \tag{5.1}$$

where the time derivative $\dot{\bullet} := \frac{\mathrm{d}}{\mathrm{d}t}\bullet$ denotes the derivative with respect to the 'slow time' t, cf. [115]. The subsystem

$$\dot{\boldsymbol{x}} = \boldsymbol{f}(\boldsymbol{x},\boldsymbol{y};\varepsilon) \in \mathbb{R}^n$$

is called the slow subsystem corresponding to a differential equation of the slow states $\boldsymbol{x} \in \mathbb{R}^n$, while the fast subsystem is identified as

$$\varepsilon\dot{\boldsymbol{y}} = \boldsymbol{g}(\boldsymbol{x},\boldsymbol{y};\varepsilon) \in \mathbb{R}^m \tag{5.2}$$

with associated fast variable $\boldsymbol{y} \in \mathbb{R}^m$. By introducing the 'fast time' variable $\tau := t\,\varepsilon^{-1}$ and the associated derivative $\bullet' := \frac{\mathrm{d}}{\mathrm{d}\tau}\bullet$, the rescaled dynamical system is given by the differential equation

$$\begin{aligned} \boldsymbol{x}' &= \varepsilon\,\boldsymbol{f}(\boldsymbol{x},\boldsymbol{y};\varepsilon) \\ \boldsymbol{y}' &= \boldsymbol{g}(\boldsymbol{x},\boldsymbol{y};\varepsilon). \end{aligned} \tag{5.3}$$

The so-called critical dynamics is obtained by setting the perturbation parameter ε to zero. Since the perturbation parameter represents the ratio of the time scales, setting ε to zero reveals the separation of slow and fast time. Depending on the representation of the singular dynamics, the focus is on one of the two time scales. Setting the perturbation parameter ε in Eq. (5.1) to zero yields the critical system

$$\begin{aligned} \dot{\boldsymbol{x}} &= \boldsymbol{f}(\boldsymbol{x},\boldsymbol{y};0) \\ 0 &= \boldsymbol{g}(\boldsymbol{x},\boldsymbol{y};0), \end{aligned}$$

which governs the dynamics on the slow time scale t. The trajectories of this system are embedded in the so-called critical manifold, which (if the Jacobian $\frac{\partial \boldsymbol{g}}{\partial \boldsymbol{y}}$ is regular) can be represented by the canonical parametrization

$$\mathscr{M}_c := \left\{ (\boldsymbol{x},\boldsymbol{y}) \in \mathbb{R}^{n+m} \,\middle|\, \boldsymbol{y} = \boldsymbol{h}_c(\boldsymbol{x}),\ \boldsymbol{x} \in \mathbb{R}^n \right\},$$

where the function $\boldsymbol{h}_c$ is an isolated solution of the implicit function $\boldsymbol{g}(\boldsymbol{x},\boldsymbol{h}_c(\boldsymbol{x});0) = 0\ \forall \boldsymbol{x}$. As the n-dimensional critical manifold $\mathscr{M}_c$ governs the dependency of the fast variables $\boldsymbol{y}$ on the slow variables $\boldsymbol{x}$, the dynamics of the critical system is fully characterized by the reduced differential equation

$$\dot{\boldsymbol{x}} = \boldsymbol{f}(\boldsymbol{x}, \boldsymbol{h}_C(\boldsymbol{x}); 0), \tag{5.4}$$

where the focus is on the slow time scale t. In contrast, setting ε to zero in the rescaled dynamics of Eq. (5.3) yields the critical boundary layer system

$$\begin{aligned} \boldsymbol{x}' &= 0 \\ \boldsymbol{y}' &= \boldsymbol{g}(\boldsymbol{x}, \boldsymbol{y}; 0). \end{aligned}$$

Due to $\boldsymbol{x}' = 0$, the dynamics of the slow states $\boldsymbol{x}$ is suppressed. Therefore, the dynamics on the fast time scale τ is determined by the fast subsystem $\boldsymbol{y}' = \boldsymbol{g}(\boldsymbol{x}, \boldsymbol{y}; 0)$, where the slow states $\boldsymbol{x}$ take the role of parameters. Equilibria of the fast dynamics $\boldsymbol{y}' = \boldsymbol{g}(\boldsymbol{x}, \boldsymbol{y}; 0) = 0$, define a set of critical points, which implicitly relates the fast variables $\boldsymbol{y}$ to the 'states' $\boldsymbol{x}$, i.e., the fast variables are expressed as a function of the slow states $\boldsymbol{x}$. This set of critical points is represented by the critical manifold $\mathcal{M}_C$. In summary, the critical manifold $\mathcal{M}_C$ can be interpreted in two different ways: On the slow time scale t, the critical dynamics is restricted to $\mathcal{M}_C$, i.e., the fast variables $\boldsymbol{y} = \boldsymbol{h}_C(\boldsymbol{x})$ only depend on the slow variables $\boldsymbol{x}$ and the dynamics is given by Eq. (5.4). On the fast time scale τ, the critical manifold characterizes the set of all critical points of the boundary dynamics $\boldsymbol{y}' = \boldsymbol{g}(\boldsymbol{x}, \boldsymbol{y}; 0)$ in dependence on the 'constant' states $\boldsymbol{x}$.

The ultimate goal of singular perturbation theory is to understand the interaction of the slow and fast time scale. However, setting $\varepsilon = 0$ separates the time scales completely, yielding only a rough estimation. It is therefore essential to consider the singularly perturbed case $\varepsilon > 0$, with nonvanishing perturbation parameter. Assuming that $\boldsymbol{g}$ is a smooth enough function, whose Jacobian $\frac{\partial \boldsymbol{g}}{\partial \boldsymbol{y}}$ is regular, then the critical points $(\boldsymbol{x}, \boldsymbol{y})$ s.t. $\boldsymbol{g}(\boldsymbol{x}, \boldsymbol{y}; 0) = \boldsymbol{0}$ (i.e., any point on the critical manifold $\mathcal{M}_C$) are normal hyperbolic [35]. If the critical manifold $\mathcal{M}_C$ is assumed to satisfy this stability condition, Fenichel's first theorem [34, 60, 67] states that there exists an n-dimensional slow invariant manifold

$$\mathcal{M}_S := \left\{ (\boldsymbol{x}, \boldsymbol{y}) \in \mathbb{R}^{n+m} \,\middle|\, \boldsymbol{y} = \boldsymbol{h}_S(\boldsymbol{x}; \varepsilon),\ \boldsymbol{x} \in \mathbb{R}^n \right\},$$

being diffeomorphic to the critical manifold $\mathcal{M}_C$.

Exploiting its invariance, the shape of the slow manifold $\mathcal{M}_S$ is obtained through a perturbation technique. Inserting the fast variable as function $\boldsymbol{y} = \boldsymbol{h}_S(\boldsymbol{x}; \varepsilon)$ as well as the associated time derivative via chain rule $\dot{\boldsymbol{y}} = \frac{\partial \boldsymbol{h}_S}{\partial \boldsymbol{x}}\big|_{\boldsymbol{x};\varepsilon} \dot{\boldsymbol{x}}$ into the fast subsystem from Eq. (5.2), yields the implicit equation

$$\varepsilon \frac{\partial \boldsymbol{h}_S}{\partial \boldsymbol{x}}\bigg|_{\boldsymbol{x};\varepsilon} \boldsymbol{f}(\boldsymbol{x}, \boldsymbol{h}_S(\boldsymbol{x}); \varepsilon) = \boldsymbol{g}(\boldsymbol{x}, \boldsymbol{h}_S(\boldsymbol{x}); \varepsilon). \tag{5.5}$$

Substitution of the regular perturbation expansion

$$\boldsymbol{h}_s(\boldsymbol{x};\varepsilon) = \boldsymbol{h}_0(\boldsymbol{x}) + \varepsilon\,\boldsymbol{h}_1(\boldsymbol{x}) + \mathcal{O}(\varepsilon^2)$$

allows to expand Eq. (5.5) up to quadratic orders of $\mathcal{O}(\varepsilon^2)$ to

$$\varepsilon\frac{\partial \boldsymbol{h}_0}{\partial \boldsymbol{x}}\bigg|_{\boldsymbol{x}} \boldsymbol{f}(\boldsymbol{x},\boldsymbol{h}_0;0) = \boldsymbol{g}(\boldsymbol{x},\boldsymbol{h}_0;0) + \varepsilon\left[\frac{\partial \boldsymbol{g}}{\partial \varepsilon}\bigg|_{\boldsymbol{x},\boldsymbol{h}_0;0} + \frac{\partial \boldsymbol{g}}{\partial \boldsymbol{y}}\bigg|_{\boldsymbol{x},\boldsymbol{h}_0;0}\boldsymbol{h}_1\right] + \mathcal{O}(\varepsilon^2).$$

The equality must be valid for all orders of ε. Comparison of ε coefficients yields:

$$\varepsilon^0: \qquad \boldsymbol{0} = \boldsymbol{g}(\boldsymbol{x},\boldsymbol{h}_0;0) \tag{5.6}$$

$$\varepsilon^1: \qquad \frac{\partial \boldsymbol{h}_0}{\partial \boldsymbol{x}}\bigg|_{\boldsymbol{x}} \boldsymbol{f}(\boldsymbol{x},\boldsymbol{h}_0;0) = \frac{\partial \boldsymbol{g}}{\partial \varepsilon}\bigg|_{\boldsymbol{x},\boldsymbol{h}_0;0} + \frac{\partial \boldsymbol{g}}{\partial \boldsymbol{y}}\bigg|_{\boldsymbol{x},\boldsymbol{h}_0;0}\boldsymbol{h}_1 \tag{5.7}$$

$$\vdots$$

As the balance of zero-orders given in Eq. (5.6) corresponds to the implicit definition of the critical manifold, the critical manifold $\mathcal{M}_c$ is identified as the zero-order approximation of the slow manifold $\mathcal{M}_s$, i.e., $\boldsymbol{h}_0 = \boldsymbol{h}_c$ holds. With invertible Jacobian $\frac{\partial \boldsymbol{g}}{\partial \boldsymbol{y}}\big|_{\boldsymbol{x},\boldsymbol{h}_0;0}$, the balance of first-orders from Eq. (5.7) can be solved to obtain the function

$$\boldsymbol{h}_1(\boldsymbol{x}) = \frac{\partial \boldsymbol{g}}{\partial \boldsymbol{y}}\bigg|^{-1}_{\boldsymbol{x},\boldsymbol{h}_0(\boldsymbol{x});0}\left[\frac{\partial \boldsymbol{h}_0}{\partial \boldsymbol{x}}\bigg|_{\boldsymbol{x}} \boldsymbol{f}(\boldsymbol{x},\boldsymbol{h}_0(\boldsymbol{x});0) - \frac{\partial \boldsymbol{g}}{\partial \varepsilon}\bigg|_{\boldsymbol{x},\boldsymbol{h}_0(\boldsymbol{x});0}\right]. \tag{5.8}$$

Subsequent application of this procedure allows to derive $\boldsymbol{h}_2, \boldsymbol{h}_3, \ldots, \boldsymbol{h}_n$, yielding an approximation of the slow manifold $\mathcal{M}_s$ up to arbitrary orders $\mathcal{O}(\varepsilon^{n+1})$. Due to this identification, the system's slow dynamics on the n-dimensional slow manifold $\mathcal{M}_s$ is approximately given by

$$\begin{aligned} \boldsymbol{h}_s(\boldsymbol{x};\varepsilon) &\approx \boldsymbol{h}_0(\boldsymbol{x}) + \varepsilon\,\boldsymbol{h}_1(\boldsymbol{x}) \\ \dot{\boldsymbol{x}} &= \boldsymbol{f}\,(\boldsymbol{x},\boldsymbol{h}_s(\boldsymbol{x};\varepsilon);\varepsilon)\,, \end{aligned} \tag{5.9}$$

neglecting orders $\mathcal{O}(\varepsilon^2)$. While the slow dynamics Eq. (5.9) governs the slow invariant behavior of solutions on the slow manifold $\mathcal{M}_s$, the full singularly perturbed system (5.1) also contains fast dynamics. To study the asymptotic behavior on the fast time scale, the 'distance' function

$$\boldsymbol{d} := \boldsymbol{y} - \boldsymbol{h}_s(\boldsymbol{x};\varepsilon)$$

is introduced. If the distance function is zero, the solution is on the slow manifold, i.e., $\boldsymbol{d} = 0 \Leftrightarrow \boldsymbol{y} \in \mathcal{M}_s$. The distance dynamics on the fast time scale yields

$$\boldsymbol{d}' = \boldsymbol{y}' - \frac{\partial \boldsymbol{h}_s}{\partial \boldsymbol{x}}\boldsymbol{x}' = \boldsymbol{y}' + \mathcal{O}(\varepsilon) = \boldsymbol{g}(\boldsymbol{x},\boldsymbol{d} + \boldsymbol{h}_s(\boldsymbol{x};\varepsilon);\varepsilon) + \mathcal{O}(\varepsilon)$$

and characterizes the asymptotic behavior. Near the slow manifold $\mathscr{M}_s$, the distance dynamics is approximately described by the linearization

$$\boldsymbol{d}' = \underbrace{\boldsymbol{g}(\boldsymbol{x},\boldsymbol{h}_0(\boldsymbol{x}),0)}_{=0} + \frac{\partial \boldsymbol{g}}{\partial \boldsymbol{y}}\Big|_{\boldsymbol{x},\boldsymbol{h}_0;0} \boldsymbol{d} + \mathscr{O}(\varepsilon) = \frac{\partial \boldsymbol{g}}{\partial \boldsymbol{y}}\Big|_{\boldsymbol{x},\boldsymbol{h}_0;0} \boldsymbol{d} + \mathscr{O}(\varepsilon),$$

around $\boldsymbol{d} = 0$. Following Lyapunov's indirect method, the slow manifold is locally attractive if the Jacobian $\frac{\partial \boldsymbol{g}}{\partial \boldsymbol{y}}\big|_{\boldsymbol{x},\boldsymbol{h}_0;0}$ is Hurwitz [63]. If this stability criterion is satisfied, solutions of the full system converge on the fast time scale τ, i.e., they seem to 'jump' with respect to the slow time t onto the slow manifold $\mathscr{M}_s$. The asymptotic behavior of the full system is then governed by the lower dimensional system from Eq. (5.9). If the slow manifold $\mathscr{M}_s$ is attractive, the slow-fast behavior implies the model reduction

$$\left.\begin{aligned} \dot{\boldsymbol{x}} &= \boldsymbol{f}(\boldsymbol{x},\boldsymbol{y};\varepsilon) \\ \varepsilon\dot{\boldsymbol{y}} &= \boldsymbol{g}(\boldsymbol{x},\boldsymbol{y};\varepsilon) \end{aligned}\right\} \in \mathbb{R}^{n+m} \quad \rightarrow \quad \dot{\boldsymbol{x}} = \boldsymbol{f}(\boldsymbol{x},\boldsymbol{h}_s(\boldsymbol{x};\varepsilon);\varepsilon) \in \mathbb{R}^n,$$

where the 'slow' evolution of the fast variables is determined by the slave dynamics

$$\dot{\boldsymbol{y}} = \frac{\partial \boldsymbol{h}_s}{\partial \boldsymbol{x}} \boldsymbol{f}(\boldsymbol{x},\boldsymbol{h}_s(\boldsymbol{x};\varepsilon);\varepsilon) \in \mathbb{R}^m.$$

This allows the dimension of the system to be naturally reduced according to its asymptotic behavior.

5.2 Fundamentals of the Melnikov function method

The origin of Melnikov theory was laid in the 20th century by MELNIKOV [80] and is in general concerned with finding conditions for chaotic dynamics, cf. [131]. In this work, the singularly perturbed structure is used to analyze the tippedisk. The following analysis shows that the asymptotic dynamics of the tippedisk describing the inversion phenomenon is mainly governed by a two-dimensional and autonomous system. Therefore, chaotic behavior cannot be observed. However, the Melnikov function method can be applied for finding heteroclinic bifurcations of autonomous perturbed Hamiltonian systems. The following section serves as a short introduction to the Melnikov function method [131].

In general, a perturbed Hamiltonian dynamical system is a system of the form

$$\begin{aligned} \dot{\boldsymbol{q}} &= \frac{\partial \mathscr{H}}{\partial \boldsymbol{p}} + \varepsilon \boldsymbol{f}(\boldsymbol{q},\boldsymbol{p}) + \mathscr{O}(\varepsilon^2), \\ \dot{\boldsymbol{p}} &= -\frac{\partial \mathscr{H}}{\partial \boldsymbol{q}} + \varepsilon \boldsymbol{g}(\boldsymbol{q},\boldsymbol{p}) + \mathscr{O}(\varepsilon^2), \end{aligned} \tag{5.10}$$

with Hamiltonian $\mathscr{H}(\boldsymbol{q},\boldsymbol{p})$ in canonical coordinates $(\boldsymbol{q},\boldsymbol{p})$, i.e., generalized positions $\boldsymbol{q} \in \mathbb{R}^n$ and generalized momenta $\boldsymbol{p} \in \mathbb{R}^n$. Here, the perturbation parameter ε is assumed to be small and positive. Setting the perturbation parameter ε in Eq. (5.10) to zero reveals the Hamiltonian structure

$$\begin{aligned} \dot{\boldsymbol{q}} &= \frac{\partial \mathscr{H}}{\partial \boldsymbol{p}}, \\ \dot{\boldsymbol{p}} &= -\frac{\partial \mathscr{H}}{\partial \boldsymbol{q}}, \end{aligned} \tag{5.11}$$

of the critical system. Since the perturbation parameter is small, higher-order perturbations $\mathscr{O}(\varepsilon^2)$ are neglected in Eq. (5.10). Occasionally in literature, it is assumed that the Hamiltonian $\mathscr{H} = \mathscr{H}_0 + \varepsilon \mathscr{H}_1 + \mathscr{O}(\varepsilon^2)$ of the system is regularly perturbed, cf. [54, 131, 98]. For the following application of the Melnikov function method to find saddle connections (i.e., heteroclinic or homoclinic orbits), however, this assumption is too restrictive.

A scalar function $\mathscr{C} : \mathbb{R}^{2n} \to \mathbb{R}$ with

$$\begin{pmatrix} \boldsymbol{q} \\ \boldsymbol{p} \end{pmatrix} \mapsto \mathscr{C}(\boldsymbol{q},\boldsymbol{p})$$

is called a conserved quantity if its time derivative vanishes for all generalized positions $\boldsymbol{q}$ and momenta $\boldsymbol{p}$:

$$\dot{\mathscr{C}}(\boldsymbol{q},\boldsymbol{p}) = \frac{\partial \mathscr{C}}{\partial \boldsymbol{q}} \dot{\boldsymbol{q}} + \frac{\partial \mathscr{C}}{\partial \boldsymbol{p}} \dot{\boldsymbol{p}} = 0$$

under the flow of the Hamiltonian system given in Eq. (5.11). Substituting the critical Hamiltonian dynamics and introducing the Poisson bracket $\{\cdot,\cdot\}$ indicates that for a conserved quantity $\mathscr{C}$, the Poisson bracket

$$\{\mathscr{C},\mathscr{H}\} := \frac{\partial \mathscr{C}}{\partial \boldsymbol{q}} \frac{\partial \mathscr{H}}{\partial \boldsymbol{p}} - \frac{\partial \mathscr{C}}{\partial \boldsymbol{p}} \frac{\partial \mathscr{H}}{\partial \boldsymbol{q}} = 0 \tag{5.12}$$

of $\mathscr{C}$ and $\mathscr{H}$ must vanish. In particular, the Hamiltonian $\mathscr{H}$ is a conserved quantity itself as $\{\mathscr{H},\mathscr{H}\} = 0$.

The critical Hamiltonian system from Eq. (5.11) may have a heteroclinic saddle connection Γ_c connecting two saddle equilibria [53]. Such a heteroclinic saddle connection may be expressed as a one-parametric integral curve

$$\begin{aligned} \Gamma_c^t : [-\infty, +\infty] &\to \mathbb{R}^{2n} \\ t &\mapsto \begin{pmatrix} \boldsymbol{q}_c(t) \\ \boldsymbol{p}_c(t) \end{pmatrix} \end{aligned}$$

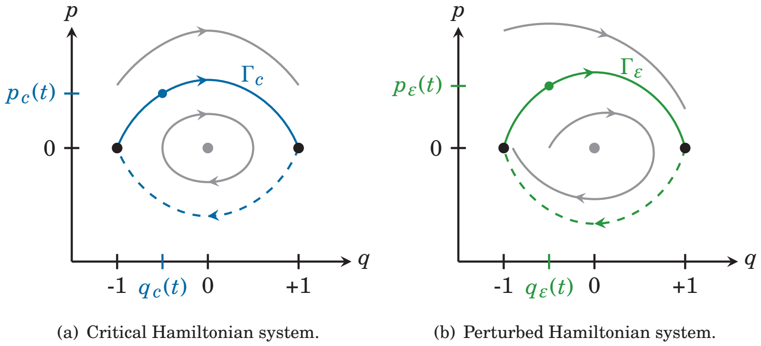

(a) Critical Hamiltonian system. (b) Perturbed Hamiltonian system.

Figure 5.1: Heteroclinic orbits connecting the 'left' $(-1,0)$ and the 'right' $(+1,0)$ saddle equilibria. The left Figure 5.1(a) shows two heteroclinic saddle connections of the critical Hamiltonian system that exist for all $\Omega \in \mathbb{R}$. The right Figure 5.1(b) depicts two heteroclinic saddle connections of the perturbed Hamiltonian system existing only for a specific parameter value $\Omega = \Omega_{\mathrm{h}}$.

with two saddle equilibria at $\Gamma_c^t(-\infty)$ and $\Gamma_c^t(+\infty)$. Instead of parametrizing the curve by time t, it is common to introduce a master coordinate q_1 that induces another parametrization of the heteroclinic saddle connection. Transformations can be applied to obtain a master coordinate so that the saddle equilibria are at $q_1 = \mp 1$. In particular, if $\dot{q}_1(t) > 0$ along Γ_c, then the mapping $\phi : t \mapsto q_1$ is strictly monotone and the integral curve Γ_c is parametrized by

$$\begin{aligned} \Gamma_c^q : [-1,+1] &\to \mathbb{R}^{2n} \\ q_1 &\mapsto \begin{pmatrix} \boldsymbol{q}_c(q_1) \\ \boldsymbol{p}_c(q_1) \end{pmatrix}. \end{aligned} \tag{5.13}$$

In order to increase readability, the abbreviation $\boldsymbol{q}_c(q_1) := \boldsymbol{q}_c(\phi^{-1}(q_1))$ has been used. In Figure 5.1(a), two heteroclinic saddle connections are shown in blue. Here, the upper saddle connection is described by the parametric curve Γ_c which may be parametrized with respect to the master coordinate q_1. For any conserved quantity $\mathscr{C}$, the function $\mathscr{C}_{\mathrm{h}}(q_1) = \mathscr{C}(\boldsymbol{q}_c(q_1), \boldsymbol{p}_c(q_1))$ takes the same value for every point on the saddle connection. If $\frac{\partial \mathscr{C}}{\partial q_1}$ is invertible on Γ_c^q, then the implicit function theorem allows to find the generalized momenta $\boldsymbol{p}_c$ and the generalized coordinates $\boldsymbol{q}_c$ as a function depending on the master coordinate q_1.

Suppose that the Hamiltonian system (5.11) depends on a system parameter Ω that affects the Hamiltonian $\mathscr{H}$ and hence changes the shape of the heteroclinic connection Γ_c, but not its existence. Moreover, it is assumed that variations of Ω do not alter the locations $(\boldsymbol{q}(q_1), \boldsymbol{p}) = (\boldsymbol{q}(\mp 1), 0)$ of the saddle equilibria. Perturbing the dynamics in form of Eq. (5.10) by adding terms, the system becomes non-Hamiltonian, and the heteroclinic connection may cease to exist for any value of the parameter Ω. However, there may be specific values $\Omega = \Omega_\mathrm{h}$ where the heteroclinic saddle connection may be present, cf. Figure 5.1(b).

The goal of the Melikov function method is to find an approximate necessary criterion for the existence of a heteroclinic connection depending on the non-zero perturbation parameter ε and the system parameter Ω.

A heteroclinic saddle connection Γ_ε of a perturbed Hamiltonian system (5.10) may be parametrized with respect to time t by

$$\begin{aligned}\Gamma_\varepsilon^t : [-\infty, +\infty] &\rightarrow \mathbb{R}^{2n} \\ t &\mapsto \begin{pmatrix} \boldsymbol{q}_\varepsilon(t) \\ \boldsymbol{p}_\varepsilon(t) \end{pmatrix}\end{aligned}$$

in analogy to the critical Hamiltonian system. Taking the conservation quantity $\mathscr{C}(\boldsymbol{q}, \boldsymbol{p})$ of the critical system and substituting the parametrization of Γ_ε, the implicit time evolution $\mathscr{C}(t) := \mathscr{C}(\boldsymbol{q}_\varepsilon(t), \boldsymbol{p}_\varepsilon(t))$ is obtained. While the expression $\mathscr{C}(t)$ along the heteroclinic connection is constant for the critical case $\varepsilon = 0$, it becomes time dependent for $0 < \varepsilon \ll 1$. Since the position of the saddle equilibria is assumed to be unaffected by the perturbation with parameter ε, the net change of the function $\mathscr{C}(t)$ along the saddle connection Γ_ε is zero, implying $\mathscr{C}(t = \mp\infty) = \mathscr{C}(\boldsymbol{q}(\mp 1), 0) = \mathscr{C}_\mathrm{h}$. This condition can be cast in integral form

$$\int_{-\infty}^{+\infty} \dot{\mathscr{C}}(t)\Big|_{\boldsymbol{q}_\varepsilon, \boldsymbol{p}_\varepsilon} \mathrm{d}t = \int_{-\infty}^{+\infty} \frac{\partial \mathscr{C}}{\partial \boldsymbol{q}} \dot{\boldsymbol{q}} + \frac{\partial \mathscr{C}}{\partial \boldsymbol{p}} \dot{\boldsymbol{p}}\Big|_{\boldsymbol{q}_\varepsilon, \boldsymbol{p}_\varepsilon} \mathrm{d}t = 0. \tag{5.14}$$

Substituting the perturbed Hamiltonian dynamics into Eq. (5.14) yields the integral balance

$$\begin{aligned}&\underbrace{\int_{-\infty}^{+\infty} \frac{\partial \mathscr{C}}{\partial \boldsymbol{q}} \frac{\partial \mathscr{H}}{\partial \boldsymbol{p}} - \frac{\partial \mathscr{C}}{\partial \boldsymbol{p}} \frac{\partial \mathscr{H}}{\partial \boldsymbol{q}}\Big|_{\boldsymbol{q}_\varepsilon, \boldsymbol{p}_\varepsilon} \mathrm{d}t}_{=:\mathscr{M}_0} \\ &+ \varepsilon \int_{-\infty}^{+\infty} \frac{\partial \mathscr{C}}{\partial \boldsymbol{q}} \boldsymbol{f}(\boldsymbol{q}, \boldsymbol{p}) + \frac{\partial \mathscr{C}}{\partial \boldsymbol{p}} \boldsymbol{g}(\boldsymbol{q}, \boldsymbol{p})\Big|_{\boldsymbol{q}_\varepsilon, \boldsymbol{p}_\varepsilon} \mathrm{d}t = 0,\end{aligned} \tag{5.15}$$

evaluated along the heteroclinic saddle connection Γ_ε of the perturbed Hamiltonian system.

In anticipation of results below, the summands of Eq. (5.15) are separated into

$$\mathscr{M}_0 + \varepsilon\left(\mathscr{M}_1 + \mathscr{O}(\varepsilon)\right) = 0,$$

where $\mathscr{M}_1$ collects terms of the second summand that only depend linearly on ε and $\mathscr{M}_0$ is given by

$$\mathscr{M}_0 = \int_{-\infty}^{+\infty} \frac{\partial \mathscr{C}}{\partial \boldsymbol{q}} \frac{\partial \mathscr{H}}{\partial \boldsymbol{p}} - \frac{\partial \mathscr{C}}{\partial \boldsymbol{p}} \frac{\partial \mathscr{H}}{\partial \boldsymbol{q}} \Big|_{\boldsymbol{q}_\varepsilon, \boldsymbol{p}_\varepsilon} \mathrm{d}t.$$

Note that $\mathscr{M}_0$ is not independent of the perturbation parameter ε as it is evaluated along the heteroclinic saddle connection Γ_ε of the perturbed Hamiltonian system. However, it vanishes per definition as the Poisson bracket (5.12) is zero for the conserved quantity for any arbitrary point $(\boldsymbol{p}, \boldsymbol{q})$.

Approximation of the heteroclinic connection Γ_ε by the regular perturbation expansion

$$\boldsymbol{q}_\varepsilon = \boldsymbol{q}_0 + \varepsilon \boldsymbol{q}_1 + \mathscr{O}(\varepsilon^2)$$
$$\boldsymbol{p}_\varepsilon = \boldsymbol{p}_0 + \varepsilon \boldsymbol{p}_1 + \mathscr{O}(\varepsilon^2)$$

reveals the zero-orders $\boldsymbol{q}_0 = \boldsymbol{q}_c$ and $\boldsymbol{p}_0 = \boldsymbol{p}_c$, i.e., the saddle connection Γ_c of the critical Hamiltonian system is the zero-order approximation of Γ_ε.

This relationship is substituted into the second summand of Eq. (5.15) to obtain the Melnikov function

$$\mathscr{M}_1 = \int_{-\infty}^{+\infty} \frac{\partial \mathscr{C}}{\partial \boldsymbol{q}} \boldsymbol{f}(\boldsymbol{q}, \boldsymbol{p}) + \frac{\partial \mathscr{C}}{\partial \boldsymbol{p}} \boldsymbol{g}(\boldsymbol{q}, \boldsymbol{p}) \Big|_{\boldsymbol{q}_0, \boldsymbol{p}_0} \mathrm{d}t, \tag{5.16}$$

evaluated along the saddle connection Γ_c. With $\mathscr{M}_0(\varepsilon) = 0$, the Melnikov function $\mathscr{M}_1$ must vanish, being the first-order term of the second summand, cf. Eq. (5.15).

Using the parametrization of the saddle connection Γ_c^q from Eq. (5.13) and the differential relation $\mathrm{d}q_1 = \dot{q}_1 \mathrm{d}t$ between time t and master coordinate q_1, the time integral (5.16) transforms to

$$\begin{aligned} \mathscr{M}_1 &= \int_{-1}^{+1} \left(\frac{\partial \mathscr{C}}{\partial \boldsymbol{q}} \boldsymbol{f}(\boldsymbol{q}, \boldsymbol{p}) + \frac{\partial \mathscr{C}}{\partial \boldsymbol{p}} \boldsymbol{g}(\boldsymbol{q}, \boldsymbol{p}) \right) \frac{1}{\dot{q}_1} \Big|_{\boldsymbol{q}_0(q_1), \boldsymbol{p}_0(q_1)} \mathrm{d}q_1 \\ &= \int_{-1}^{+1} \left(\frac{\partial \mathscr{C}}{\partial \boldsymbol{q}} \boldsymbol{f}(\boldsymbol{q}, \boldsymbol{p}) + \frac{\partial \mathscr{C}}{\partial \boldsymbol{p}} \boldsymbol{g}(\boldsymbol{q}, \boldsymbol{p}) \right) \left(\frac{\partial \mathscr{H}}{\partial p_1} \right)^{-1} \Big|_{\boldsymbol{q}_0(q_1), \boldsymbol{p}_0(q_1)} \mathrm{d}q_1 \end{aligned} \tag{5.17}$$

i.e., a definite integral with respect to the master coordinate q_1.

Considering the conservation of $\mathscr{C}$, it may be possible to compute the critical saddle connection Γ_c in closed-form. This allows to evaluate the integral (5.17) with $\boldsymbol{q}_0(q_1) = \boldsymbol{q}_c(q_1)$ and $\boldsymbol{p}_0(q_1) = \boldsymbol{p}_c(q_1)$ to obtain an algebraic expression for the Melnikov function $\mathscr{M}_1$ that depends on the system parameter Ω. With $\mathscr{M}_1 = 0$, the necessary condition for the existence of a heteroclinic saddle connection Γ_ε follows.

5.3 Singularly perturbed dynamics of the tippedisk

In Chapter 4, a reduced minimal model in $\mathbb{R}^3$ was derived that qualitatively describes the inversion behavior of the tippedisk. The linearization of the reduced system shows that the system has to be considered on different time scales. Therefore, this section applies the singular perturbation theory presented in Section 5.1 to analyze the dynamical behavior of the tippedisk in the framework of slow-fast systems.

Assuming linearized Coulomb friction from Eq. (4.61) (motivated by Coulomb–Contensou friction), a singularly perturbed dynamical system is obtained by normalizing the kinetics in Eq. (4.39) with the mass $M(\boldsymbol{x})$ and pre-multiplying by the small smoothing coefficient ε. Identifying the coordinates $\boldsymbol{x}$ from Eq. (4.34) as the slow variables and the scalar velocity $y = \eta = \dot{\beta}$ from Eq. (4.35) as the fast variable, gives the singularly perturbed dynamical system

$$\begin{aligned} \dot{\boldsymbol{x}} &= \boldsymbol{f}(\boldsymbol{x}, y) \\ \varepsilon\, \dot{y} &= g(\boldsymbol{x}, y; \varepsilon) = g_0(\boldsymbol{x}, y) + \varepsilon\, g_1(\boldsymbol{x}, y), \end{aligned} \tag{5.18}$$

which results from splitting the three-dimensional dynamics $\dot{\boldsymbol{X}} = \boldsymbol{F}(\boldsymbol{X}; \Omega) \in \mathbb{R}^3$ from Eq. (4.79) with corresponding state $\boldsymbol{X}$ defined in Eq. (4.78) into slow and fast dynamics with states $\boldsymbol{x}$ and y, respectively. The function

$$\boldsymbol{f}(\boldsymbol{x}, y) = \begin{bmatrix} \eta \\ -\Omega \cos\beta \end{bmatrix} \in \mathbb{R}^2$$

results from the kinematics Eq. (4.45). With the mass $M(\boldsymbol{x})$ from Eq. (4.40), the gyroscopic and gravitational forces from Eqs. (4.41) and (4.42), and the generalized force direction from Eq. (4.43), as well as the sliding velocity from Eq. (4.44), the expressions

$$g_0(\boldsymbol{x}, y) = -M(\boldsymbol{x})^{-1} \mu m g\, w_y(\boldsymbol{x}) \gamma_y(\boldsymbol{x}, y) \in \mathbb{R},$$

and

$$g_1(\boldsymbol{x}, y) = M(\boldsymbol{x})^{-1} \left[h(\boldsymbol{x}, y) + f_g(\boldsymbol{x}, y) \right] \in \mathbb{R}$$

are fully defined. From the singularly perturbed dynamical system (5.18), the two-dimensional slow subsystem

$$\dot{\boldsymbol{x}} = \boldsymbol{f}(\boldsymbol{x}, y) \in \mathbb{R}^2$$

and the scalar fast subsystems

$$\varepsilon\, \dot{y} = g(\boldsymbol{x}, y; \varepsilon) = g_0(\boldsymbol{x}, y) + \varepsilon\, g_1(\boldsymbol{x}, y),$$

are identified, cf. [115]. In the context of singular perturbation theory the critical dynamics

$$\begin{aligned} \dot{\boldsymbol{x}} &= \boldsymbol{f}(\boldsymbol{x}, y) \in \mathbb{R}^2 \\ 0 &= g_0(\boldsymbol{x}, y) \in \mathbb{R} \end{aligned} \tag{5.19}$$

of the singularly perturbed system (5.18) is obtained by setting the perturbation parameter ε to zero, i.e., the fast subsystem degenerates to the algebraic equation $g_0(\boldsymbol{x}, y) = 0$. Since the 'mass matrix' M (here scalar) is non-singular and the generalized force direction for $\beta \in (0, \pi)$ is non-zero[1], the critical dynamics from Eq. (5.19) can be equivalently rewritten as

$$\begin{aligned} \dot{\boldsymbol{x}} &= \boldsymbol{f}(\boldsymbol{x}, y) \\ 0 &= \gamma_y(\boldsymbol{x}, y), \end{aligned} \tag{5.20}$$

characterizing motions with zero relative sliding velocity of the contact point C, i.e., motions under perfect rolling condition. The relative velocity γ_y in Eq. (4.44) depends linearly on the fast variable $y = \dot{\beta}$ with non-zero prefactor $(r + e\mathrm{s}\gamma)\mathrm{s}\beta$ for all $\beta \in (0, \pi)$, and the Jacobian $\frac{\partial g_0}{\partial y}$ is invertible. Thus, a two-dimensional critical manifold

$$\mathscr{M}_c := \left\{ (\boldsymbol{x}, y) = (\beta, \gamma, y) \in \mathbb{R}^3 \,\middle|\, y = h_c(\boldsymbol{x}) = \frac{e \sin\beta \cos\gamma}{(r + e\sin\gamma)} \Omega \right\},$$

exists globally for $\beta \in (0, \pi)$. The corresponding two-dimensional critical dynamics is determined by the differential equation

$$\dot{\boldsymbol{x}} = \boldsymbol{f}(\boldsymbol{x}, h_c(\boldsymbol{x})) \quad \Longleftrightarrow \quad \begin{bmatrix} \dot{\beta} \\ \dot{\gamma} \end{bmatrix} = \begin{bmatrix} h_c(\beta, \gamma) \\ -\Omega \cos\beta, \end{bmatrix} \tag{5.21}$$

which characterizes the slow behavior of the tippedisk under the pure rolling condition $\gamma_y(\boldsymbol{x}, h_c(\boldsymbol{x})) \equiv 0$.

For $\varepsilon > 0$, the asymptotic dynamics of the perturbed dynamical system from Eq. (5.18) takes place on the slow manifold $\mathscr{M}_s$, which is approximated up to first orders $\mathscr{O}(\varepsilon^2)$ by

$$\mathscr{M}_s :\approx \left\{ (\boldsymbol{x}, y) \in \mathbb{R}^3 \,\middle|\, y = \frac{e \sin\beta \cos\gamma}{(r + e\sin\gamma)} \Omega + \varepsilon h_1(\boldsymbol{x}) \right\}, \tag{5.22}$$

with

$$h_1(\boldsymbol{x}) = \left. \frac{\partial g_0}{\partial y} \right|_{\boldsymbol{x}, h_c(\boldsymbol{x})}^{-1} \left[\left. \frac{\partial h_c(\boldsymbol{x})}{\partial \boldsymbol{x}} \right|_{\boldsymbol{x}} \boldsymbol{f}(\boldsymbol{x}, h_c(\boldsymbol{x})) - g_1(\boldsymbol{x}, h_c(\boldsymbol{x})) \right],$$

---

[1] For $\beta = 0$ and $\beta = \pi$, the tippedisk is horizontal, i.e., not inclined with respect to the support. During inversion the tippedisk is almost vertically oriented, ensuring a regular mass matrix.

cf. Eq. (5.8). Evaluation of the first-order part $h_1(\boldsymbol{x})$ yields after some algebra[2] the expression

$$\begin{aligned} h_1(\boldsymbol{x}) = \frac{\Omega^2 \, \mathrm{c}\beta}{\mu m g \, \mathrm{s}\beta (r + e\mathrm{s}\gamma)^4} \Big[& A\, \mathrm{c}^2\gamma (r^2 - er\mathrm{s}\gamma - 2e^2) \\ & + \bar{B} r \mathrm{s}\gamma \left(r\mathrm{s}\gamma + e + e\,\mathrm{c}^2\gamma \right) - \frac{mg(r + e\mathrm{s}\gamma)^3}{\Omega^2 \mathrm{s}\beta} \Big]. \end{aligned} \tag{5.23}$$

The critical manifold $\mathscr{M}_c$ corresponds to the zero-order approximation of the slow manifold $\mathscr{M}_s$, whose stability on the fast time scale is characterized by the distance dynamics

$$d' = \left. \frac{\partial g_0}{\partial y} \right|_{\boldsymbol{x}, h_c} d,$$

which is asymptotically stable, as the Jacobian

$$\left. \frac{\partial g_0}{\partial y} \right|_{\boldsymbol{x}, h_c} = -M(\boldsymbol{x})^{-1} \mu m g (r + e \sin\gamma)^2 \sin^2\beta$$

is strictly negative for the inclined tippedisk, i.e., $\beta \in (0, +\pi)$. Since the critical manifold $\mathscr{M}_c$ characterizes pure rolling motions, solutions on the slow manifold $\mathscr{M}_s$ are close to pure rolling. Moreover, in a basin of attraction solutions are attracted to the invariant manifold $\mathscr{M}_s$, such that the asymptotic dynamics of the tippedisk is governed by the two-dimensional system

$$\dot{\boldsymbol{x}} = \boldsymbol{f}(\boldsymbol{x}, h_c(\boldsymbol{x}) + \varepsilon h_1(\boldsymbol{x})) \Leftrightarrow \begin{bmatrix} \dot{\beta} \\ \dot{\gamma} \end{bmatrix} = \begin{bmatrix} h_c(\beta,\gamma) + \varepsilon h_1(\beta,\gamma) \\ -\Omega \cos\beta \end{bmatrix}, \tag{5.24}$$

which corresponds to the approximated dynamics on the slow manifold. Note that the perturbation reduction procedure of the singularly perturbed dynamics (5.18) yields a lower-dimensional regularly perturbed dynamical system (5.24).

Slow-fast dynamics

After revealing the singularly perturbed structure of the tippedisk from Eq. (5.18), the qualitative behavior is presented in this section. According to the linear stability analysis of Section 4.3, non-inverted spinning is always unstable. The inverted spinning equilibrium is unstable for subcritical spinning velocities $\Omega < \Omega_\mathrm{c}$ and stable for supercritical spinning velocities $\Omega > \Omega_\mathrm{c}$. Due to the ambiguity of trigonometric expressions, both the states

$$\boldsymbol{X}_1^- = \begin{bmatrix} +\frac{\pi}{2} & -\frac{\pi}{2} & 0 \end{bmatrix}^\mathrm{T} \quad \text{and} \quad \boldsymbol{X}_2^- = \begin{bmatrix} +\frac{\pi}{2} & +3\frac{\pi}{2} & 0 \end{bmatrix}^\mathrm{T} \tag{5.25}$$

---

[2] Here, 'some algebra' means several pages of tedious algebraic calculations by hand and non-trivial identifications of trigonometric expressions.

correspond to an equilibrium which characterizing non-inverted stationary spinning motions. Inverted spinning motion is represented by the equilibrium at

$$\boldsymbol{X}^{+} = \begin{bmatrix} +\frac{\pi}{2} & +\frac{\pi}{2} & 0 \end{bmatrix}^{\mathrm{T}}. \tag{5.26}$$

Figure 5.2 shows the three-dimensional, slow-fast dynamics from Eq. (5.18) for different spinning speeds Ω. The associated discrete spinning velocities are given in Figure 5.3, where the dots represent the spinning equilibria, and the red square marks correspond to stable periodic solutions.

This bifurcation diagram corresponds to the magnified version of Figure 4.7(a), which contains only the numerical shooting results from Section 4.5. In Figure 5.2, the slow manifold $\mathscr{M}_s$ defined in Eq. (5.22) is represented as gray surface. Unstable equilibria are shown as blue dots, stable ones as red dots. For each subfigure 5.2(a)-5.2(d), two blue orbits are initialized as black crosses at

$$\boldsymbol{X}_1^0 = \begin{bmatrix} +\frac{\pi}{2} & -\frac{\pi}{2} & 2 \end{bmatrix}^{\mathrm{T}} \quad \text{and} \quad \boldsymbol{X}_2^0 = \begin{bmatrix} +\frac{\pi}{2} & +\frac{\pi}{2}+0.4 & 0 \end{bmatrix}^{\mathrm{T}}.$$

For $\Omega < \Omega_{\mathrm{h}}$, solutions are repelled by the inverted spinning equilibrium, cf. Figure 5.2(a). At Ω_{h}, a heteroclinic limit cycle with period time $T = \infty$ arises, which consists of two heteroclinic saddle connections connecting both non-inverted spinning equilibria. For $\Omega_{\mathrm{h}} < \Omega < \Omega_{\mathrm{c}}$, this limit cycle is attractive and shrinks for increasing Ω (cf. Figures 5.2(b)-5.2(e)), the period time decreases according to Figure 4.7(b). At Ω_{c}, the stable periodic solution vanishes in a supercritical Hopf bifurcation, so the inverted spinning motion becomes stable (shown as a red dot) and attracts the initialized trajectories (cf. Figure 5.2(f)). According to the stability property of the slow manifold $\mathscr{M}_s$, the trajectories are attracted and converge on a fast time scale, resulting in an initial jump of the initialized trajectories on $\mathscr{M}_s$. After convergence, the orbits evolve on this two-dimensional slow manifold. This allows to project the three-dimensional dynamics onto the (β, γ)-plane of slow variables without loosing much information. In Appendix B.2, the projected trajectories from the bifurcation scenario of Figure 5.2 are shown in Figure B.1.

The considered simulations show that the bifurcation scenario in Figure 5.3 is dominated by a heteroclinic bifurcation followed by a supercritical Hopf bifurcation. In Section 4.3, a closed-form expression of the critical spinning velocity Ω_{c} has been derived, characterizing the location of the Hopf bifurcation. Combining the results of the linear stability analysis and the harmonic balance approximation from Section 4.4, the nature of the Hopf bifurcation in closed-form is identified as supercritical. In order to obtain closed-form approximations of the heteroclinic bifurcation at Ω_{h}, the Melnikov function method presented in Section 5.2 is subsequently applied.

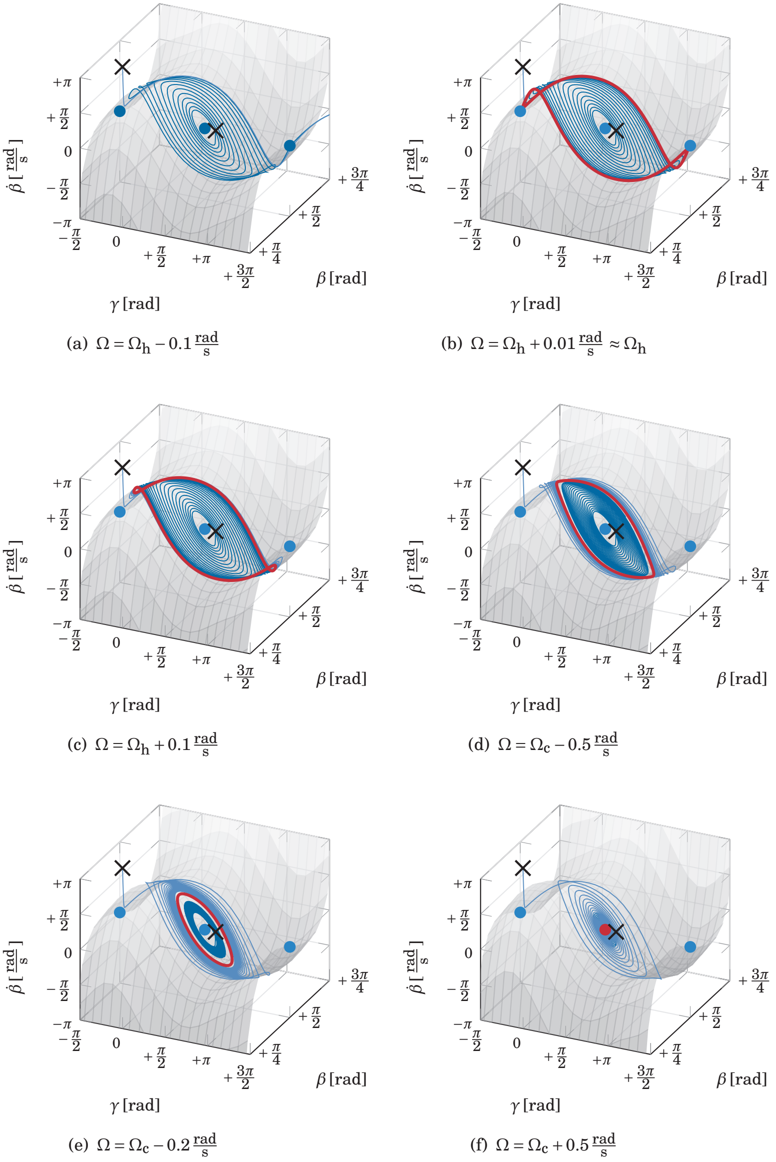

(a) $\Omega = \Omega_{\mathrm{h}} - 0.1\,\frac{\text{rad}}{\text{s}}$

(b) $\Omega = \Omega_{\mathrm{h}} + 0.01\,\frac{\text{rad}}{\text{s}} \approx \Omega_{\mathrm{h}}$

(c) $\Omega = \Omega_{\mathrm{h}} + 0.1\,\frac{\text{rad}}{\text{s}}$

(d) $\Omega = \Omega_{\mathrm{c}} - 0.5\,\frac{\text{rad}}{\text{s}}$

(e) $\Omega = \Omega_{\mathrm{c}} - 0.2\,\frac{\text{rad}}{\text{s}}$

(f) $\Omega = \Omega_{\mathrm{c}} + 0.5\,\frac{\text{rad}}{\text{s}}$

Figure 5.2: Slow-fast dynamics of the tippedisk for different spinning speeds Ω. The slow manifold $\mathscr{M}_s$ is depicted in gray. The transient solutions are initialized at the black crosses and depicted in blue. Stable periodic solutions are obtained by numerical shooting of the singularly perturbed system from Eq. (4.39) and are depicted in red. Unstable stationary spinning motions are marked as blue dots, whereas stable spinning is indicated by a red dot.

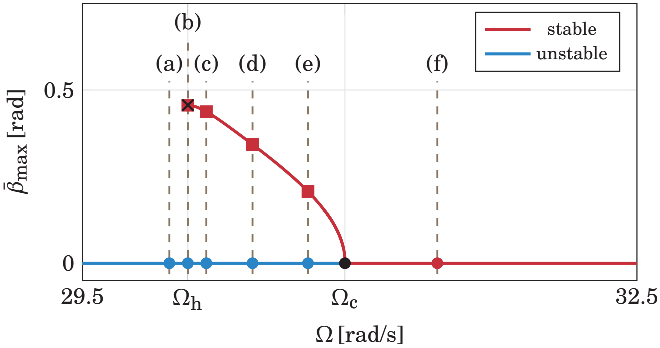

Figure 5.3: Location of the parameter values of Figure 5.2 in the associated bifurcation diagram. Unstable inverted spinning is marked as blue dots, whereas stable spinning is indicated by a red dot. Stable periodic solutions are shown as red squares. The branch of periodic solutions has been obtained by numerical shooting.

Hamiltonian structure on the critical manifold

To apply the Melnikov function method, the critical dynamics with $\varepsilon = 0$ requires a special Hamiltonian structure. The slow dynamics on the critical manifold $\mathscr{M}_c$ from Eq. (5.20) is shown in Figure 5.4 for two different spinning speeds Ω. The points

$$\left(\beta_1^-, \gamma_1^-\right) = \left(+\tfrac{\pi}{2}, -\tfrac{\pi}{2}\right) \quad \text{and} \quad \left(\beta_2^-, \gamma_2^-\right) = \left(+\tfrac{\pi}{2}, +3\tfrac{\pi}{2}\right), \tag{5.27}$$

represent the two non-inverted spinning states $\boldsymbol{x}_1^-$ and $\boldsymbol{x}_2^-$, respectively, see also the definitions from Eq. (5.25).

The inverted spinning equilibrium $\boldsymbol{x}^+$ is located at the point

$$\left(\beta^+, \gamma^+\right) = \left(+\tfrac{\pi}{2}, +\tfrac{\pi}{2}\right), \tag{5.28}$$

cf. Eq. (5.26). For all spinning speeds $\Omega \neq 0$, a heteroclinic orbit Γ_c exists for the critical dynamics, connecting the saddle equilibria $\boldsymbol{x}_1^-$ and $\boldsymbol{x}_2^-$. As both saddle equilibria correspond to non-inverted stationary spinning, we may also call the saddle connection a homoclinic orbit from a physical perspective (or on a cylindrical state-space). The projection of associated trajectories in this two-dimensional space looks the same for different spinning speeds Ω. However, comparison of two equivalent periodic orbits shows different orbital speeds, see Figure 5.4(c).

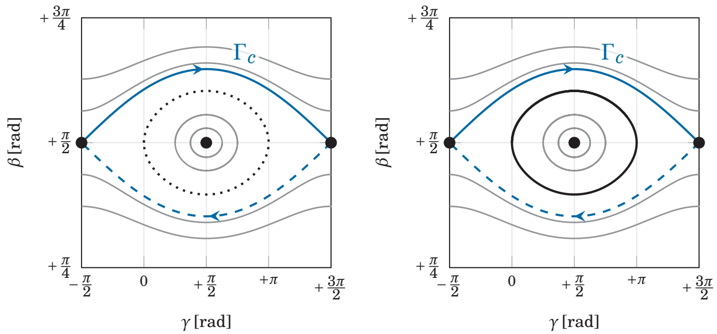

(a) $\Omega = \Omega_c - 5\,\frac{\text{rad}}{\text{s}}$ (b) $\Omega = \Omega_c + 5\,\frac{\text{rad}}{\text{s}}$

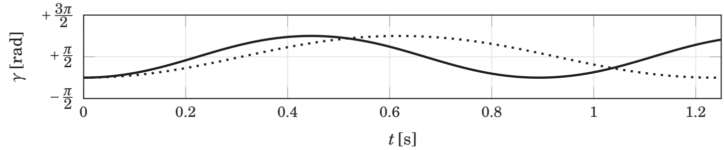

(c) Comparison of orbital speeds

Figure 5.4: Dynamics on the critical manifold for two different values of the spinning speed Ω. In Figure 5.4(a) and Figure 5.4(b), the trajectories are identical with respect to the phase portrait, as they only differ in the orbital speed. Figure 5.4(c) shows exemplarily for the two trajectories (dotted in (a) and solid in (b), respectively) that the orbital speed increases with increasing spinning speed Ω.

Since the spinning speed Ω is assumed to be constant and takes the role of a bifurcation parameter, the time derivative of $\dot{\gamma} = -\Omega\cos\beta$ (cf. Eq. (5.21)) yields

$$\ddot{\gamma} = +\Omega \sin\beta\dot{\beta}.$$

For the critical case, the slaved fast variable $\dot{\beta} = h_c(\beta,\gamma)$ can be substituted into the above differential equation as a function of the slow variables, leading to

$$\ddot{\gamma} = +\Omega^2 \sin^2\beta \frac{e\cos\gamma}{(r + e\sin\gamma)}.$$

Substitution of $\sin^2\beta = 1 - \cos^2\beta$ and identifying $\dot{\gamma}^2 = \Omega^2\cos^2\beta$ results in the second-order system

$$(r + e\sin\gamma)\ddot{\gamma} + e\cos\gamma\,\dot{\gamma}^2 - \Omega^2 e\cos\gamma = 0. \tag{5.29}$$

To identify canonical coordinates and momenta, Eq. (5.29) or an equation equivalent to it can be interpreted as if it were a Lagrangian equation of motion in the coordinate γ. In analogy, the 'kinetic' and 'potential' energies

$$\mathscr{T} = \frac{1}{2}(r + e\,\sin\gamma)^2\,\dot{\gamma}^2, \qquad \mathscr{V} = -\frac{1}{2}(r + e\,\sin\gamma)^2\,\Omega^2,$$

are introduced, implying the Lagrangian $\mathscr{L}(\gamma,\dot{\gamma}) = \mathscr{T} - \mathscr{V}$ in the coordinate γ and its associated time derivative $\dot{\gamma}$. Evaluating the Euler equation

$$\frac{\mathrm{d}}{\mathrm{d}t}\left(\frac{\partial\mathscr{L}}{\partial\dot{\gamma}}\right) - \left(\frac{\partial\mathscr{L}}{\partial\gamma}\right) = 0$$

yields the Lagrangian dynamics

$$(r + e\sin\gamma)\Big[(r + e\sin\gamma)\ddot{\gamma} + e\cos\gamma\,\dot{\gamma}^2 - \Omega^2\,e\cos\gamma\Big] = 0, \tag{5.30}$$

which characterizes the dynamics on the critical manifold, i.e., pure rolling motions. Since the outer radius r of the disk is greater than the eccentricity e, the factor $(r + e\sin\gamma)$ is non-zero for all $\gamma \in \mathbb{R}$, such that the equivalence of Eq. (5.29) and Eq. (5.30) follows directly. Therefore, the critical dynamics corresponds to a single degree of freedom Lagrangian system, for which the associated Hamiltonian system with Hamiltonian $\mathscr{H}$ can be deduced by convex conjugation, also called the Legendre–Fenchel–Transformation [103]. In canonical coordinates, namely the generalized coordinates $q = \gamma$ and the corresponding generalized momentum

$$p = \varrho = \frac{\partial\mathscr{L}}{\partial\dot{\gamma}} = (r + e\,\sin\gamma)^2\,\dot{\gamma}, \tag{5.31}$$

the associated Hamiltonian $\mathscr{H}(\gamma,\varrho) = \varrho\,\dot{\gamma} - \mathscr{L}(\gamma,\dot{\gamma})$ with $\dot{\gamma} = \dot{\gamma}(\gamma,\varrho)$ takes the form

$$\mathscr{H}(\gamma,\varrho) = \frac{1}{2}\frac{1}{(r + e\sin\gamma)^2}\varrho^2 - \frac{1}{2}(r + e\sin\gamma)^2\,\Omega^2. \tag{5.32}$$

The application of Hamilton's formalism reveals the critical Hamiltonian system

$$\begin{aligned}\dot{\gamma} &= +\frac{\partial\mathscr{H}(\gamma,\varrho)}{\partial\varrho}\\ \dot{\varrho} &= -\frac{\partial\mathscr{H}(\gamma,\varrho)}{\partial\gamma},\end{aligned} \tag{5.33}$$

whose dynamics is shown in Figure 5.5 for two different rotational velocities. With respect to the canonical coordinates γ and $\varrho = (r + es\gamma)^2\dot{\gamma}$, non-inverted spinning motion is characterized by the equilibrium points

$$\big(\gamma_1^-, \varrho_1^-\big) = \big(-\tfrac{\pi}{2}, 0\big) \quad \text{and} \quad \big(\gamma_2^-, \varrho_2^-\big) = \big(+3\tfrac{\pi}{2}, 0\big).$$

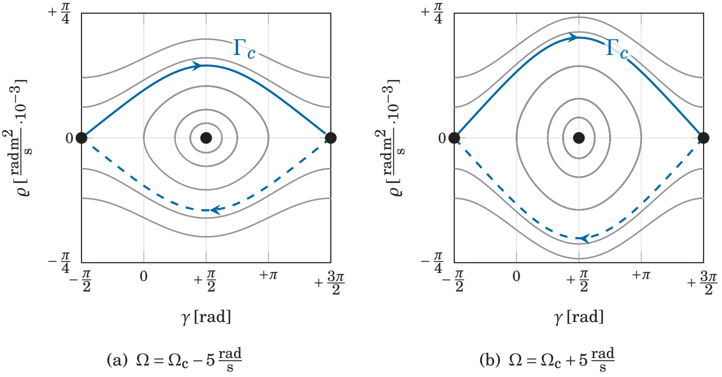

(a) $\Omega = \Omega_c - 5\,\frac{\mathrm{rad}}{\mathrm{s}}$ (b) $\Omega = \Omega_c + 5\,\frac{\mathrm{rad}}{\mathrm{s}}$

Figure 5.5: Critical Hamiltonian dynamics in canonical γ-ϱ-coordinates for two values of the spinning speed Ω.

Inverted spinning is represented by the equilibrium point at

$$(\gamma^+, \varrho^+) = \left(+\tfrac{\pi}{2}, 0\right).$$

In contrast to the critical dynamics in β-γ-coordinates from Figure 5.4, the shape of heteroclinic orbits in Hamiltonian ϱ-γ-coordinates depends on the spinning speed Ω. Although the phase portrait differs for varying bifurcation parameter Ω, the existence of the heteroclinic saddle connection Γ_c is preserved.

Heteroclinic orbit of the perturbed system

Equation (5.24) corresponds to a regularly perturbed dynamics on the slow manifold. Setting the regular perturbation parameter ε to zero results in the slow dynamics on the critical manifold $\mathscr{M}_c$ given in Eq. (5.20), which can be cast in Hamiltonian form Eq. (5.33). Therefore, the reduced dynamics on the slow manifold $\mathscr{M}_s$ from Eq. (5.24) resulting from the application of singular perturbation theory has a perturbed Hamiltonian structure. In Figure 5.6, the dynamics on the slow manifold is shown for different values of the spinning speed Ω. Solutions are initialized at the black crosses and the simulation end time is set to $t = 2\,\mathrm{s}$. Similarly to the dynamics of the singularly perturbed system, the bifurcation scenario is characterized by a heteroclinic bifurcation with associated heteroclinic orbits in green (see Figure 5.6(b)), which is followed by a supercritical Hopf bifurcation. Since the crit-

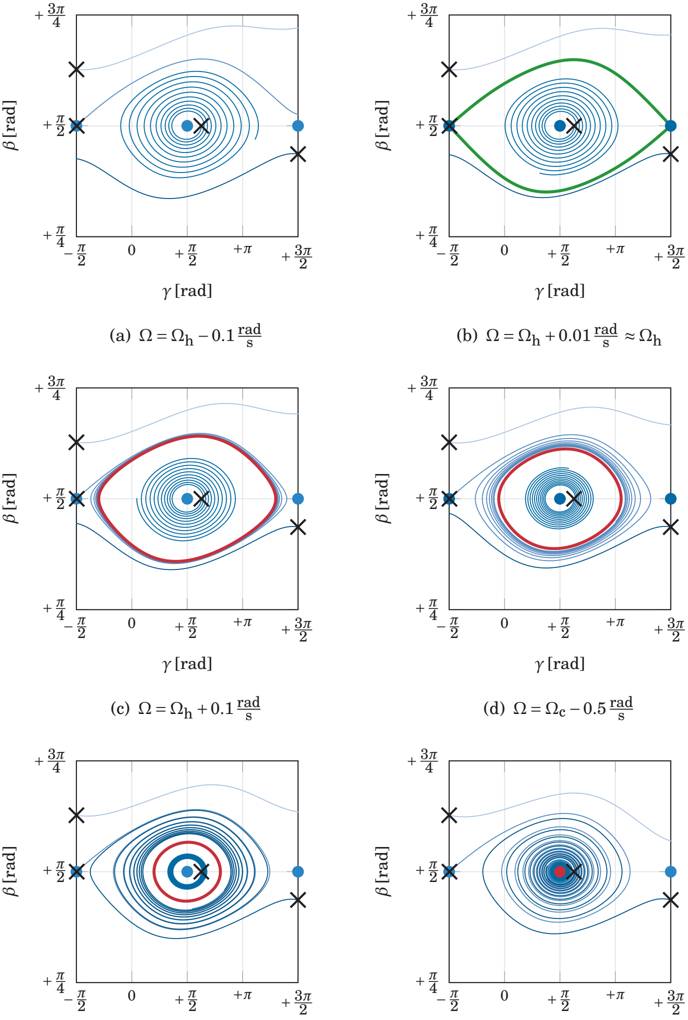

(a) $\Omega = \Omega_\mathrm{h} - 0.1\,\frac{\mathrm{rad}}{\mathrm{s}}$

(b) $\Omega = \Omega_\mathrm{h} + 0.01\,\frac{\mathrm{rad}}{\mathrm{s}} \approx \Omega_\mathrm{h}$

(c) $\Omega = \Omega_\mathrm{h} + 0.1\,\frac{\mathrm{rad}}{\mathrm{s}}$

(d) $\Omega = \Omega_\mathrm{c} - 0.5\,\frac{\mathrm{rad}}{\mathrm{s}}$

(e) $\Omega = \Omega_\mathrm{c} - 0.2\,\frac{\mathrm{rad}}{\mathrm{s}}$

(f) $\Omega = \Omega_\mathrm{c} + 0.5\,\frac{\mathrm{rad}}{\mathrm{s}}$

Figure 5.6: Dynamics on the slow manifold $\mathscr{M}_s$ from Eq. (5.24). The qualitative behavior is similar to the dynamics from Figure 5.2 of the three-dimensional singularly perturbed dynamical system, which corresponding bifurcation diagram in Figure 5.3.

ical system is Hamiltonian and contains a heteroclinic saddle connection for any rotational velocity Ω, Melnikov theory can be applied to obtain a necessary condition for the heteroclinic bifurcation point. Instead of applying Melnikov theory in its general form, i.e., in the canonical coordinates $\boldsymbol{q}$ and momenta $\boldsymbol{p}$ of the Hamiltonian system, the following analysis is performed with respect to physical system coordinates, namely the inclination angle β and rolling angle γ, well knowing and presupposing that the critical dynamics has a Hamiltonian structure and, therefore, a conserved quantity, e.g., the Hamiltonian $\mathscr{H}$, exists regardless of the choice of system parametrization. On the one hand, this avoids cumbersome algebraic manipulations. On the other hand, the physical coordinates are perfectly suited to link the dynamics with the motion of the real tippedisk.

Taking the Hamiltonian (5.32) in Hamiltonian canonical coordinate γ and momentum ϱ and inserting the transformation from Eq. (5.31) yields the Hamiltonian as a function

$$\bar{\mathscr{H}}(\gamma,\dot{\gamma}) = \frac{1}{2}(r + e\sin\gamma)^2\left(\dot{\gamma}^2 - \Omega^2\right)$$

in Lagrangian coordinates γ and $\dot{\gamma}$ with the property $\bar{\mathscr{H}}(\gamma,\dot{\gamma}) = \mathscr{H}(\gamma,\varrho(\gamma,\dot{\gamma}))$. Replacing the Lagrangian coordinate $\dot{\gamma}$ by the second kinematic relation from Eq. (5.21)

$$\dot{\gamma} = -\Omega\cos\beta,$$

the functional expression

$$\bar{\bar{\mathscr{H}}}(\beta,\gamma) = -\frac{1}{2}(r + e\sin\gamma)^2\sin^2\beta\,\Omega^2 \tag{5.34}$$

of the Hamiltonian is obtained. On the saddle connection, the Hamiltonian of the critical dynamical system remains constant. As the heteroclinic orbit connects the non-inverted equilibria $\boldsymbol{x}_1^-$ and $\boldsymbol{x}_2^-$ from Eq. (5.27), the Hamiltonian takes the constant value

$$H = -\frac{1}{2}(r-e)^2\,\Omega^2 = \bar{\bar{\mathscr{H}}}(\beta_c(\gamma),\gamma).$$

Substitution of $\dot{\beta} = h_c(\beta,\gamma)$ from Eq. (5.21) yields the implicit equation

$$0 = \dot{H} = \frac{\partial\bar{\bar{\mathscr{H}}}}{\partial\beta}\,h_c(\beta_c(\gamma),\gamma) + \frac{\partial\bar{\bar{\mathscr{H}}}}{\partial\gamma}\,\dot{\gamma}.$$

Taking a closer look at the Hamiltonian $\bar{\bar{\mathscr{H}}}(\beta,\gamma)$ and noting that the height of the COG is expressed by

$$z^s(\beta,\gamma) = (r + e\mathrm{s}\gamma)\mathrm{s}\beta, \tag{5.35}$$

shows that

$$\bar{\bar{\mathscr{H}}}(\beta,\gamma) = -\frac{1}{2}\left(z^s(\beta,\gamma)\right)^2\Omega^2$$

holds, from which it can be deduced that the COG height z^s is a conserved quantity for pure rolling motions. Since the COG height is related to the potential energy of the tippedisk, the critical system characterizes motions for which the potential energy of the mechanical system is conserved. To evaluate the Melnikov function $\mathscr{M}_1$ (cf. Eq. (5.16)), the expression has to be integrated along a heteroclinic saddle connection Γ_c of the critical system. For the non-inverted tippedisk, the COG height is $z^s = r - e$. The upper heteroclinic connection in Figure 5.4 connects two non-inverted saddle equilibria such that, with the constant COG height from Eq. (5.35), the implicit equation

$$r - e = (r + e\mathrm{s}\gamma)\mathrm{s}\beta.$$

follows. From this, it can be seen that the upper heteroclinic saddle connection for $\beta \in [\pi/2, \pi)$ is given by the curve

$$\begin{aligned} \Gamma_{\mathrm{c}}^{\gamma} : \left[-\frac{\pi}{2}, 3\frac{\pi}{2}\right] &\to \left[\frac{\pi}{2}, \pi - \sin^{-1}\left(\frac{r-e}{r+e}\right)\right] \\ \gamma &\mapsto \beta_c(\gamma) = \pi - \sin^{-1}\left(\frac{r-e}{r + e\sin\gamma}\right). \end{aligned} \tag{5.36}$$

Herein, the expression $\sin^{-1}(\bullet)$ corresponds to the standard definition of $\arcsin(\bullet)$, i.e., to the function which maps the interval $[-1, +1,] \mapsto [-\pi/2, +\pi/2]$.

Taking the Hamiltonian as the conserved quantity, the integral balance

$$0 = \int_{-\infty}^{+\infty} \dot{H}\,\mathrm{d}t = \int_{-\infty}^{+\infty} \left(\frac{\partial\bar{\bar{\bar{\mathscr{H}}}}}{\partial\beta}\dot{\beta}(\beta,\gamma) + \frac{\partial\bar{\bar{\bar{\mathscr{H}}}}}{\partial\gamma}\dot{\gamma}(\beta,\gamma)\right)\bigg|_{\beta_\varepsilon(\gamma),\gamma} \mathrm{d}t$$

yields together with the reduced dynamics on the slow manifold from Eq. (5.24) and the perturbation expansion

$$\beta_\varepsilon = \beta_c + \varepsilon\beta_1 + \mathscr{O}(\varepsilon^2)$$

the expression

$$\begin{aligned} 0 = &\int_{-\infty}^{+\infty} \left(\frac{\partial\bar{\bar{\bar{\mathscr{H}}}}}{\partial\beta} h_c(\beta,\gamma) - \frac{\partial\bar{\bar{\bar{\mathscr{H}}}}}{\partial\gamma}\Omega\cos\beta\right)\bigg|_{\beta_\varepsilon(\gamma),\gamma} \mathrm{d}t \\ &+ \varepsilon\int_{-\infty}^{+\infty} \left(\frac{\partial\bar{\bar{\bar{\mathscr{H}}}}}{\partial\beta} h_1(\beta,\gamma)\right)\bigg|_{\beta_c(\gamma),\gamma} \mathrm{d}t + \mathscr{O}(\varepsilon^2). \end{aligned}$$

Herein, the Melnikov functions

$$\mathscr{M}_0 = \int_{-\infty}^{+\infty} \left(\frac{\partial\bar{\bar{\bar{\mathscr{H}}}}}{\partial\beta} h_c(\beta,\gamma) - \frac{\partial\bar{\bar{\bar{\mathscr{H}}}}}{\partial\gamma}\Omega\cos\beta\right)\bigg|_{\beta_\varepsilon(\gamma),\gamma} \mathrm{d}t \tag{5.37}$$

and

$$\mathscr{M}_1 = \int_{-\infty}^{+\infty} \left(\frac{\partial \bar{\bar{\mathscr{H}}}}{\partial \beta} h_1(\beta,\gamma) \right) \Big|_{\beta_c(\gamma),\gamma} \mathrm{d}t \tag{5.38}$$

are identified, yielding the integral criterion

$$0 = \int_{-\infty}^{+\infty} \dot{H} \, \mathrm{d}t = \mathscr{M}_0 + \varepsilon \mathscr{M}_1 + \mathscr{O}(\varepsilon^2).$$

With $\bar{\bar{\mathscr{H}}}(\beta,\gamma)$ from Eq. (5.34), the partial derivatives

$$\frac{\partial \bar{\bar{\mathscr{H}}}(\beta,\gamma)}{\partial \beta} = -(r+e\,\mathrm{s}\gamma)^2 \,\mathrm{s}\beta\,\mathrm{c}\beta\,\Omega^2, \quad \frac{\partial \bar{\bar{\mathscr{H}}}(\beta,\gamma)}{\partial \gamma} = -e(r+e\,\mathrm{s}\gamma)\,\mathrm{s}^2\beta\,\mathrm{c}\gamma\,\Omega^2 \tag{5.39}$$

are obtained. Inserting these partial derivatives together with the natural parametrization of the critical manifold

$$h_c(\boldsymbol{x}) = \frac{e \sin\beta \cos\gamma}{(r+e\sin\gamma)} \Omega,$$

into Eq. (5.37), results in a vanishing Melnikov function

$$\begin{aligned} \mathscr{M}_0 &= -\int_{-\infty}^{+\infty} (r+e\,\mathrm{s}\gamma)\,\mathrm{s}\beta\,\mathrm{c}\beta\,\Omega^2 \Big((r+e\,\mathrm{s}\gamma) h_c(\beta,\gamma) - e\,\mathrm{s}\beta\,\mathrm{c}\gamma\,\Omega \Big) \Big|_{\beta_\varepsilon(\gamma),\gamma} \mathrm{d}t \\ &= -\int_{-\infty}^{+\infty} (r+e\,\mathrm{s}\gamma)\,\mathrm{s}\beta\,\mathrm{c}\beta\,\Omega^2 \underbrace{(e\,\mathrm{s}\beta\,\mathrm{c}\gamma\,\Omega - e\,\mathrm{s}\beta\,\mathrm{c}\gamma\,\Omega)}_{=0} \Big|_{\beta_\varepsilon(\gamma),\gamma} \mathrm{d}t \equiv 0 \end{aligned}$$

for arbitrary Ω. For any quantity $\mathscr{C}$ which is conserved for the critical dynamical system $\varepsilon = 0$, it follows that the Poisson brackets $\{\mathscr{C},\mathscr{H}\} = 0$ and therefore $\mathscr{M}_0$ vanishes identically, irrespective of the saddle connection Γ_ε defined by the function $\beta_\varepsilon(\gamma)$. Consequently, for a heteroclinic saddle-connection of the regularly perturbed dynamical system (5.24) resulting from the singular perturbation reduction procedure, the Melnikov function $\mathscr{M}_1$ (cf. Eq. (5.38)) has to vanish (approximately) on the path Γ_c, which is represented in Figure 5.7 by the solid blue line.

Inserting the critical inclination angle $\beta_c(\gamma)$ from Eq. (5.36) into the first-order term $h_1(\beta,\gamma)$ from Eq. (5.23) yields the function

$$\begin{aligned} h_1^c(\gamma) = \frac{\Omega^2}{\mu m g} \frac{\cos\beta_c(\gamma)}{(r-e)(r+e\,\mathrm{s}\gamma)^3} \cdot \Big[& A\,\mathrm{c}^2\gamma (r^2 - e r\,\mathrm{s}\gamma - 2e^2) \\ & + \bar{B} r\,\mathrm{s}\gamma \Big(r\,\mathrm{s}\gamma + e + e\,\mathrm{c}^2\gamma \Big) - \frac{mg(r+e\,\mathrm{s}\gamma)^4}{\Omega^2 (r-e)} \Big]. \end{aligned} \tag{5.40}$$

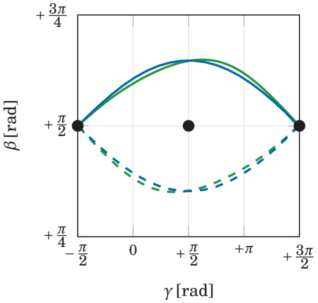

Figure 5.7: Comparison of heteroclinic orbits Γ_c of the critical system in blue and the heteroclinic connections Γ_ε of the perturbed dynamical system in green. The *upper* connections are shown in solid, the *lower* as dashed lines.

Together with the Eqs. (5.38), (5.39) and Eq. (5.40), the Melnikov function $\mathscr{M}_1$ gives the indefinite integral

$$\begin{aligned}\mathscr{M}_1 &= -\int_{-\infty}^{+\infty} (r + e\,\mathrm{s}\gamma)^2\,\Omega^2\,\mathrm{s}\beta\,\mathrm{c}\beta\,h_1^c(\gamma)\Big|_{\beta_c(\gamma),\gamma}\,\mathrm{d}t \\ &= -\frac{\Omega^4}{\mu m g}\int_{-\infty}^{+\infty} \mathrm{s}\beta_\mathrm{c}\,\frac{\mathrm{c}^2\beta_c}{(r-e)(r+e\,\mathrm{s}\gamma)}\cdot\Big[A\,\mathrm{c}^2\gamma(r^2 - er\,\mathrm{s}\gamma - 2e^2) \\ &\qquad + \bar{B}r\,\mathrm{s}\gamma\Big(r\,\mathrm{s}\gamma + e + e\,\mathrm{c}^2\gamma\Big) - \frac{mg(r+e\,\mathrm{s}\gamma)^4}{\Omega^2(r-e)}\Big]\mathrm{d}t.\end{aligned} \tag{5.41}$$

Substitution of

$$\sin\beta_c = \frac{(r-e)}{(r+e\,\mathrm{s}\gamma)},$$

simplifies the expression to

$$\begin{aligned}\mathscr{M}_1 = -\frac{\Omega^4}{\mu m g}\int_{-\infty}^{+\infty} \frac{\mathrm{c}^2\beta_c}{(r+e\,\mathrm{s}\gamma)^2}\cdot\Big[A\,\mathrm{c}^2\gamma(r^2 - er\,\mathrm{s}\gamma - 2e^2) \\ + \bar{B}r\,\mathrm{s}\gamma\Big(r\,\mathrm{s}\gamma + e + e\,\mathrm{c}^2\gamma\Big) - \frac{mg(r+e\,\mathrm{s}\gamma)^4}{\Omega^2(r-e)}\Big]\mathrm{d}t.\end{aligned} \tag{5.42}$$

Introduction of the strictly monotone mapping

$$\begin{aligned}\phi : (-\infty, +\infty) &\to [-\pi/2, +3\pi/2] \\ t &\mapsto \gamma_c(t)\end{aligned}$$

allows to transform the time parametrized *upper* critical heteroclinic connection from Figure 5.7 into a parametrization with respect to the master coordinate γ. From the kinematic equation (5.21), the relation $\mathrm{c}\beta = -\frac{\dot{\gamma}}{\Omega}$ is identified. Together with the differential relation $\mathrm{d}t = \frac{\mathrm{d}\gamma}{\dot{\gamma}}$, Eq. (5.42) is integrated by substitution, resulting in the finite γ-integral:

$$\begin{aligned}\mathscr{M}_1 = \frac{\Omega^3}{\mu m g}\int_{-\pi/2}^{+3\pi/2} \frac{\cos\beta_c(\gamma)}{(r+e\,\mathrm{s}\gamma)^2}\cdot\Big[A\,\mathrm{c}^2\gamma(r^2 - er\,\mathrm{s}\gamma - 2e^2)\\ +\bar{B}r\,\mathrm{s}\gamma\Big(r\,\mathrm{s}\gamma + e + e\,\mathrm{c}^2\gamma\Big) - \frac{mg(r+e\,\mathrm{s}\gamma)^4}{\Omega^2(r-e)}\Big]\mathrm{d}\gamma.\end{aligned}$$

As the Melnikov function $\mathscr{M}_1$ has to vanish, the constant prefactor of the integral can be neglected, which implies the introduction of the scaled Melnikov function $\hat{\mathscr{M}}_1 := \mathscr{M}_1\frac{\mu m g}{\Omega^3}$. Introducing the dimensionless parameters

$$\begin{aligned}&\text{inertia ratio:} && \zeta := \tfrac{A}{\bar{B}},\\ &\text{eccentricity ratio:} && \kappa := \tfrac{e}{r},\end{aligned} \tag{5.43}$$

as well as the integrals

$$\mathscr{I}_1(\kappa,\zeta) := \int_{-\frac{\pi}{2}}^{+3\frac{\pi}{2}} \frac{\cos\beta_c(\gamma)}{(1+\kappa\,\mathrm{s}\gamma)^2}\cdot\Big[\zeta\,\mathrm{c}^2\gamma(1-\kappa\,\mathrm{s}\gamma - 2\kappa^2) + \mathrm{s}\gamma\Big(\mathrm{s}\gamma + \kappa + \kappa\,\mathrm{c}^2\gamma\Big)\Big]\,\mathrm{d}\gamma \tag{5.44}$$

and

$$\mathscr{I}_2(\kappa,\zeta) := \int_{-\frac{\pi}{2}}^{+3\frac{\pi}{2}} \cos\beta_c(\gamma)\,\frac{(1+\kappa\,\mathrm{s}\gamma)^2}{(1-\kappa)}\,\mathrm{d}\gamma, \tag{5.45}$$

finally gives the necessary condition for a heteroclinic saddle connection:

$$0 = \hat{\mathscr{M}}_1 = \bar{B}\,\mathscr{I}_1 - \frac{mgr}{\Omega^2}\,\mathscr{I}_2 \tag{5.46}$$

The spinning velocity

$$\Omega_\mathrm{h}^2 = \frac{mgr}{\bar{B}}\,\frac{\mathscr{I}_2}{\mathscr{I}_1}, \tag{5.47}$$

solves Eq. (5.46), characterizing the heteroclinic bifurcation point. With the inertia ratio ζ and the eccentricity ratio κ from Eq. (5.43), the critical rotational velocity Ω_c of the Hopf bifurcation, from Eq. (4.74), can be rewritten as

$$\Omega_\mathrm{c} = \sqrt{\frac{mgr}{\bar{B}}\,(1+\kappa)^2}.$$

Combination of this critical spinning speed and Eq. (5.47) allows the definition of the dimensionless ratio

$$\nu(\kappa,\zeta) := \left(\frac{\Omega_\mathrm{h}}{\Omega_\mathrm{c}}\right)^2 = \frac{1}{(1+\kappa)^2}\,\frac{\mathscr{I}_2}{\mathscr{I}_1}, \tag{5.48}$$

between heteroclinic and Hopf bifurcation, in dependence of the dimensionless integrals $\mathscr{I}_1$ and $\mathscr{I}_2$.

To get an estimate of the heteroclinic spinning speed Ω_h, the two integrals $\mathscr{I}_1$ and $\mathscr{I}_2$ must be solved, but in general there is no closed-form solution.

Melnikov approximation of the heteroclinic orbit

For the tippedisk with dimensions and inertia properties from Table 2.1, the dimensionless eccentricity ratio

$$\kappa = \tfrac{e}{r} = 0.056$$

is small, and it is therefore a perturbation parameter. This motivates asymptotic expansions that subsequently provide closed-form approximations of the integrals $\mathscr{I}_{1,2}$ and thus an approximate characterization of the heteroclinic spinning speed Ω_h.

Along the *upper* critical saddle connection Γ_c, the rolling angle γ increases with time, i.e., $\dot{\gamma} > 0$. Therefore, the kinematic equation $\dot{\gamma} = -\Omega\cos\beta$ implies that the cosine $\cos\beta_\mathrm{c}$ is negative for any point on the saddle connection, i.e., the trigonometric identity

$$\cos\beta_c = -\sqrt{1-\sin^2\beta_c}$$

holds. Substitution of the parametrization $\beta_c(\gamma)$ from Eq. (5.36) and the identification of the dimensionless quantities yields

$$\cos\beta_c = -\sqrt{1-\sin^2\left(\pi - \sin^{-1}\left(\frac{1-\kappa}{1+\kappa\sin\gamma}\right)\right)}. \tag{5.49}$$

As the sine function is uneven and has 2π-periodicity, the identity $\sin(\pi - *) = -\sin(-(\pi - *)) = -\sin(* - \pi) = \sin(*)$ holds, allowing to transform Eq. (5.49) to

$$\cos\beta_c = -\sqrt{\kappa}\,\frac{\sqrt{2(\sin\gamma+1)+\kappa(\sin^2\gamma-1)}}{1+\kappa\sin\gamma}. \tag{5.50}$$

Substitution of this representation of $\cos\beta_c$ into the integral expression $\mathscr{I}_2$ from Eq. (5.45) yields

$$\mathscr{I}_2 = -\frac{\sqrt{\kappa}}{(1-\kappa)}\left[\int_{-\frac{\pi}{2}}^{+3\frac{\pi}{2}} \sqrt{2(\mathrm{s}\gamma+1)+\kappa(\mathrm{s}^2\gamma-1)}\,\big(1+\kappa\mathrm{s}\gamma\big)\,\mathrm{d}\gamma\right]. \tag{5.51}$$

Introduction of the first-order expansion

$$\sqrt{2(\mathrm{s}\gamma+1)+\kappa(\mathrm{s}^2\gamma-1)}=\sqrt{2(\mathrm{s}\gamma+1)}\left(1+\frac{\mathrm{s}\gamma-1}{4}\kappa\right)+\mathcal{O}(\kappa^2)$$

allows to approximate the integral

$$\mathscr{I}_2\approx-\frac{\sqrt{\kappa}}{(1-\kappa)}\left[\int_{-\frac{\pi}{2}}^{+3\frac{\pi}{2}}\sqrt{2(\mathrm{s}\gamma+1)}+\left(\frac{5}{4}\sqrt{2(\mathrm{s}\gamma+1)}\,\mathrm{s}\gamma-\frac{1}{4}\sqrt{2(\mathrm{s}\gamma+1)}\right)\kappa\,\mathrm{d}\gamma\right]\tag{5.52}$$

up to orders $\mathcal{O}(\kappa^{5/2})$ in the eccentricity ratio κ. However, having a close look at the prefactor

$$\frac{\sqrt{\kappa}}{(1-\kappa)}=\sqrt{\kappa}(1+\kappa)+\mathcal{O}(\kappa^{5/2})$$

reveals the presence of higher-order terms in Eq. (5.52) and thus an inconsistent approximation. Neglecting all orders $\mathcal{O}(\kappa^{5/2})$ and considering the above expansion of the prefactor results in the consistent approximation

$$\mathscr{I}_2\approx-\sqrt{\kappa}\left[\int_{-\frac{\pi}{2}}^{+3\frac{\pi}{2}}\sqrt{2(\mathrm{s}\gamma+1)}+\left(\frac{5}{4}\sqrt{2(\mathrm{s}\gamma+1)}\,\mathrm{s}\gamma+\frac{3}{4}\sqrt{2(\mathrm{s}\gamma+1)}\right)\kappa\,\mathrm{d}\gamma\right]$$

of the integral $\mathscr{I}_2$. Identification of the Integrals I_1 and I_2 from Section B.1 finally yields the definite integral

$$\mathscr{I}_2\approx-\sqrt{\kappa}\left[I_1+\left(\frac{5}{4}I_2+\frac{3}{4}I_1\right)\kappa\right]=-\sqrt{\kappa}\left[8+\frac{28}{3}\kappa\right].\tag{5.53}$$

Likewise, the integral $\mathscr{I}_1$ must be evaluated to obtain a closed-form expression for the heteroclinic rotational velocity Ω_h. Substitution of Eq. (5.50) into Eq. (5.44) yields after some basic algebraic transformations the integral

$$\begin{aligned}\mathscr{I}_1=-\sqrt{\kappa}\int_{-\frac{\pi}{2}}^{+3\frac{\pi}{2}}&\frac{\sqrt{2(\mathrm{s}\gamma+1)+\kappa(\mathrm{s}^2\gamma-1)}}{(1+\kappa\,\mathrm{s}\gamma)^3}\\&\cdot\left[\zeta\,\mathrm{c}^2\gamma\left(1-\kappa\,\mathrm{s}\gamma-2\kappa^2\right)+\mathrm{s}\gamma\left(\mathrm{s}\gamma+\kappa\left(1+\mathrm{c}^2\gamma\right)\right)\right]\mathrm{d}\gamma.\end{aligned}$$

The asymptotic Taylor series approximations

$$\frac{\sqrt{2(\mathrm{s}\gamma+1)+\kappa(\mathrm{s}^2\gamma-1)}}{(1+\kappa\,\mathrm{s}\gamma)^3}=\sqrt{2(\mathrm{s}\gamma+1)}\left(1-\frac{11\mathrm{s}\gamma+1}{4}\kappa\right)+\mathcal{O}(\kappa^2)$$

and

$$\begin{aligned}&\left[\zeta\,\mathrm{c}^2\gamma\left(1-\kappa\,\mathrm{s}\gamma-2\kappa^2\right)+\mathrm{s}\gamma\left(\mathrm{s}\gamma+\kappa\left(1+\mathrm{c}^2\gamma\right)\right)\right]\\&=1+(\zeta-1)\mathrm{c}^2\gamma+\left(\mathrm{s}\gamma+(1-\zeta)\,\mathrm{s}\gamma\,\mathrm{c}^2\gamma\right)\kappa+\mathcal{O}(\kappa^2)\end{aligned}$$

allow to approximate the integral $\mathscr{I}_1$ up to orders $\mathscr{O}(\kappa^{5/2})$ as

$$\mathscr{I}_1 = -\sqrt{\kappa}\int_{-\frac{\pi}{2}}^{+3\frac{\pi}{2}} \sqrt{2(\mathrm{s}\gamma+1)}\Big(1-\frac{11\,\mathrm{s}\gamma+1}{4}\kappa\Big) \cdot\Big[1+(\zeta-1)\mathrm{c}^2\gamma+\Big(\mathrm{s}\gamma+(1-\zeta)\mathrm{s}\gamma\,\mathrm{c}^2\gamma\Big)\kappa\Big]\mathrm{d}\gamma+\mathscr{O}(\kappa^{5/2}).$$

Decomposition of the integral $\mathscr{I}_1$ into subintegrals and neglecting higher-order κ-terms yields

$$\begin{aligned}\mathscr{I}_1 \approx -\sqrt{\kappa}\Big[&\int_{-\frac{\pi}{2}}^{+3\frac{\pi}{2}} \sqrt{2(\mathrm{s}\gamma+1)}\,\mathrm{d}\gamma\left(1-\frac{1}{4}\kappa\right)+\int_{-\frac{\pi}{2}}^{+3\frac{\pi}{2}} \sqrt{2(\mathrm{s}\gamma+1)}\,\mathrm{s}\gamma\,\mathrm{d}\gamma\left(-\frac{7}{4}\kappa\right)\\ &+\int_{-\frac{\pi}{2}}^{+3\frac{\pi}{2}} \sqrt{2(\mathrm{s}\gamma+1)}\,\mathrm{c}^2\gamma\,\mathrm{d}\gamma\,(\zeta-1)\left(1-\frac{1}{4}\kappa\right)\\ &+\int_{-\frac{\pi}{2}}^{+3\frac{\pi}{2}} \sqrt{2(\mathrm{s}\gamma+1)}\,\mathrm{s}\gamma\,\mathrm{c}^2\gamma\,\mathrm{d}\gamma\,\frac{15}{4}(1-\zeta)\kappa\Big],\end{aligned}$$

which can be simplified by identifying the definite integrals I_1, I_2, I_3, and I_4 from the Section B.1 to

$$\mathscr{I}_1 \approx -\sqrt{\kappa}\Big[I_1\left(1-\frac{1}{4}\kappa\right)+I_2\left(-\frac{7}{4}\kappa\right)+I_3\,(\zeta-1)\left(1-\frac{1}{4}\kappa\right)+I_4\,\frac{15}{4}(1-\zeta)\kappa\Big]. \tag{5.54}$$

The subsequent evaluation of the Integral $\mathscr{I}_1$ yields

$$\mathscr{I}_1 \approx -\sqrt{\kappa}\left(\left[\frac{56}{15}-\frac{116}{35}\kappa\right]+\left[\frac{64}{15}-\frac{352}{105}\kappa\right]\zeta\right). \tag{5.55}$$

Substitution of the approximated definite integrals $\mathscr{I}_1$ and $\mathscr{I}_2$ from Eq. (5.55) and Eq. (5.53) into Eq. (5.48) gives the quadratic ratio

$$\nu_1 = \frac{1}{(1+\kappa)^2}\,\frac{\left[8+\frac{28}{3}\kappa\right]}{\left(\left[\frac{56}{15}-\frac{116}{35}\kappa\right]+\left[\frac{64}{15}-\frac{352}{105}\kappa\right]\zeta\right)} \approx \nu \tag{5.56}$$

of the heteroclinic spinning speed Ω_h to the critical spinning speed Ω_c. Since the eccentricity $e \ll 1$ is very small, even linear terms in eccentricity ratio κ may be neglected, resulting in an even coarser approximation

$$\nu_2 = \frac{15}{7+8\zeta} \approx \nu \tag{5.57}$$

of the spinning speed ratio ν. For small eccentricity ratios $\kappa \ll 1$, the condition

$$\zeta > 1 \Longrightarrow \nu < 1 \Longrightarrow \Omega_\mathrm{h} < \Omega_\mathrm{c} \quad \text{and} \quad \zeta < 1 \Longrightarrow \nu > 1 \Longrightarrow \Omega_\mathrm{h} > \Omega_\mathrm{c} \tag{5.58}$$

describes whether the heteroclinic bifurcation occurs before or after the Hopf bifurcation.

Harmonic balance approximation

In Section 4.4, the Hamonic balance method is used to characterize the Hopf bifurcation at the critical spinning speed Ω_c as a supercritical one. In order to simplify the Melnikov integrals, the dimensionless quantities κ and ζ were introduced in the previous section, allowing also to reformulate the amplitude

$$C = 2\sqrt{\kappa}\sqrt{\frac{\Omega_\mathrm{c}^2 - \Omega^2}{\zeta - 1 + \mathcal{O}(\kappa)}} + \mathcal{O}(\kappa^2),$$

from Eq. (4.72), where the eccentricity ratio κ takes the role of a regular perturbation parameter. This expansion shows that the numerator $\Omega_\mathrm{c}^2 - \Omega^2$ switches sign from positive to negative at the critical spinning speed $\Omega = \Omega_\mathrm{c}$. A periodic solution exists only if the amplitude C is real, i.e., if the argument of the square root is positive. Therefore, the denominator determines the type of Hopf bifurcation, implying the condition

$$\zeta \lesseqgtr 1 + \mathcal{O}(\kappa) \tag{5.59}$$

for a subcritical (<) and supercritical (>) Hopf bifurcation. This condition is in agreement with Eq. (5.58).

5.4 Bifurcation diagram

For the specimen with dimension and mass properties from Table 2.1, the bifurcation scenario as analyzed in Section 5.3 (shown in Figures 5.2 and 5.3) is characterized by a heteroclinic saddle connection followed by a supercritical Hopf bifurcation. As a consequence of the singularly perturbed dynamical structure, the asymptotic dynamics takes place on a slow manifold $\mathscr{M}_S$. The reduced dynamics on this slow manifold is described by the two-dimensional system (5.24), with dynamics depicted in Figure 5.6. The asymptotic behavior of the three-dimensional and the reduced two-dimensional dynamics is similar. In particular, for increasing spinning speeds Ω, a heteroclinic bifurcation occurs at Ω_h, where a stable periodic solution arises. This periodic solution shrinks even further if Ω is increased and finally vanishes at a supercritical Hopf bifurcation, characterized by Ω_c.

To compare the quantitative accordance, Figure 5.8 depicts the numerical bifurcation diagram with respect to the maximal γ-amplitude $\bar{\gamma}_\mathrm{max}$ of the periodic solution, relative to the inverted spinning equilibrium at $\gamma = \frac{\pi}{2}$. Inverted spinning is characterized by the solid line at zero. For subcritical spinning speeds $\Omega < \Omega_\mathrm{c}$, the inverted equilibrium is unstable and depicted in blue. For supercritical spinning

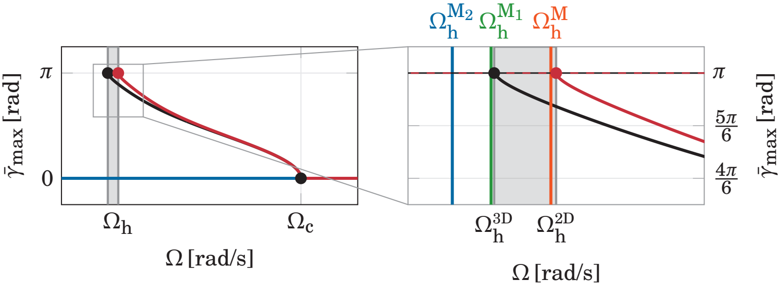

Figure 5.8: Bifurcation diagram with respect to the γ-amplitude, i.e., $\bar{\gamma}_{\max} := \max\big(\gamma(t)\big) - \frac{\pi}{2}$: The unstable inverted spinning is marked blue, whereas stable spinning is indicated by a red line at zero. The branches of stable periodic solutions have been obtained numerically, using the shooting method. The black curve characterizes periodic solutions of the three-dimensional singularly perturbed system given Eq. (5.18). The red branch corresponds to the periodic solution of the reduced system Eq. (5.24) on the two-dimensional slow manifold $\mathscr{M}_s$.

speeds $\Omega > \Omega_{\mathrm{c}}$, inverted spinning corresponds to an asymptotically stable equilibrium point, indicated by a red line at zero. The small difference between the red and black branches of periodic solutions stems from the fact that the slow manifold $\mathscr{M}_s$ has only been approximated up to first-order terms in ε, see Eq. (5.24). The accuracy of the two-dimensional dynamics on $\mathscr{M}_s$ may be increased by increasing the approximation order of the perturbation expansion. In the right magnification of Figure 5.8, $\Omega_{\mathrm{h}}^{\mathrm{3D}}$ corresponds to the heteroclinic spinning speed of the three-dimensional system from Eq. (5.18) which has been obtained in Section 4.5 by the application of numerical shooting. Equivalently, $\Omega_{\mathrm{h}}^{\mathrm{2D}}$ characterizes the heteroclinic bifurcation point of the reduced dynamics on the slow manifold. According to the Melnikov function method, the heteroclinic spinning speed is given by Eq. (5.48). The heteroclinic spinning speed $\Omega_{\mathrm{h}}^{\mathrm{M}}$ in red results from numerically solving the definite integrals $\mathscr{I}_1$ and $\mathscr{I}_2$ in the Melnikov condition Eq. (5.48). The two approximations ν_1, ν_2 from Eq. (5.56) and Eq. (5.57), which differ in accuracy, yield the closed-form approximations $\Omega_{\mathrm{h}}^{\mathrm{M}_1}$ and $\Omega_{\mathrm{h}}^{\mathrm{M}_2}$. Both periodic solutions of the three-dimensional and two-dimensional system (black and red), respectively, finally vanish at the same critical spinning speed Ω_{c} of the Hopf bifurcation given in Eq. (4.55).

In Table 5.1, a summary of the spinning speeds Ω is given, characterizing the bifurcation points.

Table 5.1: Different spinning speeds Ω characterizing the bifurcation points of *V1*.

Bifurcation	Symbol	Magnitude	Origin
Heteroclinic	$\Omega_\mathrm{h}^{\mathrm{3D}}$	$30.07\,\frac{\mathrm{rad}}{\mathrm{s}}$	Shooting method
Heteroclinic	$\Omega_\mathrm{h}^{\mathrm{M_2}}$	$30.04\,\frac{\mathrm{rad}}{\mathrm{s}}$	Melnikov approximation, Eq. (5.57)
	$\Omega_\mathrm{h}^{\mathrm{M_1}}$	$30.07\,\frac{\mathrm{rad}}{\mathrm{s}}$	Melnikov approximation, Eq. (5.56)
	$\Omega_\mathrm{h}^{\mathrm{M}}$	$30.11\,\frac{\mathrm{rad}}{\mathrm{s}}$	Melnikov analysis, Eq. (5.48)
	$\Omega_\mathrm{h}^{\mathrm{2D}}$	$30.12\,\frac{\mathrm{rad}}{\mathrm{s}}$	Shooting method
Hopf	Ω_c	$30.92\,\frac{\mathrm{rad}}{\mathrm{s}}$	Derived in Eq. (4.55)

5.5 Variants of the tippedisk

All above sections consider as system parameters the dimension and inertia properties from Table 2.1 belonging to a real specimen, which will be referred to as type *V1* tippedisk in the following. For this specimen, the dimensionless quantities from Eq. (5.43), are $\zeta = 1.112$ and $\kappa = 0.056$.

Since the eccentricity ratio $\kappa \ll 1$ is small, the approximation of Eq. (5.57) holds and states for $\zeta > 1$ that the ratio ν is smaller than one, i.e., the heteroclinic bifurcation occurs before the Hopf bifurcation. In addition, the HBM approximation of Eq. (6.11) identifies the Hopf bifurcation as a supercritical one. These statements are consistent with the bifurcation scenario presented in Figure 5.8, which shows a heteroclinic bifurcation followed by a supercritical Hopf bifurcation.

However, the question arises whether another type of tippedisk can be constructed, for which these bifurcations occur in reverse order ($\nu > 1$) and the Hopf bifurcation is subcritical ($\zeta < 1$). Such a tippedisk may perhaps be designed using a well chosen pattern of holes. Instead, here, a additional mass is added to an homogeneous disk. Figure 5.9 shows a new variant *V2* of the tippedisk, which has essentially the same geometrical dimensions as the tippedisk *V1*, but the hole is filled with a cylinder of height c. The density is chosen to be $\rho = 7700\,\mathrm{kg/m^3}$. For consistency with the previous analysis, the rounding of the disk is neglected in the calculation of moments of inertia. The associated geometry and inertia properties are shown in Table 5.2. Although the inertia properties of the tippedisk *V1* and *V2* are different, both variants exhibit the phenomenon of inversion, i.e., the rise of the center of gravity if the disk is rotated fast enough.

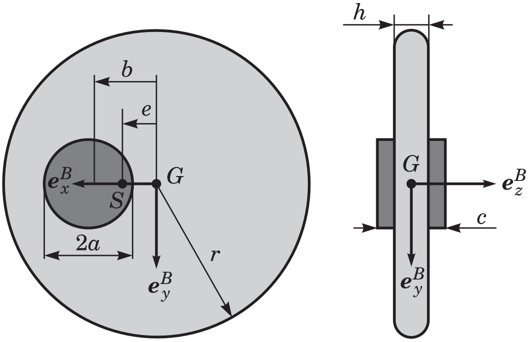

Figure 5.9: Dimensions of the tippedisk variant *V2*.

Table 5.2: Dimensions and mass properties of the tippedisk *V2* with added mass.

Property	Parameter	Magnitude	Unit
Disk radius	r	0.045	m
Cylinder radius	a	0.015	m
Distance	b	0.02	m
Mass height	c	0.02	m
Disk thickness	h	0.01	m
Eccentricity	e	$2\cdot10^{-3}$	m
Mass	m	0.544	kg
${}_B\boldsymbol{\Theta}_G(1,1)$	A	$0.258\cdot10^{-3}$	kg m^2
${}_B\boldsymbol{\Theta}_G(2,2)$	B	$0.280\cdot10^{-3}$	kg m^2
${}_B\boldsymbol{\Theta}_G(3,3)$	C	$0.524\cdot10^{-3}$	kg m^2
${}_B\boldsymbol{\Theta}_S(2,2)$	$\bar{B}$	$0.278\cdot10^{-3}$	kg m^2
Eccentricity ratio	κ	0.044	-
Inertia ratio	ζ	0.928	-

The local stability analysis of Section 4.3 and the harmonic balance results from Section 4.4 imply for type *V2* a subcritical Hopf bifurcation at

$$\text{Variant } \mathit{V2}: \qquad \Omega_\mathrm{c} = \sqrt{\frac{(r+e)^2}{r}\frac{mg}{\bar{B}}} = 30.70\,\tfrac{\mathrm{rad}}{\mathrm{s}}, \tag{5.60}$$

as $A < \bar{B} \implies \zeta < 1$ holds. For $\Omega < \Omega_\mathrm{c}$, inverted spinning is unstable. If $\Omega > \Omega_\mathrm{c}$, the inverted spinning motion is stable and locally attractive, and an unstable periodic solution shields the domain of attraction. Evaluation of the Melnikov condition Eq. (5.48) yields the approximation

$$\text{Variant } \mathit{V2}: \qquad \Omega_\mathrm{h}^\mathrm{M} = 31.36\,\tfrac{\mathrm{rad}}{\mathrm{s}},$$

characterizing a heteroclinic saddle connection at a spinning speed Ω_h larger than the critical rotational velocity Ω_c. With that, one might argue that the unstable periodic solution emerging from the Hopf bifurcation vanishes at a heteroclinic bifurcation point.

However, the numerically obtained bifurcation diagram in Figure 5.10 shows a different bifurcation scenario for the tippedisk of type *V2*. In particular, a subcritical Hopf bifurcation occurs at Ω_c. The amplitude of the emerging unstable periodic limit cycle increases with increasing spinning speed. At Ω_h, a heteroclinic bifurcation occurs, giving rise to a stable periodic orbit for $\Omega > \Omega_\mathrm{h}$. The unstable and stable periodic limit cycles collide at a fold bifurcation Ω_f and cancel out. For $\Omega > \Omega_\mathrm{f}$, the domain of attraction extends to the non-inverted spinning equilibrium, i.e., almost all trajectories are attracted by the inverted spinning motion. To obtain the bifurcation diagram, numerical shooting was used in combination with arc length continuation to overcome the fold bifurcation point with vertical tangent [2]. The two values $\Omega_\mathrm{h}^\mathrm{2D}$ and Ω_f characterizing the heteroclinic and fold bifurcations are determined from the numerical solution. The critical spinning speed is given in Eq. (5.60). Predictions of the heteroclinic spinning speed Ω_h result from the necessary condition of Eq. (5.48), where $\Omega_\mathrm{h}^\mathrm{M}$ is obtained by numerical evaluation. In contrast, the approximated heteroclinic spinning speeds $\Omega_\mathrm{h}^{\mathrm{M}_1}$ and $\Omega_\mathrm{h}^{\mathrm{M}_2}$ correspond to the asymptotic approximations in Eq. (5.56) and Eq. (5.57). Table 5.3 lists the different spinning speeds in an ascending order.

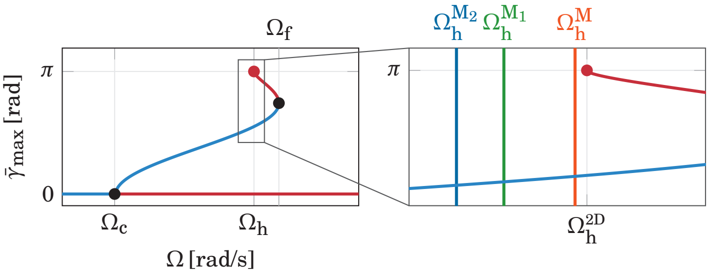

Figure 5.10: Bifurcation diagram for the singularly reduced dynamical system given in Eq. (5.24) with *V2* parameters, shown in Table 5.2: Unstable inverted spinning is marked blue, whereas stable spinning is indicated by a red line at zero. The branches of stable and unstable periodic solutions have been obtained numerically, using arc length continuation in combination with single shooting.

Table 5.3: Different spinning speeds Ω characterizing the bifurcation points of *V2*.

Bifurcation	Symbol	Magnitude	Origin
Hopf	Ω_c	$30.70\,\frac{\text{rad}}{\text{s}}$	cf. Eq. (5.60)
Heteroclinic	$\Omega_h^{M_2}$	$31.31\,\frac{\text{rad}}{\text{s}}$	Melnikov approximation, E. (5.57)
	$\Omega_h^{M_1}$	$31.33\,\frac{\text{rad}}{\text{s}}$	Melnikov approximation, Eq. (5.56)
	Ω_h^{M}	$31.36\,\frac{\text{rad}}{\text{s}}$	Melnikov analysis, Eq. (5.48)
	Ω_h^{2D}	$31.37\,\frac{\text{rad}}{\text{s}}$	Shooting method
Fold	Ω_f	$31.48\,\frac{\text{rad}}{\text{s}}$	Shooting method

CHAPTER 6

Global analysis

The previous chapters illuminated the dynamics of the tippedisk for specific specimens. Two different types with the same main geometric dimensions but different inertia properties were considered, both exhibiting the phenomenon of inversion but differing qualitatively in dynamic behavior. To obtain a better insight into the dynamics, it is advantageous to introduce dimensionless quantities to analyze the influence of parameters characterizing the qualitative behavior.

Finally, the analysis of the normalized dynamics on a slow manifold yields a complete stability chart that characterizes the qualitative behavior of the tippedisk and allows to identify different variants, implying different qualitative bifurcation scenarios.

6.1 Normalized system equations

To study the influence of parameters, the singularly perturbed system from Eq. (5.18) is normalized with respect to the slow coordinates

$$\mathsf{x} = \begin{bmatrix} \beta \\ \gamma \end{bmatrix} \in \mathbb{R}^2$$

and the dimensionless velocity $\mathsf{y} := \frac{\dot{\beta}}{\Omega} = \frac{y}{\Omega}$, all as functions of the dimensionless time $\mathsf{t} := t\Omega$.[1] Furthermore, the normalized spinning speed

$$\omega := \sqrt{\frac{\bar{B}}{mgr}}\Omega = \frac{\Omega}{\Omega_\mathrm{c}}(1+\kappa) \tag{6.1}$$

is defined. Here, without loss of generality, $\Omega > 0$ is considered and correspondingly, in view of $\kappa > 0$, $\omega > 0$. In addition, the normalized perturbation parameter $\epsilon := \frac{\varepsilon}{\Omega r}$ as well as the sphericity ψ are introduced and listed in Table 6.1, along with the dimensionless eccentricity ratio κ and the inertia ratio ζ, defined in Eq. (5.43). Moreover, the associated values for the previously discussed tippedisk types *V1* and *V2* are also listed.

Table 6.1: Dimensionless parameters of the tippedisk.

Dimensionless parameter	Definition	*V1*	*V2*
eccentricity ratio	$\kappa := \frac{e}{r} \in (0, 0.1]$	0.056	0.044
inertia ratio	$\zeta := \frac{A}{\bar{B}} \in \mathbb{R}^+$	1.112	0.928
sphericity	$\psi := \frac{mr^2}{\bar{B}} \in \mathbb{R}^+$	3.932	3.963
perturbation parameter	$\epsilon := \frac{\varepsilon}{\Omega r} \in \mathbb{R}^+$	-	-

Introducing the dimensionless quantities, the reduced dynamics of the tippedisk is governed by the three-dimensional singularly perturbed dynamical system

$$\begin{aligned} \mathbf{x}^\circ &= \mathbf{f}(\mathbf{x}, \mathsf{y}) \\ \epsilon \mathsf{y}^\circ &= \mathsf{g}_0(\mathbf{x}, \mathsf{y}) + \epsilon \mathsf{g}_1(\mathbf{x}, \mathsf{y}), \end{aligned}$$

where the time-derivative $\bullet^\circ := \frac{\partial}{\partial \mathsf{t}} \bullet$ denotes the derivative w.r.t. the dimensionless time t. Herein, the slow dynamics is determined by the function

$$\mathbf{f}(\mathbf{x}, \mathsf{y}) = \begin{bmatrix} \mathsf{y} \\ -\cos\beta \end{bmatrix},$$

whereas the fast dynamics is characterized by the zero- and first-order terms

$$\mathsf{g}_0(\mathbf{x}, \mathsf{y}) = -\mu \frac{(1+\kappa \mathrm{s}\gamma)\mathrm{s}^2\beta}{\mathsf{M}(\mathbf{x})\omega^2} \left((1+\kappa \mathrm{s}\gamma)\mathsf{y} - \kappa \mathrm{s}\beta \mathrm{c}\gamma\right),$$

---

[1] To distinguish between normalized and dimensioned quantities, a sans serif font is used to indicate normalized quantities.

and

$$\mathsf{g}_1(\mathbf{x},\mathsf{y}) = \frac{\mathrm{c}\beta}{\mathsf{M}(\mathbf{x})}\Bigg[(\zeta\mathrm{c}^2\gamma+\mathrm{s}^2\gamma)\mathrm{s}\beta - 2(\zeta-1)\mathrm{y}\,\mathrm{s}\gamma\mathrm{c}\gamma \\ +\psi\Big((1+\kappa\,\mathrm{s}\gamma)^2\mathrm{y}^2\,\mathrm{s}\beta+\kappa(1+\kappa\,\mathrm{s}\gamma)\mathrm{s}\beta\mathrm{c}^2\beta\mathrm{s}\gamma \\ -\kappa(1+\kappa\,\mathrm{s}\gamma)(3\mathrm{s}^2\beta-2)\mathrm{y}\,\mathrm{c}\gamma\Big) - \frac{(1+\kappa\mathrm{s}\gamma)}{\omega^2}\Bigg].$$

To shorten notation, the dimensionless mass 'matrix'

$$\mathsf{M}(\mathbf{x}) := \zeta\cos^2\gamma+\sin^2\gamma+\psi(1+\kappa\sin\gamma)^2\cos^2\beta$$

is used, which results from normalizing the mass matrix from Eq. (4.40) by the moment of inertia $\bar{B}$. According to the singularly perturbed structure of Eq. (5.18), the asymptotic dynamics takes place on the slow manifold $\mathscr{M}_s$. Therefore, the asymptotic normalized dynamics is governed by the dynamics

$$\mathbf{x}^{\circ} = \mathbf{f}(\mathbf{x},\mathsf{h}_s(\mathbf{x})) = \begin{bmatrix}\mathsf{h}_s(\mathbf{x})\\ -\cos\beta\end{bmatrix}, \tag{6.2}$$

on the slow manifold $\mathscr{M}_s$. Performing the singular perturbation reduction procedure up to and excluding quadratic orders $\mathscr{O}(\epsilon^2)$ yields the slow manifold

$$\mathscr{M}_s := \left\{(\mathbf{x},\mathsf{y})\in\mathbb{R}^3 \,\middle|\, \mathsf{y}=\mathsf{h}_s(\mathbf{x})=\mathsf{h}_c(\mathbf{x})+\epsilon\,\mathsf{h}_1(\mathbf{x}),\ \mathbf{x}\in\mathbb{R}^2\right\},$$

embedded in the dimensionless state-space. The associated zero- and first-order approximations are given as

$$\mathsf{h}_c(\mathbf{x}) = \frac{\kappa\mathrm{s}\beta\mathrm{c}\gamma}{1+\kappa\mathrm{s}\gamma}$$

and

$$\mathsf{h}_1(\mathbf{x}) = \frac{\omega^2\,\mathrm{c}\beta}{\mu\,\mathrm{s}\beta(1+\kappa\mathrm{s}\gamma)^4}\left[\zeta\mathrm{c}^2\gamma\Big(1-\kappa\mathrm{s}\gamma-2\kappa^2\Big)+\mathrm{s}\gamma\Big(\mathrm{s}\gamma+\kappa+\kappa\mathrm{c}^2\gamma\Big)-\frac{(1+\kappa\mathrm{s}\gamma)^3}{\omega^2\,\mathrm{s}\beta}\right].$$

6.2 Local stability analysis on the slow manifold

Chapter 4 analyzes the local behavior in the vicinity of inverted and non-inverted stationary spinning motions using Lyapunov's indirect method. In particular, the eigenvalues of the full system from Eq. (4.4) and the three-dimensional reduced system from Eq. (4.39) were linearized. In this section, Lyapunov's indirect method is applied to the two-dimensional normalized system from Eq. (6.2) to obtain local stability statements on the slow manifold. With respect to the chosen parametrization of the disk, the non-inverted stationary spinning solution is characterized by the state

$$\mathbf{x}^{-}=\begin{bmatrix}+\frac{\pi}{2} & -\frac{\pi}{2}\end{bmatrix}^{\mathrm{T}}, \tag{6.3}$$

whereas the inverted spinning equilibrium corresponds to

$$\mathbf{x}^{+}=\begin{bmatrix}+\frac{\pi}{2} & +\frac{\pi}{2}\end{bmatrix}^{\mathrm{T}}, \tag{6.4}$$

cf. the equilibria points from Eq. (5.27) and from Eq. (5.28). Due to trigonometric ambiguity, both spinning solutions occur with 2π periodicity in the rolling angle γ, e.g., the state $\mathbf{x}=\begin{bmatrix}\frac{\pi}{2}, \frac{3\pi}{2}\end{bmatrix}^{\mathrm{T}}$ is also identified as a non-inverted spinning equilibrium. As the stability properties of equivalent equilibria are the same, only $\mathbf{x}^{-}$ and $\mathbf{x}^{+}$ from Eq. (6.3) and Eq. (6.4), respectively, are considered in the following analysis.

Local stability of inverted spinning

To analyze the local stability behavior of inverted spinning on the two-dimensional slow manifold, the normalized reduced dynamics from Eq. (6.2) is linearized around the inverted stationary spinning motion $\mathbf{x}^{+}$ given in Eq. (6.4), resulting in the linear two-dimensional system

$$(\mathbf{x}-\mathbf{x}^{+})^{\circ}=\mathbf{A}^{+}(\mathbf{x}-\mathbf{x}^{+}),$$

where $\mathbf{A}^{+}$ is a constant linearization matrix given as

$$\mathbf{A}^{+}=\begin{bmatrix}a_{11}^{+} & a_{12}^{+}\\ 1 & 0\end{bmatrix}, \tag{6.5}$$

with the matrix coefficients

$$a_{11}^{+}=-\epsilon\frac{\omega^{2}-(1+\kappa)^{2}}{\mu(1+\kappa)^{3}}, \qquad a_{12}^{+}=-\frac{\kappa}{(1+\kappa)}. \tag{6.6}$$

Due to the special structure of the inverted linearization matrix $\mathbf{A}^{+}$ from Eq. (6.5), the characteristic polynomial is given by

$$p(\lambda)=\lambda^{2}-a_{11}^{+}\lambda-a_{12}^{+}$$

and has the roots

$$\lambda_{1,2}^{+}=\frac{a_{11}^{+}\pm\sqrt{{a_{11}^{+}}^{2}+4a_{12}^{+}}}{2},$$

which read after substitution of the matrix coefficients Eq. (6.6) as

$$\lambda_{1,2}^{+}=\frac{-\epsilon\big(\omega^{2}-(1+\kappa)^{2}\big)\pm\sqrt{\epsilon^{2}\big(\omega^{2}-(1+\kappa)^{2}\big)^{2}-4\mu^{2}\kappa(1+\kappa)^{5}}}{2\mu(1+\kappa)^{3}}. \tag{6.7}$$

The three-dimensional analysis of Section 4 (cf. Eq. (4.39)) reveals a Hopf bifurcation at $\Omega = \Omega_c$. Substitution of the critical spinning speed Ω_c into the definition of the normalized equivalence from Eq. (6.1) yields the critical spinning speed

$$\omega_c = 1 + \kappa \tag{6.8}$$

of the normalized system from Eq. (6.2). At $\omega = \omega_c$, a pair of complex conjugate eigenvalues

$$\lambda^+_{1,2} = \pm i \sqrt{\frac{\kappa}{1+\kappa}} \tag{6.9}$$

crosses the imaginary axis, implying again a Hopf bifurcation. Both the value of the critical spinning speed from Eq. (6.8) and the corresponding eigenvalues from Eq. (6.9) do not depend on friction parameters. In particular, the friction coefficient μ and the normalized smoothing parameter ϵ do not alter the critical value ω_c of the Hopf bifurcation. Here, the imaginary part of the complex conjugate eigenvalues of the two-dimensional normalized system on the slow manifold Eq. (6.9) corresponds to the normalized equivalent of the natural frequency at the Hopf bifurcation point, cf. the ansatz from Eq. (4.68).

The denominator of Eq. (6.7) is always greater than zero because the friction coefficient μ and the eccentricity ratio κ are both positive. The argument under the square root is negative for

$$\epsilon < 2\mu \frac{\sqrt{\kappa(1+\kappa)^5}}{\omega^2 - (1+\kappa)^2},$$

i.e., for small ϵ the stability of the inverted spinning solution is determined by the sign of

$$\Re(\lambda^+_{1,2}) \propto -1 + \left(\frac{1+\kappa}{\omega}\right)^2.$$

The real part vanishes at the critical spinning speed ω_c, validating the prediction from Eq. (6.8). For small eccentricity ratios, i.e., $\kappa \ll 1$, it holds that

$$\Re(\lambda^+_{1,2}) > 0 \quad \Leftrightarrow \quad \omega < \omega_c \quad \Leftrightarrow \quad \Omega < \Omega_c.$$

In summary, the inverted spinning configuration is unstable for $\omega < \omega_c$ and stable for $\omega > \omega_c$. This local stability statement is in accordance with the linear stability analysis of Section 4.3.

Harmonic balance approximation

Taking into account the dimensional results of the harmonic balance method in Section 4.4, the normalized amplitude

$$C = 2\,\frac{\sqrt{\kappa}}{\omega}\sqrt{\frac{(1+\kappa)^2-\omega^2}{\zeta-1+\mathcal{O}(\kappa)}} \tag{6.10}$$

results from substitution of Eq. (4.73) into the Eq. (4.72), followed by some algebra and identification of the dimensionless quantities defined in Table 6.1.

According to Eq. (6.10), the periodic solution exists if and only if the argument of the square root is positive. The numerator in the square root argument changes sign (from positive to negative) at the Hopf bifurcation point ω_c given in Eq. (6.8), while the approximate denominator is frequency independent and positive if the inertia ratio ζ is larger than one.

For $\zeta > 1$, the periodic limit cycle exists if the dimensionless spinning speed ω is subcritical, i.e., $\omega < \omega_\mathrm{c}$. Since the inverted spinning equilibrium is then unstable, the Hopf bifurcation is classified as a supercritical one. Vice versa, if $0 < \zeta < 1$, the periodic limit cycle exists for $\omega > \omega_\mathrm{c}$, implying a subcritical Hopf bifurcation where an unstable periodic solution emerges surrounding a stable equilibrium.

In summary, using the asymptotic harmonic balance approximation, the type of the Hopf bifurcation at the critical spinning speed ω_c depends on the inertia ratio

$$\zeta \lesseqgtr 1+\mathcal{O}(\kappa), \tag{6.11}$$

with $\zeta < 1$ leading to a subcritical Hopf bifurcation, while $\zeta > 1$ implies a supercritical one.

Local stability of non-inverted spinning

The above analysis showed that inverted spinning is locally asymptotically stable if the normalized spinning speed ω is larger than the critical value ω_c. If this condition is satisfied, only local attractivity of inverted spinning is guaranteed. However, the global behavior is also strongly influenced by the dynamics of the non-inverted spinning solution.

In this section, the stability properties of the non-inverted spinning configuration are studied. Linearizing the slow dynamics around equilibrium $\mathbf{x}^-$ from Eq. (6.3), which corresponds to the non-inverted spinning motion, gives the autonomous system

$$(\mathbf{x}-\mathbf{x}^-)^\circ = \mathbf{A}^-(\mathbf{x}-\mathbf{x}^-)$$

with linearization matrix

$$\mathbf{A}^{-} = \begin{bmatrix} a_{11}^{-} & a_{12}^{-} \\ 1 & 0 \end{bmatrix},$$

and corresponding coefficients

$$a_{11}^{-} = -\epsilon\frac{\omega^2 - (1-\kappa)^2}{\mu(1-\kappa)^3}, \qquad a_{12}^{-} = \frac{\kappa}{(1-\kappa)}.$$

Exploiting the κ-symmetry between inverted and non-inverted configurations, the eigenvalues for non-inverted spinning are obtained directly from Eq. (6.7) as

$$\lambda_{1,2}^{-} = \frac{-\epsilon\big(\omega^2 - (1-\kappa)^2\big) \pm \sqrt{\epsilon^2\big(\omega^2-(1-\kappa)^2\big)^2 + 4\mu^2\kappa(1-\kappa)^5}}{2\mu(1-\kappa)^3},$$

with positive denominator for $\kappa < 1$. The argument of the square root is positive for $\kappa < 1$, immediately showing that both eigenvalues are real. Since the determinant $\det A^{-} = -a_{12}^{-} < 0$ is negative, the first eigenvalue $\lambda_1^{-} > 0$ is larger and the second eigenvalue $\lambda_2^{-} < 0$ is smaller than zero, characterizing the non-inverted spinning solutions as an unstable saddle equilibrium. The same stability properties hold when linearization is performed around the second non-inverted equilibrium at $\mathbf{x}^{-} = [+\frac{\pi}{2}, +3\frac{\pi}{2}]^{\mathrm{T}}$. A heteroclinic saddle connection connecting both non-inverted spinning equilibria in β-γ-coordinates corresponds to a homoclinic orbit from a physical point of view, cf. the slow dynamics mapped on the unit sphere from Figure B.2

The stability of homoclinic orbits is determined by the saddle quantity $\sigma = \lambda_1^{-} + \lambda_2^{-}$ of the saddle equilibrium, cf. [68]. The saddle quantity of non-inverted spinning equals the first matrix coefficient

$$\sigma = a_{11}^{-} = -\epsilon\frac{\omega^2 - (1-\kappa)^2}{\mu(1-\kappa)^3}, \tag{6.12}$$

which is negative if the normalized spinning speed ω is larger than

$$\omega_\sigma = 1 - \kappa. \tag{6.13}$$

The sign of the saddle quantity σ plays an important role for the asymptotic behavior of the heteroclinic saddle connection, whose existence is discussed subsequently.

6.3 Global heteroclinic bifurcation

From the Melnikov function method applied in Section 5.3, the quadratic ratio ν between heteroclinic Ω_{h} and critical spinning speed Ω_{c} was introduced in Eq. (5.48), and allows to determine the heteroclinic spinning velocity as

$$\Omega_{\mathrm{h}}^2 = \nu \Omega_{\mathrm{c}}^2.$$

For a small eccentricity ratio $\kappa \ll 1$, the quadratic spinning speed ratio ν is approximated in closed-form by Eq. (5.57), resulting in

$$\Omega_{\mathrm{h}}^2 = \frac{15}{7+8\zeta} \Omega_{\mathrm{c}}^2,$$

from which the dimensionless heteroclinic spinning speed is obtained by normalization as

$$\omega_{\mathrm{h}} = \sqrt{\frac{15}{7+8\zeta}} (1+\kappa) > 0. \tag{6.14}$$

Subsequent identification of ω_{c} from Eq. (6.8) yields the relation

$$\omega_{\mathrm{h}} = \sqrt{\frac{15}{7+8\zeta}} \, \omega_{\mathrm{c}}. \tag{6.15}$$

According to Eq. (6.15), the relative position of the heteroclinic and the Hopf bifurcation is characterized by the dimensionless inertia ratio ζ, more precisely:

$$\zeta > 1 \Longleftrightarrow \omega_{\mathrm{h}} < \omega_{\mathrm{c}} \Longleftrightarrow \nu < 1 \Longleftrightarrow \Omega_{\mathrm{h}} < \Omega_{\mathrm{c}}. \tag{6.16}$$

A comparison of Eq. (6.11) with Eq. (6.16) shows that the two conditions, identifying the nature of the Hopf bifurcation and predicting the location of the heteroclinic saddle connection, are related. The Hopf bifurcation changes its type at $\zeta = 1$, that is, when the heteroclinic and the critical spinning speeds $\omega_{\mathrm{h}} = \omega_{\mathrm{c}}$ are equal, according to the Melnikov prediction.

The Andronov–Leontovich theorem [4] states that for planar systems the stability of a saddle connection depends on the sign of the associated saddle quantity, given in Eq. (6.12). In Eq. (6.13), the spinning velocity ω_σ is introduced which characterizes the sign change of the saddle quantity corresponding to the non-inverted spinning equilibrium. Therefore, the stability of the saddle connection at ω_{h} depends on the relative position of the heteroclinic bifurcation point with respect to the spinning speed ω_σ. It follows that the heteroclinic saddle connection is unstable from the inside if $\omega_{\mathrm{h}} < \omega_\sigma$, i.e., if σ is positive. Conversely, $\omega_{\mathrm{h}} > \omega_\sigma$ indicates a heteroclinic orbit that is stable from the inside, where σ is negative.

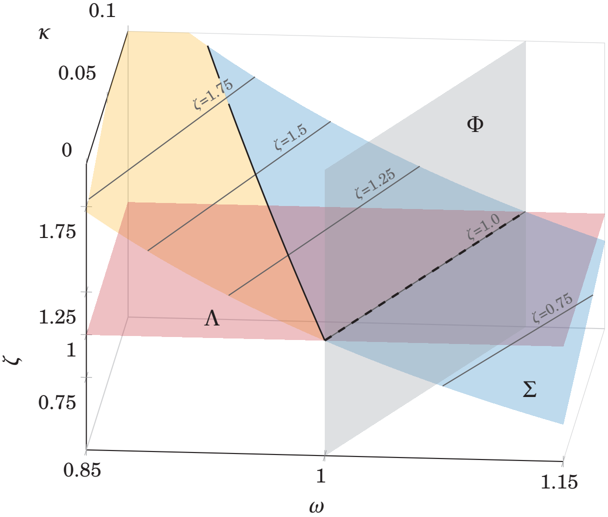

Figure 6.1: Three-dimensional parameter space, characterizing the qualitative behavior of the tippedisk. The gray manifold Φ is defined by Eq. (6.8) and specifies the critical spinning speed ω_c of the Hopf bifurcation determined by a local stability analysis of the inverted spinning equilibrium $\mathbf{x}^+$. Following the HBM approximation from Eq. (6.11), the red plane Λ, identifies the Hopf bifurcation as sub- or supercritical, with $\zeta < 1$ and $\zeta > 1$, respectively. The Melnikov approximation in Eq. (6.14) determines the location of the heteroclinic bifurcation and is represented by the manifold Σ. Following Andronov–Leontovich, this manifold is separated by Eq. (6.13) into two regions blue and yellow, classifying the heteroclinic saddle connection from the inside as stable and unstable, respectively.

6.4 Global stability chart

The behavior of the tippedisk during its inversion is governed by the asymptotic dynamics on the slow manifold. The main dimensionless parameters defining the qualitative dynamics of the corresponding normalized system from Eq. (6.2) are the eccentricity ratio κ, the inertia ratio ζ and the normalized spinning speed ω.

Figure 6.1 shows the dimensionless quantities ω, κ and ζ in the three-dimensional parameter space. The first condition of Eq. (6.8), determines the Hopf bifurcation point by a relation between the spinning speed ω_c and the eccentricity ratio κ. For

$\omega < \omega_\mathrm{c}$, the inverted spinning equilibrium is unstable. Vice versa, for $\omega > \omega_\mathrm{c}$, inverted spinning is stable. In Figure 6.1, the associated stability boundary is shown as a gray manifold Φ representing the critical spinning speed ω_c. Note that this manifold Φ does not depend on the inertia ratio ζ. Following the harmonic balance approximation from Eq. (6.11), the red hyperplane Λ at $\zeta = 1$ separates the parameter configurations by classifying the Hopf bifurcation as sub- or supercritical. Equation (6.14), defines the heteroclinic spinning speed ω_h for which a heteroclinic saddle connection occurs. According to the Andronov–Leontovich theorem [4], the saddle quantity σ of the non-inverted spinning equilibrium characterizes the stability of the corresponding heteroclinic orbit. Combination of Eq. (6.13) and Eq. (6.14) defines a manifold Σ which determines the heteroclinic spinning speed ω_h, separated into a blue and a yellow region by a solid black line representing the sign change of the saddle quantity σ at the associated heteroclinic spinning speed from Eq. (6.13). The blue region identifies the heteroclinic orbit as stable from the inside, while the yellow region implies a saddle connection that is unstable from inside. In addition, for five different inertia ratios $\zeta \in \{0.75, 1, 1.25, 1.5, 1.75\}$, the corresponding ζ-isoclines on the heteroclinic manifold Σ are shown by solid gray lines. The intersection of the red hyperplane Λ with the gray and blue manifolds Φ and Σ, respectively, coincides with the ζ-isocline for $\zeta = 1$ and is shown as a black dashed line. This relationship has already been discussed in short form in Section 6.3, cf. Eq. (6.16).

In summary, the qualitative behavior of the tippedisk is described by the four conditions specified in Eq. (6.8), Eq. (6.11), Eq. (6.13), and Eq. (6.14), which characterize the three-dimensional parameter space from Figure 6.1. To facilitate readability and interpretation of the three-dimensional parameter space, Figure 6.2 presents two two-dimensional projections, which offer a simplified visual representation for better comprehension.

Figure 6.2(a) shows the ζ-projection onto the ω-κ-plane. Here, the red and blue domains are separated by the dashed line that marks the Hopf bifurcation point. The solid black line representing the sign change of the saddle quantity σ from Eq. (6.12) separates the blue and yellow domain. In accordance to Figure 6.1, the ζ-isoclines are shown as gray curves. As Figure 6.2(a) results from a parallel projection in ζ-direction, and the critical spinning speed ω_c given in Eq. (6.8) does not depend on the inertia ratio ζ, the gray manifold from Figure 6.1 in this projection coincides with the dashed black intersection in this reduced representation.

From physical intuition, it seems obvious to take a specific tippedisk with fixed dimensions and inertia properties and to study the qualitative behavior in dependence of the rotational velocity. More precisely, the dimensionless velocity ω takes

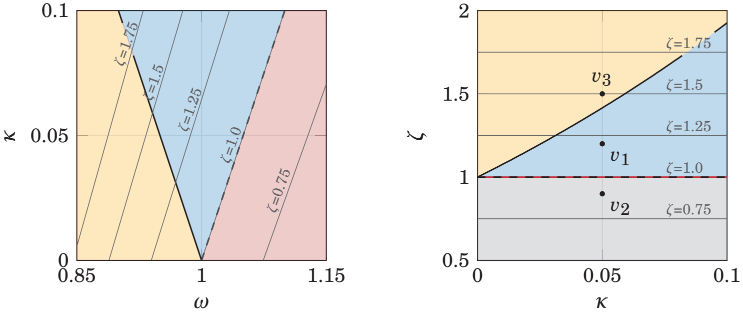

(a) ω-κ-projection

(b) κ-ζ-projection

Figure 6.2: Projected parameter space.

the role of a bifurcation parameter, whereas the dimensionless quantities κ and ζ are fixed parameters.

Figure 6.2(b) shows the projection of Figure 6.1 in ω-direction corresponding to the two-dimensional κ-ζ-parameter space which characterizes a real specimen. With respect to this parameter space, three different bifurcation scenarios are identified, represented by three parameter domains in gray, blue and yellow, separated by the solid and dashed black lines. Thus, there exist three different types of the tippedisk, which show inherently different qualitative behavior.

To study the qualitative behavior of each type, three characteristic points v_1, v_2, and v_3 are chosen in the κ-ζ-space from Figure 6.2(b), with the same fixed eccentricity ratio $\kappa = 0.05$, but varying inertia ratio $\zeta \in \{0.9, 1.2, 1.5\}$. Each point represents a type of tippedisk and thus implies a particular bifurcation scenario. According to Figure 6.1, only one manifold depends on the inertia ratio ζ, namely the manifold corresponding to the heteroclinic spinning velocity of the Melnikov estimate, so it suffices to study the projection of the three-dimensional parameter space onto the two-dimensional ω-κ-plane without loss of information. Therefore, Figure 6.3 shows a magnified ω-κ-projection and identifies the three regions I, II, and III separated by the solid and dashed black lines, respectively.

The black horizontal line at $\kappa = 0.05$ intersects the dashed line at the square mark. Therefore, all three variants have the same critical spinning speed $\omega_{\mathrm{c}}^{\star}$. The intersections with the respective ζ-isoclines determine the individual heteroclinic spinning speeds ω_{h_i}. To visualize the stability properties of the associated heteroclinic saddle connection, the points on the ζ-isocline are colored in red when the

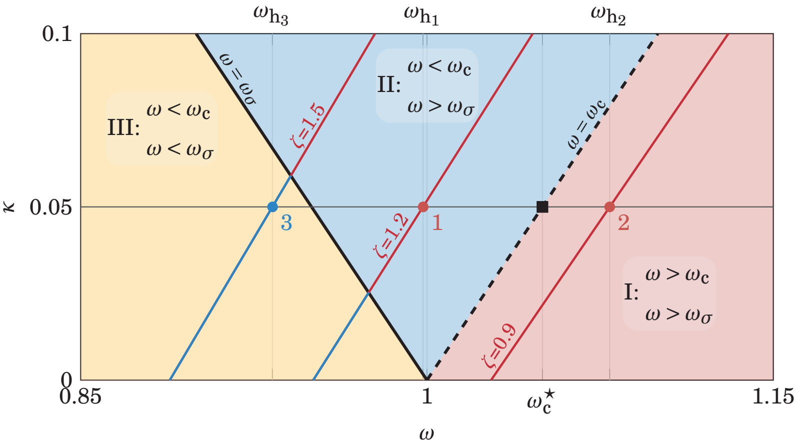

Figure 6.3: Stability chart for $0 < \kappa < 0.1$.

saddle quantity σ is negative. If $\kappa = 0.05$ intersects the red part of the ζ-isocline in the domain I or II, the heteroclinic saddle connection is from the inside stable. Vice versa, a blue intersection in the domain III indicates a from the inside unstable heteroclinic orbit. The two types v_1 and v_2 selected in Figure 6.2(b) result in the two corresponding intersections, denoted by the two red points 1 and 2 in Figure 6.3, characterizing two stable heteroclinic orbits at $\omega_{h_1} < \omega_c^\star$ and $\omega_{h_2} > \omega_c^\star$, respectively. Type v_3 yields the blue intersection 3, implying an unstable saddle connection at $\omega_{h_3} < \omega_c^\star$.

Consequently, the stability chart from Figure 6.3 determines the existence and stability properties of limit sets and classifies local Hopf bifurcations and global heteroclinic saddle connections of all tippedisk variants. All curves are given by closed-form expressions resulting from regular expansions. According to the stability chart, three different global bifurcation scenarios can be observed for three pairs of parameter combinations with $\kappa = 0.05$ and $\zeta \in \{0.9, 1.2, 1.5\}$, which are shown in Figure 6.4.

The left bifurcation diagrams depict the γ-amplitude in dependence on the bifurcation parameter ω, accompanied by the evolution of the period time T in the right diagrams. This representation of the γ-amplitude is advantageous because the periodic solution degenerates to a heteroclinic connection with dimensionless orbital time $T = \infty$, when the periodic solution approaches the non-inverted spinning equilibrium at $\gamma = 3\pi/2$. Since the spinning velocities ω_{h_i} at the heteroclinic bifurcation points result from ϵ-approximations in the Melnikov function theorem, there is a small discrepancy between predicted and real heteroclinic spinning speeds in Figure 6.4. Bifurcation points are shown as dots, with blue and red dots denoting unstable and stable heteroclinic saddle connections, respectively. All bifurcation diagrams are obtained using numerical shooting in combination with pseudo-arclength continuation to overcome fold bifurcations [3]. As the eccentricity ratio $\kappa = 0.05$ is kept constant, the eigenvalues for all three variants are the same, cf. Eq. (6.7). Using the critical eigenvalues from Eq. (6.9), the dimensionless time is defined as

$$\mathrm{T_c} := \frac{2\pi}{\mathscr{I}\left(\lambda_{1,2}^{+}\right)} = \frac{2\pi}{\sqrt{\frac{\kappa}{1+\kappa}}} \approx 28.79, \tag{6.17}$$

characterizing the normalized period time T of the periodic solution at the Hopf bifurcation point. For the three types v_1, v_2, and v_3 defined in Figure 6.2(b), the stability chart in Figure 6.3 predicts the following bifurcation scenarios.

v_1 $\kappa = 0.05$ and $\zeta = 1.2$: For subcritical normalized spinning speeds $\omega < \omega_{\mathrm{c}}^{\star}$, inverted spinning is unstable. At $\omega = \omega_{\mathrm{c}}^{\star}$, a supercritical Hopf bifurcation follows, characterized by a stable periodic solution surrounding the unstable equilibrium. If $\omega > \omega_{\mathrm{c}}^{\star}$, inverted spinning corresponds to a stable equilibrium. The Melnikov estimate of the heteroclinic bifurcation point $\omega_{\mathrm{h}_1} < \omega_{\mathrm{c}}^{\star}$ predicts the vanishing of a stable heteroclinic saddle connection.

Since both the periodic solution near the Hopf and the heteroclinic bifurcation point are stable, no additional fold bifurcation occurs so that the respective bifurcation points are directly connected, cf. the bifurcation diagram 6.4(a). Figure 6.4(b) reveals that with decreasing spinning speeds, the period time T increases from $\mathrm{T_c}$ at the Hopf bifurcation and diverges to $\mathrm{T} = \infty$ at the heteroclinic bifurcation point.

v_2 $\kappa = 0.05$ and $\zeta = 0.9$: At $\omega = \omega_{\mathrm{c}}^{\star}$, there is a subcritical Hopf bifurcation, where an unstable periodic orbit emerges from an equilibrium branch. The inverted spinning equilibrium at $\gamma = \pi/2$ is unstable for $\omega < \omega_{\mathrm{c}}^{\star}$ and stable for $\omega > \omega_{\mathrm{c}}^{\star}$. A global heteroclinic bifurcation follows for $\omega = \omega_{\mathrm{h}_2}$, where a stable heteroclinic saddle connection between the two non-inverted equilibria occurs.

The bifurcation diagram 6.4(c) is in accordance with the qualitative predictions. However, since the unstable periodic solution arising from the subcritical Hopf bifurcation degenerates into a stable heteroclinic saddle connection, an additional fold bifurcation must occur, altering the stability properties of the periodic orbit. The bifurcation scenario starts with a subcritical Hopf bifurcation at $\omega_{\mathrm{c}}^{\star}$, where an unstable periodic orbit is created. At ω_{h_2}, a stable periodic orbit arises from a heteroclinic saddle connection. Finally, the stable and unstable periodic orbits collide and vanish in a fold bifurcation at ω_{f_2}. The diagram from Figure 6.4(d) shows the corresponding period time T, with vertical tangent at the heteroclinic bifurcation point ω_{h_2}. Approaching the Hopf bifurcation causes the period time to converge to $\mathrm{T_c}$ defined in Eq. (6.17).

v_3 $\kappa = 0.05$ and $\zeta = 1.5$: Following the stability chart from Figure 6.3, the bifurcation scenario for type v_3 is characterized by a heteroclinic bifurcation at ω_{h_3} and a supercritical Hopf bifurcation at $\omega_{\mathrm{c}}^{\star}$. In contrast to the previous variants, the corresponding heteroclinic saddle connection is unstable from the inside, as the saddle quantity of the non-inverted spinning equilibria is positive. Consequently, an additional bifurcation must occur to achieve dynamic consistency.

The bifurcation diagram from Figure 6.4(e) shows that the stability of the periodic solution changes through an additional fold bifurcation, allowing to connect the unstable heteroclinic saddle connection with the branch of stable periodic orbits arising from the supercritical Hopf bifurcation. According to Figure 6.4(f), the period time at $\omega_{\mathrm{c}}^{\star}$ equals $\mathrm{T_c}$ and increases until it diverges to $\mathrm{T} = \infty$. In between, the period time takes the value $\mathrm{T}_{\mathrm{f}_3} = 64.53$ at the occurring fold bifurcation point $\omega_{\mathrm{f}_3} \approx 1.14$.

In summary, the stability chart from Figure 6.3 combines several closed-form conditions of the local stability analysis around the inverted and non-inverted spinning equilibria from Eq. (6.8) and (6.13), results of the harmonic balance method Eq. (6.11) and the approximation of the heteroclinic bifurcation using the Melnikov function method, cf. Eq. (6.14). Combining these conditions, three different domains I, II and III are distinguished, implying three different bifurcation scenarios, see Figures 6.4(c), 6.4(a) and 6.4(e). For a specific specimen, the intersection of the horizontal κ- and ζ-isocline characterizes the location and stability properties of the heteroclinic bifurcation point. The critical spinning velocity $\omega_{\mathrm{c}}^{\star}$, determining the Hopf bifurcation, depends only on the eccentricity ratio κ, while the inertia ratio ζ classifies the Hopf bifurcation as sub- or supercritical. In general, the qualitative dynamics of the tippedisk is characterized by a heteroclinic bifurcation, where a periodic solution arises from a heteroclinic saddle connection that shrinks and eventually vanishes in a Hopf bifurcation.

However, if the stability properties of the periodic solution do not agree with the stability properties of the heteroclinic saddle connection, an additional bifur-

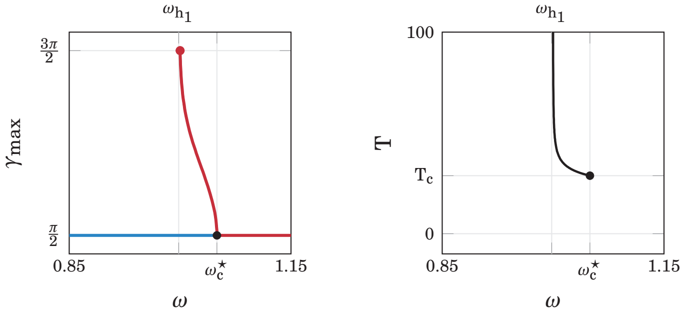

(a) Type v_1: γ-amplitude (b) Type v_1: Period time T

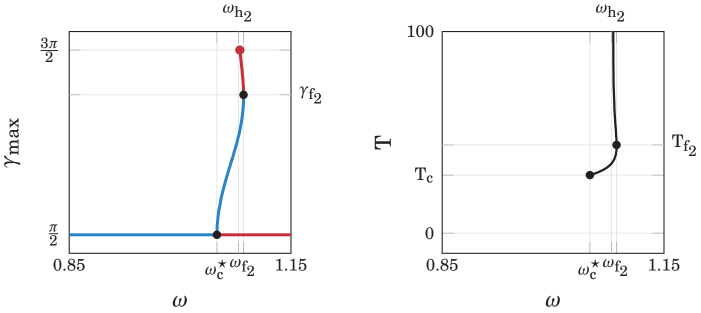

(c) Type v_2: γ-amplitude (d) Type v_2: Period time T

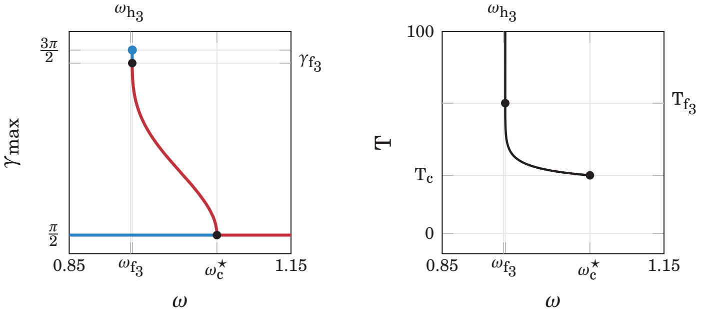

(e) Type v_3: γ-amplitude (f) Type v_3: Period time T

Figure 6.4: Bifurcation scenarios which correspond to the types v_1, v_2, and v_3 defined in Figure 6.2(a), each being a representative of an equivalence class with respect to the global behavior. The left diagrams show the γ-amplitude of periodic solutions and the inverted equilibrium at $\gamma = \pi/2$. Stable limit sets are shown in red, unstable ones in blue. The right graphs depict the period time T of the corresponding periodic limit cycles.

cation must occur in between that changes the stability properties of the periodic solution. As the normalized dynamics from Eq. (6.2) on the slow manifold $\mathscr{M}_s$ is time autonomous, one Floquet multiplier equals unity representing the freedom of phase. Due to the dimension of the system and the uniqueness of solutions, it is a priori known that period doubling or symmetry breaking bifurcations cannot occur [48, 63]. Therefore, the second Floquet multiplier can leave the unit circle only at +1, which implies a fold bifurcation. From this, the following conclusion is deduced, which consistently completes the prediction of the qualitative dynamics of the tippedisk: If the stability of the heteroclinic and the periodic orbit near the Hopf bifurcation do not have the same stability properties, at least one fold bifurcation must occur.

All bifurcation scenarios from Figure 6.4 agree with the predictions of the stability diagram in Figure 6.3, which numerically validates the statement of the diagram. The presented stability chart explains the bifurcation scenario of all three types v_1, v_2 and v_3 for $0 < \kappa < 0.1$, $0.5 < \zeta < 2$ and $0.85 < \omega < 1.15$.

To embed the previously introduced specimens *V1* and *V2* with mass and inertia properties from Table 2.1 and Table 5.2, respectively, their qualitative dynamics can be compared with the bifurcation scenarios from Figure 6.4. Considering the proportional relationship between the spinning speed Ω and its corresponding normalized quantity ω, it is observed that the specimen with hole (variant *V1*) has qualitatively the same behavior as in the bifurcation diagram 6.4(a) of type v_1, while the specimen with added mass (variant *V2*) corresponds to the dynamics of the bifurcation scenario of type v_2 from Figure 6.4(c). Plotting the corresponding dimensionless eccentricity ratio κ and inertia ratio ζ from Table 6.1 into the two-dimensional parameter space in Figure 6.2(b), the tippedisk with hole (variant *V1*) is located in the blue region, while the specimen with additional mass (variant *V2*) is in the gray domain. Therefore, the tippedisk with hole and the type v_1 are elements of the same equivalence class, i.e., the class characterized by the bifurcation scenario from Figure 6.4(a). The tippedisk with added mass is associated with the representative point v_2 in Figure 6.2, which classifies the qualitative behavior from Figure 6.4(c). Since the global behavior of the real specimens and the equivalence classification according to the domains of the two-dimensional parameter space agree with the predictions of the stability chart, this again confirms the qualitative statements.

In summary, the presented stability chart from Figure 6.3 allows statements about the stability of inverted and non-inverted spinning solutions, the prediction and classification of the Hopf bifurcation, and the existence of stable or unstable (from the inside) heteroclinic saddle connection. If the stability properties of the connected heteroclinic orbit and the periodic solution evolving from the Hopf bifurcation do not match, there must be at least one fold bifurcation in between where the periodic solution changes its stability. Thus, the existence of a fold bifurcation is inferred from dynamic consistency and is not directly characterized. Therefore, the question arises whether the stability chart is complete or whether additional bifurcation scenarios with more than one fold bifurcation occur. Assuming that at most two periodic solutions coexist surrounding the inverted spinning equilibrium, at most one fold bifurcation can occur. This hypothesis is supported by various numerical experiments and could be examined by introducing a Poincaré map. Since the solution of the system is not given in closed-form, the investigation of the Poincaré map would also yield only numerical statements.

In conclusion, the dynamical behavior of the tippedisk appears to be completely characterized by the stability chart from Figure 6.3, explaining all presented types of bifurcation scenarios. Thus, the normalized analysis captures the dynamics of all unbalanced disk-like variants from Figure 1.6.

Chapter 7

Experimental investigation

With the ultimate goal of nonlinear dynamics to understand real-world phenomena, this chapter presents the experimental study of the tippedisk *V1* to supplement the theoretical analysis of the previous chapters.

To measure the motion of the rapidly rotating objects, the author has developed a custom object tracking system from scratch based on off-the-shelf consumer cameras and the state-of-the-art OpenCV computer vision library, capable of tracking at high-speed with multiple cameras.

7.1 Laboratory setup

The tracking system consists of six Sony RX0 II high-speed cameras that are connected by six Sony CCB-WD1 camera control boxes to synchronize the timing, cf. Figure 7.1. The camera control boxes are connected to an Aruba HP 1820-8G switch by Cat-5 cables.

Five of the cameras are mounted on an adjustable frame made of square aluminum profiles with a cross-sectional width of 20 mm while the sixth camera is attached to a portable magnetic tripod. The cameras are arranged in a circle-like fashion to capture the motion of the target from different perspectives and various angles. To capture blind spots or focus on specific details, the tripod-mounted camera can be moved. Therefore, the arrangement and synchronization of multiple high-speed cameras provides an estimate of the target's position and orientation at any given time instant. The tracking system is complemented by a high-performance

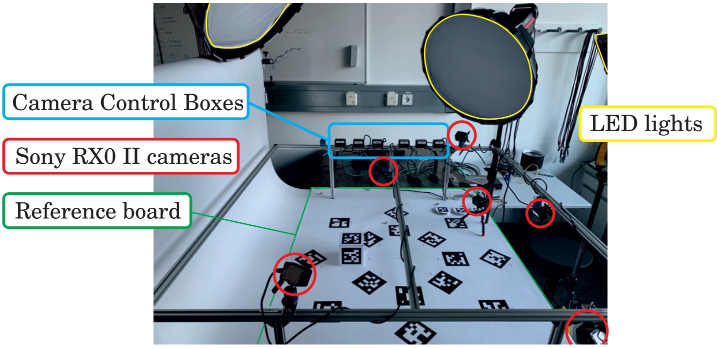

Figure 7.1: Hardware for object tracking. Five cameras are mounted on a frame and are supplemented by a sixth camera on a portable tripod. The camera control boxes can be seen in the background. The setup is complemented by five high-performance LED spots.

LED lighting setup, so that sufficient lighting is available even at high frame rates. Specifically, an Aputure LS C300D MKII, two Aputure LS 300X, two Dedo DLED7-D and the corresponding softboxes were used for the following experiments. Instead of identifying tracked objects through object recognition, fiducial 6 × 6-ArUco markers are used, to simplify identification and allow for higher precision [42].

In general, object tracking systems measure the relative position and orientation of a marker point relative to the camera. Therefore, a camera is often first calibrated with respect to an origin. Based on this calibration, the subsequent measurement takes place. This concept has the disadvantage that the camera must be stationary during the measurement. To overcome this disadvantage, a marker reference board was designed containing 16 ArUco (100 × 100 mm) markers distributed circularly around an origin O, with corresponding inertial frame I, cf. Section 3.4. In this setting, each camera measures its current configuration with respect to the selected origin if at least one reference marker is detected.

To measure the configuration of the tippedisk, two ArUco markers with identifiers *id0* and *id1* and dimensions of 50 × 50 mm are placed as target markers on either side of the disk. The markers are orientated with respect to the body-fixed B-frame such that the second $\boldsymbol{e}_y^{T_i}$-axis of the marker points in opposite $\boldsymbol{e}_x^B$-direction defined in Section 3.4. Also, the geometric center T_i of each target marker is directly above/below the geometric center G of the tippedisk, so the markers are shifted by half the disk height h in the positive/negative $\boldsymbol{e}_z^B$-direction. Thus, the target mark-

Table 7.1: Relative position and orientation of the target markers with respect to the body-fixed B-frame and the geometric center G of the tippedisk.

Property	*id0*	*id1*	unit	Property	*id0*	*id1*	unit
$\boldsymbol{e}_x^B \cdot \boldsymbol{r}_{GT_i}$	0	0	mm	$\boldsymbol{e}_x^B$	$\boldsymbol{e}_y^{T_0}$	$\boldsymbol{e}_y^{T_1}$	[-]
$\boldsymbol{e}_y^B \cdot \boldsymbol{r}_{GT_i}$	0	0	mm	$\boldsymbol{e}_y^B$	$-\boldsymbol{e}_y^{T_0}$	$\boldsymbol{e}_x^{T_1}$	[-]
$\boldsymbol{e}_z^B \cdot \boldsymbol{r}_{GT_i}$	5	−5	mm	$\boldsymbol{e}_z^B$	$\boldsymbol{e}_z^{T_0}$	$-\boldsymbol{e}_z^{T_1}$	[-]

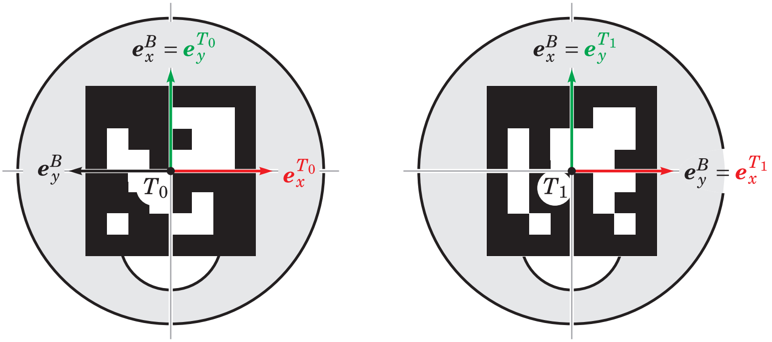

(a) target *id0*

(b) target *id1*

Figure 7.2: Alignment of the target markers *id0* and *id1* on the tippedisk variant *V1*. The respective relative position and orientation are given in Table 7.1.

ers are uniquely aligned with respect to the body-fixed B-frame of the tippedisk. The corresponding relative orientations are given in Table 7.1, where the center of the respective marker is denoted as T_i, with associated relative vector $\boldsymbol{r}_{GT_i}$, for $i = 1,2$. In addition, Figure 7.2 depicts the relative position of the target markers with respect to the body-fixed B-frame. The left Figure 7.2(a) shows the first target marker *id0*, while the right Figure 7.2(b) depicts the second target marker *id1*.

The following high-speed measurements were captured at a frame rate of 500 fps under ‘Quality Priority’ with a recording setting of 50p 50M at a resolution of 1920 × 1080 pixels. At 500 frames per second and a theoretical spinning speed of about 60 rad/s, the frame-to-frame resolution in the orientation angle is about 7°. Results of a comparative benchmark experiment show that the achieved measurement accuracy in the given setup was approximately ±1 mm in position and a deviation of less than 1° in angular measurement. As the absolute position of the tippedisk is not of great interest, the position accuracy has no influence on the results. Regardless, the accuracy of the angle measurement is more than sufficient to characterize the qualitative behavior.

At the above high-speed settings, the Sony RX0 II can only record a maximum shooting time of approximately 2 s due to its hardware limitations. In other words, the camera's hardware constrains the duration of the high-speed measurement. Since the focus is on the inversion of the tippedisk, which is a transient phenomenon on a relatively short time scale, the limited recording time is sufficient to measure the behavior during the first phase of motion.

Ultimately, one wants to have repeatable experiments that can be reproduced exactly every time. However, since the tippedisk is a freely spinning rigid body in frictional contact, it is not trivial to start an experimental run by initiating the body with a certain body state, i.e., a predefined configuration and a specific velocity field. Without significantly increasing the engineering effort, this can hardly be realized by a technical apparatus, not even by additional finesse like automation. Therefore, it seems best to start various experiments by hand and then determine the corresponding initial conditions in a following post-processing step, which subsequently allows to select specific experiments of particular interest.

This manual initialization requires some experience if the angular spinning velocity about the vertical axis should be of similar magnitude, but can be trained in a relatively short time with manageable effort. Since the acceleration of the tippedisk is manual and without sensors, there is no trigger that automatically starts the recording of the cameras. Therefore, the camera recording is also started manually.

Figure 7.3 shows a stroboscopic sequence of an experiment in which the tippedisk was manually started in a non-inverted spinning configuration, as seen by camera 1. The first and second pictures of the sequence show a phase of acceleration, followed by the release phase in which the tippedisk is released. After release, the disk rotates in an almost non-inverted configuration and begins to invert its orientation until the inverted spinning configuration is reached, see the third and fourth images of the sequence.

Since the tippedisk is always in spinning state, each high-speed camera captures either a target marker with *id0* or *id1*, or neither if the tippedisk is oriented orthogonally to the image plane. For example, in the release phase shown in Figure 7.3(b), camera 1 does not detect any target markers. In particular, the recording of each individual camera therefore only allows an estimate of the body configuration for distinct time intervals. As the cameras are synchronized, the individual measure-

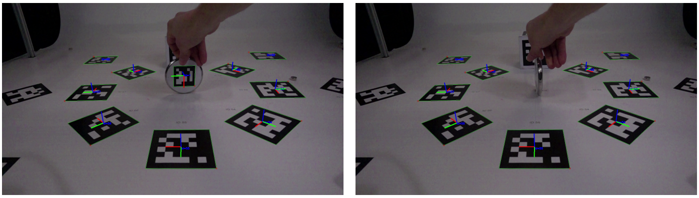

(a) Acceleration phase (b) Release phase

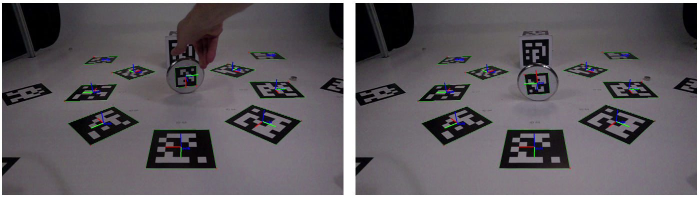

(c) Perturbed non-inverted spinning (d) Almost inverted spinning

Figure 7.3: Stroboscopic sequence from view of camera 1, showing the starting procedure of the experiment. The sequence is taken from a post-processed video so that the orthonormal, right-handed trihedrons of the target and reference markers are shown in the RGB convention.

ments from all cameras are fused to obtain a continuous measurement of the body configuration.

The manufacturer Sony claims that the cameras are synchronized up to ten microseconds. However, when the experiments were evaluated, it was found that the synchronization was off by up to about 1×10^{-2}s, and together with spinning speeds up to $70\,\frac{\text{rad}}{\text{s}}$ this time delay gives an angular error of about 40°. The fusion of non-continuous, time interval measurements that are not perfectly synchronized results in a signal with jumps and a large variance. To prevent this effect, a numerical time-shift algorithm was implemented that optimizes the time delay by minimizing the difference between the individual camera measurements.

7.2 Experimental results

Both Figure 7.4 and Figure 7.5 show four different experimental runs each starting with a perturbed inverted and non-inverted configuration of the tippedisk, respectively. For each experiment, the tippedisk type *V1* is started manually in a perturbed stationary spinning configuration indicated by the crosses. Since the author is right-handed, the disk is started clockwise in vertical spinning direction, which results in a negative spinning speed $\dot{\alpha}$. In contrast to the previous analysis with positive spinning speeds, the trajectories are spiraling counter-clockwise. Due to symmetry, both solutions with positive and negative rotational speed are equivalent in terms of physical behavior. Figure 7.4 and Figure 7.5 show the evolution of the spinning angle α, the inclination angle β, and the rolling angle γ, obtained by object tracking. In addition, the corresponding spinning speed $\dot{\alpha}$ determined by numerical differentiation is presented in Figure 7.4(b) and Figure 7.5(b), respectively.

Figure 7.4 shows four experiments labeled *inv* that start from a perturbed, inverted spinning motion. In Figure 7.4(a), the evolution of the spinning angle α is shown as solid line, accompanied by the dashed linear extrapolation assuming a constant initial spinning velocity. The corresponding spinning velocities $\dot{\alpha}$ are presented in Figure 7.4(b). The inclination angle β and the rolling angle γ are shown in Figure 7.4(c) and Figure 7.4(d), respectively. Following the previous analysis, the inversion behavior of the tippedisk is well characterized by the two-dimensional β-γ-space, which motivates the projection in Figure 7.4(e). In this projection, the inverted spinning equilibrium is marked as a black dot. The α- and $\dot{\alpha}$-graphs reveal that the spinning speed decreases due to dissipation. However, the decay is relatively small. The red trajectories of the experiment *inv* 1 correspond to the fastest spinning speeds and show a converging behavior to the asymptotically stable inverted spinning equilibrium. At lower spinning speeds, as in the experiments *inv* 2 and *inv* 4, in green and yellow, respectively, the inverted equilibrium also appears to attract the solutions. However, the corresponding orbits do not reach the inverted spinning state in the limited experimental time. Therefore, it is not clear whether the solutions converge to the inverted spinning equilibrium or end up in small oscillations around it. In contrast, the blue orbit of the experiment *inv* 3 at slowest spinning velocity is repelled by the inverted equilibrium.

Figure 7.5 presents experiments that start from a perturbed non-inverted spinning configuration. According to the β- and γ-graphs from Figure 7.5(c) and Figure 7.5(d), respectively, the initial fast spinning solutions *non* 1 and *non* 4 (red and yellow), initialized close to non-inverted equilibrium, converge to inverted spinning and end in a small oscillation. In the corresponding β-γ-projection, inverted and non-inverted equilibria are shown as black dots. Neglecting the time-shift, the two experiments appear to be qualitatively similar with a slight decrease in the magnitude of the spinning velocity, cf. Figure 7.5(b). The corresponding vertical spinning angle is shown in Figure 7.5(a). The experiment *non* 2 in green has approximately

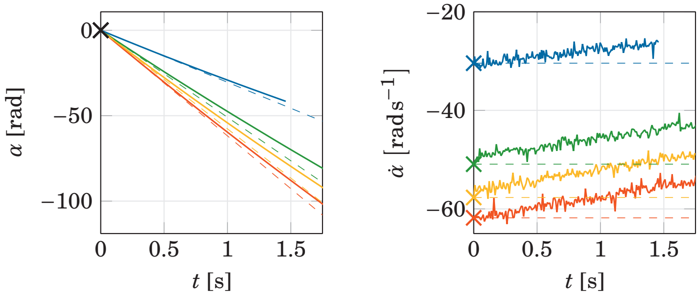

(a) α (b) $\dot{\alpha}$

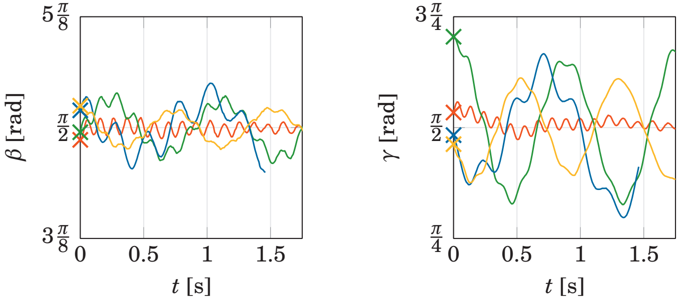

(c) β (d) γ

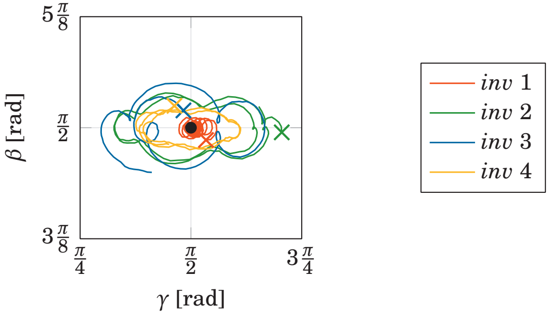

(e) β-γ-space

Figure 7.4: Four different inverted-spinning experiments in which the tippedisk is initialized by hand in an inverted configuration.

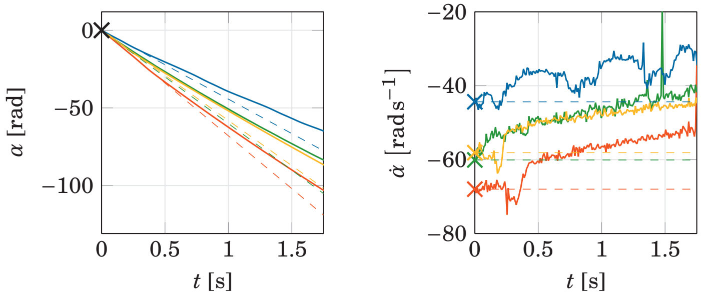

(a) α (b) $\dot{\alpha}$

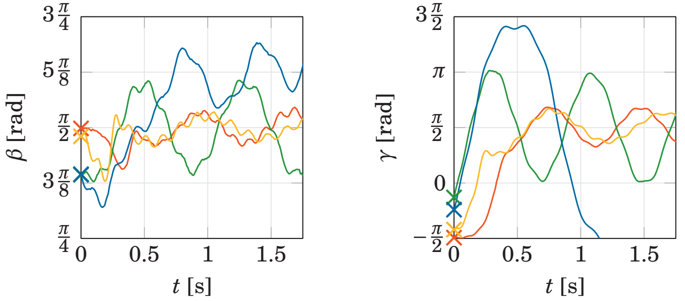

(c) β (d) γ

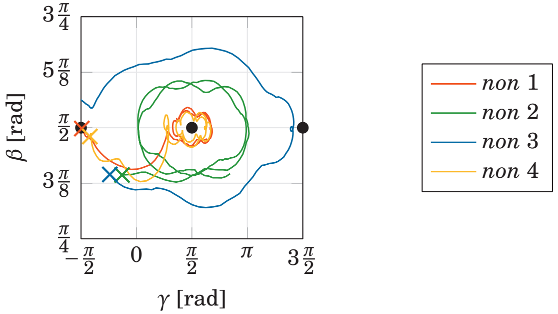

(e) β-γ-space

Figure 7.5: Four different non-inverted spinning experiments in which the tippedisk is initialized by hand in a non-inverted configuration.

the same initial spinning speed as the *non* 4, but starts farther away from the non-inverted spinning configuration.

According to the projection onto the β-γ-space, the corresponding orbit ends in an oscillation about the inverted spinning equilibrium. The initial configuration of the experiment *non* 3 in blue is similar to that of experiment *non* 2 and differs only in the initial velocity, but results in a qualitatively different behavior. The experiment *non* 3 at the slowest initial spinning speeds shows no inversion of the disk as the rolling angle γ diverges with increasing time, accompanied by a decrease in the inclination angle β.

For experiments *non* 1, *non* 2 and *non* 4, the tippedisk oscillates around a vertically inclined configuration, as the inclination angle remains close to $\beta = \pi/2$. In contrast, the oscillation in the blue experiment *non* 3 is superimposed by an increase in the inclination angle, which characterizes a falling of the tippedisk where the height of the geometric center G decreases.

7.3 Comparison of experiments and simulation

Figure 7.6 and Figure 7.7 compare the experimental results of the two experiments *inv* 2 and *non* 1 presented above with the corresponding simulation results of the rigid body system Model 1.1 of Table 4.1 and the reduced dynamics from Eq. (5.24) on the slow manifold. The parameters, friction and smoothing coefficients, were chosen to be $\mu = 0.3$ and $\varepsilon = 0.001\,\mathrm{m/s}$, respectively, and were identified by manual inspection of the results.

Simulations are initialized with the same initial conditions as the experiment, as far as possible. Since the orientation is measured by visual object tracking, the angles α, β and γ are determined directly. However, the corresponding initial angular velocities $\dot{\alpha}$, $\dot{\beta}$, and $\dot{\gamma}$ must be determined by numerical differentiation, which introduces some additional uncertainty in the initial conditions.

In Figure 7.6, the measurements of experiment *inv* 2 are depicted in green. The simulation results of Model 1.1 and the dynamics on the slow manifold is shown in black and blue, respectively. Qualitatively, the results of the experiment and the simulation behave similarly. However, the experiment and the full model simulation show that the corresponding orbits oscillate around the virtual slow manifold in β-γ-$\dot{\beta}$-space, while the slow dynamics is constrained to this manifold.

Figure 7.7 presents the experiment *non* 1 in red, where the tippedisk is initialized in a perturbed non-inverted spinning configuration. Model 1.1 in black shows qualitatively similar behavior, while the reduced dynamics on the slow manifold in blue deviates slightly. In addition, a second solution of the dynamics on the

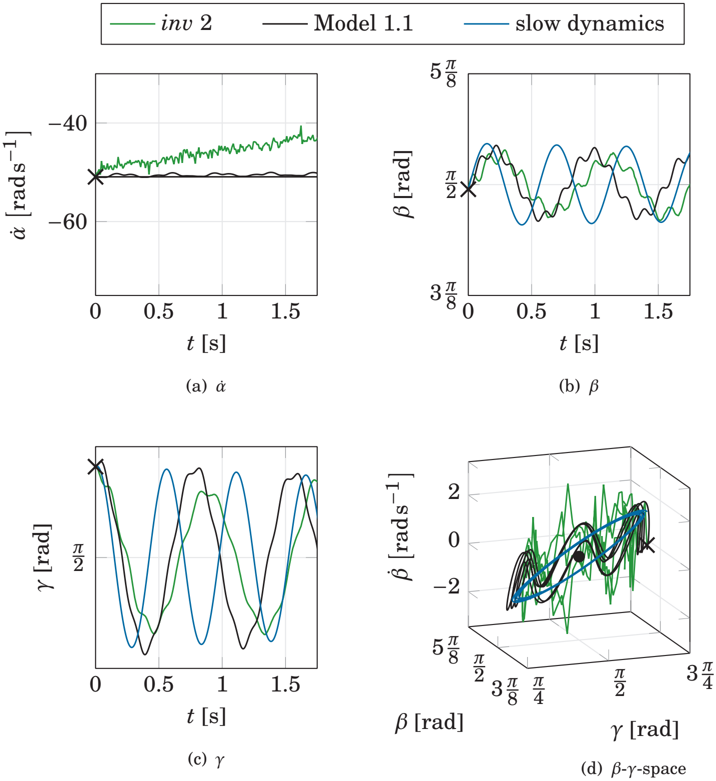

(a) $\dot{\alpha}$
(b) β
(c) γ
(d) β-γ-space

Figure 7.6: Inverted spinning experiment *inv* 2 in comparison with the rigid body model (Model 1.1) defined in Table 4.1 and the dynamics on the slow manifold from Eq. (5.24). Both simulations are started with the same initial conditions as the experiment.

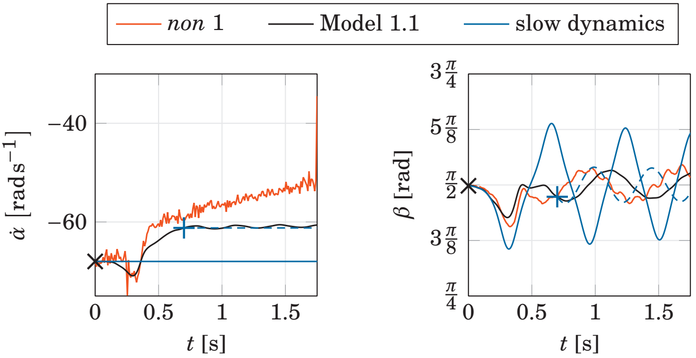

(a) $\dot{\alpha}$

(b) β

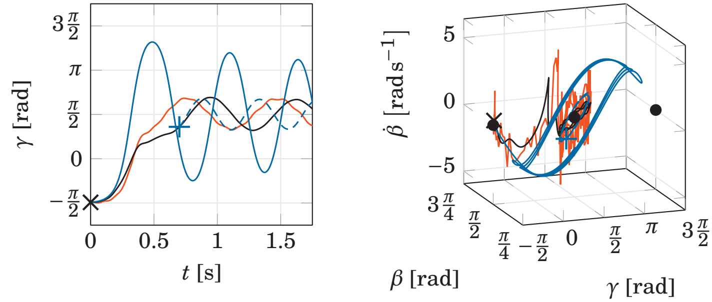

(c) γ

(d) β-γ-space

Figure 7.7: Non-inverted spinning experiment *non* 1 in comparison with the rigid body model (Model 1.1) defined in Table 4.1 and the dynamics on the slow manifold from Eq. (5.24). The simulations shown as solid lines are started with the same initial conditions as the experiment in red, while the dashed blue line is determined by the reduced dynamics on the slow manifold initialized with the state of Model 1.1 at $t = 0.7$s.

slow manifold is shown as a dashed blue line, initialized according to the state of Model 1.1 at time $t = 0.7$ s. The corresponding initial condition is indicated by the plus sign. The solution of the Model 1.1 simulation is close to the experiment *non* 1 and ends in an oscillation around inverted spinning. According to Figure 7.7(d), both corresponding orbits oscillate around the virtual slow manifold.

7.4 Discussion of experiments

As the experiments are started manually, the time instant of release cannot directly be obtained from measurements, i.e., the first time instant for which the disk is spinning freely. To avoid false identifications of the starting point, the release of the disk can be conservatively estimated to exclude movements where the target touches the starting hand. Therefore, the start time of the experiment must be determined based on the object tracking results, which can be extremely difficult for specific experiments. Together with the constraint of the maximum recording time 2 s of the used cameras in high-speed mode, the experimental time is severely limited. In Figure 7.5, for example, the time origin at $t = 0\,\mathrm{s}$ for the experiments *non* 2 and *non* 3 (green and blue) does not correspond to the actual release point, as the measurement was started manually with a slight time delay. Therefore, the associated graphs do not capture the entire inversion process and somewhat disregard the very first phase of motion. However, the state at $t = 0\,\mathrm{s}$ is a valid initial condition of a freely spinning tippedisk in a (strongly) perturbed configuration.

The qualitative analysis from the preceding sections yields an asymptotically attractive inverted spinning configuration if the spinning speed $\dot{\alpha} = \Omega$ is large enough.

According to the experiments started close to inverted spinning, the inverted spinning equilibrium attracts solutions when the initial spinning speed is large, cf. Figure 7.4. In experiment *inv* 1, the tippedisk ends up in a perfect inverted spinning configuration. For slow initial spinning speeds, the solutions are repelled by the inverted spinning equilibrium, cf. experiment *inv* 3. This is consistent with the local stability analysis performed in Section 4. For intermediate spinning speeds, the tippedisk ends in a oscillating state around inverted spinning, as in experiments *inv* 2 and *inv* 4.

Following the initially non-inverted experiments from Figure 7.5, the tippedisk inverts its orientation and oscillates around inverted spinning if spun fast enough. Even for extremely fast spinning speeds, the tippedisk does not exhibit a full inversion. At first glance, this appears to be in contradiction to the qualitative analysis, which predicts an asymptotically attractive inverted spinning equilibrium when the spinning speed is above the critical value $\Omega_\mathrm{c} = 30.92\,\frac{\mathrm{rad}}{\mathrm{s}}$. However, due to the limited recording time, it is hardly possible to conclude from the experiments whether or not the disk eventually converges to the inverted spinning equilibrium. Another reason for this contradiction could be the assumption of a horizontally immobile COG, since translational velocities may cause additional frictional disturbances leading to superimposed oscillations. This hypothesis is supported by the comparison of the experimental results in Figure 7.6 and Figure 7.7 with their corresponding simulation results, as the solutions of Model 1.1 simulations are superimposed by oscillations which are not present in the dynamics on the slow manifold. Neglecting superimposed oscillations, the slow invariant dynamics gives a good prediction of the experiment initialized at inverted spinning.

The experiment *non* 1 and the corresponding simulation results of the reduced Model 1.1 in Figure 7.7 show a different behavior than the dynamics on the slow manifold, initialized at the same initial condition at $t = 0\,\mathrm{s}$. However, the asymptotic dynamics on the slow manifold initialized at $t = 0.7\,\mathrm{s}$ seems qualitatively close to the asymptotic dynamics of experiment *non* 1 and the corresponding simulation of Model 1.1. Since the dynamics on the slow manifold characterizes the slow dynamics after an initial phase of fast motion, the reduced model describes the asymptotic behavior of the tippedisk close to pure rolling. If the initial state is close to pure rolling motions, the dynamics on the slow manifold is a valid approximation of the initial phase of the motion. Therefore, the asymptotic dynamics on the slow manifold initialized at $t = 0.7\,\mathrm{s}$ with the angles of the simulation of Model 1.1, i.e., after a fast transient phase, is qualitatively close to the asymptotic dynamics of the experiment *non* 1 and the corresponding simulation of Model 1.1 with respect to the evolution of the inclination and the rolling angles β and γ.

Since the total energy of the tippedisk is mainly determined by the spinning speed, the $\dot{\alpha}$-diagrams in Figure 7.6(a) and Figures 7.7(a) are suited to estimate the dissipation losses. It is evident that the two models (Model 1.1 and the dynamics on the slow manifold), which neglect pivoting and contour friction or even aerodynamic drag, exhibit much lower dissipation rates compared to the real experiments. Therefore, the time scales of the real system in contact with a frictional support are more blurred than in the case of the idealized simulation models. As a consequence, it is difficult to decompose the motion of the real tippedisk into three different phases, namely, convergence to almost pure rolling motions on a fast time scale, the inversion on an average time scale, followed by a dissipation-driven falling of the disk on the slow time scale.

In summary, the experiment and the reduced dynamics is reasonably consistent in qualitative terms. However, the experimental setup does not allow for a more accurate comparison because both the recording time of the system is limited and the numerical derivative of the angle measurements leads to uncertainties in the angular velocities.

To improve the measurement, additional microelectromechanical gyroscopes that directly measure the angular velocity of the body could be mounted on the tippedisk, allowing more accurate measurement through sensor fusion. However, this experimental setup presents additional challenges because the application of an electronic sensor with a non-negligible mass and inertia tensor alters the inertia properties of the tippedisk, which must be taken into account. Here the use of lightweight target markers has its own appeal, since the inertia properties of the tippedisk can be easily determined from measurement and trivial calculations without additional inaccuracies, with the disadvantage that there is no direct access to the angular velocity. Therefore, the application of more specialized high-speed cameras with unlimited recording time and higher frame rates would allow longer and more precise measurements with a finer time resolution and thus the possibility of the application of signal filters. For more accurate measurements, it is also recommended to optimize system parameters such as friction and smoothing coefficient to increase the quantitative agreement between measurements and simulation.

Chapter 8

Conclusion and Outlook

In this monograph, the tippedisk was introduced as a novel mechanical-mathematical archetype exhibiting a counterintuitive friction-induced inversion phenomenon. The holistic analysis ranges from the theoretical research fields of nonsmooth rigid body dynamics, through global bifurcation analysis in the context of nonlinear dynamics, to high-speed experiments in the domain of applied physics. The analysis was performed exemplarily on a real physical specimen and generalized by a subsequent dimensionless analysis.

8.1 Conclusion

A rigorous mathematical description of the tippedisk in the framework of nonsmooth dynamics serves as the foundation for a holistic analysis of its peculiar and fascinating dynamics. Therefore, as a first step, a full mechanical model was introduced, based on first principles and taking into account various smooth and set-valued friction laws as well as frictional contact. Physical system coordinates, referred to as the spinning, inclination, and rolling angles of the disk, were identified from a coordinate-free description. To derive a description in generalized coordinates, two different models were deduced, one based on a quaternion formulation and one parametrized in Euler angles. The quaternion-based model has the advantage of much simpler system equations due to a symmetric structure, allowing more efficient numerical integration.

However, the major drawback lies in the non-physical parametrization, as the associated generalized coordinates cannot be directly identified with the physical configuration of the tippedisk. In contrast, the system equations of the model in Euler angles are highly nonlinear, intrinsically asymmetric, and extremely tedious to deduce. Approaches to derive the system equations with symbolic computations were not feasible because trigonometric ambiguities resulted in extremely large nonlinear system equations that could not be simplified in a manageable way. With the ultimate aim to perform a qualitative analysis, compact expressions are favorable. Consequently, a diligent two-week process of rigorous hand calculations was required to derive equations that were reasonably compact. The identification of the Euler angles with the physical spinning, inclination, and rolling angles showed the relevance of this parametrization. Due to the high rotational speed of the tippedisk and its inherent slow-fast behavior, convergence with the first-order Moreau's time-stepping scheme was anything but trivial. However, the redundant parametrization made it possible to compare the simulation results in order to check convergence on the one hand and to numerically validate the derived system equations on the other hand. A numerical study of full model simulations showed that set-valued Coulomb friction is not suitable to describe the inversion behavior, as the tippedisk ends in pure rolling motions without inverting its orientation. This stands in contrast to the tippetop, which can be described using dry Coulomb friction, cf. [31]. By incorporating both spinning and tangential sliding friction in the set-valued Coulomb–Contensou friction law, the mechanical model of the tippedisk successfully captured the qualitative behavior. Comparison of short- and long-term simulations revealed that the dynamical behavior of the tippedisk is governed by multiple time scales. By focusing on the inversion behavior, additional dissipation mechanism, as contour and pivoting friction play a minor role, which only have a significant effect on the long-term behavior. During inversion, the tippedisk is in spinning state, which, under the assumption of Coulomb–Contensou friction, yields a smooth force law. Therefore, by neglecting pivoting torques, and simultaneously taking the smooth friction behavior into account, the model with smooth Coulomb friction captures the essence of the inversion phenomenon. Moreover, numerical simulations showed that the tippedisk remains in persistent contact with the flat support. Considering the persistence of the contact point and the application of a smooth friction law, an ordinary differential equation describing the physical motion of the tippedisk was established.

The local stability behavior of stationary spinning solutions was analyzed using Lyapunov's indirect method, which required prior reparametrization. Numerical evaluation of the eigenvalues, showed that the dynamics of the tippedisk is characterized by three different time scales suggesting slow-fast system behavior. To investigate the stability of permanent rotations, the spinning speed was found to be the bifurcation parameter. Here, the eigenvalues prove the existence of a Hopf bifurcation, where an unstable two-dimensional subspace of inverted spinning becomes stable when the spinning velocity is large enough.

Due to the high dimensionality of the full mechanical system, a closed-form analysis was not possible. Therefore, a reduction procedure was performed to obtain a lower-dimensional model that captures the main features of the dynamical behavior of the tippedisk. Based on the simulations of the full model and observations from preliminary experiments, it was assumed that the contact point is bilaterally constrained. Under the postulate of a homogeneous frictional support, the absolute horizontal position of the disk has no influence on the dynamical behavior. Neglecting the frictional forces caused by a slow wandering of the disk led to a gyroscopic master dynamics to which the translational dynamics is enslaved. With the emphasis on the inversion phenomenon characterized by the orientation of the disk, the enslaved translational dynamics was hidden by the assumption of a horizontally immobile center of gravity. Similar simplification assumptions are present in the analysis of spinning eggs [82] and the tippetop [20], and are common for fast spinning objects [66]. Numerical validation also showed that the relative sliding velocity of the contact point during inversion is small, i.e., the inversion is close to a pure rolling motion, which justifies the assumption of pure rolling in the tangential rolling direction. The results of the analysis within the singular perturbation theory are consistent with this assumption and prove the attractiveness of almost pure rolling motions.

Inspired by the local stability analysis, the spinning speed was chosen as bifurcation parameter that foliates the state-space. However, the corresponding assumption of a constant spinning speed leads to energetic inconsistencies. More precisely, assuming a constant spinning speed, the kinetic energy is the same for inverted and non-inverted stationary spinning motion, as opposed to the potential energy, which is higher in the inverted configuration. Consequently, the net total energy must increase during inversion if the spinning speed is kept constant, which is not physical. Nevertheless, the reduced dynamics properly describes the qualitative inversion behavior. Application of perturbation expansions on the linearized reduced model and the subsequent application of the harmonic balance method, have led to closed-form approximations which characterize both the critical spinning speed and the type of Hopf bifurcation as supercritical.

Assuming a smooth but ‘stiff’ friction law induces dynamics in the form of a singularly perturbed dynamical system. Therefore, the physical behavior of the tippedisk is related to the mathematical concept of slow-fast dynamics and allows to identify pure rolling motions with the critical manifold. Studying the singularly perturbed dynamical structure revealed that the asymptotic dynamics of the tippedisk takes place on a two-dimensional slow manifold, which allows to obtain a two-dimensional dynamics that characterizes the inversion behavior. Unlike the tippetop, which is always in spinning state [90], the inversion phenomenon of the tippedisk is described by motions close to pure rolling. Consequently, the tippedisk is not merely an asymmetrical version of the tippetop, but exhibits a different qualitative behavior, and thus defines its own mechanical-mathematical archetype. Since the asymptotic dynamics in physical coordinates is equivalent to a perturbed Hamiltonian structure, the Melnikov function method was applied, allowing to obtain a necessary condition for the existence of a heteroclinic saddle connection. By using perturbation expansion, the heteroclinic bifurcation parameter is approximately derived in closed-form. Furthermore, the dimensionless quantities arise almost naturally as a consequence of this approximation.

Normalization of the closed-form expressions that characterize the Hopf and heteroclinic bifurcations and the analysis of the normalized dynamics on the slow manifold allowed to obtain a stability chart characterizing the qualitative behavior of the tippedisk. From this stability chart, three different variants of the tippedisk with qualitatively different dynamics were identified. The corresponding bifurcation scenarios were computed numerically to demonstrate the validity of the dimensionless analysis.

The theoretical analysis has been complemented by high-speeds experiments that are compared to the full mechanical model and the reduced dynamics on the slow manifold. Analogous to the Euler disk, aerodynamic drag is not the main dissipation mechanism [17] and the inversion phenomenon is caused by the interaction of gyroscopic, normal and frictional forces. In a qualitative analysis of the dynamics on a short time scale, the effect of aerodynamic drag can be neglected. However, the long-term behavior can be influenced by air friction.

8.2 Outlook

Although the presented analysis explains the inversion phenomenon of the tippedisk, there are some open questions. Based on intuition, it is natural to consider the spinning velocity as a bifurcation parameter. However, if dissipation is assumed to be negligible during inversion, i.e., on a short time scale, this yields energetic inconsistencies. Therefore, it would be preferable to choose the total energy as a bifurcation parameter. For non-inverted and inverted spinning motions, respectively, the total energy and the spinning speed are directly related as the potential energy is given naturally by the orientation of the disk. Neglecting dissipation does not result in energetic inconsistencies.

Axisymmetric rigid bodies [116] exhibit self-induced jumping for larger spinning speeds. The inversion behavior of the tippedisk is characterized by almost pure rolling motions in persistent contact. Nevertheless, there may be motions for which the disk detaches from the ground, motivating to study the phenomenon of self-induced jumping.

Although the reduced dynamics captures the essence of the counterintuitive inversion phenomenon, the reduction procedure may somehow ignore even more rich and interesting dynamics, e.g., quasiperiodic solutions of the full system could be forced to periodic ones in the reduced dynamics. Instead of performing the model order reduction procedure, the singular perturbation analysis may be directly applied on the full mechanical model where only the contact is assumed to be persistent. Because the inversion behavior is characterized by almost pure rolling motions, the relative sliding velocities correspond to fast variables, which motivates to formulate the system with respect to minimal velocities that contain the relative sliding velocities.

To improve the experimental measurements, the application of high-speed cameras with infinite recording time is highly recommended. Furthermore, higher frame rates would allow a better estimation of the initial condition and thus improved comparability of simulations. Based on the adapted experiments, a parameter optimization would allow to characterize the influence of additional dissipation mechanisms, such as aerodynamic drag and pivoting friction.

Due to the extremely rich dynamics induced by gyroscopic and contact forces, the tippedisk is an excellent benchmark example for nonsmooth integration schemes, e.g., nonsmooth Ruge-Kutta methods [50]. In particular, the tippedisk allows to check constraint satisfaction and the convergence of higher-order schemes. From the stability chart, system parameters can be chosen to obtain a particular dynamics that includes sub- or supercritical Hopf bifurcations, stable or unstable heteroclinic saddle connections, and even a fold bifurcation. Therefore, the reduced dynamics is suited to test numerical methods that predict and characterize periodic limit cycles and heteroclinic saddle connections, e.g., the stability analysis of periodic solutions through Koopman analysis [11].

The analysis of the tippedisk showed how certain friction laws induce a singularly perturbed dynamical structure, motivating to apply the methodology to engineering applications. In particular, systems from vehicle dynamics, such as the over- and understreer behavior of automobiles [118], the instability of towed wheels [5], the hunting motion [41, 6], or the behavior of aircrafts during ground maneuvers [100] may be analyzed in the framework of singular perturbation theory since their nominal motion is close to pure rolling.

To summarize, the tippedisk exhibits extremely rich and interesting dynamics and shows a counterintuitive inversion phenomenon. Its nonlinear dynamic analysis reveals a singularly perturbed dynamical structure, which is naturally induced by a peculiar friction law. Consequently, the tippedisk forms not only an excellent mathematical-mechanical archetype for friction-induced instabilities, but also an archetype system for singular perturbation theory.

APPENDIX A

Description of rotations

A.1 Coordinate map

The coordinate map ${}_{A}\mathscr{K}$ maps a vector $\boldsymbol{v}$ of the Euclidean space $\mathbb{E}^3$ to coordinates ${}_{A}\boldsymbol{v} \in \mathbb{R}^3$ of the basis A and is defined as:

$$\begin{aligned} {}_{A}\mathscr{K} &: \mathbb{E}^3 \to \mathbb{R}^3 \\ & \boldsymbol{v} \mapsto {}_{A}\boldsymbol{v} = \left(\boldsymbol{v} \cdot \boldsymbol{e}_i^A\right) {}_{A}\boldsymbol{e}_i^A . \end{aligned}$$

The projection of the vector $\boldsymbol{v}$ onto the unit basis vectors $\boldsymbol{e}_i^A$ is identified as i-coordinate $\boldsymbol{v}_i^A = \left(\boldsymbol{v} \cdot \boldsymbol{e}_i^A\right)$ w.r.t. the basis A. The coordinate map ${}_{A}\mathscr{K}$ is linear[1]:

$${}_{A}\mathscr{K}(\alpha\boldsymbol{a} + \beta\boldsymbol{b}) = \alpha\, {}_{A}\mathscr{K}\,\boldsymbol{a} + \beta\, {}_{A}\mathscr{K}\,\boldsymbol{b}$$

The inverse coordinate mapping

$$\begin{aligned} {}_{A}\mathscr{K}^{-1} &: \mathbb{R}^3 \to \mathbb{E}^3 \\ & {}_{A}\boldsymbol{v} \mapsto \boldsymbol{v} = \boldsymbol{v}_i^A\, \boldsymbol{e}_i^A . \end{aligned}$$

maps coordinates ${}_{A}\boldsymbol{v} \in \mathbb{R}^3$ w.r.t the basis A onto the associated vector $\boldsymbol{v} \in \mathbb{E}^3$.

---

[1] This directly results from the fact that $\mathbb{E}^3$ and $\mathbb{R}^3$ are both linear vector spaces.

$$\begin{tikzcd}
& \boldsymbol{v} \in \mathbb{E}^3 \arrow[dl, "\mathscr{K}_A"'] \arrow[dr, "\mathscr{K}_B"] & \\
{}_A\boldsymbol{v} \in \mathbb{R}^3 & & {}_B\boldsymbol{v} \in \mathbb{R}^3 \arrow[ll, "\boldsymbol{A}_{AB}"]
\end{tikzcd}$$

Figure A.1: Transformation: Commutative diagram

A.2 Coordinate transformation

The coordinate transformation

$$\begin{aligned} \boldsymbol{A}_{AB} &: \mathbb{R}^3 \to \mathbb{R}^3 \\ &\quad {}_B\boldsymbol{v} \mapsto {}_A\boldsymbol{v} = \boldsymbol{A}_{AB}\,{}_B\boldsymbol{v} \end{aligned}$$

maps the vector B-coordinates ${}_B\boldsymbol{v}$ onto the A-coordinates ${}_A\boldsymbol{v}$. According to the commutative diagram Figure A.1, the coordinate transformation is equal to

$$\boldsymbol{A}_{AB} = {}_A\mathscr{K} \circ {}_B\mathscr{K}^{-1}.$$

The action of $\boldsymbol{A}_{AB}$ on ${}_B\boldsymbol{v}$ then yields

$$\boldsymbol{A}_{AB}\,{}_B\boldsymbol{v} = {}_A\mathscr{K} \circ {}_B\mathscr{K}^{-1}\left({}_B\boldsymbol{v}\right) = \left(v_j^B \boldsymbol{e}_j^B \cdot \boldsymbol{e}_i^A\right) {}_A\boldsymbol{e}_i^A,$$

from which we deduce the transformation matrix

$$\boldsymbol{A}_{AB} = \begin{bmatrix} (\boldsymbol{e}_1^A \cdot \boldsymbol{e}_1^B) & (\boldsymbol{e}_1^A \cdot \boldsymbol{e}_2^B) & (\boldsymbol{e}_1^A \cdot \boldsymbol{e}_3^B) \\ (\boldsymbol{e}_2^A \cdot \boldsymbol{e}_1^B) & (\boldsymbol{e}_2^A \cdot \boldsymbol{e}_2^B) & (\boldsymbol{e}_2^A \cdot \boldsymbol{e}_3^B) \\ (\boldsymbol{e}_3^A \cdot \boldsymbol{e}_1^B) & (\boldsymbol{e}_3^A \cdot \boldsymbol{e}_2^B) & (\boldsymbol{e}_3^A \cdot \boldsymbol{e}_3^B) \end{bmatrix} = \begin{bmatrix} {}_A\boldsymbol{e}_1^B & {}_A\boldsymbol{e}_2^B & {}_A\boldsymbol{e}_3^B \end{bmatrix}.$$

Due to symmetry it follows that $\boldsymbol{A}_{BA} = \boldsymbol{A}_{AB}^{\mathrm{T}} = \boldsymbol{A}_{AB}^{-1}$.

A.3 General rotations

An orthogonal tensor $\boldsymbol{Q}$ is a bilinear mapping from $\mathbb{E}^3$ to $\mathbb{E}^3$

$$\begin{aligned} \boldsymbol{Q} &: \mathbb{E}^3 \to \mathbb{E}^3 \\ &\quad \boldsymbol{v} \mapsto \boldsymbol{v}' := \boldsymbol{Q} \cdot \boldsymbol{v}, \end{aligned}$$

which preserves relative angles $\boldsymbol{v} \cdot \boldsymbol{w} = \boldsymbol{v}' \cdot \boldsymbol{w}'$ and the length $\|\boldsymbol{v}\| = \|\boldsymbol{v}'\|$ of a vector. From these conditions we conclude with

$$\boldsymbol{v} \cdot \boldsymbol{w} = (\boldsymbol{Q}\boldsymbol{v}) \cdot (\boldsymbol{Q}\boldsymbol{w}) = \boldsymbol{v} \cdot \boldsymbol{Q}^{\mathrm{T}} \boldsymbol{Q}\, \boldsymbol{w},$$

that $\boldsymbol{Q}^{\mathrm{T}}\boldsymbol{Q} = \mathbb{1}$ has to hold. As $\boldsymbol{Q}$ is orthogonal, the inverse $\boldsymbol{Q}^{-1}$ is equal to the transpose $\boldsymbol{Q}^{\mathrm{T}}$. Moreover, we conclude from the orthogonality

$$\det(\boldsymbol{Q}^{\mathrm{T}}\boldsymbol{Q}) = \det(\boldsymbol{Q})^2 = 1 \implies \det(\boldsymbol{Q}) = \pm 1.$$

If $\det(\boldsymbol{Q}) = +1$ holds, we identify $\boldsymbol{Q}$ as a 'proper' rotation $\boldsymbol{R}$. Proper rotations $\boldsymbol{R}$ do not reflect bases, such that

$$(\boldsymbol{e}_i \times \boldsymbol{e}_j) \cdot \boldsymbol{e}_k = (\boldsymbol{R}\,\boldsymbol{e}_i \times \boldsymbol{R}\,\boldsymbol{e}_j) \cdot \boldsymbol{R}\,\boldsymbol{e}_k$$

holds.

A.4 Rotation induced frames

Any rotation $\boldsymbol{R}_{AI}$ induces intrinsically for any right-handed reference I-frame a rotated, right-handed A-frame as the mapping

$$\begin{aligned} \boldsymbol{R}_{AI} : \mathbb{E}^3 &\to \mathbb{E}^3 \\ \boldsymbol{e}^I_i &\mapsto \boldsymbol{e}^A_i := \boldsymbol{R}_{AI} \cdot \boldsymbol{e}^I_i, \end{aligned}$$

can be applied on each basis vector $\boldsymbol{e}^I_i$ of the reference frame I and preserves angles, length and orientations. The rotation $\boldsymbol{R}_{AI}$ is therefore a tensor of second-order and can be identified as[2]

$$\begin{aligned} \boldsymbol{R}_{AI} &= \delta_{ij}\, \boldsymbol{e}^A_i \otimes \boldsymbol{e}^I_j \\ &= (\boldsymbol{e}^A_j \cdot \boldsymbol{e}^I_i)\, \boldsymbol{e}^I_i \otimes \boldsymbol{e}^I_j \\ &= (\boldsymbol{e}^I_i \cdot \boldsymbol{e}^A_j)\, \boldsymbol{e}^I_i \otimes \boldsymbol{e}^I_j \\ &= \boldsymbol{e}^A_i \otimes (\boldsymbol{e}^I_i \cdot \boldsymbol{e}^A_j)\, \boldsymbol{e}^A_j \\ &= (\boldsymbol{e}^I_i \cdot \boldsymbol{e}^A_j)\, \boldsymbol{e}^A_i \otimes \boldsymbol{e}^A_j. \end{aligned} \tag{A.1}$$

By introducing the components

$$R^I_{AI,ij} := \boldsymbol{R}_{AI}(\boldsymbol{e}^I_i, \boldsymbol{e}^I_i) = (\boldsymbol{e}^I_i \cdot \boldsymbol{e}^A_j)$$

---

[2] In Eq. (A.1) the commutativity of the dot product $\cdot$ and the linearity of the tensor $\boldsymbol{R}$ are used.

and

$$R^{A}_{AI,ij} := \boldsymbol{R}_{AI}(\boldsymbol{e}^{A}_{i}, \boldsymbol{e}^{A}_{i}) = (\boldsymbol{e}^{I}_{i} \cdot \boldsymbol{e}^{A}_{j}),$$

one observes that $R^{I}_{AI,ij} = R^{A}_{AI,ij}$ holds. For more compact expressions, the shorter notation $R_{AI,ij} := R^{I}_{AI,ij} = R^{A}_{AI,ij}$ is introduced. At this point we have to keep in mind that the components $R_{AI,ij}$ of the rotation-tensor $\boldsymbol{R}_{AI}$ are associated with pure bases, i.e., $\boldsymbol{e}^{I}_{i} \otimes \boldsymbol{e}^{I}_{j}$ or $\boldsymbol{e}^{A}_{i} \otimes \boldsymbol{e}^{A}_{j}$.

The inverse rotation $\boldsymbol{R}_{IA} = \boldsymbol{R}^{-1}_{AI}$ induces the mapping

$$\begin{aligned} \boldsymbol{R}_{IA} = \boldsymbol{R}^{-1}_{AI} : \mathbb{E}^{3} &\rightarrow \mathbb{E}^{3} \\ \boldsymbol{e}^{A}_{i} &\mapsto \boldsymbol{e}^{I}_{i} := \boldsymbol{R}^{-1}_{AI} \cdot \boldsymbol{e}^{A}_{i}, \end{aligned}$$

which rotates $\boldsymbol{e}^{A}_{i}$ onto $\boldsymbol{e}^{I}_{i}$ and is identified as

$$\begin{aligned} \boldsymbol{R}_{IA} &= \delta_{ij}\, \boldsymbol{e}^{I}_{i} \otimes \boldsymbol{e}^{A}_{j} \\ &= \boldsymbol{e}^{I}_{j} \otimes (\boldsymbol{e}^{A}_{j} \cdot \boldsymbol{e}^{I}_{i})\boldsymbol{e}^{I}_{i} \\ &= (\boldsymbol{e}^{A}_{i} \cdot \boldsymbol{e}^{I}_{j})\boldsymbol{e}^{I}_{i} \otimes \boldsymbol{e}^{I}_{j} \\ &= (\boldsymbol{e}^{I}_{j} \cdot \boldsymbol{e}^{A}_{i})\boldsymbol{e}^{A}_{i} \otimes \boldsymbol{e}^{A}_{j} \\ &= (\boldsymbol{e}^{A}_{i} \cdot \boldsymbol{e}^{I}_{j})\boldsymbol{e}^{A}_{i} \otimes \boldsymbol{e}^{A}_{j}. \end{aligned} \tag{A.2}$$

The comparison of Eq. (A.1) and Eq. (A.2) implies that the inverse rotation

$$\boldsymbol{R}_{IA} = \boldsymbol{R}^{-1}_{AI} = \boldsymbol{R}^{\mathrm{T}}_{AI}$$

is equal to the transpose of $\boldsymbol{R}_{AI}$.

As $\boldsymbol{e}^{I}_{i}$ spans the basis I and $\boldsymbol{e}^{A}_{i}$ spans the basis A, each vector $\boldsymbol{v}$ can be decomposed into a linear combination

$$\boldsymbol{v} = (\boldsymbol{v} \cdot \boldsymbol{e}^{I}_{i})\boldsymbol{e}^{I}_{i} = v^{I}_{i}\, \boldsymbol{e}^{I}_{i}, \tag{A.3}$$

spanned by the basis of I with coordinates $v^{I}_{i} := (\boldsymbol{v} \cdot \boldsymbol{e}^{I}_{i})$, or into the linear combination

$$\boldsymbol{v} = (\boldsymbol{v} \cdot \boldsymbol{e}^{A}_{i})\boldsymbol{e}^{A}_{i} = v^{A}_{i}\, \boldsymbol{e}^{A}_{i},$$

w.r.t. basis of A and coordinates $v^{A}_{i} := (\boldsymbol{v} \cdot \boldsymbol{e}^{A}_{i})$. For any given vector $\boldsymbol{v}$, the rotation $\boldsymbol{R}_{AI}$ induces a rotated vector

$$\boldsymbol{v}' = \boldsymbol{R}_{AI}\, \boldsymbol{v} = (\boldsymbol{v} \cdot \boldsymbol{e}^{I}_{i})\boldsymbol{e}^{A}_{i} = v'^{A}_{i}\, \boldsymbol{e}^{A}_{i}. \tag{A.4}$$

The comparison of Eq. (A.3) and (A.4) implies the I-coordinates of the vector $\boldsymbol{v}$ and the A-coordinates of the rotated vector $\boldsymbol{v}' = \boldsymbol{R}_{AI}\,\boldsymbol{v}$ are equal, i.e., ${}_A\boldsymbol{v}' = {}_I\boldsymbol{v}$ holds, see Figure A.2.

As the rotation $\boldsymbol{R}_{AI}$ intrinsically induces a rotated A-frame, the vector $\boldsymbol{v}$ can be expressed in both I- and A-coordinates. Expressing the vector $\boldsymbol{v} = v_i^A\,\boldsymbol{e}_i^A$ as linear combination with respect to the A-basis, one obtains after applying the coordinate map $\mathscr{K}_I$

$$ {}_I\boldsymbol{v} = v_i^A\,{}_I\boldsymbol{e}_i^A = v_i^A\,{}_I(\boldsymbol{R}_{AI}\,\boldsymbol{e}_i^I) = v_i^A\,{}_I\boldsymbol{R}_{AI}\,{}_I\boldsymbol{e}_i^I = {}_I\boldsymbol{R}_{AI}\,{}_A\boldsymbol{v}, $$

from which

$$ \boldsymbol{A}_{IA} = {}_I\boldsymbol{R}_{AI} $$

is deduced. In summary, the transformation matrix $\boldsymbol{A}_{IA}$ is connected with the rotation $\boldsymbol{R}_{AI}$ by the components $A_{IA,ij} = R_{AI,ij}$.

$$\begin{tikzcd}
 & \boldsymbol{v} \arrow[rr, "\boldsymbol{R}_{AI}"] \arrow[dl, "\mathscr{K}_A"'] \arrow[dr, "\mathscr{K}_I"] & & \boldsymbol{v}' \arrow[dl, "\mathscr{K}_A"'] \\
{}_A\boldsymbol{v} \arrow[rr, "\boldsymbol{A}_{IA}"'] & & {}_I\boldsymbol{v} = {}_A\boldsymbol{v}' &
\end{tikzcd}$$

Figure A.2: Rotation vs. transformation

A.5 Relative rotations

Introducing rotations $\boldsymbol{R}_{AI}$, $\boldsymbol{R}_{BI}$, we obtain the rotation and transformation matrices

$$ {}_I\boldsymbol{R}_{AI} = {}_A\boldsymbol{R}_{AI} = \boldsymbol{A}_{IA} $$
$$ {}_I\boldsymbol{R}_{BI} = {}_B\boldsymbol{R}_{BI} = \boldsymbol{A}_{IB}. $$

The relative rotation $\boldsymbol{R}_{BA}$ from A to B is defined as

$$ \boldsymbol{R}_{BA} := \delta_{ij}\,\boldsymbol{e}_i^B \otimes \boldsymbol{e}_i^A = \boldsymbol{R}_{BI}\,\boldsymbol{R}_{AI}^{\mathrm{T}} $$

with associated rotation and transformation matrices

$$ {}_A\boldsymbol{R}_{BA} = {}_B\boldsymbol{R}_{BA} = \boldsymbol{A}_{AB}. $$

$$\begin{tikzcd}
& I \arrow[dl, "\boldsymbol{R}_{AI}"'] \arrow[dr, "\boldsymbol{R}_{BI}"] & \\
A \arrow[rr, "\boldsymbol{R}_{BA}"'] & & B
\end{tikzcd}$$

Figure A.3: Relative rotations

The rotation $\boldsymbol{R}_{BI}$ can be constructed by rotating $\boldsymbol{e}_i^I$ onto $\boldsymbol{e}_i^A$, which are subsequently rotated onto $\boldsymbol{e}_i^B$ and yields

$$\boldsymbol{R}_{BI} = \boldsymbol{R}_{BA}\,\boldsymbol{R}_{AI},$$

see Figure A.3. Often, one searches for absolute orientations with respect to a reference frame I, expressed in I-coordinates, i.e.,

$$\begin{aligned}
{}_I\boldsymbol{R}_{BI} &= {}_I\boldsymbol{R}_{BA}\,{}_I\boldsymbol{R}_{AI} \\
&= \boldsymbol{A}_{IA}\,{}_A\boldsymbol{R}_{BA}\,\boldsymbol{A}_{IA}^{\mathrm{T}}\,{}_I\boldsymbol{R}_{AI} \\
&= \boldsymbol{A}_{IA}\,{}_A\boldsymbol{R}_{BA}\,\boldsymbol{A}_{IA}^{\mathrm{T}}\,\boldsymbol{A}_{IA} \\
&= \boldsymbol{A}_{IA}\,\boldsymbol{A}_{AB} \\
&= \boldsymbol{A}_{IB},
\end{aligned}$$

which also can be written as

$${}_I\boldsymbol{R}_{BI} = {}_I\boldsymbol{R}_{AI}\,{}_A\boldsymbol{R}_{BA}.$$

Introducing parameters $\boldsymbol{\varphi}$, it is convenient to parametrize rotations $\boldsymbol{R}_{BA}(\boldsymbol{\varphi})$, in coordinates $R^A_{BA,ij}(\boldsymbol{\varphi}) = R_{BA,ij}(\boldsymbol{\varphi})$, such that

$$\boldsymbol{R}_{BA}(\boldsymbol{\varphi}) = R_{BA,ij}(\boldsymbol{\varphi})\,\boldsymbol{e}_i^A \otimes \boldsymbol{e}_j^A$$

holds, which also implies

$${}_A\boldsymbol{R}_{BA}(\boldsymbol{\varphi}) = \boldsymbol{A}_{AB}(\boldsymbol{\varphi}).$$

A.6 Tensor stacking

To shorten expressions, ‘matrix notation’ for tensors is used. Bold capital letters $\boldsymbol{A}, \boldsymbol{B}, \boldsymbol{C}, \boldsymbol{D} \in L(\mathbb{E}^3;\mathbb{E}^3)$ imply bilinear mappings. Bold lower case letters $\boldsymbol{a}, \boldsymbol{b}, \boldsymbol{u}, \boldsymbol{v} \in \mathbb{E}^3$

denote elements of the euclidean space $\mathbb{E}^3$. In Chapter 3 the following properties are used.

Property 1:

$$\begin{bmatrix} \boldsymbol{a} \\ \boldsymbol{b} \end{bmatrix}^{\mathrm{T}} \cdot \begin{bmatrix} \boldsymbol{u} \\ \boldsymbol{v} \end{bmatrix} := \boldsymbol{a} \cdot \boldsymbol{u} + \boldsymbol{b} \cdot \boldsymbol{v} \in \mathbb{R}$$

Property 2:

$$\begin{bmatrix} \boldsymbol{A} & \boldsymbol{B} \\ \boldsymbol{C} & \boldsymbol{D} \end{bmatrix} \begin{bmatrix} \boldsymbol{u} \\ \boldsymbol{v} \end{bmatrix} := \begin{bmatrix} \boldsymbol{A}\boldsymbol{u} + \boldsymbol{B}\boldsymbol{v} \\ \boldsymbol{C}\boldsymbol{u} + \boldsymbol{D}\boldsymbol{v} \end{bmatrix} \in \mathbb{E}^{3+3}$$

Property 3:

$$\begin{bmatrix} \boldsymbol{a} \\ \boldsymbol{b} \end{bmatrix}^{\bullet} := \begin{bmatrix} \dot{\boldsymbol{a}} \\ \dot{\boldsymbol{b}} \end{bmatrix}$$

APPENDIX B

Supplementary material

B.1 Integrals

To evaluate the Melnikov expressions $\mathscr{I}_1$ and $\mathscr{I}_2$ from Eq. (5.53) and Eq. (5.54), respectively, the expressions can be decomposed into four sub-integrals presented in this Appendix.

The corresponding definite integrals I_1, I_2, I_3 and I_4 are defined and yield

$$I_1 := \int_{-\frac{\pi}{2}}^{3\frac{\pi}{2}} \sqrt{2(\mathrm{s}\gamma+1)}\,\mathrm{d}\gamma = 8,$$

$$I_2 := \int_{-\frac{\pi}{2}}^{3\frac{\pi}{2}} \sqrt{2(\mathrm{s}\gamma+1)}\mathrm{s}\gamma\,\mathrm{d}\gamma = \frac{8}{3},$$

$$I_3 := \int_{-\frac{\pi}{2}}^{3\frac{\pi}{2}} \sqrt{2(\mathrm{s}\gamma+1)}\mathrm{c}^2\gamma\,\mathrm{d}\gamma = \frac{64}{15},$$

and

$$I_4 := \int_{-\frac{\pi}{2}}^{3\frac{\pi}{2}} \sqrt{2(\mathrm{s}\gamma+1)}\mathrm{s}\gamma\,\mathrm{c}^2\gamma\,\mathrm{d}\gamma = \frac{64}{105}.$$

B.2 Projected dynamics

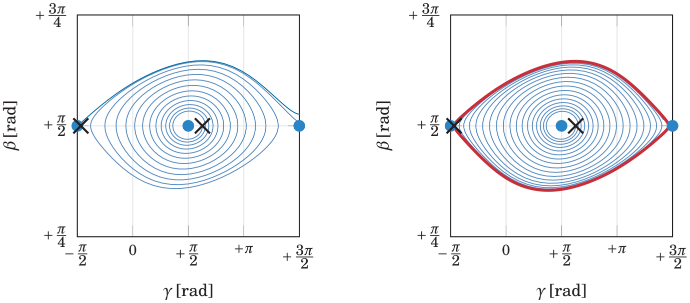

(a) $\Omega = \Omega_\mathrm{h} - 0.1\,\frac{\mathrm{rad}}{\mathrm{s}}$ (b) $\Omega = \Omega_\mathrm{h} + 0.01\,\frac{\mathrm{rad}}{\mathrm{s}} \approx \Omega_\mathrm{h}$

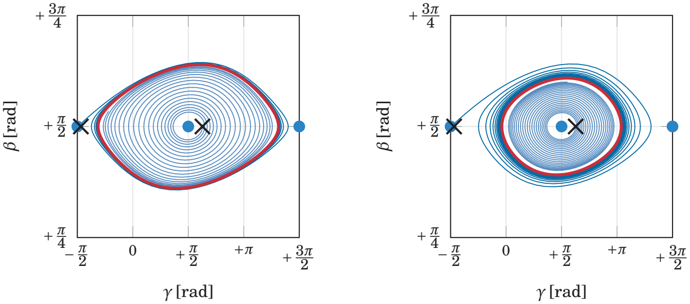

(c) $\Omega = \Omega_\mathrm{h} + 0.1\,\frac{\mathrm{rad}}{\mathrm{s}}$ (d) $\Omega = \Omega_\mathrm{c} - 0.5\,\frac{\mathrm{rad}}{\mathrm{s}}$

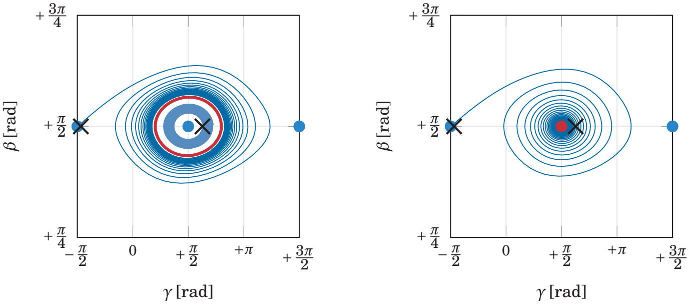

(e) $\Omega = \Omega_\mathrm{c} - 0.2\,\frac{\mathrm{rad}}{\mathrm{s}}$ (f) $\Omega = \Omega_\mathrm{c} + 0.5\,\frac{\mathrm{rad}}{\mathrm{s}}$

Figure B.1: Projection of the three-dimensional dynamics from Figure 5.2 onto the β-γ-plane. Unstable inverted or non-inverted equilibria are indicated by blue dots, while a stable inverted spinning equilibrium is marked in red. The blue orbits result from transient simulations and are initialized at the black crosses, which are not necessarily on the slow manifold. Both the stable periodic limit cycles and the heteroclinic saddle connections, are obtained by applying numerical shooting. The corresponding bifurcation diagram is shown in Figure 5.3.

(a) $\Omega = \Omega_\mathrm{h} - 0.1\,\frac{\mathrm{rad}}{\mathrm{s}}$ (b) $\Omega = \Omega_\mathrm{h} + 0.01\,\frac{\mathrm{rad}}{\mathrm{s}} \approx \Omega_\mathrm{h}$

(c) $\Omega = \Omega_\mathrm{h} + 0.1\,\frac{\mathrm{rad}}{\mathrm{s}}$ (d) $\Omega = \Omega_\mathrm{c} - 0.5\,\frac{\mathrm{rad}}{\mathrm{s}}$

(e) $\Omega = \Omega_\mathrm{c} - 0.2\,\frac{\mathrm{rad}}{\mathrm{s}}$ (f) $\Omega = \Omega_\mathrm{c} + 0.5\,\frac{\mathrm{rad}}{\mathrm{s}}$

Figure B.2: Mapping of the two-dimensional slow dynamics from Figure 5.6 onto the unit sphere. If the inclination angle β and the rolling angle γ are interpreted as spherical coordinates, where γ takes the role of the polar and β that of the azimuthal coordinate, respectively, the heteroclinic saddle connection becomes homoclinic. Initial conditions are resembled by crosses. The black dots denote the north and south poles of the spheres implying a horizontal orientated disk. Configurations on the black dashed equator corresponds to a vertically inclined tippedisk. The unstable non-inverted spinning equilibrium is located on the left rear side of the sphere and is represented by a blue dot. The inverted spinning equilibrium is located at the front right and is shown as a blue or red dot, depending on whether it is unstable or stable.

Bibliography

[1] V. Acary and B. Brogliato. *Numerical Methods for Nonsmooth Dynamical Systems: Applications in Mechanics and Electronics*, volume 35 of *Lecture Notes in Applied and Computational Mechanics*. Springer Verlag, Berlin, 2008.

[2] E. L. Allgower and K. Georg. *Numerical Continuation Methods: An Introduction*, volume 13 of *Springer Series in Computational Mathematics*. Springer Verlag, Berlin, Heidelberg, 1 edition, 1990.

[3] E. L. Allgower and K. Georg. *Introduction to Numerical Continuation Methods*. Society for Industrial and Applied Mathematics, 2003.

[4] A. A. Andronov, E. A. Leontovich, I. I. Gordon, and A. G. Maier. Theory of Bifurcations of Dynamical Systems on a Plane. *Israel Program for Scientific Translations, Jerusalem*, 1971.

[5] M. Antali and G. Stépán. On the nonsmooth dynamics of towed wheels. *Meccanica*, 55(12):2523–2540, 2020.

[6] M. Antali, G. Stépán, and S. J. Hogan. Kinematic oscillations of railway wheelsets. *Multibody Syst Dyn*, 34:259–274, 2015.

[7] P. Appell. Sur L'intégration des équations du mouvement d'un corps pesant de révolution roulant par une arête circulaire sur un plan horizontal; cas particulier du cerceau. *Rendiconti del Circolo Matematico di Palermo (1884-1940)*, 14:1–6, 1900.

[8] M. S. Ashbaugh, C. C. Chicone, and R. H. Cushman. The twisting tennis racket. *J. Dyn. Differ. Equ.*, 3(1):67–85, 1991.

[9] M. Batista. Steady motion of a rigid disk of finite thickness on a horizontal plane. *Int J Non Linear Mech*, 41(4):605–621, 2006.

[10] M. Batista. The nearly horizontally rolling of a thick disk on a rough plane. *Regul. Chaot. Dyn.*, 13:344–354, 2008.

[11] F. Bayer and R. I. Leine. Sorting-free Hill-based stability analysis of periodic solutions through Koopman analysis. *Nonlinear Dyn*, 111:8439–8466, 2023.

[12] K. Y. Billah and R. H. Scanlan. Resonance, Tacoma Narrows bridge failure, and undergraduate physics textbooks. *Am. J. Phys.*, 59(2):118–124, 02 1991.

[13] I. A. Bizyaev and I. S. Mamaev. Permanent Rotations in Nonholonomic Mechanics. Omnirotational Ellipsoid. *Regul. Chaot. Dyn.*, 27(6):587–612, 2022.

[14] A. M. Bloch. *Nonholonomic Mechanics and Control. Interdisciplinary Applied Mathematics*, volume 24. Springer, New York, 2003.

[15] A. M. Bloch, J. E. Marsden, and D. V. Zenkov. Nonholonomic Dynamics. *Notices of the AMS*, 52(3):320–329, 2005.

[16] A. V. Borisov and A. P. Ivanov. Dynamics of the Tippe Top on a Vibrating Base. *Regul. Chaot. Dyn.*, 25(6):707–715, 2020.

[17] A. V. Borisov, A. A. Kilin, and Y. L. Karavaev. Retrograde motion of a rolling disk. *Phys.-Usp.*, 60(9):931, 2017.

[18] A. V. Borisov and I. S. Mamaev. Strange attractors in rattleback dynamics. *Phys.-Usp.*, 46(4):393, 2003.

[19] A. V. Borisov, I. S. Mamaev, and A. A. Kilin. Dynamics of rolling disk. *Regul. Chaot. Dyn.*, 8(2):201–212, 2003.

[20] N. M. Bou-Rabee, J. E. Marsden, and L. A. Romero. Tippe Top Inversion as a Dissipation-Induced Instability. *SIAM J. Appl. Dyn. Syst.*, 3(3):352–377, 2004.

[21] C. M. Braams. The Symmetrical Spherical Top. *Nature*, 170:31, 1952.

[22] M. Branicki, H. K. Moffatt, and Y. Shimomura. Dynamics of an axisymmetric body spinning on a horizontal surface. III. Geometry of steady state structures for convex bodies. *Proc. R. Soc. A.*, 462(2066):371–390, 2006.

[23] M. Branicki and Y. Shimomura. Dynamics of an axisymmetric body spinning on a horizontal surface. IV. Stability of steady spin states and the 'rising egg' phenomenon for convex axisymmetric bodies. *Proc. R. Soc. A.*, 462(2075):3253–3275, 2006.

[24] H. Bremer. *Dynamik und Regelung mechanischer Systeme*, volume 67. Vieweg+Teubner Verlag, Wiesbaden, 1988.

[25] B. Brogliato. Inertial couplings between unilateral and bilateral holonomic constraints in frictionless Lagrangian systems. *Multibody Syst Dyn*, 29(3):289–325, 2013.

[26] B. Brogliato. *Nonsmooth Mechanics. Models, Dynamics and Control*. Communications and Control Engineering. Springer, Cham, 3rd edition, 2016.

[27] I. N. Bronshtein and K. A. Semendyayev. *Analytic Geometry*, pages 235–276. Springer, New York, NY, 1973.

[28] S. A. Chaplygin. On a motion of a heavy body of revolution on a horizontal plane. *Regul. Chaot. Dyn.*, 7(2):119–130, 2002.

[29] M. C. Ciocci and B. Langerock. Dynamics of the tippe top via Routhian reduction. *Regul. Chaot. Dyn.*, 12(6):602–614, 2007.

[30] F. H. Clarke, Y. S. Ledyaev, R. J. Stern, and P. R. Wolenski. *Nonsmooth Analysis and Control Theory*, volume 178. Springer, New York, NY, 2008.

[31] R. J. Cohen. The tippe top revisited. *Am. J. Phys.*, 45(1):12–17, 1977.

[32] R. Cross. Why does a spinning egg rise? *Eur. J. Phys.*, 39(2):025002, 2018.

[33] S. R. Eugster and C. Glocker. On the notion of stress in classical continuum mechanics. *MEMOCS*, 5(3-4):299–338, 2017.

[34] N. Fenichel. Geometric singular perturbation theory for ordinary differential equations. *J Differ Equ*, 31(1):53–98, 1979.

[35] N. Fenichel and J. K. Moser. Persistence and Smoothness of Invariant Manifolds for Flows. *Indiana Univ. Math. J.*, 21(3):193–226, 1971.

[36] G. Floquet. Sur les équations différentielles linéaires à coefficients périodiques. *Ann. Sci. de l'Ecole Norm. Superieure*, 2e série, 12:47–88, 1883.

[37] A. D. Fokker. The rising top, experimental evidence and theory. *Physica*, 8(6):591–596, 1941.

[38] E. G. Gallop. On the rise of a spinning top. *Trans. Camb. Phil. Soc*, 19:356–373, 1904.

[39] Z. Gan, Y. Yesilevskiy, P. Zaytsev, and C. D. Remy. All common bipedal gaits emerge from a single passive model. *J. R. Soc. Interface.*, 15(146):20180455, 2018.

[40] A. Garcia and M. Hubbard. Spin reversal of the rattleback: theory and experiment. *Proc. R. Soc. Lond. A*, 418(1854):165–197, 1988.

[41] V. K. Garg and R. V. Dukkipati. *Dynamics of Railway Vehicle Systems*. Academic Press, London, 1984.

[42] S. Garrido-Jurado, R. Muñoz-Salinas, F. J. Madrid-Cuevas, and M. J. Marín-Jiménez. Automatic generation and detection of highly reliable fiducial markers under occlusion. *Pattern Recognition*, 47(6):2280–2292, 2014.

[43] C. W. Gear, B. Leimkuhler, and G. K. Gupta. Automatic integration of Euler-Lagrange equations with constraints. *Comp. Appl. Math.*, 12:77–90, 1985.

[44] C. Glocker. *Set-valued Force Laws: Dynamics of Non-smooth Systems*, volume 1 of *Lecture Notes in Applied Mechanics*. Springer, Berlin, 2001.

[45] C. Glocker. Simulation of Hard Contacts with Friction: An Iterative Projection Method. In A. Johann, H.-P. Kruse, F. Rupp, and S. Schmitz, editors, *Recent Trends in Dynamical Systems*, pages 493–515. Springer, Basel, 2013.

[46] A. S. Gonchenko, S. V. Gonchenko, and A. O. Kazakov. Richness of chaotic dynamics in nonholonomic models of a celtic stone. *Regul. Chaot. Dyn.*, 18:521–538, 2013.

[47] Grand Illusions. Orbit Spinning Tops — youtube.com. `https://www.youtube.com/watch?v=9pV7iaaR1QY`, 2013. [Accessed 26-May-2023].

[48] J. Guckenheimer and P. Holmes. *Nonlinear Oscillations, Dynamical Systems, and Bifurcations of Vector Fields*, volume 42. Springer New York, NY, 2013.

[49] E. Hairer and G. Wanner. *Solving Ordinary Differential Equations II*. Springer, Berlin Heidelberg, 2002.

[50] J. Harsch, G. Capobianco, S. R. Eugster, and R. I. Leine. A nonsmooth RATTLE algorithm for mechanical systems with frictional unilateral constraints. *NAHS*, 2023.

[51] J. Harsch, S. Sailer, and S. R. Eugster. A total Lagrangian, objective and intrinsically locking-free Petrov–Galerkin SE(3) Cosserat rod finite element formulation. *Int. J. Numer. Methods Eng.*, 124(13):2965–2994, 2023.

[52] E. G. Hemingway and O. M. O'Reilly. Perspectives on Euler angle singularities, gimbal lock, and the orthogonality of applied forces and applied moments. *Multibody Syst Dyn*, 44(1):31–56, 2018.

[53] P. J. Holmes. Averaging and Chaotic Motions in Forced Oscillations. *SIAM J. Appl. Math.*, 38(1):65–80, 1980.

[54] P. J. Holmes and J. E. Marsden. Melnikov's method and Arnold diffusion for perturbations of integrable Hamiltonian systems. *J. Math. Phys.*, 23(4):669–675, 1982.

[55] P. J. Holmes and D. A. Rand. Bifurcations of the forced van der Pol oscillator. *Q Appl Math*, 35(4):495–509, 1978.

[56] P. J. Holmes and D. Whitley. On the attracting set for Duffing's equation: II. A geometrical model for moderate force and damping. *Physica D: Nonlinear Phenomena*, 7(1):111–123, 1983.

[57] A. Hurwitz. On the conditions under which an equation has only roots with negative real parts. *Selected papers on mathematical trends in control theory*, 65:273–284, 1964.

[58] M. Jean. The non-smooth contact dynamics method. *Comput. Methods Appl. Mech. Eng.*, 177(3):235–257, 1999.

[59] J. H. Jellett. *A Treatise on the Theory of Friction*. Hodges Foster, Leuven, 1872.

[60] C. Jones. Geometric Singular Perturbation Theory in Dynamical Systems, Montecatini Terme. In L. Arnold, editor, *Lecture Notes in Mathematics*, volume 1609. Springer-Verlag, Berlin, 1994.

[61] A. V. Karapetyan and A. A. Zobova. Tippe-top on visco-elastic plane: steady-state motions, generalized smale diagrams and overturns. *Lobachevskii J Math*, 38(6):1007–1013, 2017.

[62] P. Kessler and O. M. O'Reilly. The ringing of Euler's disk. *Regul. Chaot. Dyn.*, 7(1):49–60, 2002.

[63] H. K. Khalil. *Nonlinear Systems*. Pearson Education, London, 3rd edition, 2002.

[64] H. K. Khalil. *Lyapunov's Stability Theory*, pages 685–690. Springer, London, 2015.

[65] A. A. Kilin and E. N. Pivovarova. The influence of the first integrals and the rolling resistance model on tippe top inversion. *Nonlinear Dyn*, 103(1):419–428, 2021.

[66] A. A. Kilin and E. N. Pivovarova. Dynamics of an Unbalanced Disk with a Single Nonholonomic Constraint. *Regul. Chaot. Dyn.*, 28(1):78–106, 2023.

[67] C. Kuehn. *Multiple Time Scale Dynamics*, volume 191. Springer, Cham, 2015.

[68] Y. A. Kuznetsov. Elements of Applied Bifurcation Theory. In *Applied Mathematical Sciences*, volume 112. Springer, New York, 2004.

[69] J. L. Lagrange. *Mécanique Analytique*, volume 1. Mallet-Bachelier, Paris, 1853.

[70] C. Le Saux, R. I. Leine, and C. Glocker. Dynamics of a Rolling Disk in the Presence of Dry Friction. *J Nonlinear Sci*, 15(1):27–61, 2005.

[71] R. I. Leine. Experimental and theoretical investigation of the energy dissipation of a rolling disk during its final stage of motion. *Arch Appl Mech*, 79(11):1063–1082, 2009.

[72] R. I. Leine, G. Capobianco, P. Bartelt, M. Christen, and A. Caviezel. Stability of rigid body motion through an extended intermediate axis theorem: application to rockfall simulation. *Multibody Syst. Dyn.*, 52(4):431–455, 2021.

[73] R. I. Leine and C. Glocker. A set-valued force law for spatial Coulomb–Contensou friction. *Eur. J. Mech. A*, 22(2):193–216, 2003.

[74] R. I. Leine and H. Nijmeijer. *Dynamics and Bifurcations of Non-Smooth Mechanical Systems*, volume 18 of *Lecture Notes in Applied and Computational Mechanics*. Springer, Berlin, 2013.

[75] R. I. Leine and N. van de Wouw. *Stability and Convergence of Mechanical Systems with Unilateral Constraints*, volume 36 of *Lecture Notes in Applied and Computational Mechanics*. Springer, Berlin, 2008.

[76] J. Lunze. *Regelungstechnik 1*, volume 10. Springer, Heidelberg, 2013.

[77] K. Magnus. *Kreisel*. Springer, Berlin, 1971.

[78] K. Magnus. Zur Theorie der Keltischen Wackelsteine. *Zeitschrift für angewandte Mathematik und Mechanik*, 5:54–55, 1974.

[79] A. J. McDonald and K. T. McDonald. The rolling motion of a disk on a horizontal plane, 2002.

[80] V. K. Melnikov. On the stability of the center for time periodic perturbations. *Tr. Mosk. Mat. Obs.*, 12:3–52, 1963.

[81] H. K. Moffatt. Euler's disk and its finite-time singularity. *Nature*, 404(6780):833–834, 2000.

[82] H. K. Moffatt and Y. Shimomura. Spinning eggs — a paradox resolved. *Nature*, 416(6879):385–386, 2002.

[83] H. K. Moffatt, Y. Shimomura, and M. Branicki. Dynamics of an axisymmetric body spinning on a horizontal surface. I. Stability and the gyroscopic approximation. *Proc. R. Soc. A.*, 460(2052):3643–3672, 2004.

[84] J. J. Moreau. Bounded Variation in Time. In J. J. Moreau, P. D. Panagiotopoulos, and G. Strang, editors, *Topics in Nonsmooth Mechanics*, pages 1–74. Birkhäuser Verlag, Basel, 1988.

[85] J. J. Moreau. Unilateral contact and dry friction in finite freedom dynamics. In J. J. Moreau and P. D. Panagiotopoulos, editors, *Non-Smooth Mechanics and Applications*, volume 302 of *CISM Courses and Lectures*, pages 1–82. Springer, Wien, 1988.

[86] A. H. Nayfeh and B. Balachandran. *Applied Nonlinear Dynamics: Analytical, Computational, and Experimental Methods*. John Wiley & Sons, Weinheim, 2008.

[87] G. Nützi. *Non-Smooth Granular Rigid Body Dynamics with Applications to Chute Flows*. PhD thesis, ETH Zurich, 2016.

[88] S. O'Brien and J. L. Synge. The Instability of the Tippe-Top Explained by Sliding Friction. *Proc. R. Ir. Acad. Secti. A, Math. Astron. Phys. Sci.*, 56:23–35, 1953.

[89] M. G. Olsson. Coin spinning on a table. *Am. J. Phys.*, 40(10):1543–1545, 1972.

[90] A. C. Or. The dynamics of a tippe top. *SIAM J. Appl. Math.*, 54(3):597–609, 1994.

[91] O. M. O'Reilly. The dynamies of rolling disks and sliding disks. *Nonlinear Dyn*, 10(3):287–305, 1996.

[92] H. B. Pacejka. The wheel shimmy phenomenon: a theoretical and experimental investigation with particular reference to the non-linear problem. 1966.

[93] J. G. Papastavridis. *Analytical Mechanics: A Comprehensive Treatise On The Dynamics Of Constrained Systems (Reprint Edition)*. World Scientific, New Jersey, 2014.

[94] P. Paris and L. Zhang. A disk rolling on a horizontal surface without slip. *Math. Comput. Model.*, 36(7-8):855–860, 2002.

[95] F. Pfeiffer and C. Glocker. *Multibody Dynamics with Unilateral Contacts*. John Wiley & Sons, Weinheim, 1996.

[96] F. Pfeiffer and T. Schindler. *Einführung in die Dynamik*. Springer, Berlin, 2014.

[97] L. Poinsot. *Theorie Nouvelle de la Rotation des Corps*. Bachelier, Paris, 1834.

[98] L. Polcar and O. Semerák. Free motion around black holes with discs or rings: Between integrability and chaos. VI. The Melnikov method. *Phys. Rev. D*, 100(10):103013, 2019.

[99] M. Przybylska and S. Rauch-Wojciechowski. Dynamics of a rolling and sliding disk in a plane. Asymptotic solutions, stability and numerical simulations. *Regul. Chaot. Dyn.*, 21(2):204–231, 2016.

[100] J. Rankin, E. Coetzee, B. Krauskopf, and M. Lowenberg. Bifurcation and stability analysis of aircraft turning on the ground. *J. Guid. Control Dyn.*, 32(2):500–511, 2009.

[101] S. Rauch-Wojciechowski. What does it mean to explain the rising of the tippe top? *Regul. Chaot. Dyn.*, 13(4):316–331, 2008.

[102] S. Rauch-Wojciechowski and M. Przybylska. Understanding reversals of a rattleback. *Regul. Chaot. Dyn.*, 22(4):368–385, 2017.

[103] R. T. Rockafellar. *Convex Analysis*. Princeton Landmarks in Mathematics. Princeton University Press, Princeton, New Jersey, 1970.

[104] E. J. Routh. *A Treatise on the Stability of a Given State of Motion, Particularly Steady Motion, Being the Essay to which the Adams Prize was Adjudged in 1877, in the University of Cambridge*. Macmillan and Co., London, 1877.

[105] E. J. Routh. *The Advanced Part of A Treatise on the Dynamics of a System of Rigid Bodies: Being Part II of a Treatise on the Whole Subject. With Numerous Examples*. Macmillan and Co., London, 1905.

[106] L. Ruby. Applications of the Mathieu equation. *Am. J. Phys.*, 64(1):39–44, 1996.

[107] S. Sailer, S. R. Eugster, and R. I. Leine. The tippedisk: a tippetop without rotational symmetry. *Regul. Chaot. Dyn.*, 25(6):553–580, 2020.

[108] S. Sailer, S. R. Eugster, and R. I. Leine. The tippedisk: A minimal model for friction-induced inversion. In *Proceedings of the ECCOMAS Thematic Conference on Multibody Dynamics, Budapest*, 2021.

[109] S. Sailer and R. Leine. A complete stability chart for the tippedisk. In *Proceedings of the NODYCON 2023 Conference, Rome*, 2023.

[110] S. Sailer and R. I. Leine. Model reduction of the tippedisk: a path to the full analysis. *Nonlinear Dyn*, 105(3):1955–1975, 2021.

[111] S. Sailer and R. I. Leine. Singularly perturbed dynamics of the tippedisk. *Proc. R. Soc. A*, 477(2256), 2021.

[112] S. Sailer and R. I. Leine. Why does the tippedisk invert? Theory and experiments. In *Proceedings of the ENOC 2020+2 Conference, Lyon*, 2022.

[113] S. Sailer and R. I. Leine. Heteroclinic bifurcation analysis of the tippedisk through the use of Melnikov theory. *Proc. R. Soc. A*, 2023.

[114] R. Seydel. *Practical Bifurcation and Stability Analysis*, volume 5 of *Interdisciplinary Applied Mathematics*. Springer, New York, 2009.

[115] E. Shchepakina, V. Sobolev, and M. P. Mortell. *Singular Perturbations*, volume 2114 of *Lecture Notes in Mathematics*. Springer, Cham, 2014.

[116] Y. Shimomura, M. Branicki, and H. K. Moffatt. Dynamics of an axisymmetric body spinning on a horizontal surface. II. Self-induced jumping. *Proc. R. Soc. A.*, 461(2058):1753–1774, 2005.

[117] H. Sperl. Patentschrift nr. 63261: Wendekreisel. *Kaiserliches Patentamt Berlin*, 1892.

[118] A. Steindl, J. Edelmann, and M. Plöchl. Limit cycles at oversteer vehicle. *Nonlinear Dyn*, 99(1):313–321, 2020.

[119] S. H. Strogatz. *Nonlinear Dynamics and Chaos with Student Solutions Manual: With Applications to Physics, Biology, Chemistry, and Engineering*. CRC press, Boca Raton, 2018.

[120] A. Tesi, E. H. Abed, R. Genesio, and H. O. Wang. Harmonic balance analysis of period-doubling bifurcations with implications for control of nonlinear dynamics. *Automatica*, 32(9):1255–1271, 1996.

[121] T. Theodorsen. General theory of aerodynamic instability and the mechanism of flutter. Technical report, 1949.

[122] L. N. Trefethen, Á. Birkisson, and T. A. Driscoll. *Exploring ODEs*. SIAM, Philadelphia, 2018.

[123] H. True. Dynamics of a rolling wheelset. *ASME. Appl. Mech. Rev.*, 46(7):438–444, 1993.

[124] C. Ucke. *Physics, toys and art*, page 96. 2004.

[125] F. Verhulst. Methods and Applications of Singular Perturbations: Boundary Layers and Multiple Timescale Dynamics. In *Texts in Applied Mathematics*, volume 50. Springer, New York, 2005.

[126] F. Verhulst. Singular perturbation methods for slow–fast dynamics. *Nonlinear Dyn*, 50(4):747–753, 2007.

[127] Veritasium. Spinning Disk Trick — youtube.com. `https://www.youtube.com/watch?v=hOSZZTBQmEs`, 2012. [Accessed 26-May-2023].

[128] Veritasium. Spinning Disk Trick Solution — youtube.com. `https://www.youtube.com/watch?v=tDr26U49_VA`, 2012. [Accessed 26-May-2023].

[129] G. Walker. The quarterly journal of pure and applied mathematics. chapter On a Dynamical Top, pages 175–184. Longmans, London, 1896.

[130] S. Wiggins. *Normally Hyperbolic Invariant Manifolds in Dynamical Systems*, volume 105 of *Applied Mathematical Sciences*. Springer, New York, 1994.

[131] S. Wiggins. *Introduction to Applied Nonlinear Dynamical Systems and Chaos*, volume 2 of *Texts in Applied Mathematics*. Springer, New York, 2003.

[132] J. Wittenburg. *Dynamics of Systems of Rigid Bodies*, volume 33 of *Leitfäden der angewandten Mathematik und Mechanik*. Teubner, Stuttgart, 1977.